Performance Optimization of Pd-Ag Based Catalytic Membrane Reformer for 'On-Site' Hydrogen Production via Methanol Steam Reforming

A thesis

submitted in partial fulfillment of the requirements

for the degree of

DOCTOR OF PHILOSOPHY

by

Keshav Kumar

(Roll No. 176107017)

DEPARTMENT OF CHEMICAL ENGINEERING

INDIAN INSTITUTE OF TECHNOLOGY GUWAHATI

ASSAM - 781039, INDIA

JUNE 2025

Certificate

It is certified that the work contained in the thesis entitled **"Performance Optimization of Pd-Ag Based Catalytic Membrane Reformer for 'On-Site' Hydrogen Production via Methanol Steam Reforming"** submitted by **Keshav Kumar**, a student in the Department of Chemical Engineering, Indian Institute of Technology Guwahati, Assam-781039, India, for the award of the degree of Doctor of Philosophy, has been carried out under our supervision and this work has not been submitted elsewhere for the degree.

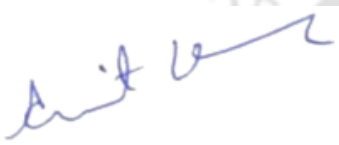

Prof. Amit Kumar
Professor
Department of Chemical Engineering
Indian Institute of Technology Guwahati
Guwahati, Assam-781039, India

Prof. Rajesh Kumar Upadhyay
Professor
Department of Chemical Engineering and Technology
Indian Institute of Technology (BHU) Varanasi
Varanasi, Uttar Pradesh-221005, India

Acknowledgments

I express profound gratitude to my supervisor, Prof. Amit Kumar, and Prof. Rajesh Kumar Upadhyay, for imparting essential knowledge about the experiments and providing continuous guidance throughout the process. Their input on the outcomes and analysis greatly aided in my comprehension of this domain. Their astute counsel enabled me to thoroughly investigate the research issues. Moreover, their time-to-time motivation to go beyond what I thought was not possible and push my limits beyond my expectations helped me to complete the work.

I sincerely express my gratitude to the Department of Chemical Engineering at the Indian Institute of Technology (IIT) Guwahati, Assam, India for providing me with the lab facilities to conduct the experiments. I would like to express my gratitude to Prof. Bishnupada Mandal, Prof. Anugrah Singh, Prof. Kaustubha Mohanty, and Prof. Subrata Kumar Majumder, who have served as the current and previous heads of the Department of Chemical Engineering, at IIT Guwahati. Their kind provision of access to the department's sophisticated infrastructure has played a crucial role in ensuring the effective execution of my research projects. Additionally, I am grateful to the Central Instrumentation Facility (CIF), IIT Guwahati, for the characterization equipment and timely analysis of my samples. My sincere thanks to my Doctoral Committee members Prof. Bishnupada Mandal (Chairman), Prof. Pankaj Tiwari, and Prof. Sandip Paul (External Member) for their critical suggestions and views during my Annual Progress Seminar. Their guidance helped me a lot to improve my experiment process and data analysis skills throughout my Ph.D. tenure. My kind appreciation to all the staff members of IIT Guwahati who helped me in any form to make my stay smooth and steady.

I express my deep gratitude to the Department of Chemical Engineering and Technology at the Indian Institute of Technology (Banaras Hindu University) Varanasi, Uttar Pradesh, India for granting me access to their laboratory facilities and essential analytical equipment for conducting my experiments and analyzing my samples during my tenure at the institute. Additionally, I would like to extend a special thanks to Prof. V. L. Yadav, the Head of the Department of Chemical Engineering and Technology at IIT (BHU), for allowing me to work there. I express my gratitude to the entire personnel of IIT (BHU) Varanasi for their prompt assistance whenever I approached them.

Acknowledgments

I want to take this opportunity to convey my sincere gratitude to Dr. Shilpi Verma from the School of Energy and Environment at Thapar Institute of Engineering and Technology in Patiala, Punjab, India. Her unwavering support, guidance, and motivation during my entire Ph.D. journey have been invaluable to me. I would like to sincerely thank Dr. Tanveer Rasool and Dr. Sashikant Kumar, Assistant Professor at the National Institute of Technology Hazratbal, Srinagar, India, for inspiring me to engage in research and pursue higher studies in Chemical Engineering immediately after completing my Bachelor's degree.

I gratefully acknowledge the financial support received from the Department of Science and Technology, India under grant agreement number TMD/CERI/MDME/2016/087 and DST/TMD-EWO/AHFC-2021/2021/200. Moreover, I would like to thank MHRD (Ministry of Human Resources and Development) for providing the assistantship during the period of my Ph.D.

I also wish to express my sincerest thanks to my present and past lab mates in the Chemical Process Engineering Laboratory both at IIT Guwahati and IIT (BHU) Varanasi for their kind suggestions and for helping me out while performing the experiments and data analysis, especially Punampriya Borgohain, Sachin Kumar Vishwakarma, Anjali Boudh, Roushni Kumari, and Kumar Shanu. Without their support and motivation, this Ph.D. journey would not have been that easy. I will also thank my seniors Dr. Richa Sharma, Dr. Lipika Kalo, Dr. Jitendra Singh Rawat, Dr. Trilokpati Tribedi, and Dr. Premsagar Pillajetti for helping me out whenever I needed.

In addition, I derive great fortitude from the persistent backing of friends and my therapists in the Energy Conversion Technology Laboratory, particularly Bibari Boro, Govind Dubey, Vishal Dhar, Sachin Kuriachan E, Shilpa Nandi, and Onkar Hemant Chowkekar. Accomplishing this thesis was a significant achievement, and it would not have been attainable without the unwavering encouragement, entertainment, various celebrations, and enjoyable experiences shared with them. I express my gratitude to every one of you for the endless humor and for consistently preventing me from excessively prioritizing my importance. Their exceptional talent for finding reasons to celebrate every occasion ensured that I never overlooked the significant aspects of life.

Just as importantly I want to acknowledge how much support my family has provided me throughout these years, despite the fact that the prospect of pursuing a Ph.D. may seem

improbable. I am eternally grateful to my family, particularly my parents, maternal grandmother, and grandfather, who have consistently supported me, whether through emotional support or by motivating me to achieve my objectives. Each accomplishment is equally theirs as it is mine. I am extremely grateful to all of my previous teachers and mentors, particularly Mr. Nagendra Kumar Choudhary and Mr. Shiv Kumar Jha, who taught me the fundamental principles of life that have facilitated my emotional, mental, and intellectual development since the very beginning of my formal education.

Finally, I would like to extend my heartfelt appreciation to all those who have assisted me during my research endeavors and provided unwavering guidance and support.

Date: 13th June, 2025 **Keshav Kumar**

Abstract

Hydrogen being the most abundant element on the earth has not been exploited to its full capacity till now. Despite having the highest energy-to-weight ratio (141.9 kJ g^{-1}) among other parallel competitors like gasoline (47.5 kJ g^{-1}) and diesel (44.5 kJ g^{-1}), the potential of hydrogen is still underutilized. The commercial exploitation of hydrogen as a renewable energy carrier has been the subject of significant effort over the past two decades. Safe storage and transportation are the primary impediments to commercialization. In order to overcome these challenges, producing and utilizing H_2 at the application site (on-site) is deemed to be advantageous. However, hydrogen is perpetually present in its compounded forms, including alcohols, water, coal, biomass, and other hydrocarbons. In order to extract hydrogen from these sources, a variety of methods are employed, including steam reforming (SR), autothermal reforming (ATR), partial oxidation (POX), pyrolysis, gasification, and fermentation. Steam reforming of hydrocarbons is the most prevalent commercial method owing to its high efficiency (70-85%). Hydrogen produced using these methods is always accompanied by gases (CO_2, CO, CH_4, N_2, and O_2). Membrane technology plays a crucial role due to its operational flexibility, ability to produce ultra-pure hydrogen, and compatibility with simultaneous reaction-separation processes, hence enhancing overall efficiency. Furthermore, they are quite practical for small-scale and portable applications and produce high-purity hydrogen at the cost of minimal energy and space. Pd-based dense composite membranes have always been the favorite for efficient hydrogen separation. From a practical standpoint, a Pd-based membrane offers high hydrogen permeability with ideally infinite selectivity. Additionally, it can operate at high temperatures and pressure for extended periods while consuming little energy and requiring little maintenance. Among different sources of H_2 generation, methanol is the simplest alcohol and has the potential to revolutionize the process of producing hydrogen onboard/onsite because of its abundance of availability, low cost, high hydrogen density, environmental friendliness, and ease of transport and storage under ambient conditions. Moreover, its energy density is 80% higher than that of liquid hydrogen, with a gravimetric and volumetric hydrogen storage capacity of 12.5 (wt%) and 99 kg m^{-3}, respectively. There is more hydrogen in a cubic meter of methanol (99 kg m^{-3}, atm) than there is in a cubic meter of liquid hydrogen (70 kg m^{-3}, 20 K), formic acid (53 kg m^{-3}, atm), H_2 compressed cylinder (39.9 kg m^{-3}, 70000 kPa), and even AlH_3 based metal-organic framework (85 kg m^{-3}, achieved in practice). Its low reforming temperature (523-623 K) due to the absence of a C-C bond also

lowers the possibility of coke production at high temperatures. The presence of the –OH functional group is also a good attribute, as it reduces the amount of water consumed in the steam reforming reaction to produce hydrogen, hence reducing the steam reforming process temperature. To fully utilize hydrogen's potential, it must be separated from methanol due to its lower heating value (119.9 MJ kg^{-1}) which is roughly 6.5 times higher than methanol's (18.1 MJ kg^{-1}). Consequently, methanol can serve as a future 'Hydrogen Carrier' that can be readily accommodated by the existing infrastructure. Hence, to integrate the simultaneous methanol steam reforming (MSR) and H_2 separation in a compact device, novel membrane reformers (MR) devices are currently being conceptualized that integrate hydrogen production and separation into a single reactor unit. The fundamentals of MR are derived from Le Chatelier's principle, which states that the continuous removal of the H_2 through the membrane shifts the thermodynamic equilibrium towards the desired product resulting in enhanced conversion.

While the basic idea behind an MR may seem straightforward, the task of combining a high-temperature, low-pressure steam reforming reaction with a low-temperature, high-pressure membrane separation process presents a significant obstacle. The heat and mass transfer limitation of the packed bed reactor limits its large-scale application, especially for endothermic reactions like MSR. Concentration polarization and the reactive nature of other gases negatively affect the membrane performance. A tradeoff between selectivity and flux needs to be tuned to attain the best possible membrane performance as well as catalytic activity. The reactor geometry, such as the membrane configuration, reactor dimensions, and reactor shape, can influence the mass transfer of reactants and products, heat transfer, and fluid dynamics within the reactor.

The main aim of the present study is to perform a comprehensive investigation of the design of membrane reformers and the production of fuel cell grade high-purity hydrogen through methanol steam reforming using Pd-Ag membrane. In order to achieve the objectives outlined earlier in Chapeter-1, a composite Pd-Ag membrane is prepared using the ELP technique over the alumina support. Multiple cycles of deposition are performed to obtain a dense Pd-Ag membrane till 400 kPaG. After the preliminary leak test, the membrane performance is examined by subjecting it to pure H_2 and N_2 under varying temperatures (573-773 K) and pressure (100-300 kPaG) conditions. The investigation also encompasses the examination of the effect of mixture gases, such as H_2/N_2, H_2/CO_2, H_2/CH_4, H_2/CO, and feed load on the performance of the membrane. In addition to this, the long-term thermal heat cycle stability of the membrane is performed to assess its potential for commercial exploitation. However, the

effect of concentration polarization significantly reduces the H_2 permeation capacity of the membrane. Therefore, a multi-pass membrane separator (MPMS) is designed to have four passes and multiple feed injection facilities to enhance the H_2 recovery from the mixture gas. This configuration not only improved the regulation of the H_2 partial pressure across the separator but also optimized the interaction between the feed gas and the membrane. MPMS performance is tuned for various locations inside the separator, baffle proximity, feed load, and membrane-to-pass ratio. The study demonstrated that multi-pass membrane separators minimize concentration polarization. Additionally, multiple membranes with baffles improved the separator performance to a higher degree compared to the same case without baffles. At last the effect of feed distribution in different pass over the separator performance was studied. It was observed that proper feed distribution is crucial to maintain the hydrogen partial pressure inside each pass. This significantly improved the overall hydrogen recovery while minimizing the effect of concentration polarization. After optimizing the MPMS, the same system is integrated with an additional membrane reformer unit to recover more hydrogen from the retentate side. The MR was packed with the SiC-foam-supported Cu-Fe/AZZ catalyst prepared via a wash-coating technique. The use of a SiC-based foam significantly reduced the heat and mass transfer issue in endothermic MSR, owing to its exceptional thermal conductivity. Initially, the performance of the MR is evaluated with varying operational parameters such as weight hourly spase velocity (WHSV), temperature (523-673 K), pressure (100-400 kPaG), and number of membranes. At last, the effect of adding MPMS is examined at the same operating parameters, and the entire system is termed a Double Stage Membrane Reformer (DSMR). A comparative study of the traditional reformer (TR), MR and DSMR is done based on the various parameters including conversion, hydrogen recovery, hydrogen yield, H_2 production rate, and overall permeate H_2 purity.

Table of Contents

Table of Contents

List of Tables

List of Tables

List of Figures

List of Figures

List of Figures

List of Figures

List of Figures

List of Abbreviations

Abbreviations	Definition
AIC	Adsorption Inhibition Coefficient
AFC	Alkaline Fuel Cell
AZZ	Alumina-Zinc-Zirconia
ALD	Atomic Layer Deposition
ATR	Autothermal Reforming
BPR	Backpressure Regulator
BJH	Barrett–Joyner–Halenda
BCC	Body-Centered Cubic
BET	Brunauer-Emmett-Teller
BFM	Bubble Flow Meter
CAPEX	Capital Expenditures
CCUS	Carbon Capture Utilization and Storage
CNTs	Carbon Nanotubes
CMC	Catalytic Methane Cracking
CV	Check Valve
CVD	Chemical Vapor Deposition
COD	Coefficient of Determination
CR	Cold Rolling

Abbreviations

CRDW	Cold Rolling and Diffusion Welding
CFD	Computational Fluid Dynamics
CDR	Condenser
CR	Cryogenic Distillation
DC	Direct current
DI	De-Ionized
DFT	Density Functional Theory
DOE	Department of Energy
DND	Detonation Nano-Diamonds
DMFC	Direct Methanol Fuel Cell
DSMR	Double-Stage Membrane Reformer
EACPC	Effective Average Concentration Polarization
EV	Electric Vehicle
ELP	Electroless Plating
ELPP	Electroless Pore Plating
EPD	Electro-Plating Deposition
EDS	Energy Dispersive Spectroscopy
EDTA	Ethylenediaminetetraacetic Acid
FCC	Face-Centered Cubic
FD	Feed Distribution
F	Filter

FBR	Fluidized Bed Reactor
GC	Gas Chromatography
GLS	Gas-Liquid Separator
HHV	Higher Heating Value
PAN	Infrared Pyrolyzed Polyacrylonitrile
IC	Internal Combustion
ID	Internal Diameter
IPCC	Intergovernmental Panel on Climate Control
IV	Isolation Valve
ELR	Left-Right Direction
LI	Level Indicator
LOHC	Liquid Organic Hydrogen Carriers
LPM	Liters Per Minute
LHV	Lower Heating Value
MFC	Mass Flow Controller
MR	Membrane Reactors
MPR	Membrane-To-Pass Ratio
MOCVD	Metal-Organic Chemical Vapor Deposition
MOF	Metal-Organic Frameworks
MSR	Methanol Steam Reforming
MOFC	Molten Carbonate Fuel Cell

MPMS	Multi-Pass Membrane Separator
MWCNTs	Multi-Walled Carbon Nanotube
NHM	National Hydrogen Mission
NV	Needle Valve
NZE	Net Zero Emission
NRV	Non-Return Valve
OPEX	Operational Expenditures
OD	Outer Diameter
OIC	Overall Inhibition Coefficient
OSR	Oxidative Steam Reforming
PB	Packed Bed
R&D	Research and Development
POX	Partial Oxidation
PAFC	Phosphoric Acid Fuel Cell
PVD	Physical Vapor Deposition
PPI	Pores Per Inch
PSS	Porous Stainless Steel
PH	Pre Heater
P_rO_x	Preferential Oxidation
PG	Pressure Gauge
PSA	Pressure Swing Adsorption

Abbreviations

PEMFCs	Proton Exchange Membrane Fuel Cells
RMM	Reformer-Membrane Module
RWGS	Reverse Water Gas Shift Reaction
SEM	Scanning Electron Microscope
SOFC	Solid Oxide Fuel Cell
SP	Spray Pyrolysis
SS	Stainless Steel
SHE	Standard Hydrogen Electrode
SMR	Steam Methane Reforming
SR	Steam Reforming
STD	Standard
TSA	Temperature Swing Adsorption
TCD	Thermal Conductivity Detector
TC	Thermocouple
3D	Three-Dimensional
TR	Traditional Reformer
TWE	Two Way Valve
USD	United State Doller
UN	United Nation
WGS	Water Gas Shift
WHSV	Weight Hour Space Velocity

YSZ	Yttria Stabilized Zirconia

List of Nomenclatures

Symbol	Name
E_{Pe}	Activation energy for hydrogen permeation (J mol^{-1})
E_S	Activation energy for hydrogen permeation (J mol^{-1})
E_D	Activation energy for hydrogen permeation (J mol^{-1})
K_{CO}	Adsorption equilibrium constant
α	Alpha
atm	Atmospheric pressure
P_{avg}	Average pressure of retentate and permeate (bar)
β	Beta
cm	Centimeter
R^2	Coefficient of determination
C	Concentration (mol m^{-3})
$\partial C/\partial x$	Concentration gradient (mol m^{-4})
ºC	Degree Celsius
D	Diffusivity (m^2 s^{-1})
D_o	Diffusivity at infinite temperature (m^2 s^{-1})
$	Doller
F_{in}/A	Feed load per unit membrane area (L min^{-1} $m^{-2}_{membrane}$)
γ	Gamma

Nomenclature

M	Gas molecular weight (g mol^{-1})
η	Gas viscosity (Pa s)
GJ	Gigajoule
GW	Gigawatt
g	Gram
$P_{H_{2,p}}$	H_2 partial pressure in permeate (kPa)
$P_{H_{2,r}}$	H_2 partial pressure in retentate (kPa)
S_H	Henry's law constant (mol m^{-3} atm^{-1})
h	Hour
C_{H_2}	Hydrogen concentration (mol m^{-3})
J_{H_2}	Hydrogen molar flux (mol m^{-2} s^{-1})
$\alpha_{H_2/i}$	Ideal perm-selectivity of the hydrogen to the other gas
K	Kelvin
kPa	Kilo pascal
Kt	Kilo tons
kWh	Kilo watt hour
kg	Kilogram
kg_{feed}	Kilogram of feed (kg)
kJ	Kilojoule
km	Kilometer

Nomenclature

kPaG	Kilopascal gauge
kW	Kilowatt
μ_K	Knudsen geometric factor coefficient
L	Liter
P_{max}	Maximum pressure (Pa)
MJ	Megajoule
m	Meter
µm	Micrometer
mg	Milligram
ml	Milliliter
mm	Millimeter
mM	Milli-molarity
mmol	Millimole
Mt	Million tons
min	Minute
$F(H_2)_{permeate}$	Molar flow rate of hydrogen in the permeate (mol h^{-1})
$F(H_2)_{retentate}$	Molar flow rate of hydrogen in the retentate (mol h^{-1})
$F(CH_3OH)_{feed}$	Molar flow rate of methanol in the feed (mol h^{-1})
J	Molar flux of diffusing species (mol m^{-2} s^{-1})
J_i	Molar flux of other gases (mol m^{-2} s^{-1})
M	Molarity

Nomenclature

mol	Moles
nm	Nanometer
δ	Number of oxygen vacancies
$J_{H_2}^K$	Overall permeate H_2 flux for Knudsen flow (mol m^{-2} s^{-1})
$J_{H_2}^T$	Overall permeate H_2 flux for nonabsorbable gases (mol m^{-2} s^{-1})
$J_{H_2}^V$	Overall permeate H_2 flux for Viscous flow (mol m^{-2} s^{-1})
P_{CO}	Partial pressure of CO (Pa)
ppm	Parts per million
%	Percentage
P_e	Permeability (mol m^{-1} s^{-1} Pa^{-1})
P_o	Permeability at infinite temperature (mol m^{-1} s^{-1} Pa^{-1})
P	Permeance (mol m^{-2} s^{-1} Pa^{-1})
J_{H_2} and J_o	Permeate hydrogen flux in the presence of pure H_2 (mol m^{-2} s^{-1})
$J_{H_2/i}$	Permeate hydrogen flux in the presence of the mixture of H_2 with i = N_2, CO_2, CH_4, and CO (mol m^{-2} s^{-1})
$J_{H_2/N_2/CO}$	Permeate hydrogen flux in the presence the mixture of H_2, N_2, and CO (mol m^{-2} s^{-1})
π	Pie
d	Pore diameter (m)
ε	Porosity
pH	Potential of hydrogen

Nomenclature

n	Pressure exponent
α	Reduction factor
s	Second
S	Solubility (mol m^{-3} Pa^{-1})
S_o	Solubility at infinite temperature (mol m^{-3} Pa^{-1})
$\Delta P_{H_2}^{0.5}$	Square root of the pressure difference between the feed and permeate sides of the membrane ($kPa^{0.5}$)
S/C	Steam: Carbon ratio
T	Temperature (K)
ΔP	Transmembrane pressure difference (kPa)
R	Universal gas constant (J mol^{-1} K^{-1})
P_{Gas}	Vapor pressure (atm)
μ_V	Viscous geometric factor coefficient
V	Voltage
$F_{H_{2,permeate}}$	Volumetric flow rate of H_2 in permeate (mol h^{-1})
$F_{H_{2,feed}}$	Volumetric flow rate of H_2 in permeate (mol h^{-1})
W	Watt
wt. %	Weight percentage

CHAPTER 1: Introductions

Abstract

This chapter covers the characteristics of hydrogen energy status in the Global Market Trends and challenges faced toward the commercialization of “on-site/onboard” applications. Brief specifics about hydrogen generation and separation techniques have been discussed. The use of Pd-alloy-based membranes for H_2 separation and its integration in membrane reformers/reactors (MR) for simultaneous hydrogen production and separation through Methanol Steam Reforming (MSR) is described. The potential application and various issues in the pathway of MR toward commercialization are highlighted. Finally, the motivation and objectives of the thesis are described along with the overall outline of each chapter.

1.1. Hydrogen Energy

Antoine Lavoisier discovered the properties of hydrogen in 1783 and gave it its name, which is derived from the Greek words "hydro" for water and "genes" for formation. Hydrogen being the most abundant element on the earth has not been exploited to its full capacity till now. Despite having the highest energy-to-weight ratio (141.9 kJ g^{-1}) among other parallel competitors like gasoline (47.5 kJ g^{-1}) and diesel (44.5 kJ g^{-1}), the potential of hydrogen is still underutilized [1]. However, in the last two decades, a lot of efforts have been made for the commercial exploitation of hydrogen as a clean energy carrier. In addition, hydrogen can be used as a storage medium for fluctuating electricity generated from renewable sources and as an energy carrier for off-grid areas that require an electrical supply. In the next five years, the global demand for hydrogen is anticipated to increase by 4–5% per year. This is due to the demand for crude oil refining and the synthesis of methanol and ammonia. The market value for hydrogen generation is projected to reach 154.74 billion USD in 2022, up from 115.25 billion USD in 2017. However, hydrogen always exists in combined forms like alcohols, water, coal, biomass, and other hydrocarbons. Hydrogen can be extracted from these sources via several routes such as steam reforming (SR), autothermal reforming (ATR), partial oxidation (POX), pyrolysis, gasification, fermentation, etc. as illustrated in Figure 1.1. Steam reforming of hydrocarbon is mainly used commercially due to its high efficiency (70-85%). Hydrogen produced using these methods is always accompanied by gases (CO_2, CO, CH_4, N_2, and O_2) or impurities such as (H_2S, NO_x, and SO_x). Consequently, separating the hydrogen from the gas mixture before usage is a crucial step. However, the purification of hydrogen with the presently

available technologies like pressure swing adsorption (PSA), temperature swing adsorption (TSA), and cryogenic distillation (CR) are not economically viable due to their energy-intensive equipment and low hydrogen purification efficiency [2]. Here comes the role of membrane technology with an edge over others due to its continuous operation flexibility, producing ultra-pure hydrogen (>99.999%), and can be clubbed with the simultaneous reaction-separation operation to enhance the overall efficiency of the process. Furthermore, they are quite practical for small-scale and portable applications and produce high-purity hydrogen at the cost of minimal energy and space expenditure [3]. Metal-based, particularly palladium/palladium alloy-based, dense inorganic membranes have always been the favorite for efficient hydrogen separation. From a practical standpoint, a Pd-based membrane offers high hydrogen permeability with ideally infinite selectivity. Additionally, it can operate at high temperatures and pressure for extended periods while consuming little energy and requiring little maintenance [4,5]. Currently, hydrogen produced has a variety of applications in different sectors such as metal treatment industries, chemical refineries, transportation (cars, aviation, and marine), electricity, food hydrogenation, etc. as illustrated in Figure 1.1 [6]. Also, hydrogen can reduce our reliance on fossil fuels while simultaneously being a clean energy source as its combustion gives water vapors only. Future industrial decarbonization and energy security will both be supported by hydrogen. As of now, the CO_2 concentration has increased from 280 ppm in 2005 to 379 ppm in 2018 and it is projected to exceed 400 ppm by 2030. According to the Intergovernmental Panel on Climate Control (IPCC), a 50-85% reduction in total CO_2 emissions is required by 2050 to combat the 2 K increase in world temperature [7]. Moreover, power generation using proton exchange membrane fuel cells (PEMFCs) received huge attention recently because of their high energy efficiency (>80%) [8]. In place of 24 kg of gasoline, just 8 kg of hydrogen is required to go 400 km in a typical combustion engine vehicle. When the combustion engine is replaced with a fuel cell, the same result can be obtained with 4 kg of hydrogen. The exhaust stream is only water vapor, thereby no environmental impact [9]. The majority of hydrogen, however, is industrially produced and used for chemical and hydrocarbon treatment. Its use as a source of energy for transportation and electricity generation has not yet been thoroughly investigated. The primary obstacle to commercialization revolves around safe storage and transport. Therefore, producing and utilizing H_2 at the application site (on-site) is a preferable option.

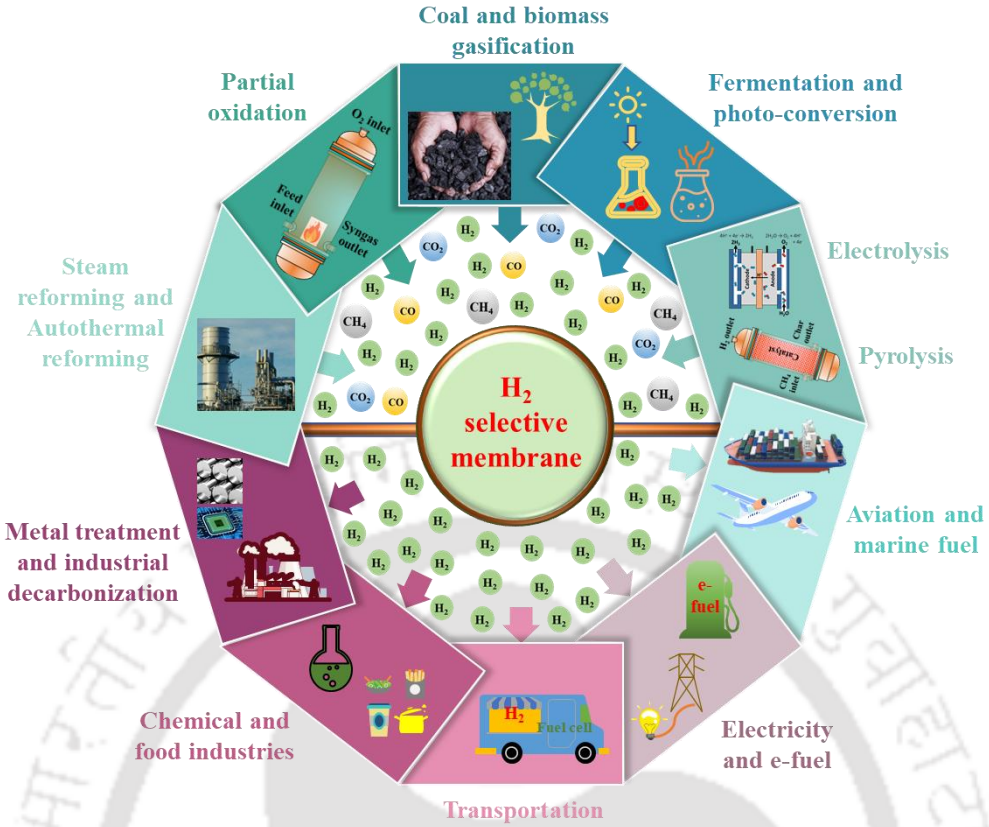

Figure 1. 1. Hydrogen production via different routes and its application after purification using an H_2 selective membrane.

1.1.1. Challenges toward Commercialization

To meet the goal of the Parise Climate Agreement (COP-21, 2015, France) 197 countries assured to take measures to limit the increase in the global average temperature well below 2^{o}C. The same was again reiterated in the recently concluded UN-Climate Change Conference in Glasgow (COP-26, 2021, UK) where the countries will take steps to keep the cap at 1.5 ^{o}C only. It was agreed by several countries that steps will be taken to phase out the coal and fossil fuel based inefficient power generation systems to reduce CO_2 emissions by 45% by 2050 [10]. Therefore, governments throughout the world are looking into using hydrogen in the energy and transportation sectors to attain the objective of net zero emissions. The safe transportation and storage of hydrogen is the main bottleneck to its commercialization. Figure 1.2 shows the challenges associated with different modes of hydrogen transport and its storage. In the end, the tremendous inflammability of hydrogen constantly raises questions about potential safety risks while handling and using it.

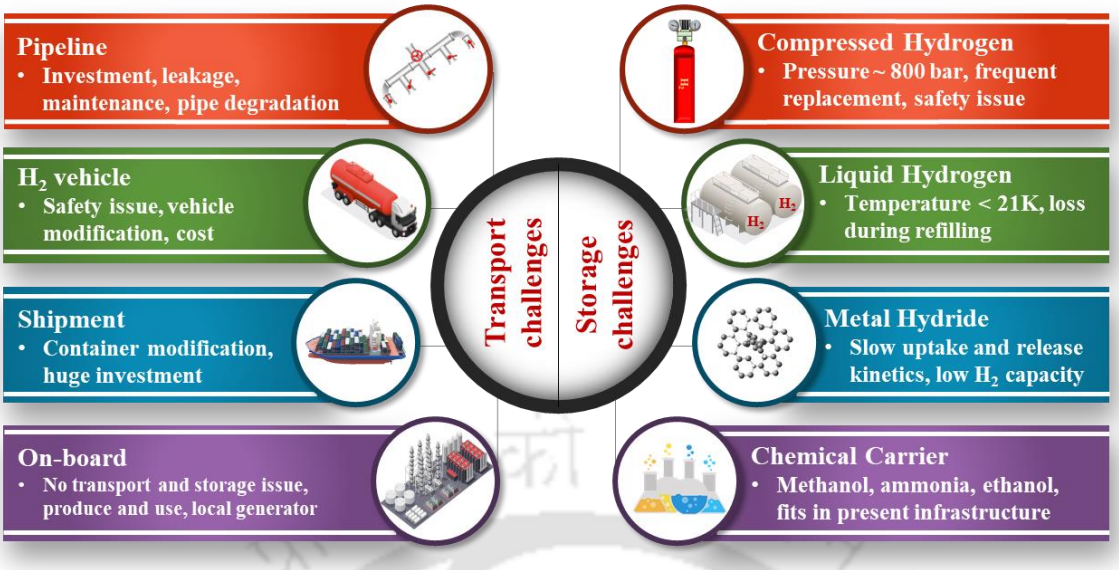

Figure 1. 2. Challenges associated with different modes of hydrogen transport and its storage.

Currently, hydrogen is produced at a specific plant and then transported to the application site either in liquid form in cryogenic containers or pressurized cylinders. Volumetric hydrogen storage density at atmospheric pressure is too low to be taken into account for any useful application. Therefore, hydrogen must be pressurized in cylinders at 60000–80000 kPa for use in fuel cell-powered cars to be used on board. It takes a lot of energy to compress at such extreme pressure which reduces the overall energy efficiency of the process. Recently carbon fiber-based compressed hydrogen cylinders are getting attention due to their high pressure tolerance to 80000 kPa [11]. Additionally, a temperature of 21 K is needed to store liquid hydrogen at atmospheric pressure. Unfortunately, the storage of liquid hydrogen has a very low density of 0.071 g cm^{-3} due to inevitable evaporation loss (0.3 to 3% per day depending on vessel size), which is quantified as the vessel size increases. Refueling the liquid hydrogen on board causes an additional loss of between 10 to 25 percent. The infrastructural expense of insulation and energy expenditure for liquefaction (10 kWh per kg of H_2) further restrict the utilization of liquid hydrogen for commercial purposes. Liquification of liquid hydrogen results in a loss of one-third of its total energy contained in hydrogen. Metal hydride and metal-organic frameworks (MOF) have great potential for storing hydrogen, but they are still in the early stages of development and yet not match the current standards for hydrogen storage capacity. Additionally, it is heavier for onboard use under desirable conditions because of its poor energy-to-weight ratio followed by the decomposition of storage material, and slow reaction kinetics [12,13]. Similar amounts of investment and upkeep will be needed for the

transportation of hydrogen via pipelines, H_2 vehicles, and shipment through ports. Additionally, from an economic standpoint, upgrading entire containers and transport facilities is not an option. However, while in transit there is always a risk to safety, hydrogen embrittlement, and hydrogen leakage. Due to its high volumetric and gravimetric hydrogen storage density, liquid hydrogen carriers in the form of hydrocarbons may be a long-term sustainable solution. With the currently in place infrastructure and at ambient temperatures, chemical carriers can be carried and stored with ease without any additional modification or expenditure [14]. These liquid chemical carriers can be coupled with PEMFCs to produce onboard/onsite hydrogen for use in power generation. Hydrogen production and utilization at the application site will eliminate the issue of its storage and transport. However, PEMFCs need ultra-pure (99.999%) hydrogen with a CO level of less than 10 ppm, which can't be produced from the hydrocarbons' thermochemical breakdown. As a result, additional purification will need a hydrogen separation auxiliary unit. One viable alternative is to combine hydrogen generation and separation into a single unit to produce fuel cell grade hydrogen. Membrane reformer may be a potential solution for this in future. Other than this there are other obstacles to the commercialization of hydrogen, including:

- **Cost and investment:** Lowering costs and removing restrictions to boost the demand for hydrogen. At the international level, action must be taken to commercialize hydrogen.
- **Technology and development:** Focus on R&D work, durability, scale-up, and de-risking of the technology. To ensure that everyone may access hydrogen technology, private investment should be encouraged.
- **Infrastructure and standards:** Ramping up the present infrastructure for hydrogen ready. For worldwide adoption, there must be clarity on standardization, regulations, certification, and asset development throughout the supply chain.
- **Social acceptance and demand:** Stable hydrogen supply and demand must be ensured if worldwide decarbonization is to be accomplished. Additionally, society needs to be ready to appropriately accept hydrogen-based technologies. It is important to raise public knowledge of the hydrogen issue to educate people about the security and safety of hydrogen. A long-term government strategy must be developed to support the substantial initial outlay. It is important to promote environmentally friendly products including methanol, ammonia, aviation fuel, and ethanol.

1.1.2. Hydrogen and Fuel Cell in Global Market Trends

Given that coal-fired thermal power generation will continue to be the primary source of electricity, it is predicted that by 2030, total worldwide power generation will be roughly 1.6 times greater than it was in 2010. Nevertheless, it is envisioned that alcohols like ethanol, methanol, glycerol, or other bio-fuels like acetic acid, biogas, etc. could have a significant impact on future applications. The development of green energy is anticipated to reduce greenhouse gas emissions by around 60%. For an energy transition from conventional fossil fuel-based to renewable sources, green hydrogen energy is essential. Currently, the steam reforming method is used to manufacture more than 95% of the hydrogen that is produced from fossil fuels, primarily natural gas (60%). Hydrogen production using water electrolysis and carbon capture utilization and storage (CCUS) accounts for 0.03% and 0.7% of total hydrogen produced in 2022 respectively. Approximately 10 kilograms of CO_2 are released just to make 1 kg of hydrogen. The market for hydrogen generation is currently valued at about 137 billion USD, and by 2030, it is anticipated to reach over 225 billion USD [15]. In 2020 the global hydrogen demand was 90 million tons (Mt) among which most of the demand was from the refinery (38 Mt of H_2), chemicals (45 Mt of H_2), iron-steel industries (4-5 Mt of H_2), and others (2-3 Mt of H_2). Others include transport, industrial applications (semiconductors, food, etc.), grid injection, and electricity generation while chemicals include ammonia, methanol, ethanol, and other chemical production as shown in Figure 1.3 (a). In 90 Mt of total H_2 produced 70 Mt is used in its pure form while about 20 Mt of H_2 is used in mixed form with carbon-containing gases for methanol and steel production. In addition to this, about 30 Mt of the H_2 produced is used in industries to generate heat and power. Only 0.02% (20 kt of H_2) of hydrogen demand is made by the transportation industry. By 2050 total hydrogen production will jump to 500 Mt of H_2. Most hydrogen produced will have a low carbon footprint, and industry and transportation will account for half of its demand as given in Figure 1.3 (b). In Net Zero Emission (NZE) scenarios by 2050, hydrogen and hydrogen-based fuel will supply 13% of the entire energy consumption [16]. In India, more than 7 Mt of H_2 was utilized in 2020, with 45% going toward refining, 35% going toward chemicals, and about 20% going toward iron and steel. India uses one-fourth of the world's hydrogen supply. India committed to increasing its hydrogen demand to 11 Mt of H_2 by 2030 as part of the recently announced National Hydrogen Mission (NHM). The NHM will concentrate on producing hydrogen from renewable energy sources and connecting India's expanding capacity for renewable energy with the hydrogen industry. The 2021–2022 budget included funding of Rs. 1500 crore for the NHM and the

development of renewable energy, which gave India's ambitious aim of installing 175 GW of renewable energy capacity by 2022 further momentum. In addition to helping India meet its emissions targets under the Paris Agreement, the use of hydrogen will lessen its reliance on imported fossil fuels as well.

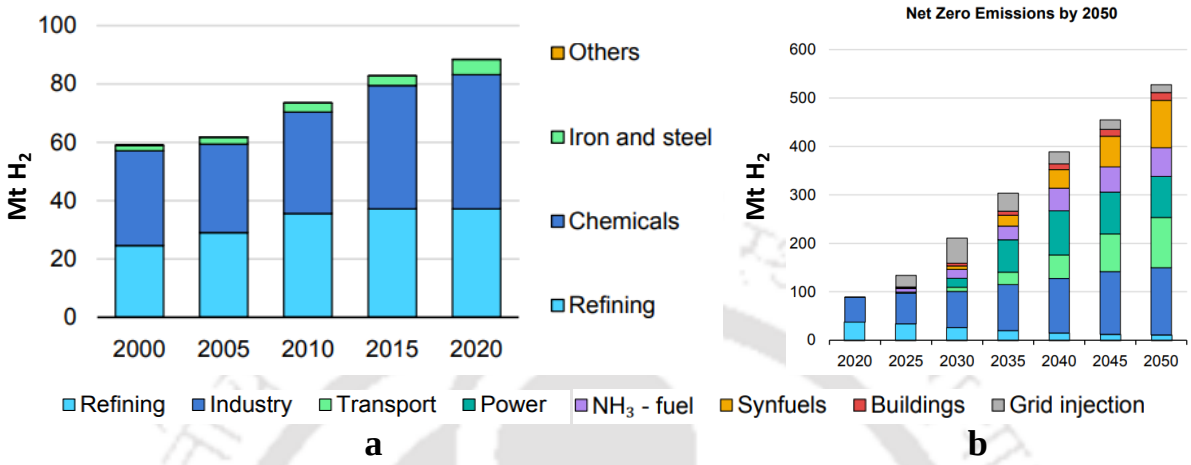

Figure 1. 3. (a) Sector-wise hydrogen demand from 2000 to 2022 (b) hydrogen demand by sector in NZE scenarios (hydrogen used for making ammonia is included in the Industry subsector) (reproduced from [16]).

The accompanying demand for fuel cells is anticipated to develop significantly along with the rising demand for hydrogen energy in the transportation and power sectors. Fuel cells experienced a significant milestone following their development in the early 1960s by Willard Thomas Grubb and Leonard Niedrach. There are presently fuel cells with power capacities ranging from kilowatts to megawatts that can run on several different fuels, including hydrogen, methanol, ethanol, gasoline, etc. Additionally, it can be used for a range of applications, including portable (road, maritime, and aviation) and stationary ones (residential heating and portable power generation). According to the electrolyte that is utilized, there are primarily six different types of fuel cells namely (i) Proton exchange membrane fuel cell, (ii) Alkaline fuel cell (AFC), (iii) Phosphoric acid fuel cell (PAFC), (iv) Molten carbonate fuel cell (MOFC), (v) Solid oxide fuel cell (SOFC), and Direct methanol fuel cell (DMFC). Because of its superior power density, high conversion efficiency, compactness, and low operating temperature, PEMFCs technology can be perfectly suited for transportation applications [8]. The cost of fuel cells is a significant barrier to commercialization, though. A system that cost 60000 USD in 2005 is expected to sell for 3000 USD by 2030 thanks to the significant advancements made in fuel cell technology over the past 20 years. While fuel cells can run at an efficiency level of 60% or even reach up to 85% when internal heat created is further utilized, hydrogen

combustion engines operate at a level of efficiency of about 20–25% [8]. By 2030, mass-produced fuel cell systems will be able to compete with battery-powered devices. For fuel cells to be affordable to the general public, their cost per kW of hydrogen for stationary usage must fall between 1000 to 1500 USD and their life must be between 40000 to 60000 hours. For the entire system to profit, the cost of hydrogen should be approximately 18 USD per gigajoule (GJ) and the overall cost of fuel cells for the transportation sector must be in the range of 30–50 USD per kW. For a 400 km drive in a fuel cell vehicle, only 4 kg of hydrogen is required instead of 24 kg of gasoline [17]. More than 80% of the fuel cells are used for stationary applications. The main disadvantages of PEMFCs include the use of a Pt-based catalyst at the anode, which can only withstand 10 ppm of CO, exhaust heat, which is difficult to manage, the use of a precious metal-based electrode that is expensive, and membrane deterioration over time. In addition, it is portable, has a rapid starting time, is very energy-efficient, operates at low temperatures (333–363 K), and has a high power density (kW m^{-1}) = 3.8–6.5, making it a viable alternative energy source in the future [18].

The idea of integrating membrane reformers with PEMFCs for power generation just began to take shape. However, the development of this technology is still in its early stages. A Pd-based metallic membrane can be used to separate the mixture gas into ultra-pure hydrogen with a CO level of less than 10 ppm. Practically high-grade hydrogen can be recovered from a membrane reformer beyond the thermodynamic barrier of a traditional reactor. To generate electricity for stationary and electric vehicle (EV) applications, this hydrogen can be supplied directly to PEMFCs. Online integration of MR with fuel cells will solve the problem of hydrogen storage and transportation. However, there are many obstacles in the way of its commercialization, including long-term hydrogen purity, online fuel cell, and reactor integration, supply and demand matching, cost, the viability from an economic position, and overall energy efficiency of the complete unit [19,20].

1.2. Hydrogen Generation

Even today, more than 95% of the hydrogen is produced using fossil fuels such as natural gas, coal, oil, and naphtha without the use of CCUS. This produces 830 Mt of CO_2 annually by using 205 billion metric cubic feet of CH_4 and 107 Mt of coal. Only 4% of the world's hydrogen is produced by water electrolysis, which requires a significant amount of electricity, which is once again produced using conventional fossil fuel-based electricity generation technologies. CCUS is typically disregarded in plants since it will raise the cost of producing hydrogen. With CCUS, more than 90% of CO_2 emissions can be eliminated, however, there are only a very

small number of plants operational today producing 0.5 Mt of H_2 annually with CCUS. The most widely used methods of producing hydrogen today include steam reforming (which uses water as an oxidant), partial oxidation (which uses oxygen in the air as an oxidant), autothermal reforming (which uses both air and water as oxidants), gasification (which turns coal and biomass into synthesis gas), and electrolysis (which splits water into hydrogen and oxygen) [16]. Among these, SR is frequently used to produce hydrogen from naphtha, liquefied petroleum gas, and natural gas. POX is used to produce synthesis gas ($CO + H_2$) from coal and heavy hydrocarbons to some extent. According to Table 1.1, SR maintained its leading position in hydrogen generation among its parallel competitors due to its maximum efficiency (75-80%), proven technology, and economics. But SR, ATR, POX, and gasification, despite being commercialized and having improved efficiency, are still dependent on fossil fuels, releasing a lot of CO_2 in the process [21]. One such example is steam methane reforming (SMR) must be carried out at a higher temperature (>1173 K) and pressure to get a high conversion (300-2500 kPa). Since CO, a byproduct of SMR, cannot always be released immediately, a second reaction is needed for CO to be converted to CO_2 at a lower temperature via the Water Gas Shift (WGS) process (523 to 623 K). For the preferential oxidation (P_rO_x) of CO to CO_2, a third reactor is occasionally required followed by a PSA-based H_2/CO_2 separation unit to get ultra-pure hydrogen for fuel cells. SMR is a well-established technology, but it is constantly overlooked because of problems with heat and mass transport, thermodynamic limitations, coke deposition, frequent catalyst deactivation, and poor process stability. Additionally, the Ni/alumina-based catalysts have a significant sintering issue that can be solved with the novel metal-based catalysts (e.g. Ru, Rh, and Pd), but their cost and availability provide a significant challenge. Methane has a low volumetric density at ambient temperature and pressure, further limiting its utility for onboard exploitation [22,23]. Another big contributor to hydrogen production is coal having 4-6 wt.% of hydrogen that may be gasified at high temperatures (1023 K) and pressure (1000 kPa) and mainly produces CO and H_2 in the presence of steam. However, product gases are accompanied by SO_x, H_2S, NO_x, ash, tar, HCl, and other elements in the trace. Carbon management and removal of these gases will require a series of purification techniques. Similar to MSR, coal gasification will also require WGS and P_rO_x reactor to get fuel cell grade hydrogen [24,25]. The need for CO-free hydrogen is the only constraint on hydrogen generation for use in fuel cells. To avoid this methane can be directly broken down into H_2 and carbon as one of the solutions. However, the procedure is problematic due to kinetic constraints and the large activation energy needed to break the C-H bond. The reaction must be carried out at a temperature greater than 1473 K to get a significant conversion. To meet

this challenge, the catalytic methane cracking (CMC) method, which operates similarly to SMR between 873 and 1173 K, entered the picture. Coke formation, which significantly deactivates the catalyst's active sites, is the main bottleneck. Additionally, because of surface and pore deformation, it is virtually impossible to restore the catalyst to its original activity. The process's capacity to scale up and run in batches while still replacing the catalyst and cleaning the reactor periodically is also a major concern [26,27]. Moving toward a more green and continuous process, water electrolysis is one of the alternatives. It ensures zero pollution when produced using a renewable energy source. It uses electricity to split water into hydrogen and oxygen. However, electrolysis is expensive and has a low overall efficiency (40–60%) when compared to alternative technologies as listed in Table 1.1. In addition to this, the cost of hydrogen production using electrolysis (10.3 USD per kg of H_2) is almost 5 times compared to steam reforming (2.27 USD per kg of H_2) [28]. Matching the hydrogen supply and consumption rates for onboard use is still far from being realistic. Also, the installation of renewable energy sources has an impact on the environment and a carbon footprint. Since it is impossible to always have access to renewable energy sources, electrolyzers will once again become dependent on conventional fossil fuel-based electricity, which is a bad concept [29]. Other technologies, such as photofermentation, bio photolysis, and photo electrolysis, have the lowest levels of conversion and, as a result, produce the least hydrogen, making them unsuitable for usage on board. Although biomass pyrolysis is the most cost-effective method for producing hydrogen (1.59-1.70 USD kg^{-1} H_2), contaminants in the feedstock result in significant amounts of tar and mixed gas, whose further purification is a critical challenge. Similarly, dark fermentation, which can produce hydrogen in the absence of sunlight, but whose commercial viability is further constrained by both its low conversion efficiency and huge reactor volume [21]. Therefore, SR is the most cost-effective and efficient method (74-85%) for hydrogen production. SR is a well-established, mature technology for H_2 production that integrates seamlessly with the existing infrastructure. In addition, the use of LOHC, particularly methanol, can substantially reduce emissions of SO_x, NO_x, and other particulates. The captured and recycled CO_2 can be used to produce renewable methanol, making the entire process environmentally friendly. The fully integrated ecosystem featuring cutting-edge technology revolutionizes the entire energy industry. There have been different classifications of hydrogen proposed, each of which is contingent on the method of H_2 production and the management of its released carbon footprint.

Table 1. 1. Comparison of different hydrogen generation processes (adapted from [21,28]).

Process	Efficiency (%)	Cost (USD kg^{-1} H_2)	Major advantages	Major disadvantages
SR	74-85	2.27	Most developed technology, existing infrastructure	CO_2 by-product, dependence on fossil fuels
POX	60-75	1.48	Proven technology, existing infrastructure	CO_2 by-product, dependence on fossil fuels
ATR	60-75	1.48	Proven technology, existing infrastructure	CO_2 by-product, dependence on fossil fuels
Biomass pyrolysis	35-50	1.59-1.70	CO_2-neutral, abundant, and cheap feedstock	Tar formation, varying H_2 content, and feedstock impurities
Biomass gasification	70-80	1.77-2.05	CO_2-neutral, abundant, and cheap feedstock	Tar formation, varying H_2 content, and feedstock impurities
Bio photolysis	10	2.13	CO_2-consumed, O_2 is the only by-product, operation under mild conditions	Requires sunlight, low H_2 rates, and yields, large reactor volume, O_2 sensitivity, high raw material cost
Dark Fermentation	60-80	2.57	CO_2-neutral, simple, can produce H_2 without light, contributes to waste recycling, no O_2 limitation	Fatty acids removal, low H_2 rates, and yields, low conversion efficiency, large reactor volume
Photo-fermentation	0.1	2.83	CO_2-neutral contributes to waste recycling and can use different organic wastes and wastewater	Requires sunlight, low H_2 rates, and yields, low conversion efficiency, large reactor volume, O_2 sensitivity
Electrolysis	40-60	10.30	No pollution with renewable sources, existing infrastructure, and abundant feedstock, O_2 is the only by-product	Low overall efficiency, high capital costs
Thermolysis	20-45	7.98-8.40	Clean and sustainable, abundant feedstock, O_2 is the only by-product	Elements toxicity, corrosive problems, high capital costs
Photo-electrolysis	0.06	8-10	Emission-free, abundant feedstock, O_2 is the only by-product	Requires sunlight, low conversion efficiency, the ineffective photocatalytic material

Figure 1.4 shows different categorizations of H_2 based on the pathway of hydrogen generation. The least carbon-intensive of them is green hydrogen (electrolysis), which is produced from a non-fossil fuel source (e.g. water), however, it is too expensive (10-15 USD per kg of H_2) [30]. The cost of producing hydrogen must be reduced to between 1-2 USD per kg of H_2 to compete in the market. Additionally, the expensive equipment and related accessories demand a heavy initial investment. The primary prerequisite for going green is using renewable energy, which already has its own limitations described earlier. Furthermore, the cost of hydrogen storage, transportation, and distribution will impose an extra financial burden of 1-3 USD per kg of H_2 for the end user. Therefore, a sudden shift in the entire hydrogen supply chain to a green way of production and utilization is not realistic in the near future. Even by 2050, more than 50% of the total hydrogen produced will be derived from fossil fuel based energy efficient low carbon technology like CCUS. In addition, the affordability and established technology of fossil fuel-based hydrogen production will keep being relevant in the years to come [31].

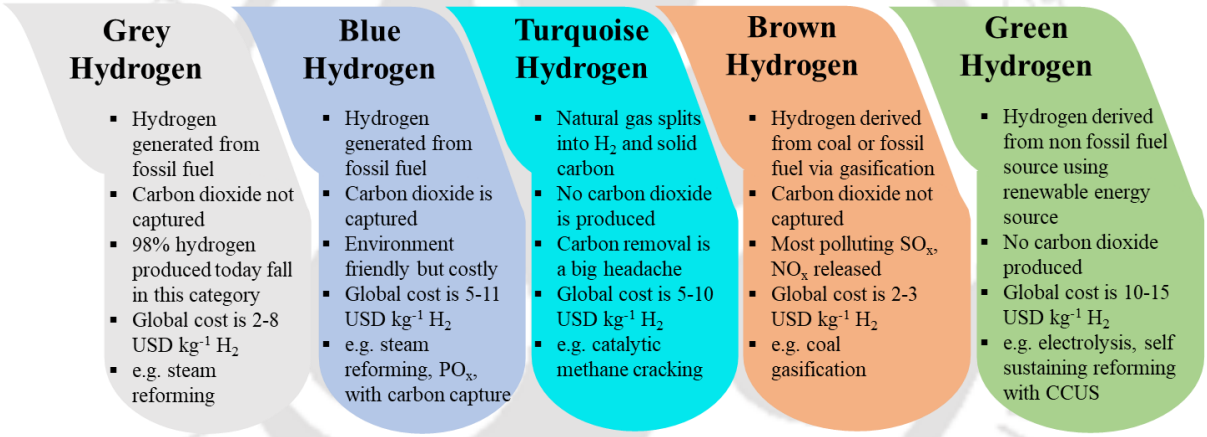

Figure 1.4. Types of hydrogen are based on the different pathways of hydrogen generation (adapted from [30]).

One could argue that rather than creating new infrastructure for hydrogen storage, transportation, and distribution, efforts should be focused on utilizing and improving the currently installed infrastructure to make it compatible with the hydrogen supply chain's future requirements. One such possibility gaining traction for onboard/onsite use is low-carbon hydrogen generation using liquid organic hydrogen carriers (LOHC) and ammonia [14]. Among LOHC methanol is the simplest alcohol and has the potential to revolutionize the process of producing hydrogen onboard/onsite because of its accessible availability, low cost, high hydrogen density, environmental friendliness, and ease of transport and storage under

ambient conditions. Consequently, methanol can serve as a future 'Hydrogen Carrier' that can be readily accommodated by the existing infrastructure.

1.2.1. Methanol: A Hydrogen Carrier

From 148 million metric tons in 2019 to over 310 million metric tons in 2030, global methanol output is projected to triple [31]. Its energy density is 80% higher than that of liquid hydrogen, with a gravimetric and volumetric hydrogen storage capacity of 12.5 (wt. %) and 99 kg m^{-3}, respectively. Its energy content is equal to 18.1 MJ kg^{-1} (LHV). There is more hydrogen in a cubic meter of methanol (99 kg m^{-3}, atm) than there is in a cubic meter of liquid hydrogen (70 kg m^{-3}, 20 K), formic acid (53 kg m^{-3}, atm), H_2 compressed cylinder (39.9 kg m^{-3}, 70000 kPa), and even AlH_3 based metal-organic framework (85 kg m^{-3}, achieved in practice) [32,33]. In terms of volumetric energy density (based on LHV), liquid methanol (15.8 MJ L^{-1}, atm) once more outperforms other substances like liquid H_2 (8 MJ L^{-1}, 20 K), H_2 compressed cylinder (~ 4.5 MJ L^{-1}, 70000 kPa), and CH_4 compressed cylinder (~ 16.5 MJ L^{-1}, 70000 kPa) [34]. Accounting for the cost per kilogram of hydrogen storage, methanol (3.57 USD) once again has an advantage compared to compressed hydrogen (> 12 USD, 70000 kPa) and liquid H_2 (~ 8 USD, 20 K). To fully utilize hydrogen's potential, it must be separated from methanol due to its lower heating value (119.9 MJ kg^{-1}) which is roughly 6.5 times higher than methanol's (18.1 MJ kg^{-1}) [1]. To achieve this, methanol can be converted into hydrogen through a number of processes, including thermal decomposition, POX with oxygen, and steam reforming with water. The only method among these that releases three moles of hydrogen for every mole of methanol consumed is steam reforming with water, which uses water to supply one mole of hydrogen for the reforming reaction. With a volumetric hydrogen storage density of roughly 150 kg m^{-3}, methanol mixed with water together has the highest hydrogen storage density. Its low reforming temperature (523-623 K) is due to the absence of a C-C bond which also lowers the possibility of coke production at high temperatures. The presence of the –OH functional group is also a good attribute, as it reduces the amount of water consumed in the steam reforming reaction to produce hydrogen, hence reducing the steam reforming process temperature. The endothermic nature of methanol steam reforming (MSR), which prefers high temperatures and low pressure (generally atmospheric), can be accommodated with careful waste stream heat integration. It's interesting to note that both hydrogen and CO_2, which are emitted during steam reforming, are stored in the methanol-water mixture. A high concentration of CO_2 in the steam-reforming product gas should make it simpler to capture, store, and recycle. Additionally, the classic natural gas-based method and the generation of

methanol from CO_2 are not very diverse. Commercially, both processes use $Cu/Zn/Al_2O_3$ or $Cu/Zn/SiO_2$-based catalysts operating at 493–353 K, which release heat due to their exothermic nature and can be integrated back into the steam reforming process. The price of reforming methanol is nearly one-third that of reforming natural gas [35]. Methanol is the fuel with the highest energy efficiency (35%) when compared to ethanol and diesel [36]. While ethanol and glycerol offer larger hydrogen yields than methanol, they also produce more CO and coke during the process. Since the process is endothermic, a high temperature (>773 K) is needed to get an adequate hydrogen yield. Acetaldehyde, methane, and numerous other low-chain alkanes are also produced in addition to H_2, CO, and CO_2. Catalyst sintering and deactivation are other key issues that call for frequent catalyst regeneration. Another low-temperature WGS reactor will be needed to reduce CO formation, which will again increase the overall cost [37,38]. Other than LOHC, ammonia is also projected as a potential substitute for methanol as a hydrogen carrier due to its higher hydrogen storage density. Liquid ammonia (NH_3) at 1000 kPa has a very high hydrogen storage density of 17.7 (wt. %) gravimetrically and 123 kg m^{-3} volumetrically, making it an attractive hydrogen storage medium. However, the methanol-water mixture's volumetric hydrogen storage density (150 kg m^{-3}) for steam reforming is significantly higher than ammonia. Despite methanol alone having a lower hydrogen storage density both gravimetrically and volumetrically, methanol enjoys a high energy density (20.1 MJ kg^{-1}) compared to ammonia (18.6 MJ kg^{-1}). Additionally, due to the exothermic nature of the reaction, the Haber-Bosch Process does not require external heating to produce ammonia; but, to create thermodynamically favorable conditions, high temperatures (573-823 K) and pressures (20000-35000 kPa) are needed. However, due to safety concerns and high apparent toxicity that is three orders of magnitude more than methanol, its acceptance as a potential energy carrier for onsite applications is likely to be constrained [39]. In contrast to methanol, the proper handling of ammonia will necessitate skilled personnel and specific equipment. The most difficult technical hurdle for onboard/onsite application is its thermal dehydrogenation. Even the most active Ru-based catalysts require high temperatures (> 923 K), which are very expensive. The temperature required yet again rises to 1173 K for less active Ni-based catalysts [33]. Additionally, the energy required to extract hydrogen from ammonia (30.6 kJ mol^{-1} of H_2) is rather significantly high compared to methanol (16.3 kJ mol^{-1} of H_2) [40]. Ammonia is also very reactive with the acidic electrolyte of PEMFCs, which reduces their performance drastically. A continuous ammonia concentration of less than 1 ppm is required to address this problem. It is impossible to ignore the formation of NO_x during the entire process which is even more hazardous than CO_2. Contrarily, MSR does not result in the production of SO_x, NO_x,

or other particulates. Therefore, it doesn't appear that ammonia's techno-economic properties will soon be in favor of use in actual onboard/onsite applications for H_2 production [41,42].

Hence, the most economical approach for developing a 'Hydrogen Economy' is through the generation and storage of hydrogen in methanol, which is already on the route to decarbonization. Methanol becomes a net carbon-neutral fuel that is in line with climate change objectives to reduce greenhouse gas emissions when it is produced from renewable feedstocks like captured CO_2 and biomass. Though it is toxic, it is neither carcinogenic nor mutagenic, unlike other common liquid petroleum fuels. Methanol can also be used directly as fuel in vehicles such as cars, trucks, buses, ships, fuel cells, boilers, and cooking fuel in addition to hydrogen carriers. When burned in internal combustion engines, its inherent clean-burning characteristics and high octane number (100) result in decreased pollutants (while enhancing fuel efficiency). Additionally, the exceptionally low freezing point of methanol and water (202 K) makes it an all-weather fuel without affecting the capacity to produce hydrogen [43]. Reduced temperatures result in cheaper materials, less insulation, fewer components, and a significantly lower cost for the hydrogen generator as a whole. Many nations, including India, are aggressively trying to encourage the world to adopt the 'Methanol Economy' concept. The Indian government aims to utilize methanol in gasoline because it can lower greenhouse gas emissions by more than 20% and cut crude oil imports by 15%. More than 6000 diesel railway engines will be upgraded to run entirely either on methanol or hydrogen. Similar actions will be taken for domestic and international cargo transportation. In the coming years, platforms based on methanol reactors integrated with the fuel cells would be able to completely replace diesel-based power modules of mobile towers (approximately 750000 of them) and apartments in India. In addition, this large-scale methanol reforming-based hydrogen generator will be encouraged for decentralized hydrogen production and utilization [44]. As a result, the 'Methanol Economy will play a crucial role in the future of the 'Hydrogen Economy'.

It is clear from the explanation above that hydrogen production using MSR is the most practical option for onboard and onsite applications. Using the produced hydrogen in PEMFCs is the best option to produce electricity. Theoretically, PEMFCs should have 100% efficiency, giving them an advantage over IC engines, which, under Carnot's cycle rule, have a maximum theoretical efficiency of 40% only. Moreover, PEMFCs don't have any mobile elements, hence preventing any dissipation of valuable energy caused by friction [45].

However, CO concentration levels higher than 10 ppm may deactivate the Pt-catalyst at the anode in PEMFCs [17]. According to numerous reports in the literature, in addition to CO_2 and

H_2, some CO is also generated during MSR as a result of the degradation of methanol and the reverse water gas shift reaction (RWGS). Hence, the selection of the process, operating conditions, and catalyst for methanol conversion into hydrogen are crucial to minimize the CO formation and achieve the maximum H_2 yield. In addition to this, H_2 purification of the downstream gases is necessary to achieve fuel cell-grade hydrogen.

1.2.2. Hydrogen Production via Methanol Steam Reforming

An alternative route to utilize hydrogen energy is to in situ convert methanol into hydrogen onsite. The absence of a C-C bond facilitates the reforming of methanol at mild conditions (temperature ~ 473-573 K). In addition to this, a high H/C ratio, low sulfur contents, low cost, ease of availability, and ability to be produced from a renewable source such as biomass and captured CO_2 make it an ideal source of hydrogen [46]. Its energy content is equal to 19.9 MJ kg^{-1} (LHV), a volumetric energy density of 15.8 MJ L^{-1} (atm, LHV), and a volumetric hydrogen storage density of roughly 150 kg m^{-3} when mixed with water. Accounting for the cost per kilogram of hydrogen storage, methanol (3.57 USD) once again has an advantage compared to compressed hydrogen (> 12 USD, 70000 kPa) and liquid H_2 (~ 8 USD, 20 K). To fully utilize hydrogen's potential, it must be separated from methanol due to its lower heating value (119.9 MJ kg^{-1}) which is roughly 6.5 times higher than methanol's (18.1 MJ kg^{-1}) [1]. Several techniques, including SR, POX, ATR, and oxidative steam reforming (OSR), can be utilized to extract hydrogen from methanol. SR is the most efficient method and the only method that produces three molecules of hydrogen for every mole of methanol where one mole of H_2 is contributed by water [21]. Equation 1.1 represents the fundamental MSR reaction. In addition to the primary reaction, the literature describes two secondary reactions termed ‘Methanol Decomposition’ and ‘Water Gas Shift’ as shown in Equations 1.2 and Equation 1.3 respectively. These reactions occur simultaneously, with CO and H_2 being produced by the methanolysis reaction and CO reacting with H_2O to produce CO_2 and H_2 via the WGS reaction.

$$CH_3OH + H_2O \rightleftarrows CO_2 + 3H_2 \qquad \Delta H = 49.7 \text{ kJ mol}^{-1} \qquad (1.1)$$

$$CH_3OH \rightleftarrows CO + 2H_2 \qquad \Delta H = 90.2 \text{ kJ mol}^{-1} \qquad (1.2)$$

$$CO + H_2O \rightleftarrows CO_2 + H_2 \qquad \Delta H = -41.2 \text{ kJ mol}^{-1} \qquad (1.3)$$

Methanol dehydrogenates to produce methyl formate and hydrogen as shown in Equation 1.4 then methyl formate is hydrolyzed to form formic acid and methanol as given in Equation 1.5, followed by the decomposition of formic acid to form carbon dioxide and hydrogen as depicted in Equation 1.6. Hence following reaction mechanism has been suggested [47]:

$$2CH_3OH \rightarrow HCOOCH_3 + 2H_2 \quad (1.4)$$

$$HCOOCH_3 + H_2O \rightarrow CH_3OH + HCOOH \quad (1.5)$$

$$HCOOH \rightarrow H_2 + CO_2 \quad (1.6)$$

Another mechanism is also proposed where formaldehyde and formic acid intermediates in the steam reforming reaction over Cu-based catalysts as presented in Equation 1.7 to 1.9 [48]:

$$CH_3OH \rightarrow HCHO + H_2 \quad (1.7)$$

$$HCHO + H_2O \rightarrow HCOOH + H_2 \quad (1.8)$$

$$HCOOH \rightarrow CO_2 + H_2 \quad (1.9)$$

In the mechanisms suggested above CO is not produced, hence WGS reaction is the main source of CO formation previously given in Equation 1.2. The formation of CO may damage the Pt-based catalyst in the PEMFCs. Consequently, a second low-temperature 'Shift Reactor' is required to reduce CO formation, thereby increasing the overall cost of the reactor. To maximize H_2-selectivity and minimize CO-selectivity, catalysts are indispensable. It follows that the catalyst, support, and promoters should be selected to maximize methanol conversion. Due to their high H_2 selectivity and low carbon formation, Cu-based catalysts have been intensively studied in the past. However, thermal stability and catalyst sintering over the long term continue to be a challenge. The comparatively low operating temperature of Cu-based catalyst for MSR is supported by the rising order of metal stability as follows: Ag > Cu > Au > Pd > Fe > Ni > Co > Pt > Rh > Ru > Ir > Os > Re. The incorporation of alkali promoters such as Fe, Mn, ZnO, ZrO_2, and CeO_2, as well as other alkali metal oxide supports, has been shown to inhibit catalyst sintering and deactivation [49,50]. The availability of acidic and basic sites is essential for catalyst activity and adherence to a specific reaction mechanism. Highly acidic sites facilitate the RWGS reaction, which reduces CO selectivity. On the other hand, the enhanced acidic sites facilitate in situ CO_2 sorption, thereby enhancing H_2 selectivity [51]. The Pd, Pt, and Ni catalysts have been observed to promote the formation of syngas, whereas the Cu-based catalyst promotes the formation of H_2 with high CO_2 selectivity. The addition of ZnO to Cu-based catalysts enhances the dispersion of Cu over the support and enhances CO oxidation. Incorporating alumina into the $CuO/ZnO/Al_2O_3$-based catalyst further improves the reduced catalyst's thermal stability and surface area. Alumina possesses the ability to absorb and activate methanol for subsequent reactions [50,52]. It has been reported that with the increase in temperature, contact time of feed, and pressure the formation of CO is favored. The high concentration of H_2 and CO_2 on the product side makes carbon monoxide (CO) an

inevitable byproduct of the RWGS reaction, however, Agrell et al. [53] experimentally verified that a short residence time for the feed over the catalyst substantially reduces CO formation. The reformate gas consists of around 74%-75% H_2, 24%-25% CO_2, and 1-2% CO. The generation of CO is also restricted by the increased Cu dispersion and interaction over the support. Therefore, the performance of the catalyst is highly dependent on the process of catalyst synthesis, the choice of support, and the metal composition. In addition to this, catalyst packing inside the rector optimizes the heat, and mass transfer is the key to achieving maximum conversion with minimum catalyst requirement. Moreover, the design of the reactor and H_2 separation is significantly more crucial parameters to optimize the overall system efficiency and stability to produce H_2 more efficiently during scale-up. Packed bed (PB) reactors have traditionally been widely used due to their simplicity and operational flexibility. Mass transfer, heat transmission, and material cost pose the greatest obstacle to scale-up. By increasing the fluid transfer rate, the transfer of heat and mass can be enhanced; however, this will eventually result in a huge pressure drop across the reactor. Because noble metal catalyst is typically used to maintain excellent catalytic activity and reduce coking, the cost of catalyst accounts for a significant portion of total material costs. In highly endothermic MSR, structured catalysts like monoliths, porous metal fibre, 3D-solid foam, and 3D-printed catalysts have interconnected void frameworks, particularly SiC-based foam, which intensifies heat transfer and reduces the radial variation in temperature. In addition to this, it improves conversion by supplying a large surface area and turbulent mixing within an interconnected three-dimensional framework. The catalyst-coated foam structure can further reduce the quantity of catalyst required for a specific output, allowing for the design of compact reactors such as membrane reactors (MR) [54–56]. MR has garnered attention for their enhanced MSR conversion in a compact unit, onsite/onboard high purity H_2 generation, and enhanced overall thermal efficiency of the system. Giaconia et al. [55] investigated pilot-scale solar heating-based methane reforming using molten salt for 0.17 kg h^{-1} of H_2 production. The developed prototype consists of 10 catalysts (sintered SiC supported)/membrane (Pd-based) compartment. The catalyst is wash-coated over the SiC foam and installed around the membrane. The permeate is > 9.8% pure with <100 ppm of CO. Another study by Yan and Cheng [56] showed that more than 78% of the catalyst amount can be reduced while achieving 100% catalyst utilization. A wash-coated Ru/α-Al_2O_3 catalyst is applied to a SiC foam and compared to a spherical particle catalyst. Compared to conventional spherical particles-packed MR, foam-structured MR enhances radial heat transfer (e.g., increase membrane side temperature by about 20 K) and radial mass transfer (more rapid H_2 transfer to the membrane surface). Moreover, the implication of the

membrane inside the SiC foam reduced the concentration polarization. Kim et al. [57] investigated the techno-economic analysis of the PSA-based PB reactor and MR for 1.33 kg h^{-1} of H_2 production via MSR. Based on process simulation results, a unit H_2 production cost was calculated by dividing the annual cost by the annual H_2 production yield for a PB reactor and the MR. They claimed that the capital expenditures (CAPEX) for the MR reactor are only 3%, compared to 17% for the PB reactor, primarily as a result of the abolition of PSA. Based on the itemized cost estimation for a unit of H_2 production, the MR (7.24 $ per kg of H_2) reactor is 23% less expensive than the PB reactor (9.37 $ per kg of H_2). In an MR, a methanol conversion of greater than 50% is achievable at temperatures between 473-573 K, whereas in a TR, more than 50% of methanol conversion is only possible at temperatures between 573-673 K. However, at elevated temperatures, the CO selectivity increases, and several studies have reported a serious problem with a decrease in catalyst activity owing to coking [58].

The selection of the catalyst, the design of the reactor, the packaging of the catalysts, and the efficient separation of H_2 from the mixture gases are among the biggest obstacles to the commercialization and scaling up of MSR-based MR. All of these crucial parameters must be optimized to maximize the system's overall performance. Several MSR catalysts have been documented in the scientific literature and even marketed commercially. However, they encounter a significant deactivation problem due to coking at a high feed flow rate as well as heat and mass transfer difficulties. Therefore, the catalyst's packing within the reactor is the key to averting these phenomena during long-term operation. The separation of H_2 efficiently in MR can further enhance performance and conversion. Nevertheless, the selection of the membrane to achieve the desired H_2 recovery will play a vital role in MR, as any trace of CO in the permeate can further deteriorate the fuel cell.

1.3. Hydrogen Separation

Steam methane reforming, naphtha reforming, and coal gasification are the most prevalent methods for hydrogen production worldwide. This procedure generates a mixture of gases including H_2, CO, CO_2, H_2S, CH_4, charcoal, and asphalt. Even in electrolysis, oxygen must be removed because a high concentration of oxygen can damage the proton exchange membrane, a vital component of the fuel cell. The reaction between oxygen and membrane material can result in the formation of radicals that can damage the membrane and reduce its lifespan. Oxygen can react with catalyst material to generate oxides that inhibit the catalyst. In order to effectively utilize H_2 in fuel cells and other industrial processes, additional H_2 purification is

required. This is generally achieved through PSA, cryogenic distillation, metal hydride, and membrane separation.

1.3.1. Comparison of Different Hydrogen Purification Technology

PSA has typically been utilized in industrial settings for the purification of hydrogen using batch-wise or continuous operating modes using adsorbents including activated carbon, zeolite, alumina, and carbon molecular sieve. Hydrogen gas is adsorbed at high pressure (10-40 bar) until equilibrium loading is reached, after which it is desorbed from the adsorbent at low pressure (typically at ambient conditions). However, these adsorbents also have a high affinity for N_2 and CO, so the purity (99.99%) is compromised. In addition, an increase in temperature decreases the adsorption affinity as a result of a moderate Vander Walls interaction, resulting in a decrease in H_2 purity and recovery (70-85%) once again. To obtain fuel cell grade H_2, the PSA in series is utilized, which contributes to an increase in the production costs as a whole. In addition to this, hydrogen of such high purity is given at less than 200 kPa, therefore expensive additional post-process compression is required. For onboard/onsite applications, PSA is extremely cumbersome and energy-intensive to achieve the desired purity and recovery [59,60]. PSA functions at high and medium volumes, but it is impractical to scale it down for small-scale or portable applications.

Cryogenic distillation is another common method for purifying H_2. The supply gas is compressed and then cooled to a temperature lower than the cryogenic temperature of H_2 (which is 20 K). Using the difference in boiling temperature of the fluid mixture, another cryogenic distillation column separates the hydrogen into liquid form. However, if the feed contains CO_2 and CO, a methane wash is used to further reduce their concentration. At moderate H_2 purity (90-98%), a high hydrogen recovery (98%) could be accomplished. Practically, fuel cell-grade H_2 purity cannot be achieved [61]. Cryogenic distillation is an environmentally friendly process because it does not involve the use of chemicals and does not generate secondary pollutants. Among the disadvantages of this technique is its high capital and operating costs, as it requires an enormous amount of energy. Unfortunately, the storage of liquid hydrogen has a very low density of 0.071 $g.cm^{-3}$ due to inevitable evaporation loss (0.3 to 3% per day depending on vessel size), which is quantified as the vessel size increases. Refueling the liquid hydrogen on board causes an additional loss of between 10 to 25 percent. The infrastructural expense of insulation and energy expenditure for liquefaction (10 kWh per kg of H_2) further restrict the utilization of liquid hydrogen for commercial purposes. Liquification of liquid hydrogen results in a loss of one-third of its total energy contained in

hydrogen [13]. The cryogenic method is well suited for large industrial operations, however, it is not adequate for purifying small amounts of hydrogen at hydrogen filling stations for hydrogen fuel cells. As a result, it is not appropriate for portable applications that can be used onboard or on-site because of the equipment involved during operation.

Metal hydrides have demonstrated potential for the recovery of high-purity (> 99%) hydrogen with moderate efficiency (74-95%). This method employs a reversible reaction over metal alloys for absorption and desorption, which is measured by adjusting the temperature and pressure of the feed gas. At a certain pressure threshold, hydrogen forms metal hydride (MH_x, M is metal), whereas below this pressure, pure H_2 is discharged. By lowering the temperature and increasing the pressure, a metal alloy converts hydrogen molecules into H-atoms. Hydrides are formed through diffusion, phase transition, combination reaction, and other processes involving H-atoms and metals, whereas the other gases remain entrapped within the metal particles. Recently AB_5 type metal hydrides that are composed of a rare earth or transition metal (A) and five hydrogen atoms (B5) per metal atom have got attention due to their cubic crystal structure that exhibits a high hydrogen storage capacity at normal temperature (273 to 373 K) and pressure (100 to 1000 kPa). Before practical application, heat and mass transfer considerations, adsorption/desorption reaction kinetics, temperature, pressure, bed volume with large capacity, enthalpy, and cycle time must be optimized [60].

Membrane separation techniques have attracted an enormous amount of interest in H_2 separation as a result of their low cost, simplicity of operation, low energy demand, continuous operation, compactness, and geometry versatility. A metallic membrane is a selective physical barrier that allows a particular species to pass through itself in response to a driving force. In the case of gases, the driving force is primarily concentration differences, which are directly related to the difference in partial pressure across the membrane. Consequently, partial pressure of the particular species in the feed and permeate sides is the most important parameter governing membrane performance. Critical parameters that define the performance of the membrane include flux (volumetric flow rate per unit membrane area), selectivity (the ability of the membrane to separate the desired gas), and mechanical and thermal stability. Organic (polymeric) and inorganic (ceramic, zeolite, carbon molecular sieve, and metallic) are the most common classifications of H_2 separation membranes. Ceramic, zeolite, and carbon molecular sieve-based inorganic membranes are classified as porous (mesoporous and microporous), whereas metallic membranes are non-porous (dense). The metallic membrane is further subdivided into Pd-based and Non-precious metal-based. Membranes made from nickel,

palladium, and platinum in group 10 and some metallic elements in groups 3-5 of the periodic table can dissociate and dissolve hydrogen, but only palladium membranes demonstrate an exceptional ability to transport hydrogen through the metal due to a much higher solubility of hydrogen in its bulk over a wide temperature range [60,61]. Metallic membranes particularly dense Pd-based provide fuel cell grade purity (>99.999) and greater than 99% hydrogen recovery from any gas mixture. In addition, the membrane can be directly incorporated into the MR unit for simultaneous separation, thereby shifting the catalytic reversible reforming reaction to the product side and enhancing hydrogen conversion [62]. However, the fabrication of a dense membrane that is self-supported is prohibitively expensive and results in a low H_2 flux. In addition, these membranes are incapable of withstanding the elevated pressure. As a result, an asymmetric composite supported membrane has been developed, which involves coating a thin dense metallic layer over a porous support. Several porous supports, such as porous alumina, porous stainless steel (PSS), porous vycor glass, and porous inconel, have been proposed as viable options. Supported membranes can be fabricated with palladium layers that are significantly thinner, resulting in lower costs; consequently, substantial effort has been expended to develop methods of fabrication employing supports. Certainly, each has its own set of advantages and disadvantages. The choice of support is largely determined by the application, operating conditions, pore size distribution, and expansion coefficient. Coating a dense, selective Pd metallic layer on the substrate is a challenge in and of itself, as a thick layer will result in a low H_2 flux and a thin layer will result in a decrease in selectivity. The H_2 selectivity, on the other hand, did not exhibit any direct dependency on the top layer thickness. Instead, it was affected by imperfections in the layer, such as faults or pinholes on the surface. These imperfections are not determined by the thickness, but rather by the quality of the top metal layer. Several methods, including electroless plating (ELP), chemical vapor deposition (CVD), physical vapor deposition (PVD), cold rolling (CR), spray pyrolysis, and electro-plating deposition (EPD), have been reported for Pd coating over these supports. ELP is widely reported for coating because of its ease of coating even on irregular support, low cost, and simple equipment [63]. A brief comparison of the H_2 purification technique is summarized in Table 1.2 based on several parameters such as operating principle, inlet feed gas, H_2 recovery, H_2 purity, and scope for scale-up.

Table 1. 2. Comparison of hydrogen purification technique (reproduced from [62]).

Technique	Principle	Typical feed gas	H_2 recovery (%)	H_2 purity (%)	Scale of use	Issues
Cryogenic separation	Partial condensation of gas mixtures at low temperatures	Petrochemical and refinery off-gases	Up to 98	90-98	Large scale	Purification step necessary to remove CO_2, H_2S, and Water
Dense palladium membrane	Selective diffusion of hydrogen through a palladium-alloy membrane	Any H_2-containing gas stream	Up to 99	>99.999	Small to medium	Sulfur compounds and unsaturated hydrocarbon affects the permeability
Metal hydride separation	The reversible reaction of hydrogen with metals to form hydrides	Ammonia pure gas	75-95	99	Small to medium	Hydrogen absorption poisoned by O_2, N_2, CO, and S
Polymeric membrane	Differential rate of diffusion of gases through a permeable membrane	Refinery off gases and ammonia purge gas	95	92-98	Small to large	He, CO_2, and H_2O may also permeate through the membrane
PSA	Selective adsorption of impurities from the gas stream	Any H_2-rich gas	70-85	99.99	Large scale	Recovery is low as high hydrogen is lost in the purging step

1.3.2. Membrane for Hydrogen Separation

For on-site/on-board H_2 purification, commercial methods such as PSA and cryogenic distillation are inefficient and energy-intensive. In addition, none of these methods provides adequate purity and H_2 recovery for fuel cells. Therefore, membrane-based technology is regarded as the most promising method for on-site/on-board production of H_2 with high purity. Broadly hydrogen selective membrane is classified into four categories including polymeric, carbon molecular sieve, ceramic, and metallic based on the types of material being used. Membrane performance widely depends on the membrane material, therefore the selection of the membrane for particular requirements is critical. However, each type of membrane has its own set of advantages and disadvantages when it comes to the separation and purification of H_2 which are essentially determined by the chemical, thermal, and mechanical stabilities of membranes themselves. Even the mechanism by which gases are transported through the membrane plays a significant role in determining the performance and efficiency characteristics, i.e. flux and selectivity. Separation processes involving H_2 can be ascribed to one (or more) of the following five mechanisms as shown in Figure 1.5: (i) Knudson diffusion (pore diameter is smaller than the mean free path of the gas molecules), (ii) surface diffusion (adsorption of permeating molecules on the surface and migration along the surface), (iii) capillary condensation (transfer of relatively large gas molecules that condense within the pores due to capillary forces), (iv) molecular sieving (operate on a size-exclusion principle), and (v) solution diffusion (gas molecules diffuse through the dense selective layer due to concentration difference) [64].

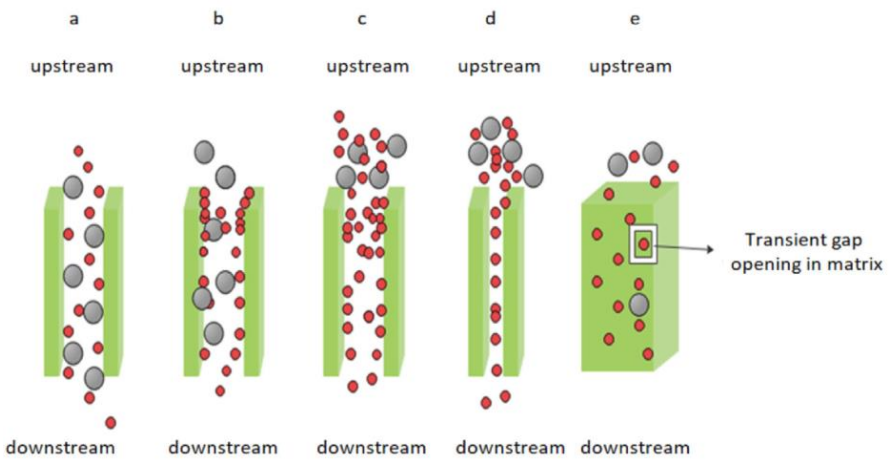

Figure 1. 5. The mechanism for H_2 separation through the membrane:) Knudsen diffusion, (b) surface diffusion, (c) capillary condensation, (d) molecular sieving, and (e) solution diffusion (reproduced from [64]).

Table 1.3 provides a comparison of different H_2 separating membranes including polymeric membrane, carbon molecular sieve, ceramic membrane, and metallic membrane based on various parameters, including temperature, pressure, flux, selectivity, transport mechanism, and membrane stability. The details of these membranes are discussed below:

Polymeric membranes are of two types glassy (higher selectivity and lower flux) and rubbery (lower selectivity and higher flux), mostly used for H_2 separation from mixture gases consisting of N_2, CO, and other hydrocarbons. The polymeric membrane is an attractive choice due to its minimal pressure drop, flexibility in fabrication, and low cost. Polyimide, polycarbonate, polysulfone, polyethersulfone, Polybenzimidazole, and polyetherimide are the most commonly used membranes for H_2 separation. However, the H_2 selectivity and flux are insufficient for practical applications. Additionally, polymer aging and plasticization at higher temperatures (> 373 K) are significant problems. Polymeric membranes are less appealing for commercial exploitation due to their low mechanical strength, swelling, and susceptibility to additional gases such as HCl, SO_x, and CO_2 [61,64]. Therefore, the polymeric membrane has limitations of temperature and pressure for on-site/onboard application in reforming reactions when integrated into MR.

The carbon molecular sieve membrane can function at temperatures ranging from 773 to 1173 K. Polymer blending is used to preserve the porosity and pore structure. The partial collapse of the pores caused by high-temperature thermal treatment results in reduced H_2 flux. Multiple layers are required during preparation which increases the packing density reducing the flow space and resulting in high pressure drop. Controlling the pore size is another challenge during preparation. Additionally, the membrane is prone to oxidation and vapor adsorption (H_2S, NH_3, or chlorofluorocarbons), which block the pores and sharply reduce the H_2 permeability simultaneously. Even the best-reported H_2/CO_2 selectivity is less than 60, which is a crucial element in practically all industrial and reforming product gas. The further applicability of this membrane is further constrained by the fact that it is brittle [65].

Ceramic membranes are often categorized as micro-porous ceramic dense ceramic or proton conducting ceramic. While solution diffusion is used in dense ceramics, molecular sieving is used in microporous ceramics to separate H_2. Although micro-porous ceramic generally comprises Al_2O_3, TiO_2, ZrO_2, zeolite, and silica oxides and exhibits high flux, its applicability for high-purity hydrogen separation is constrained by low H_2 selectivity. On the other hand, dense ceramic membranes mostly include dense ceramics-perovskite such as $SrCeO_{3-\delta}$, and $BaCeO_{3-\delta}$ (δ denotes the number of oxygen vacancies). H_2 transports through the membrane in

the form of ions (protons) which makes them highly selective for hydrogen. In addition to this, these membranes can be operated at high temperatures (873-1173 K). However, due to the presence of CO_2 in the gas streams the formation of undesirable compounds such as $SrCO_3$, and $BaCeO_3$ occurs that lower the H_2 permeance. Additionally, the membrane selectivity is significantly decreased by the micro-pores and cracks that develop as a result of continuous steam exposure. The main challenges for on-site/onboard application are material deterioration, low flux, and long-term performance [61,66].

Metallic membranes have recently attracted a lot of attention for H_2 separation due to their high hydrogen selectivity and flux. In addition, they can be operated at a wide range of temperatures (573-873 K) and pressures. The protons and electrons that makeup H_2 can pass through metallic membranes, which are typically dense sheets or films. The operating temperature can be lowered to even room temperature when alloyed with other metals, specifically. The metallic membranes have demonstrated exceptional mechanical and thermal resilience. In these membranes, H_2 is transported through a solution diffusion mechanism. Several metals such as Pd, Ni, Pt, Cu, Ag, Au, V, Ta, Nb, Mo, etc. have been investigated for practical application. High purity of H_2 (99.999%) can be achieved through dense metallic membranes especially Pd and its alloy-based membrane. Pd also has one of the highest diffusivities and solubilities for H_2 in its crystal structure. Pd-based membranes provide nearly infinite selectivities and make it possible to produce ultra-pure hydrogen with a purity level of 99.99999% [67]. Pd is more resistant to H_2S and CO poisoning and less susceptible to H_2 embrittlement when alloyed with other metals including Ag, Cu, and Au. Among the membranes discussed previously, Pd is the most appropriate choice for hydrogen separation since it naturally can catalyze the H_2 dissociation and reassociation over the surface. The cost of developing a 50 μm thick palladium-based membrane is approximately $5500 per square meter. A polymeric membrane costs approximately $500 per square meter. More importantly, the hydrogen permeability of Pd-based membranes is 1000 to 10000 times higher. Consequently, Pd-based membranes are the most favorable option [61]. In addition, Pd-based metallic membranes with excellent selectivity and flux can be incorporated into MR for on-site/onboard H_2 separation. Notably, both conventional and emerging technologies have limitations, and it is difficult to achieve the desired level of purity using only one method. Therefore, separation systems based on Pd-based metallic membranes are required to match the H_2 purity requirements for fuel cells or other high-end applications.

Table 1. 3. Comparison of different H_2 selective membranes (adapted from [61,66]).

Parameter	Dense Metallic (Pd-alloy)	Dense polymer (Polymer, polyimide, cellulose, acetate, polysulfone)	Micro-porous ceramic (Silica, alumina, zirconia, titania, zeolites, metal-organic frameworks-MOF)	Dense ceramic (Persovskites $SrCeO_{3-\delta}$, $BaCeO_{3-\delta}$)	Porous carbon (Carbon)
Temperature (K)	573-873	<373	473-873	873-1173	773-1173
Hydrogen Selectivity	> 1000	Low	5-139	> 1000	4-20
Hydrogen Flux (10^{-3} mol m^2 sec) ΔP = 100 kPa	60-300	Low	60-300	6-80	Medium
Mechanism	Solution diffusion	Solution diffusion	Molecular sieving	Solution diffusion	Surface diffusion/ Molecular sieving
Development status	Not commercial	Commercialized	Commercialized	Small testing	Small sample testing
Cost	Moderate	Low	Low	Low	Low
Stability Issue	H_2 embrittlement/ Phase transition	Swelling, mechanical strength	Unstable in H_2O	Unstable in CO_2	Brittle, Oxidizing
Poisoning issue	H_2S, HCl, CO	HCl, SO_x, CO_2	--	H_2S	Strong adsorbing vapors, organics

1.4. Membrane Reformer (MR)

The most prevalent element in the universe is hydrogen (90% of the visible universe). It is the third most abundant element in the earth's crust after oxygen and silicon. Hydrogen occurs naturally on Earth in liquid, gaseous, and solid compounds with other elements (primarily oxygen and carbon). Utilizing hydrogen as an energy carrier mandates its extraction from the compound and additional purification (separation) prior to its use. Hydrogen production is gaining increasing interest, not only for large-scale applications in refineries but also for smaller applications such as power generation. For the production of hydrogen from LOHC such as methane, methanol, and ethanol via steam reforming, multiple reactors and a separator unit are required to attain the desired hydrogen purity. To increase the efficiency and decrease the intended volume of reactors and separators, novel membrane reformers (MR) are currently being conceptualized. A membrane reformer is a device where hydrogen production and separation (using a Pd-based membrane) are integrated into a single compact reactor unit. According to Le Chatelier's principle, continuous removal of the H_2 through the membrane alters the thermodynamic equilibrium towards the desired product resulting in enhanced conversion. Consequently, the membrane reformer can operate under milder conditions (temperature and pressure), enhancing the overall efficiency of the process.

Hunter reported the first Pd-alloy-based metallic membranes for H_2 separation in 1960 [68]. Vladimir Gryaznov (1964, Moscow University) is the first to propose the MR for cyclohexane degradation to benzene in a dense tubular Pd reactor in which Pd served as both an H_2 permeable membrane and a catalyst [69]. The first MR was commercialized by Johnson Matthey in 1964. They fabricated different modules ranging from 166 L min^{-1} to 833 l min^{-1} of hydrogen production with purity levels up to 99.9999%. Further, they developed a methanol-water-based H_2 generator with 416 L min^{-1} of capacity. However, a small unit of 33 L min^{-1} of H_2 production was successfully installed for the British Antarctica Survey in 1974 [70,71]. The first pilot-scale membrane reformer for hydrogen production is conceptualized by Tokyo Gas Company Ltd. Steam Methane reforming (SMR) coupled with water gas shift reaction is performed to produce hydrogen over a catalytic bed. 66 L min^{-1} of hydrogen is produced with purity > 99.999%. In addition to this, the MR is further connected to a 5 kW DC electricity polymer electrolyte fuel cell to examine the operational effectiveness of the concept. Then a scaled-up 250 L min^{-1} MR is developed and operated for 1500 h with 40 start-up and shut-down cycles (H_2 purity of 99.99%). Further, they demonstrated a 666 L min^{-1} MR with a higher heating value (HHV) efficiency of 76%, H_2 purity of 99.99%, and hydrogen production energy

efficiency of 80%. The H_2 purity decreased after operating for 3000 h with 60 start-up and shut-down cycles [72]. De Falco et al. [73] designed a reformer and a membrane module for the purification of 333 L min-1 of hydrogen from the mélange of gases produced by reforming natural gas. They obtained a conversion rate of 57.3% at 873 K and over 1000 hours of testing without any discernible degradation in membrane performance. Pd-based membrane reformer module by REB Research and Consulting (Michigan, US) offers high-purity hydrogen (> 99.9999%) with an H_2 production rate ranging from 1.5 L min^{-1} to 100 L min^{-1} [74]. The methanol-based membrane reformer developed by Element1 Powering Innovation (Oregon, United States) generates hydrogen with an efficiency of over 70%. In addition, they offer a variety of hydrogen generators with production rates ranging from 1 L min^{-1} to 1300 L min^{-1} (purity = 99.95%) [75]. H_2 Site Hydrogen On-site, S.L. (Bizkaia, Spain) designed a Pd-Ag membrane-based natural gas reformer with a 32 L min^{-1} to 833 L min^{-1} (purity = 98-99.99%) H_2 production rate [76]. Viviente et al. [77] developed a bio-ethanol-based MR for H_2 production through Pd-Ag/Al_2O_3 membrane at the rate of 53.33 l min^{-1}. They further optimized the thermal integration to enhance the overall efficiency of the system by more than 90% and hydrogen recovery of 76%. It was determined that 0.44 m^2 of Pd-based membranes is required to separate the said hydrogen amount using steam as the sweep gas. In the majority of cases, H_2 recovery has remained a challenge during scale-up, and a significant amount of H_2 is lost in the retentate stream. Therefore, the innovative design of the MR system to enhance recovery has significant research and development potential. To overcome this challenge introduction of the baffles has recently been reported. Horizontal or vertical baffles may be deployed to alter the flow field around the membrane breaking the barrier of concentration polarization, thereby improving the H_2 flux [78,79]. Ma et. al., [80] reported that the recirculation of product gases significantly improved the H_2 recovery in a multi-tube membrane module. While scaling up from 7 to 19 tube modules the effect of concentration polarization is more severe with uneven tube-to-tube performance at lower feed flow rate. Radial mass transfer limitation is observed as a major issue with large-scale membrane modules. Therefore, further research and development are needed to optimize the membrane materials and design, as well as the operating conditions. Design of the reactor during scale-up is the key to ensuring optimal performance and efficiency of MR.

1.4.1. Traditional Reformer (TR) Vs Membrane Reformer (MR)

More than 95% of hydrogen is still produced via steam reforming of methane and naphtha oil, and coal gasification in multi-tubular fixed bed reactors, where desired hydrogen purification

is accomplished using a series of PSA. The product gases coming from steam reforming, partial oxidation, and autothermal reforming contain H_2, carbon oxides, unreacted reagents, and other byproducts. These reactions are mainly kinetically and thermodynamically constrained which do not allow conversion beyond equilibrium limits. To overcome this challenge membrane reformers proposed to integrate the reaction and separation into a single unit. Simultaneous separation of products prevents the buildup of reactants and intermediates that could inhibit the reaction or cause unwanted side reactions. By removing the products from the reaction mixture, the equilibrium of the reaction is shifted towards the product side (Shift Effect – Due to the low product-to-reactant concentration ratio, the direct reaction proceeds more rapidly to achieve equilibrium composition), resulting in higher conversion due to Le Chatelier's principle [45].

In the traditional MSR process, there are at least three stages of reactors, including a steam reforming reactor, two WGS reactors, and a purification system such as PSA as shown in Figure 1.6. To accomplish the desired H_2 purity, a complex system consisting of a high-temperature heat exchanger and energy integration between multiple process units is necessary [81]. In contrast, performing the same reaction in a dense Pd-based MR reduces the number of stages to one while simultaneously producing ultra-pure hydrogen at milder reaction conditions as illustrated in Figure 1.6. Raich and Foley [82] stated that the continuous and selective removal of H_2 from the reactor is sufficient to overcome the thermodynamic limit of TR as well as accomplish a higher conversion, particularly for endothermic reactions. Basile et al. [83] mentioned that in the case of MR, thermodynamic equilibrium is only associated with a dense Pd-based membrane and represents a reaction that is not constrained by any type of chemical kinetics; consequently, the feed gas is presumed to be continuously at equilibrium within the MR. Due to the continuous permeation of H_2, the feed gas composition alters. This indicates that the reaction rate is not a limiting factor, as all molecules in contact with the catalyst are assumed to react with an infinite velocity without any kinetic resistance. Removing the product from the reaction zone enhances the overall conversion rate of reactants from a reaction kinetics perspective by decreasing the reverse reaction rate. Therefore, the thermodynamic equilibrium conversion is restricted to TR (closed system) and not MR (open system). MR also improves the mass transfer of reactants, intermediates, and products by regulating the flow rate and distribution of reactants and products through the membrane. This can contribute to a more uniform distribution of reactants and products throughout the reactor, resulting in a more efficient utilization of reactants and a better conversion. In addition, MR allows for a prolonged residence time for the reactants and products, resulting in a more complete reaction. This can

be crucial for reactions with slow kinetics or those that require high temperatures or pressures to proceed [84].

However, the design and optimization of the membrane reformer must be meticulously considered to maximize these advantages over TR. Innovative MR design and configuration have the potential to reduce capital expenditures, enhance yield and selectivity, and reduce the purification process in subsequent stages. Due to the small size of the MR and its numerous advantages over the TR, its application as a hydrogen generator at the place of application (on-site/onboard) is viewed as the future of the hydrogen energy ecosystem, as it reduces the risk associated with hydrogen storage and transportation. In addition, MR's adaptability to various feedstock makes it a versatile technology according to the needs and availability of the feedstock. Consequently, MR may be a more viable option for realizing a portable, off-grid H_2 generation unit than large-scale, centralized H_2 production combined with transport and storage.

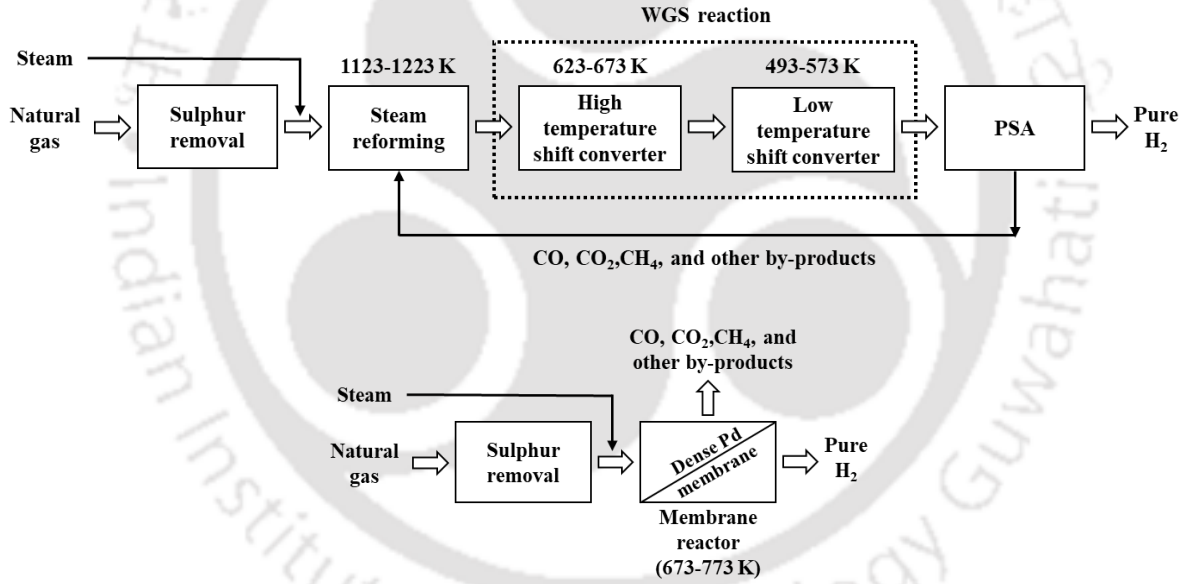

Figure 1. 6. Pure hydrogen production through natural gas in TR and MR (adapted from [83]).

1.4.2. Application of Membrane Reformers

The feasibility of the Pd-based MR is established from the above discussions. Membrane reformers provide a compact and efficient method of producing hydrogen from a variety of feedstocks, making them suitable for a vast array of applications in the energy sector, onboard power for transportation, and chemical industries as given in Figure 1.7. Given its wide range of temperature and pressure operability, MR can be effectively scaled up for medium to large

industries [85,86]. MR with the ability to enhance reaction rates, selectivity, and product yields, and reduce reactant consumption, energy consumption, and waste generation finds several applications including:

- **Fuel cell vehicle:** Membrane reformers can be used to produce hydrogen onboard fuel cell vehicles. The reactor can use the vehicle's stored fuels, such as natural gas, methanol, and ethanol, to produce hydrogen, which can then be delivered directly into the fuel cell to generate power [87]. Heavy-duty vehicles such as buses, trucks, and cargo ships are the possible targets for MR toward decarbonization of the transportation sector.

- **Stationary power generation:** A membrane reformer can also be used to produce hydrogen for stationary power generation. In this application, the reactor can use a variety of feedstocks, including natural gas, biogas, and renewable fuels, to produce hydrogen for use in fuel cells or combustion engines. This may serve as a clean alternative to traditional diesel or petrol-based stationary power sources currently being used in mobile towers, apartments, and emergency power backup.

- **H_2 fuel station:** A huge demand for hydrogen refueling stations is anticipated in the future due to the rising number of hydrogen vehicles. At the H_2 fuel station, a membrane reformer can be deployed for the continuous production of hydrogen. Hydrogen is stored and refueled within the vehicle.

- **Industrial processes:** A membrane reformer can be used in various industrial processes, such as ammonia production, dehydrogenation, fuel for industrial heating, etc. H_2 is directly burned in the furnace for a variety of industrial applications such as metal heat treating, glass melting, and ceramic production. In addition to this, MR can directly be used in water gas shift (WGS) reactions which is an essential part of several industrial processes such as steam reforming of hydrocarbons, coal gasification, ammonia production, methanol synthesis, etc.

- **Nuclear power plant*:*** Tritium is a radioactive isotope of hydrogen that is produced when a nuclear power facility operates. Tritium can be extracted from reactor coolant using membrane reformers. This is accomplished through the use of a Pd-based membrane that is permeable to hydrogen but not to other gases or impurities. Nevertheless, their application in nuclear power facilities is still in the research and development phase, and additional research is required to evaluate their viability and potential benefits for further exploitation [88].

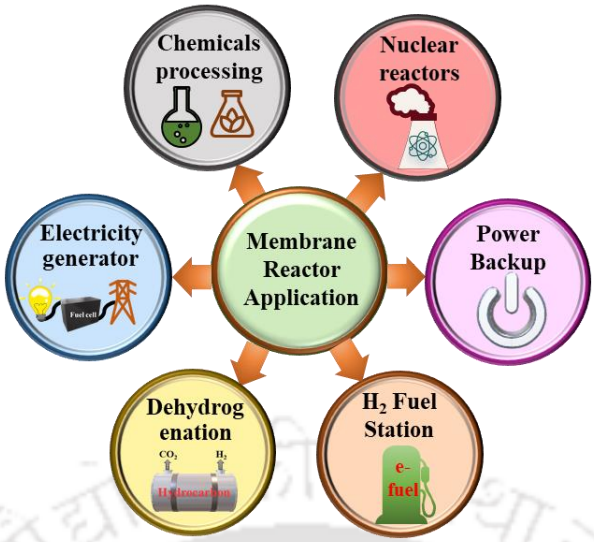

Figure 1. 7. Potential application of membrane reformer.

1.4.3. Challenges in Membrane Reformers Technology

Membrane reactors are the most compact technology for on-site hydrogen generation, with several of the aforementioned applications. However, despite their potential benefits and applications, membrane reformers still face several challenges that need to be overcome for successful commercial applications. Some of these challenges include membrane stability, catalyst stability, scale-up strategies, integration with fuel cells, and high cost [89]. To overcome these challenges, extensive research and development must be conducted in membrane reformer design, materials science, and process engineering. Innovative solutions, such as the development of more robust membranes and catalysts, the implementation of novel membrane reformer module designs, and the optimization of operating conditions, can help overcome these obstacles and make membrane reformers more suitable for commercialization. In this section, we will examine some of the pertinent challenges in more detail.

- **Membrane preparation:** The preparation of dense, highly permeable, hydrogen selective membranes at low cost to satisfy the variable demand for hydrogen on-site is a significant issue in MR. In addition to this, the thermal and chemical stability of the membrane during operation remains a barrier to commercialization. Hydrogen permeability is typically inversely proportional to selectivity and cost, necessitating a well-balanced trade-off for MR integration. For instance, the requirement of a thick Pd layer to obtain high selectivity compromises the membrane's permeance, thereby increasing its price. Moreover, the driving force, such as pressure and temperature, is crucial in determining permeability and selectivity (purity). At high pressure, permeability increased, but always at the expense of selectivity. At elevated

temperatures, the hydrogen permeability and selectivity are enhanced, but this could accelerate the membrane's degradation [90,91]. Further, the effect of concentration polarization due to N_2, CO_2, etc. over the membrane surface retards the hydrogen permeability. This effect is more noticeable at high pressure. The competitive adsorption of CO on the Pd layer obstructs the active sites of catalytic dissociation of H_2, which has a detrimental effect on permeability [92]. The effect of CO_2 is primarily the result of concentration polarization at low temperatures (623 K) and a combination of concentration polarization and chemical reactions at higher temperatures (723 and 823 K) [93]. In the case of a fluidized bed reactor, the continuous striking of the moving fluidized particle on the Pd membrane slowly starts eroding or damaging the membrane surface (called membrane abrasion). This phenomenon may damage the membrane permanently affecting the hydrogen permeate purity [94]. Therefore, the preparation of thin dense selective membranes with better thermal stability is critical for the overall performance of the membrane reformer.

- **Catalyst preparation:** MR is dependent on catalyst synthesis to obtain high conversion and the necessary product gas selectivity. Typically, the catalyst for methanol steam reforming is a metal oxide, such as copper oxide (CuO) or zinc oxide (ZnO), supported on a high-surface-area material, such as alumina. (Al_2O_3). In general, these catalysts are operated at elevated temperatures (around 473-673 K). However, the reformate gases contain CO, which increases with temperature and pressure. It is desired to synthesize a catalyst with a low CO concentration in product gases. If CO production is reduced at the reaction level, not only will catalyst performance be improved, but membrane permeability will also be maintained [95]. Additionally, the accumulation of carbonaceous deposits on the surface of catalysts can lead to their deactivation over time. These deposits might block the active sites on the surface of the catalyst and reduce its activity. Moreover, elevated temperatures can cause the metal particles in the catalyst to sinter or aggregate, reducing the catalyst's activity. To improve the performance of the MR, it is anticipated that catalyst materials and a better reactor design will be required to increase the efficacy and durability of methanol steam reforming catalysts [96,97].

- **Membrane reformer optimization:** When it comes to the integration of hydrogen production and simultaneous separation, all parameters, including temperature, pressure, WHSV, S: C ratio, sweep gas effect, membrane surface area, and reactor design, must be optimized. However, the opposing operating condition of MSR (low temperature and pressure) and Pd membrane (high temperature and pressure) is the major bottleneck. On the one hand,

the Pd membrane necessitates high temperature and pressure for hydrogen separation, whereas MSR necessitates low temperature and pressure for CO reduction [58]. Since high hydrogen recovery from a mixture of gases should be the top priority for meeting the on-site demand for electrical capacity with fuel cells, it is essential to maximize the amount of hydrogen recovery from the reformate gases. Therefore, an equilibrium must be reached between temperature and pressure for reaction and separation. In addition, membrane sealing to the reactor with graphite ferrule, glass enamel, and glaze is frequently compromised by the reaction environment, resulting in a significant reduction in permeate hydrogen purity. The key to the MR's overall efficacy is therefore the reactor's design, which must optimize all the desired parameters [98,99].

- **Online integration with fuel cells:** Direct integration of the fuel cell with the membrane reformer to produce electricity for onsite application is crucial. PEMFCs require ultra-pure hydrogen (>99.999%) with CO content of not more than 10 ppm as CO damages the platinum-based catalyst inside the fuel cell. Direct integration of MR with the fuel cell thus requires constant checks over the hydrogen purity being fed [100]. In addition, the fluctuating demand for and supply of hydrogen must be matched to prevent power fluctuations. Also, the start-up time of MR to provide instantaneous hydrogen on demand is a challenge. Adding a buffer tank storage at low to moderate pressure may, however, alleviate the start-up problem and allow the system to operate for a time. Putting the entire system into standby mode is also a possibility, but the duration of standby and net hydrogen consumption will be determined by the accessories' continuous power consumption [89]. The inclusion of a buffer tank will once again introduce a potential safety risk. At this stage, the stability of the Pd membrane to produce high-purity H_2 in a harsh reformate gas environment of MSR is essential for long-term continuous operation.

- **Cost of membrane reformer:** In the last two decades significant progress has been accomplished in the design and development of compact membrane reformers. However, for commercialization, the high cost of different components involved like the metal-based catalyst for MSR, Pd-based membrane for hydrogen separation, reactor cost, PEMFCs, and other accessories still doesn’t match the expectation of the end user. In general, the commercial CuO-ZnO-Al_2O_3-based catalyst is used for MSR. However, these catalysts suffer from the critical issues of sintering and deactivation. To circumvent this issue, novel metal-based catalysts such as Pd, Pt, and Ru are utilized, which increases the overall cost of the catalyst.

The cost of the membrane prepared using Pd again adds to the overall cost. The 2015 target set by the Department of Energy, United States (DOE, US) for the hydrogen flux is 1.13 mol m^{-2} s^{-1} with a purity of 99.99% (selectivity > 9,999), even in gas mixture conditions. The requirement must be satisfied at a differential partial pressure of H_2 of 138 kPa, temperature of 673 K, durability of 5 years, recovery of above 90%, and a cost of less than $4400 per meter square. With this objective, the requisite membrane thickness to meet the objective is on the order of 0.1 μm (ultra-thin membrane) [101]. Unit costs for Pd-based membrane reformers can range from a few thousand to tens of thousands of dollars. Utilizing an ultra-thin Pd membrane is anticipated to result in a significant reduction in membrane-related capital expenditures. For instance, a Pd-based membrane reformer module by REB Research and Consulting (Michigan, US) offers high-purity hydrogen (> 99.9999%) with an H_2 production rate ranging from 0.5 L min^{-1} to 120 L min^{-1} at the cost of $3150 to $87000 respectively [74]. The methanol-based membrane reformer developed by Element1 Powering Innovation (Oregon, United States) generates hydrogen at $3 to $4 per kg of H_2 with an efficiency of over 70%. In addition, they offer a variety of hydrogen generators with production rates ranging from 1 L min^{-1} to 1300 L min^{-1} (purity = 99.95%) [75]. Recently Tokyo Gas Co., Ltd (Tokyo, Japan) developed a natural gas-based membrane reformer for H_2 production at the rate of 666.66 L min^{-1} with a production efficiency of 76% (purity = 99.99%). The cost of the reformer is not mentioned [72]. H_2 Site Hydrogen On-site, S.L. (Bizkaia, Spain) designed a PdAg membrane-based natural gas reformer with a 32 L min^{-1} to 833 L min^{-1} (purity = 98-99.99%) H_2 production rate. The production of hydrogen costs between $1.50 and $2 per kg of H_2 [76]. Johnson Matthey likewise developed a hydrogen generator in 1975 comprised of a Pd-based membrane reformer fed with a mixture of methanol and water mixture. The maximum hydrogen production rate reported is 416 L min^{-1} [70].

However, almost in all cases the rector modification and design have not been investigated in detail. Reactors being used are mostly of traditional types like the packed bed or the fluidized bed. The heat and mass transfer limitation of the packed bed reactor limits its large-scale application, especially for endothermic reactions like MSR. Furthermore, in the case of a fluidized bed reactor, the continuous striking of the moving fluidized particle on the Pd membrane slowly starts eroding or damaging the membrane surface. Concentration polarization and the reactive nature of other gases negatively affect the membrane performance. Hence, an innovative design of the MR is crucial for enhancing hydrogen recovery and overall process efficiency. The reactor geometry, such as the membrane configuration, reactor

dimensions, and reactor shape, can influence the mass transfer of reactants and products, heat transfer, and fluid dynamics within the reactor. The geometry of the reactor should be optimized for maximum efficacy. The operating conditions must be optimized to maximize the reaction's conversion and selectivity. Membrane reformers are regarded as comparatively costly due to the high price of Pd membranes and the complexity of their production. However, the long-term advantages of using a Pd-based membrane reformer for onsite hydrogen generation can counterbalance the initial expense through increased efficiency and decreased energy consumption. In addition to this, MR is a grid-independent power source that has the potential to completely transform the entire ecosystem of the clean hydrogen energy sector [86,102,103].

1.4.4. Membrane Reactors for On-site Hydrogen Generation

On-site H_2 production and industrial-scale H_2 production combined with H_2 transport and distribution are the two primary techniques of H_2 supply. The absence of the risk associated with storing large quantities of flammable and explosive H_2 and the sophisticated infrastructure required to mitigate this risk should result in substantially reduced operating and capital expenses for the MR. A cost-effective and efficient on-site H_2 production unit is therefore regarded as a key enabling technology for H_2-based infrastructure [104]. The basic structure of the on-site hydrogen generation and refueling station consists of feed storage, a membrane reformer, a compressor, a storage tank, and a dispenser. As shown in Table 1.4, numerous studies on the production of hydrogen through MR with varying capacities for on-site and small-scale applications have been published.

Table 1. 4. MR for onsite or small-scale hydrogen production capacity.

Membrane	Feed	Capacity (kg h^{-1})	Reference
Pd-based	Methane + Steam	8.91	[105]
Pd-based	Methane + Steam	7.12	[106]
Pd-alloy	Natural gas + Steam	3.58	[107]
Pd-based	Natural gas + Steam	3.58	[108]
Pd-based	Methane + Steam	1.79	[73]
Pd-alloy	Methane + Steam	2.5	[109]
Pd-based	Methanol + Steam	0.64	[74]
PdCu-based	Methanol + Steam	6.95	[75]
$PdAg/Al_2O_3$	Natural gas + Steam	4.45	[76]
Pd-based	Methanol + Steam	2.22	[70]
PSA	Natural gas + Steam	6.14	[110]
Pd-based	Natural gas + Steam	3.56	[72]

Only a few companies are pursuing the development of on-site hydrogen production units utilizing MR. The cost and dimensions of the MR are ultimately determined by the required rate of pure H_2 production on the permeate side [111]. For instance, HyGear (Arnhem, Netherlands) developed natural gas based on three models namely Hy.GEN 50 (783 L min^{-1}), Hy.GEN 100 (1566 L min^{-1}), and Hy.GEN 150 (2350 L min^{-1}) depending on the H_2 requirement. They used PSA for hydrogen purification up to 99.999% at an outlet pressure of 150-700 kPa. With the increase in the H_2 production rate, the size and weight of the model increased from 6 m to 12 m and 7300 kg to 15000 kg respectively. In addition to this, the electricity consumption has doubled from 14.5 kW (Hy. GEN 50) to 29.5 kW (Hy. GEN 150). Moreover, the startup time from shutdown (cold) mode is 3 h, and from standby (warm) is 30 minutes to achieve the full hydrogen output capacity [110]. Another such device is proposed by Element1 (Oregon, United States) developed three series of methanol-water-based membrane reformers namely S-series (up to 130 L min^{-1}), M-series (up to 400 L min^{-1}), and L-series (up to 1300 L min^{-1}) for fuel cell grade H_2 production onsite (purity > 99.97%, and CO < 1%). The PdCu-based membrane is exploited for hydrogen separation. The output H_2 pressure ranges between 69 kPa to 200 kPa. The overall power consumption of the S-series is 700 W (100 W for standby) and for the L-series is 6 kW while generating H_2. Depending on the application, the space required for these reformers ranges from 7.2 to 15 m^2 and the weight ranges from 600 to 3000 kg [75]. There are other enterprises such as H_2-site (Spain), ENEA (Italy), MRT Ltd. (Canada), Pall Corporation (USA), Power & Energy Inc. (USA), Tecnimont Kinetic Technology (Italy), Tokyo Gas Co. Ltd. (Japan), and SK Corporation (South Korea) who developed Pd-based MR for hydrogen production. However, the H_2 production rate is less than 10 kg h^{-1} and further scale-up is required. The reactor type is limited to either a packed bed or a fluidized bed. The crucial challenge of on-site MR is the cost-competitiveness of the Pd membrane and its long-term stability owing to pore-collapse above 823–923 K. Therefore, MSR reforming below 773 K is widely acknowledged. However for natural gas or methane high-temperature operability (> 873 K) may lead to membrane failure to achieve good conversion [112]. In addition to this, the dead volume of the furnace for a large-volume reactor consequently translates into non-thermal uniformity across the reactor. Catalyst packaging within the reactor is also crucial for overcoming heat and mass transfer limitations. It has been reported that catalyst types such as macro size, monoliths, honeycomb, and foam-shaped structures exhibit exceptional heat flux and a large surface area for the catalyst distribution [113]. MR modification and process conditions must be taken into account for various grades and types of available feedstock for the end user. In addition to this, the cost of hydrogen

production as per the Department of Energy, United States (DOE, US) should be maintained below $2 per kg of H_2. Another problem is the carbon sequestration formed during the thermochemical reaction in MR. For the long-term viability of MR, additional effort must be devoted to this area. Advanced technologies, such as Sorption-enhanced H_2 production and Chemical looping H_2 production, should be researched to make the overall process more efficient and environmentally friendly. Hence, MR needs to be scalable to different hydrogen demands from various applications, all while maintaining safety standards to limit the possibility of hydrogen leaks.

1.5. Motivation

The overall goal of this study is to investigate the viability of employing membrane reformers on a large scale in the production of on-site small-scale portable hydrogen generators as part of a commercial enterprise. MR offers a rewarding and challenging future path that contributes to the development of sustainable energy ecosystems. To satisfy the ever-increasing need for green energy, technological advances in the generation of hydrogen are absolutely necessary. Hydrogen is a promising fuel source that has the potential to be utilized in a variety of applications including power generation, transportation, and others. Membrane reformers present an opportunity for a problem that has been puzzling researchers for some time: how to efficiently and cleanly produce hydrogen. The advancement of technology for membrane reformers, including their development and improvement, can contribute to the growth of sustainable energy systems. The dependability and longevity of membrane reformers can be improved by the discovery of new materials and the enhancement of the performance of those already in use. The ability to work on cutting-edge research projects and collaborate with corporate partners, academic scholars, and government organizations is one of the benefits of MR. This can lead to opportunities for building professional networks, getting exposed to a variety of perspectives, and gaining access to materials that can contribute to one's professional development.

Researchers and innovators are driven to change the current energy system into a new one that is based on hydrogen once they recognize the challenges, opportunities, and scope of innovation presented by these issues. The concept of a membrane reformer appears to have a lot of potential, but successfully scaling it up presents several challenges, the most significant of which is the challenge of integrating the processes of reforming and separation under conflicting operating conditions. There is a requirement for an improved understanding of the overall optimization and workability of the process including fuel cells. A step towards

commercialization will be taken once a more in-depth understanding of the operational parameters of MR scale-up has been achieved. Because reliance on the existing fuel system and vehicle technology will not be sustainable in the long run from an ecological point of view. Hence, there is an urgent need to make the transition from conventional means of energy production to more environmentally friendly renewable energy-based technology. Future work will be required to understand the variables that can be tuned and engineered to overcome the limitations of a membrane reformer configuration to understand the design concept of the MR and its experimental evaluation.

1.6. The Objective of the Ph.D. Thesis

The global objective of the present study is to perform a comprehensive investigation for the design of membrane reformers and to produce fuel cell grade hydrogen through methanol steam reforming. Based on the scope of research determined in the preceding section, the specific objectives of the present work are as follows:

1. Preparation, characterization, and testing of dense supported Pd-Ag/α-Al_2O_3 composite membranes.
    - Preparation of Pd-Ag membrane using an Electroless Plating Technique
    - Characterization of the membranes
    - Performance testing of the membrane using pure as well as mixture gas
    - Long-term thermal cycle stability of the membrane
2. Performance study and optimization of multi-pass membrane separator (MPMS) for enhanced hydrogen recovery.
    - Effect of multi-pass over membrane performance and concentration polarization
    - Effect of the membrane-to-pass ratio over hydrogen recovery
    - Impact of feed load, membrane position, and feed distribution facility
    - Comparison of separator performance with and without baffles for scale-up
3. Experimental investigation of double-stage multi-pass membrane reformer for methanol steam reforming.
    - Preparation, characterization, and testing of structured SiC-based MSR catalyst

- Effect of temperature, pressure, space velocity, and membrane surface area on reformer performance
- Integration of MPMS with membrane reformer for enhanced H_2 recovery

1.7. Structure of the Thesis

The following outline constitutes the overall structure of the thesis:

Chapter 2: This chapter covers different aspects of the literature review regarding all three aspects of membrane reformers for hydrogen production including palladium membrane, methanol steam reforming, and membrane reactor design. Characteristics of palladium membrane for hydrogen separation, its preparation methodologies, and its applicability for commercial scale are discussed in detail. In addition to this, the literature review comprises diverse facets pertaining to methanol reforming, encompassing a comparative analysis of the different approaches employed in the reforming process. A thorough review of different approaches for catalyst preparation is provided to select the most appropriate procedure. At last detailed review of the latest developments in the reactor related to the MSR is examined to determine the current obstacles and research opportunities. Various reactor systems are analyzed to determine the most practical reactor design and innovations for improving the overall efficiency of the entire system.

Chapter 3: This chapter provides an overview of the key attributes shown by Pd-Ag membranes in the context of hydrogen separation. A concise overview of hydrogen separation through the Pd-Ag membrane with specific emphasis on recent advancements in various support types and materials employed for surface modification. Following the overview a composite Pd-Ag membrane is prepared using the ELP technique over the alumina support. The surface pore-mouth of the support is modified using a 2B-graphite lead owing to its enhanced ductility, thermo-electrical conductivity, and exceptional resistance to thermal shocks, all at a relatively economical price. Multiple cycles of deposition are performed to obtain a dense Pd-Ag membrane till 400 kPaG. The surface morphology and elemental composition are further monitored using a scanning electron microscope (SEM) and energy dispersive spectroscopy (EDS) respectively. After the preliminary leak test using the rising water bubble point technique, the permeation properties of the membrane are examined by subjecting it to pure H_2 and N_2 under varying temperatures (573-773 K) and pressure (100-300 kPaG) conditions. The investigation also encompasses the examination of the effect of mixture gases, such as H_2/N_2, H_2/CO_2, H_2/CH_4, and H_2/CO, on the performance of the membrane. In

addition to this, the long-term thermal heat cycle stability of the membrane is performed to assess its potential for commercial exploitation followed by surface characterization after testing. Lastly, the effect of feed load is investigated with pure H_2 as well as H_2/N_2 mixture gas with varying compositions to assess its separation ability for enhanced hydrogen separation. The optimized conditions are then utilized to further evaluate the performance of the membrane separator utilizing multiple membranes during scale-up.

Chapter 4: This chapter discusses the design, testing, and optimization of the multi-pass membrane separator (MPMS) to enhance hydrogen recovery from mixture gas. Hydrogen separation through the palladium-based membrane is evident due to its unique features of high hydrogen permeability and ideally infinite hydrogen perm-selectivity. However, the continuous permeation of hydrogen leads to the development of a mass transfer boundary layer. This layer consists of non-permeable gases that accumulate at the surface of the membrane, a phenomenon known as concentration polarization. To mitigate concentration polarization, the membrane separator incorporates three longitudinal baffles, resulting in the formation of four distinct passages (multi-pass). This configuration not only improved the regulation of the H_2 partial pressure across the separator but also optimized the interaction between the feed gas and the membrane. As a result, more time was available for hydrogen to move from the bulk of the retentate to the surface of the membrane, thereby improving the H_2 recovery. Starting with a single membrane, the multi-pass membrane separator performance is tuned for various locations inside the separator, baffle proximity, and feed load. Following the outcomes, a scale-up study with four and then ten membranes is performed. Finally, the effect of inlet feed distribution in each pass on separator performance is examined.

Chapter 5: This chapter discusses the integration of Pd-based membranes with methanol steam reforming for simultaneous hydrogen production and separation to solve the challenge associated with hydrogen storage and transport. The use of a SiC-based significantly reduced the heat and mass transfer issue in endothermic MSR. Moreover, continuous separation of hydrogen through the membrane drives the overall reaction toward the desired product according to Le Chateliers' principle. Both the membrane and MSR are compatible in the temperature range of 573 K to 673 K and pressure range of 100-300 kPaG. However, the hydrogen separation from the reaction mixture in the same membrane reformer was not sufficient. Therefore, a separate multi-pass membrane separator is integrated on the retentate side to further recover more hydrogen. The overall membrane reformer combined with MPMS is optimized to improve the overall system efficiency. Further, the integration of MPMS on the

retentate side of the MR significantly helped to recover the leftover hydrogen from the retentate of the MR. Therefore, the DSMR configuration demonstrated superior performance compared to MR and TR in terms of methanol conversion and hydrogen production rates. The dual-stage configuration facilitated enhanced hydrogen separation and promoted equilibrium shifting.

Chapter 6: This chapter provides a concise overview of the main findings made during the research and evaluates the initial goals established while determining the objective of the thesis. Moreover, a comprehensive perspective on the importance of the study is discussed. Subsequently, this chapter also outlines potential avenues for future research and practical implementations based on the results of our study.

References

[1] I. Dincer, C. Acar, Review and evaluation of hydrogen production methods for better sustainability, International Journal of Hydrogen Energy, 40 (2014), pp. 11094–11111.

[2] P. Li, Z. Wang, Z. Qiao, Y. Liu, X. Cao, W. Li, J. Wang, S. Wang, Recent developments in membranes for efficient hydrogen purification, Journal of Membrane Science, 495 (2015), pp. 130–168.

[3] S.M.M. Jokar, A. Farokhnia, M. Tavakolian, M. Pejman, P. Parvasi, J. Javanmardi, F. Zare, M.C. Gonçalves, A. Basile, The recent areas of applicability of palladium based membrane technologies for hydrogen production from methane and natural gas: A review, International Journal of Hydrogen Energy, 48 (2023), pp. 6451–6476.

[4] G.S. Burkhanov, N.B. Gorina, N.B. Kolchugina, N.R. Roshan, D.I. Slovetsky, E.M. Chistov, Palladium-based alloy membranes for separation of high purity hydrogen from hydrogen-containing gas mixtures, Platinum Metals Review, 55 (2011), pp. 3–12.

[5] D. Alique, D. Martinez-Diaz, R. Sanz, J.A. Calles, Review of supported Pd-based membranes preparation by electroless plating for ultra-pure hydrogen production, Membranes, 8 (2018), pp. 1–39.

[6] F. Safari, I. Dincer, A review and comparative evaluation of thermochemical water splitting cycles for hydrogen production, Energy Conversion and Management, 205 (2020), pp. 112182.

[7] A. Pachauri, R.K and Reisinger, Climate Change 2007: Synthesis Report. Contribution of Working Groups I, II and III to the Fourth Assessment Report of the Intergovernmental Panel on Climate Change, Intergovernmental Panel on Climate Change, 4 (2007), pp. 1–104.

[8] A. Kirubakaran, S. Jain, R.K. Nema, A review on fuel cell technologies and power electronic interface, Renewable and Sustainable Energy Reviews, 13 (2009), pp. 2430–2440.

[9] S. Sharma, S.K. Ghoshal, Hydrogen the future transportation fuel: From production to applications, Renewable and Sustainable Energy Reviews, 43 (2015), pp. 1151–1158.

[10] Glasgow Climate Pact, Decision -/CP.26: Glasgow Climate Pact, COP26, 1 (2021), pp. 1–8.

[11] X. Zhao, Y. Yan, J. Zhang, F. Zhang, Z. Wang, Z. Ni, Analysis of multilayered carbon fiber winding of cryo-compressed hydrogen storage vessel, International Journal of Hydrogen Energy, 47 (2022), pp. 10934–10946.

[12] F. Schüth, Challenges in hydrogen storage, European Physical Journal: Special Topics, 176 (2009), pp. 155–166.

[13] P. Preuster, A. Alekseev, P. Wasserscheid, Hydrogen storage technologies for future energy systems, Annual Review of Chemical and Biomolecular Engineering, 8 (2017), pp. 445–471.

[14] D. Teichmann, W. Arlt, P. Wasserscheid, Liquid Organic Hydrogen Carriers as an efficient vector for the transport and storage of renewable energy, International Journal of Hydrogen Energy, 37 (2012), pp. 18118–18132.

[15] International Energy Agency for G20, The Future of Hydrogen: Seizing today's opportunities, IEA Publications, 1 (2019), pp. 1–203.

[16] International Energy Agency, Global Hydrogen Review 2021, Global Hydrogen Review 2021, (2021), pp. 0–223.

[17] N. Behling, Solving the fuel cell dilemma, Fuel Cells Bulletin, 2012 (2012), pp. 12–14.

[18] A.Z. Weber, T.E. Lipman, Fuel Cells and Hydrogen Production: Introduction, 2019.

[19] J. Han, I.S. Kim, K.S. Choi, Purifier-integrated methanol reformer for fuel cell vehicles, Journal of Power Sources, 86 (2000), pp. 223–227.

[20] A. Basile, Hydrogen production using Pd-based membrane reactors for fuel cells, Topics in Catalysis, 51 (2008), pp. 107–122.

[21] P. Nikolaidis, A. Poullikkas, A comparative overview of hydrogen production processes, Renewable and Sustainable Energy Reviews, 67 (2017), pp. 597–611.

[22] S.M. Jokar, M.R. Rahimpour, A. Shariati, A. Iulianelli, G. Bagnato, A. Vita, F. Dalena, A. Basile, Pure hydrogen production in membrane reactor with mixed reforming reaction by utilizingwaste gas: A case study, Processes, 4 (2016),.

[23] G. Ji, J.G. Yao, P.T. Clough, J.C.D. Da Costa, E.J. Anthony, P.S. Fennell, W. Wang, M. Zhao, Enhanced hydrogen production from thermochemical processes, Energy and Environmental Science, 11 (2018), pp. 2647–2672.

[24] A. Midilli, H. Kucuk, M.E. Topal, U. Akbulut, I. Dincer, A comprehensive review on

hydrogen production from coal gasification: Challenges and Opportunities, International Journal of Hydrogen Energy, 46 (2021), pp. 25385–25412.

[25] D.A.J. Rand, R.M. Dell, Fuels – Hydrogen Production: Coal Gasification, in: Encyclopedia of Electrochemical Power Sources, Elsevier, 2009: pp. 276–292.

[26] M. Msheik, S. Rodat, S. Abanades, Methane cracking for hydrogen production: A review of catalytic and molten media pyrolysis, Energies, 14 (2021), pp. 1–36.

[27] A.M. Amin, E. Croiset, W. Epling, Review of methane catalytic cracking for hydrogen production, International Journal of Hydrogen Energy, 36 (2011), pp. 2904–2935.

[28] S. Shiva Kumar, V. Himabindu, Hydrogen production by PEM water electrolysis – A review, Materials Science for Energy Technologies, 2 (2019), pp. 442–454.

[29] J. Chi, H. Yu, Water electrolysis based on renewable energy for hydrogen production, Cuihua Xuebao/Chinese Journal of Catalysis, 39 (2018), pp. 390–394.

[30] SG H2 Energy, SG H2 Energy, Fueling A Clean Energy Future, Today, SG H2 Energy, (2023),. https://www.sgh2energy.com/economics/#econheader.

[31] International Energy Agency, Net Zero by 2050: A Roadmap for the Global Energy Sector, 2021.

[32] G.D. Berry, J. Martinez-Frias, F. Espinosa-Loza, S.M. Aceves, Hydrogen Storage and Transportation, Encyclopedia of Energy, 3 (2004), pp. 267–281.

[33] J. Andersson, S. Grönkvist, Large-scale storage of hydrogen, International Journal of Hydrogen Energy, 44 (2019), pp. 11901–11919.

[34] Suhaib Muhammed Ali, Solar-Hydrogen Systems for Remote Area Power Supply, 2007.

[35] A. Goeppert, M. Czaun, J.P. Jones, G.K. Surya Prakash, G.A. Olah, Recycling of carbon dioxide to methanol and derived products-closing the loop, Chemical Society Reviews, 43 (2014), pp. 7995–8048.

[36] S.M. Mousavi Ehteshami, S.H. Chan, Techno-Economic Study of Hydrogen Production via Steam Reforming of Methanol, Ethanol, and Diesel, Energy Technology & Policy, 1 (2014), pp. 15–22.

[37] S. Nanda, R. Rana, Y. Zheng, J.A. Kozinski, A.K. Dalai, Insights on pathways for hydrogen generation from ethanol, Sustainable Energy and Fuels, 1 (2017), pp. 1232–1245.

[38] D.C. Andrea Fasolini, R.C. , Tommaso Tabanelli, F. Cavani, Hydrogen from Renewables : A Case Study of Glecerol Reforming, MDPI Catalysts, 9 (2019), pp. 1–21.

[39] A. Klerke, C.H. Christensen, J.K. Nørskov, T. Vegge, Ammonia for hydrogen storage: Challenges and opportunities, Journal of Materials Chemistry, 18 (2008), pp. 2304–2310.

[40] M. Aziz, A. TriWijayanta, A.B.D. Nandiyanto, Ammonia as effective hydrogen storage: A review on production, storage and utilization, Energies, 13 (2020), pp. 1–25.

[41] V.M. Medisetty, R. Kumar, M.H. Ahmadi, D.V.N. Vo, A.A.V. Ochoa, R. Solanki, Overview on the Current Status of Hydrogen Energy Research and Development in India, Chemical Engineering and Technology, 43 (2020), pp. 613–624.

[42] S. Chatterjee, R.K. Parsapur, K.W. Huang, Limitations of Ammonia as a Hydrogen Energy Carrier for the Transportation Sector, ACS Energy Letters, 6 (2021), pp. 4390–4394.

[43] IRENA and Methanol Institute, Innovation Outlook: Renewable Methanol, 2021.

[44] V.K. Saraswat, R. Bansal, India's Leapfrog to Methanol Economy, 2017.

[45] T.Y. Amiri, K. Ghasemzageh, A. Iulianelli, Membrane reactors for sustainable hydrogen production through steam reforming of hydrocarbons: A review, Chemical Engineering and Processing - Process Intensification, 157 (2020), pp. 108148.

[46] M. Rivarolo, D. Bellotti, L. Magistri, A.F. Massardo, Feasibility study of methanol production from different renewable sources and thermo-economic analysis, International Journal of Hydrogen Energy, 41 (2016), pp. 2105–2116.

[47] K. Takahashi, N. Takezawa, H. Kobayashi, The mechanism of steam reforming of methanol over a copper-silica catalyst, Applied Catalysis, 2 (1982), pp. 363–366.

[48] N. Takezawa, N. Iwasa, Steam reforming and dehydrogenation of methanol: Difference in the catalytic functions of copper and group VIII metals, Catalysis Today, 36 (1997), pp. 45–56.

[49] M. Rostami, A.H. Farajollahi, R. Amirkhani, M.E. Farshchi, A review study on methanol steam reforming catalysts: Evaluation of the catalytic performance, characterizations, and operational parameters, AIP Advances, 13 (2023), pp. 030701.

[50] S.T. Yong, C.W. Ooi, S.P. Chai, X.S. Wu, Review of methanol reforming-Cu-based catalysts, surface reaction mechanisms, and reaction schemes, International Journal of Hydrogen Energy, 38 (2013), pp. 9541–9552.

[51] H. Li, H. Tian, S. Chen, Z. Sun, T. Liu, R. Liu, S. Assabumrungrat, J. Saupsor, R. Mu, C. Pei, J. Gong, Sorption enhanced steam reforming of methanol for high-purity hydrogen production over Cu-MgO/Al2O3 bifunctional catalysts, Applied Catalysis B: Environmental, 276 (2020), pp. 119052.

[52] M. Mrad, C. Gennequin, A. Aboukaïs, E. Abi-Aad, Cu/Zn-based catalysts for H2 production via steam reforming of methanol, Catalysis Today, 176 (2011), pp. 88–92.

[53] J. Agrell, H. Birgersson, M. Boutonnet, Steam reforming of methanol over a Cu/ZnO/Al2O3 catalyst: A kinetic analysis and strategies for suppression of CO formation, Journal of Power Sources, 106 (2002), pp. 249–257.

[54] M. Patrascu, M. Sheintuch, On-site pure hydrogen production by methane steam reforming in high flux membrane reactor: Experimental validation, model predictions and membrane inhibition, Chemical Engineering Journal, 262 (2015), pp. 862–874.

[55] A. Giaconia, G. Iaquaniello, G. Caputo, B. Morico, A. Salladini, L. Turchetti, G. Monteleone, A. Giannini, E. Palo, Experimental validation of a pilot membrane reactor for hydrogen production by solar steam reforming of methane at maximum 550 °C using molten salts as heat transfer fluid, International Journal of Hydrogen Energy, 45 (2020), pp. 33088–33101.

[56] P. Yan, Y. Cheng, Foam structured membrane reactor for distributed hydrogen production, Journal of Membrane Science, 661 (2022), pp. 120927.

[57] S. Kim, S.W. Yun, B. Lee, J. Heo, K. Kim, Y.T. Kim, H. Lim, Steam reforming of methanol for ultra-pure H2 production in a membrane reactor: Techno-economic analysis, International Journal of Hydrogen Energy, 44 (2019), pp. 2330–2339.

[58] A. Iulianelli, P. Ribeirinha, A. Mendes, A. Basile, Methanol steam reforming for hydrogen generation via conventional and membrane reactors: A review, Renewable and Sustainable Energy Reviews, 29 (2014), pp. 355–368.

[59] D.K. Moon, D.G. Lee, C.H. Lee, H2 pressure swing adsorption for high pressure syngas from an integrated gasification combined cycle with a carbon capture process, Applied Energy, 183 (2016), pp. 760–774.

[60] M. Amin, A.S. Butt, J. Ahmad, C. Lee, S.U. Azam, H.A. Mannan, A.B. Naveed, Z.U.R. Farooqi, E. Chung, A. Iqbal, Issues and challenges in hydrogen separation technologies, Energy Reports, 9 (2023), pp. 894–911.

[61] S. Adhikari, S. Fernando, Hydrogen membrane separation techniques, Industrial and Engineering Chemistry Research, 45 (2006), pp. 875–881.

[62] G.J.J. Grashoff, C.E.E. Pilkington, C.W.W. Corti, Purification of Hydrogen., Platinum Metals Review, 27 (1983), pp. 157–169.

[63] S. Yun, S. Ted Oyama, Correlations in palladium membranes for hydrogen separation: A review, Journal of Membrane Science, 375 (2011), pp. 28–45.

[64] N. Pal, M. Agarwal, Advances in materials process and separation mechanism of the membrane towards hydrogen separation, International Journal of Hydrogen Energy, 46 (2021), pp. 27062–27087.

[65] N.W. Ockwig, T.M. Nenoff, Membranes for Hydrogen Separation, Chemical Reviews, 110 (2009), pp. 2573–2574.

[66] N.A. Al-Mufachi, N. V. Rees, R. Steinberger-Wilkens, Hydrogen selective membranes: A review of palladium-based dense metal membranes, Renewable and Sustainable Energy Reviews, 47 (2015), pp. 540–551.

[67] G. Bernardo, T. Araújo, T. da Silva Lopes, J. Sousa, A. Mendes, Recent advances in membrane technologies for hydrogen purification, International Journal of Hydrogen Energy, 45 (2019), pp. 7313–7338.

[68] J.B. Hunter, A new hydrogen purification process, Platinum Metals Review, 4 (1960), pp. 130–131.

[69] V.P.P. M. Gryaznov, E.V.K. E.M. Savitskii, L. Frades, and G.V.S. E. Khuares, Influence of the nature and amount of the second component of binary-Palladium alloys on their catalytic activity with respect to the dehydrogenation of cyclohexane, Kluwer Academic Publishers-Plenum Publishers, 1 (1970), pp. 2368–2371.

[70] M.J. Cole, The generator of pure hydrogen for industrial applications, Platinum Metals Review, 25 (1981), pp. 12–13.

[71] J.E. Philpott, Hydrogen Diffusion Technology., Platinum Metals Review, 29 (1985), pp. 12–16.

[72] Y. Shirasaki, I. Yasuda, Membrane reactor for hydrogen production from natural gas at the Tokyo Gas Company: A case study, Woodhead Publishing Limited, 2013.

[73] M. De Falco, G. Iaquaniello, A. Salladini, Experimental tests on steam reforming of natural gas in a reformer and membrane modules (RMM) plant, Journal of Membrane Science, 368 (2011), pp. 264–274.

[74] Robert Buxbaum, Membrane Reactors, Fundamentals and commercial advantages for methanol reforming, REB Research & Consulting Co. (US), (2023),. https://www.rebresearch.com/MRessay.html (accessed April 15, 2023).

[75] Element1, Affordable Hydrogen Generation, Element 1, (2022), pp. 1–3. https://www.e1na.com/resource/affordable-hydrogen-generation (accessed April 15, 2023).

[76] H2 Site Hydrogen On-site, S.L. (Bizlaia, Spain), (2020),. https://www.h2site.eu/en/.

[77] J.L. Viviente, J. Meléndez, D.A. Pacheco Tanaka, F. Gallucci, V. Spallina, G. Manzolini, S. Foresti, V. Palma, C. Ruocco, L. Roses, Advanced m-CHP fuel cell system based on a novel bio-ethanol fluidized bed membrane reformer, International Journal of Hydrogen Energy, 42 (2017), pp. 13970–13987.

[78] N. Mori, T. Nakamura, K.I. Noda, O. Sakai, A. Takahashi, N. Ogawa, H. Sakai, Y. Iwamoto, T. Hattori, Reactor configuration and concentration polarization in methane steam reforming by a membrane reactor with a highly hydrogen-permeable membrane, Industrial and Engineering Chemistry Research, 46 (2007), pp. 1952–1958.

[79] W.H. Chen, W.Z. Syu, C.I. Hung, Y.L. Lin, C.C. Yang, Influences of geometry and flow pattern on hydrogen separation in a Pd-based membrane tube, International Journal of Hydrogen Energy, 38 (2013), pp. 1145–1156.

[80] R. Ma, B. Castro-Dominguez, A.G. Dixon, Y.H. Ma, Scalability of multitube membrane modules for hydrogen separation: Technical considerations, issues and solutions, Journal of Membrane Science, 564 (2018), pp. 887–896.

[81] F. Alrashed, U. Zahid, Comparative analysis of conventional steam methane reforming and PdAu membrane reactor for the hydrogen production, Computers and Chemical Engineering, 154 (2021), pp. 107497.

[82] B.A. Raich, H.C. Foley, Ethanol dehydrogenation with a palladium membrane reactor: An alternative to wacker chemistry, Industrial and Engineering Chemistry Research, 37

(1998), pp. 3888–3895.

[83] A. Basile, J. Tong, P. Millet, Inorganic membrane reactors for hydrogen production: An overview with particular emphasis on dense metallic membrane materials, in: Handbook of Membrane Reactors, Woodhead Publishing Limited, 2013, 2013: pp. 42–148.

[84] G. Di Marcoberardino, J. Knijff, M. Binotti, F. Gallucci, G. Manzolini, Techno-economic assessment in a fluidized bed membrane reactor for small-scale h2 production: Effect of membrane support thickness, Membranes, 9 (2019), pp. 116–137.

[85] E. Palo, A. Salladini, B. Morico, V. Palma, A. Ricca, G. Iaquaniello, Application of Pd-based membrane reactors: An industrial perspective, Membranes, 8 (2018), pp. 1–15.

[86] F. Gallucci, E. Fernandez, P. Corengia, M. van Sint Annaland, Recent advances on membranes and membrane reactors for hydrogen production, Chemical Engineering Science, 92 (2013), pp. 40–66.

[87] P. Parvasi, S.M. Jokar, A. Basile, A. Iulianelli, An on-board pure H2 supply system based on a membrane reactor for a fuel cell vehicle: A theoretical study, Membranes, 10 (2020), pp. 1–17.

[88] A. Basile, F. Gallucci, S. Tosti, Synthesis, Characterization, and Applications of Palladium Membranes, Membrane Science and Technology, 13 (2008), pp. 255–323.

[89] K. Babita, S. Sridhar, K. V. Raghavan, Membrane reactors for fuel cell quality hydrogen through WGSR - Review of their status, challenges and opportunities, International Journal of Hydrogen Energy, 36 (2011), pp. 6671–6688.

[90] Hani W. Abu El Hawa, Synthesis and characterizations of thermally stable palladium-based composite membranes for high temperature application, 2015.

[91] H.W. Abu El Hawa, S.N. Paglieri, C.C. Morris, A. Harale, J. Douglas Way, Identification of thermally stable Pd-alloy composite membranes for high temperature applications, Journal of Membrane Science, 466 (2014), pp. 151–160.

[92] J. Melendez, E. Fernandez, F. Gallucci, M. van Sint Annaland, P.L. Arias, D.A. Pacheco Tanaka, Preparation and characterization of ceramic supported ultra-thin (~1 μm) Pd-Ag membranes, Journal of Membrane Science, 528 (2017), pp. 12–23.

[93] Y. Yang, X. Li, X. Liang, R. Chen, J. Guo, H. Fu, D. Liu, Preparation of thin (~2 μm) Pd membranes on ceramic supports with excellent selectivity and attrition resistance,

International Journal of Hydrogen Energy, 48 (2023), pp. 662–675.

[94] A. Arratibel, A. Pacheco Tanaka, I. Laso, M. van Sint Annaland, F. Gallucci, Development of Pd-based double-skinned membranes for hydrogen production in fluidized bed membrane reactors, Journal of Membrane Science, 550 (2018), pp. 536–544.

[95] S.H. Israni, M.P. Harold, Methanol steam reforming in Pd-Ag membrane reactors: Effects of reaction system species on transmembrane hydrogen flux, Industrial and Engineering Chemistry Research, 49 (2010), pp. 10242–10250.

[96] A.M. Ranjekar, G.D. Yadav, Steam Reforming of Methanol for Hydrogen Production: A Critical Analysis of Catalysis, Processes, and Scope, Industrial and Engineering Chemistry Research, 60 (2021), pp. 89–113.

[97] S. Sá, H. Silva, L. Brandão, J.M. Sousa, A. Mendes, Catalysts for methanol steam reforming-A review, Applied Catalysis B: Environmental, 99 (2010), pp. 43–57.

[98] F. Gallucci, J.A. Medrano, E. Fernandez, J. Melendez, M. Van Sint Annaland, D.A. Pacheco-Tanaka, Advances on high temperature Pd-based membranes and membrane reactors for hydrogen purifcation and production, Journal of Membrane Science and Research, 3 (2017), pp. 142–156.

[99] N. de Nooijer, A.A. Plazaola, J.M. Rey, E. Fernandez, D.A.P. Tanaka, M. van S. Annaland, F. Gallucci, Long-term stability of thin-film Pd-based supported membranes, Processes, 7 (2019),.

[100] S.T. Sá, Methanol Steam Reforming for Fuel Cell Applications, 2011.

[101] U.S. Department of Energy, Report of the DOE Workshop on Hydrogen Separations and Purification, U.S. Department of Energy Office of Hydrogen, Fuel Cells & Infrastructure Technologies, US, Arlington, VA, 2004.

[102] S. Tosti, A. Basile, L. Bettinali, F. Borgognoni, F. Gallucci, C. Rizzello, Design and process study of Pd membrane reactors, International Journal of Hydrogen Energy, 33 (2008), pp. 5098–5105.

[103] A. Criscuoli, A. Basile, E. Drioli, O. Loiacono, An economic feasibility study for water gas shift membrane reactor, Journal of Membrane Science, 181 (2001), pp. 21–27.

[104] J. Il Yang, T.W. Kim, J. Chan Park, T.H. Lim, H. Jung, D.H. Chun, Development of a

stand-alone steam methane reformer for on-site hydrogen production, International Journal of Hydrogen Energy, 41 (2016), pp. 8176–8183.

[105] A. Li, C.J. Lim, J.R. Grace, Staged-separation membrane reactor for steam methane reforming, Chemical Engineering Journal, 138 (2008), pp. 452–459.

[106] M. De Falco, Pd-based membrane steam reformers: A simulation study of reactor performance, International Journal of Hydrogen Energy, 33 (2008), pp. 3036–3040.

[107] Y. Shirasaki, T. Tsuneki, Y. Ota, I. Yasuda, S. Tachibana, H. Nakajima, K. Kobayashi, Development of membrane reformer system for highly efficient hydrogen production from natural gas, International Journal of Hydrogen Energy, 34 (2009), pp. 4482–4487.

[108] T. Kume, Y. Ikeda, T. Iseki, H. Yakabe, H. Tanaka, H. Hikosaka, Y. Takagi, M. Ito, Performance evaluation of membrane on catalyst module for hydrogen production from natural gas, International Journal of Hydrogen Energy, 38 (2013), pp. 6079–6084.

[109] A. Shigarov, V. Kirillov, I. Landgraf, Computational study of Pd-membrane CH4 steam reformer with fixed catalyst bed: Searching for a way to increase membrane efficiency, International Journal of Hydrogen Energy, 39 (2014), pp. 20072–20093.

[110] Hygear, Hy . Gen on-Site Hydrogen Generation Syestem, 2023.

[111] M. Voldsund, K. Jordal, R. Anantharaman, Hydrogen production with CO2 capture, International Journal of Hydrogen Energy, 41 (2016), pp. 4969–4992.

[112] B. Anzelmo, J. Wilcox, S. Liguori, Natural gas steam reforming reaction at low temperature and pressure conditions for hydrogen production via Pd/PSS membrane reactor, Journal of Membrane Science, 522 (2017), pp. 343–350.

[113] J. Kang, Y. Song, T. Kim, S. Kim, Recent trends in the development of reactor systems for hydrogen production via methanol steam reforming, International Journal of Hydrogen Energy, 47 (2022), pp. 3587–3610.

CHAPTER 2: Literature Review: Palladium Membrane, Methanol Steam Reforming, and Membrane Reactor for MSR

Abstract

This chapter covers different aspects of the literature review regarding all three aspects of membrane reformers for hydrogen production including palladium membrane, methanol steam reforming, and membrane reactor design. Characteristics of palladium membrane for hydrogen separation, its preparation methodologies, and its applicability for commercial scale are discussed in detail. In addition to this, the literature review comprises diverse facets pertaining to methanol reforming, encompassing a comparative analysis of the different approaches employed in the reforming process. A thorough review of different approaches for catalyst preparation is provided to select the most appropriate procedure. At last detailed review of the latest developments in the reactor related to the MSR is examined to determine the current obstacles and research opportunities. Various reactor systems are analyzed to determine the most practical reactor design and innovations for improving the overall efficiency of the entire system.

2.1. Literature Review on Palladium Membrane

This section provides an in-depth literature assessment of the Palladium-based membrane and its specific properties for hydrogen separation. The section discusses various approaches used for membrane preparation and explores the mechanics involved in hydrogen separation. Furthermore, this section explores different parameters and factors that influence the permeability of hydrogen through the Pd-based membrane and its alloys. Lastly, the feasibility study of these membranes in context with the industrial application and different challenges associated with the commercial deployment are analyzed to effectively utilize the potential of the Pd-based membrane.

2.1.1. Characteristics of Palladium for Hydrogen Separation

Palladium was first discovered in the year 1803 by the renowned chemist William Hyde Wollaston who designated the name derived from the appellation of the celestial body known as asteroid Pallas [1]. The discovery of H_2 separation through a thin Pd tube, made by Thomas Grahm in 1866, had a significant role in the subsequent development of the dense Pd membrane. Additionally, Grahm revealed that Pd has the ability to absorb hydrogen gas at a ratio of 600 times its own volume, commonly termed as 'occlusion'. However, the membranes developed initially had a thickness on the order of millimeters, which leads to high costs for manufacturing that with low permeability [2]. Over the course of several decades, there has been a notable reduction in the thickness of tubular dense unsupported Pd-based membranes (< 50 µm) [3,4]. However, it is important to note that this performance improvement has come at the expense of reduced mechanical resistance. In recent times, researchers have made advancements in the development of asymmetric composite membranes having thin Pd layers with the aim of attaining high hydrogen permeability and mechanical durability at a reduced expense compared to unsupported membranes. This is achieved by depositing a thin layer of Pd onto a porous support material. The majority of these supports primarily consist of porous alumina ceramic tubes, hastelloy, and porous stainless steel (PSS) [5–7]. Hence, it is desirable to strike a balance between the optimal thickness of the membrane and its corresponding cost. Membranes comprised of nickel and platinum from group 10, as well as other metals in groups 3-5, have proven the capability to dissociate and dissolve H_2 within their crystal lattice. However, it is remarkable that only palladium has exhibited a distinguished capacity for hydrogen transport. The observed behavior can be primarily ascribed to the impressive solubility and diffusivity characteristics that span a broad temperature range (573-773 K, potentially higher in some instances) and pressure range (100-6000 kPaG), as illustrated in Figure 2.1 (a) and Figure 2.1 (b) respectively [8–11]. The hydrogen permeability of Nb, V, and Ta exhibits a decrease as temperature increases. The observed behavior can be attributed to the differential rates of change between the solubility of hydrogen, which decreases, and the diffusion coefficient, which increases. Despite the fact that Nb, Ta, and V exhibit permeability levels approximately 10-15 times higher than Pd, their practical application as hydrogen separation membranes is hindered due to the formation of oxide layers [12].

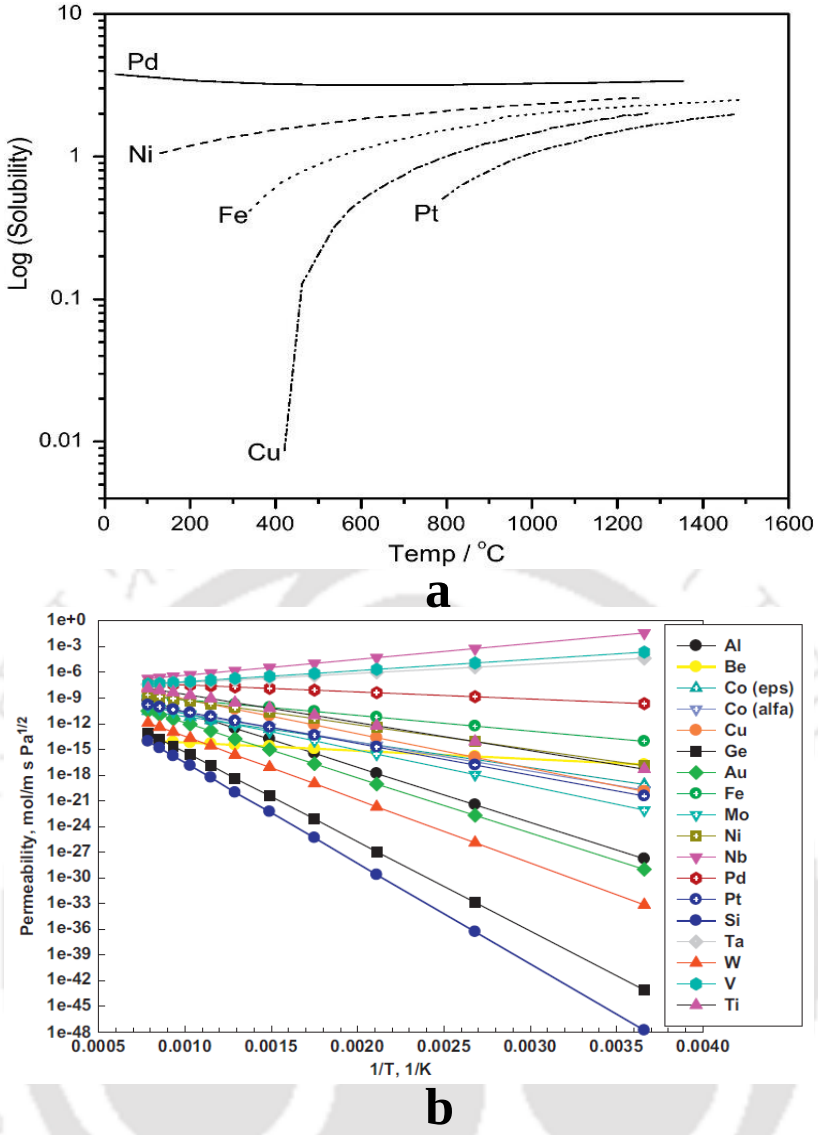

Figure 2. 1. (a) A comparison of the hydrogen solubility in various metals at 1 atm pressure as a function of increasing temperature (ºC, STD cm^3 of H_2 per 100 g of metal) (reproduced from [10]), and (b) H_2 permeability through various metals as a function of the inverse of increasing temperature (1/K) (reproduced from [11]).

2.1.2. Pd-H System and Pd Alloy-H System

One of the constraints associated with the use of Pd as a hydrogen-selective membrane is its structural composition, which consists of both α- and β-phases. This coexistence of phases leads to discrepancies in the Pd lattices when exposed to hydrogen at temperatures below the critical threshold of 571 K and 2000 kPaG [9]. The coexistence of both phases is observed in a pure Pd membrane, which displays a face-centered cubic (FCC) lattice structure. In the case of an H_2-free Pd membrane, the lattice parameters of the crystal unit cell exhibit an increase

from 0.3890 nm to 0.3895 nm (H/Pd < 0.03) in the α-phase, while in the β-phase, the increase is up to 0.410 nm (H/Pd < 0.6). During the process of temperature cycling, the transformation from the α phase to the β phase is anticipated to cause a volumetric expansion of approximately 10%. This significant expansion has the potential to induce substantial deformation, hence increasing the risk of membrane failure. Figure 2.2 illustrates a progressive transition from the α to β-phase as the H/Pd atomic ratio is increased with respect to equilibrium temperature and pressure. As a consequence, a change in the crystal volume is observed causing the structural failure of the membrane due to mechanical stress and the formation of the micro-cracks due to the β-phase nucleation. The term frequently used to describe these phenomena is hydrogen embrittlement which ultimately leads to a complete loss of hydrogen permselectivity. Finally, to measure the maximum pressure (P_{max}) at which the maximum transformation in α-phases is attained with the increase in the temperature a correlation has been given by Gillespie and Galstaun [13] as depicted by Equation 2.1.

$$\log(P_{max}) = 4.6018 - \frac{1877.82}{T} \quad (2.1)$$

Shu et al. [14] suggested several mechanisms for the occurrence of H_2 embrittlement such as (i) pressure theory, (ii) reduced surface energy theory, (iii) de-cohesion theory, (iv) H_2 phase change theory, and (v) H_2 enhanced local plasticity theory. Among these theories, the pressure hypothesis is the most widely acknowledged. According to this concept, hydrogen that is dissolved in a palladium lattice creates molecules. These molecules induce localized stress points of high pressure, leading to the formation of micro-cracks. The phenomenon of fracture propagation in metals can be explained by the reduced surface energy theorem, which claims that the absorption of hydrogen leads to a decrease in the surface free energy of the metal. The de-cohesion theory establishes a connection between hydrogen embrittlement and a reduction in the strength of metal bonds when hydrogen is present. Conversely, in accordance with the hydrogen-related phase transition theory, the phenomenon of embrittlement can be attributed to the concurrent effects of hydrogen presence and stress fields surrounding crack tips, resulting in the stabilization of a brittle hydride phase. The hydrogen-enhanced local plasticity process is responsible for linking the start and propagation of fractures with hydrogen embrittlement, resulting in increased ductility at the crack points. The elevated critical temperature associated with the phase change in the Pd-H system presents a limitation for the commercial utilization of Pd membranes. As a result, it became imperative to conduct operations on the pure Pd membrane at temperatures exceeding 571 K to prevent H_2 embrittlement.

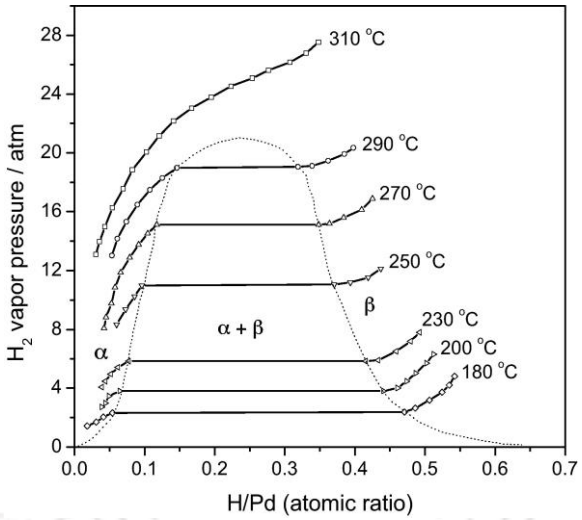

Figure 2. 2. The hydrogen vapor pressure as a function of the H/Pd ratio at different temperatures (reproduced from [9,10]).

Researchers have proposed the incorporation of several metals, such as Ag, Cu, Au, Pt, Ni, Fe, Y, Ce, Ru, etc., into Pd alloys as a potential solution to address the difficulties associated with phase change and H_2 embrittlement [15–21]. The α to β-phase transition exhibits a notable decrease in both the critical temperature and average bond distance. This decrease has the effect of lowering the extent of crystal lattice distortion caused by the cyclic absorption and desorption of H_2. For instance, the critical temperature is even lowered to 298 K for Pd-Cu (8% Cu), Pd-Pt (19% Pt), and Pd-Ni (19% Ni), whereas it is 323 K when more than 20-30 wt.% of Ag is alloyed with Pd [22,23]. Similar behavior is also exhibited by Ni, Rh, and Au toward phase transition. In addition, it has been reported that the H_2 permeability of certain binary and ternary Pd-alloys, such as Pd-Ag, Pd-Cu, Pd-Y, Pd–Ru–In, Pd–Ag–Ru, Pd–Ag–Rh, etc., can be increased compared to pure palladium membranes through precise control of the metal composition. The observed behavior is mostly ascribed to the typical bond distance exhibited by the alloy formed, in addition to the diffusivity and solubility characteristics of the alloying metals [8,10,17,24]. The diffusion of atomic hydrogen is facilitated by a larger bond distance, as evidenced by the data presented in Table 2.1.

Table 2. 1. Effect of Pd-alloy and its content over the average bond distance and Pd-alloy/Pd permeation ratio (adapted from [8,10,17]).

Pd-alloy	Wt. % of alloy metal	Average bond distance [b] (nm)	Permeation ratio Pd-alloy/Pd
Pd	0	0.275	1.0
Pd-Y	6.6	0.281	3.5
Pd-Y	10	0.284	3.8
Pd-Ag	23	0.278	1.7
Pd-Ce	7.7	0.280	1.6
Pd-Cu	10	0.272	0.48
Pd-Cu	40	0.274	1.1
Pd-Au	5	0.275	1.1
Pd-Ru-In	0.5, 6	0.278	2.8
Pd-Ag-Ru	30.2	0.279	2
Pd-Ag-Ru	19.1	0.278	2.6

[b] Average bond distance: Σ_i bond distance of M_iX_i, M_i: metal, X_i: mole fraction.

Figure 2.3 shows the relative permeability between Pd alloy and Pd as a function of the alloying metal contents at 773K and 623 K. The inclusion of binary alloys, specifically Pd-Ag (0-23% Ag), Cu (40% Ag), Ce (0-8% Ce), and Y (0-12% Y) exhibited a favorable impact on the permeability of H_2. However, Ni and Ru demonstrated a negative impact on the H_2 permeability when alloyed with Pd due to the reduced H_2 diffusivity and solubility. The H_2 permeability exhibited an initial rise at 623 K when the silver (Ag) concentration in palladium (Pd) reached 23 wt. % but thereafter reduced as the Ag concentration was further increased. Nevertheless, Gryaznov [17] reported that the H_2 permeability exhibited a consistent rise at 773 K with the effect observed up to a silver content of 40 wt. %. Figure 2.4 shows that the solubility of H_2 increases whereas the diffusivity of H_2 decreases at 673 K as the Ag content in the alloy increases. An intersection of Ag solubility and diffusivity is achieved at 23 wt. % which may be considered as the optimum value for maximum H_2 permeability of 1.6-1.8 times compared to pure Pd permeability. Furthermore, it has been shown that silver has a similar electron-donating effect to that of hydrogen in palladium. Consequently, both silver and hydrogen engage in a competitive process to occupy the electron vacancies in the 4d band of

palladium. Later on, Makrides [25] reported that the Pd-Ag alloy exhibits two notable effects on solubility. Firstly, at low pressures (below the critical pressure for the α-β phase transition), the solubility of hydrogen increases up to a silver content of 25 atomic percent. This increase can be attributed to an interaction between an interstitial hydrogen atom and a silver ion. Secondly, as the silver content exceeds 30 atomic percent, the maximum solubility of hydrogen decreases. This decrease is likely due to alterations in the electronic structure of the Pd-Ag resulting from the introduction of silver into the palladium lattice. Moreover, the crystal structure variation from FCC to body-centered cubic (BCC) with changing temperature also contributes toward enhanced H_2 permeability. Nevertheless, it has been observed that palladium, which possesses FCC crystal structure, exhibits greater resistance to hydrogen embrittlement when compared to elements such as vanadium (V), sodium (Na), niobium (Nb), and others, which possess BCC crystal structure. The primary cause of this phenomenon can be traced to the relatively low solubility of hydrogen gas in metals with an FCC crystal structure, as opposed to those having a BCC crystal structure. Therefore, it is crucial to understand the process by which hydrogen is transported over the palladium membrane and how it interacts with the crystal unit cell of palladium to enhance the permeability of H_2. The subsequent section of this chapter focuses on an overview of the hydrogen transport process through the Pd-based membrane.

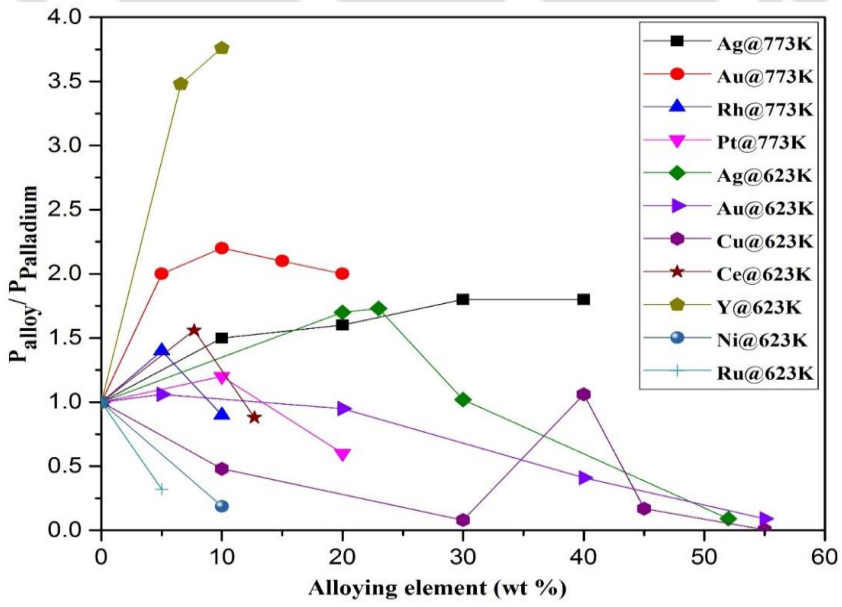

Figure 2. 3. Relative permeability between Pd alloy and Pd with various alloying metal contents at 773 K by Gryaznov [17] and 623 K at 2040 kPa by Knapton et al. [8] (data adapted to redraw the graph).

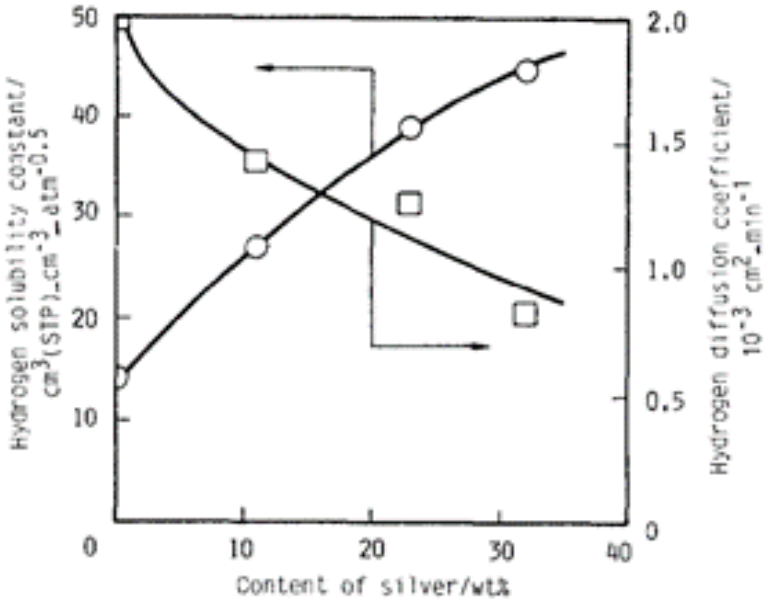

Figure 2. 4. Hydrogen solubility constant and diffusivity constant as a function of silver content (% by wt.) at 673 K (reproduced from [26]).

2.1.3. Hydrogen Transport Mechanism in Pd-Membrane

Pd has the unique ability to dissociate molecular hydrogen into its monatomic form, making it suitable for rapid diffusion through its lattice. Palladium's electronic structure contains a comparatively high concentration of empty d-orbitals, allowing for the efficient adsorption and dissociation of hydrogen molecules. The electronic configuration of Pd elements $1s^2$ $2s^2p^6$ $3s^2p^6d^{10}$ $4s^2p^6d^{10}$ $5s^0$ is largely responsible for this behavior. It is characteristic of transition metals to have energy bands that overlap between the 4d and 5s energy bands. This provides Pd with a strong affinity for electron donors from other elements. The released electron preferentially fills the low-energy 5s energy band over the higher-energy 4d band as soon as the H_2 molecules dissociate over the Pd membrane. The formation of Pd-H bonds, which involves the transfer of electron density from hydrogen to the palladium surface, is essential for stabilizing the dissociated hydrogen atoms on the surface [27].

The primary mode of hydrogen permeation through the dense Pd-based membrane is predominantly governed by the solution diffusion mechanism, as illustrated in Figure 2.5. The process of H_2 transport from the high-pressure retentate side to the low-pressure permeate side can be divided into seven different steps as follows: (i) The diffusion of H_2 molecules from the bulk of the retentate, which is at high pressure, to the surface of the membrane, (ii) the reversible dissociative adsorption of H_2 molecules on the membrane surface, where the H_2 molecules dissociate into protons and electrons, (iii) the dissolution of H-atom from the surface

into the bulk of the Pd membrane, (iv) the diffusion of H-atom through the bulk of the Pd membrane towards the surface already at low pressure, (v) the association of H-atoms and electrons on the membrane surface, (vi) the desorption of hydrogen molecules from the membrane surface, (vii) the diffusion of H_2 molecules from the surface to the bulk of the permeate [24,28]. The primary factor that drives the transportation of H_2 across the Pd membrane is the difference in hydrogen partial pressure existing between the feed side and the permeate side of the membrane.

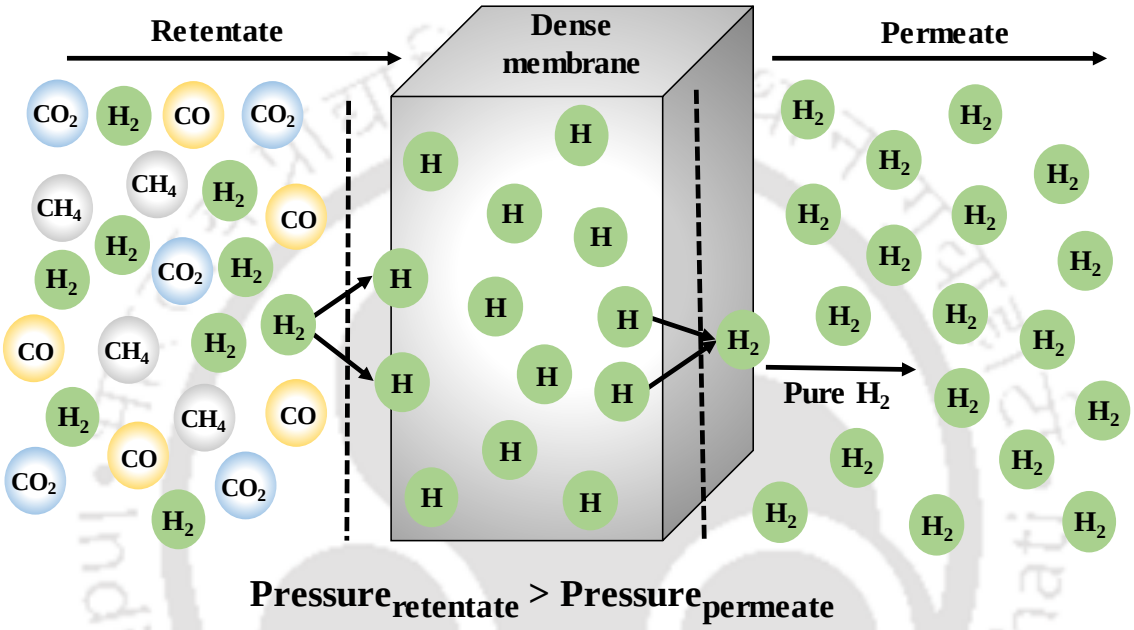

Figure 2. 5. Schematic representation of hydrogen transport through the Pd membrane via a solution diffusion mechanism.

In addition to this, Kher [29] reported the role of temperature in hydrogen transport through dense metallic membranes such as Pd. At significantly low temperatures, the presence of thermal vibrations is nearly negligible, resulting in the trapping of hydrogen atoms within the relaxed metal lattice. These atoms then undergo transit to neighboring interstitial sites by a quantum mechanical phenomenon known as "band propagation." The transportation of hydrogen atoms is facilitated by a ‘thermally activated tunneling’ mechanism, wherein the increase in temperature provides the necessary kinetic energy for the hydrogen atoms to tunnel beyond the energy barrier of interstitial sites. At elevated temperatures ranging from 473 to 873 K, hydrogen atoms are treated as classical particles and are capable of performing ‘jumps over energy barriers’ to adjacent interstitial locations. At elevated temperatures beyond 873 K, hydrogen atoms exhibit ‘fluid-like diffusion’ without getting trapped inside the interstitial sites. Given that the majority of operations involving Pd-based membranes are anticipated to take

place within the temperature range of 473 to 873 K, it may be inferred that the primary mechanism facilitating transportation through the crystal structure is the movement of hydrogen atoms between interstitial sites. The crystal structure, specifically FCC and BCC structures commonly observed in Pd and Pd-alloy-based membranes, has a substantial role in determining solubility and diffusivity. Dolan [30] observed that the BCC crystal structure is characterized by the presence of three octahedral and six tetrahedral sites. In contrast, the FCC crystal structure exhibits only one octahedral and two tetrahedral sites. When compared to the FCC crystal structure, the BCC crystal structure exhibits a reversed relationship between the size of tetrahedral and octahedral sites relative to the atomic radius of the metal. Specifically, in BCC structures, the tetrahedral sites are relatively larger than the octahedral sites, whereas, in FCC structures, the opposite holds true. Hydrogen atoms are more likely to occupy the tetrahedral sites in BCC structures, but they tend to select the octahedral sites in FCC structures due to the latter's greater stability. In the literature, it has been reported that in the Pd-H and Pd-alloy-H systems, hydrogen atoms have the ability to occupy both tetrahedral and octahedral positions. H-atom typically hops from one octahedral site to another by merely traversing the tetrahedral site. Therefore, for Pd-based membrane hydrogen atoms are treated as classical particles and are capable of performing 'jumps over energy barriers' to adjacent interstitial locations. In addition, it is observed that the dissolution of hydrogen in palladium exhibits mostly exothermic behavior, resulting in a decrease in solubility as temperature rises. This behavior is most probably due to the formation of ordered Pd-H at high H-atom concentration. In the case of BCC metals, the primary determinant of permeability is solubility, but for Pd, the primary factor is diffusivity [27]. Moreover, the permeability of a Pd-based membrane is determined by the combined effects of solubility and diffusivity as shown in Equation 2.5, and it plays a crucial role in determining the membrane's overall performance. The mathematical modeling and description of permeability are accomplished by the utilization of Fick's laws of diffusion. Fick's law is characterized by the flux, which is the moles of H_2 diffusing through a unit cross-sectional area of the membrane per unit of time. Equation 2.2 describes the flux of H_2 in the steady-state condition. When the hydrogen gas concentration is not known, Henry's law, as represented by Equation 2.3, is utilized. This law indicates that the concentration of a gas is dependent on its partial pressure. Subsequently, Adolf Sieverts made additional modifications to Henry's law, denoted as Equation 2.4, in order to incorporate the dissociation of H_2 molecules into monoatomic hydrogen on the surface of the membrane. Sieverts conducted an experiment to investigate the relationship between hydrogen solubility in metals and the pressure of hydrogen in the gas phase. He showed that the solubility of

hydrogen in metals is proportional to the square root of the pressure of hydrogen. In order to investigate the relationship between the H_2 flux through the membrane and the H_2 partial pressure, Fick's law is adjusted to Sievert's law, as presented in Equation 2.5. This equation is subsequently reformulated in terms of the H_2 partial pressure in the retentate and permeate, as demonstrated in Equation 2.7. Moreover, the concept of permeance is characterized by the ratio of permeability to the thickness of the membrane, as seen in Equation 2.8. Equation 2.9 provides the relationship between H_2 flux and permeance, as well as the H_2 partial pressure across the membrane. The calculation of permeability can be readily performed given the availability of the following parameters: the hydrogen's steady-state flow rate, the membrane's active area, the membrane's thickness, and the gas pressure on both sides of the membrane. Porous membranes are subject to the principles of Henry's law, which assumes a value of n = 1 and involves the phenomenon known as Knudsen diffusion. The phenomenon of hydrogen diffusion through a dense metal membrane can be described by Sieverts' law, where the exponent value of 0.5 is applicable. The value of n is 0.5 when the rate-determining step is the diffusion of H_2 across the bulk of the Pd membrane. On the other hand, the value of n approaches 1 when the rate-determining step is the associative and/or dissociative chemisorption [31,32]. When the pressure exponent is close to unity, it implies that the penetration rate through the membrane is too high, which typically reflects a thin palladium layer of less than 5 µm in thickness. In the scenario involving Pd layers with a thickness exceeding 5 µm, values of n greater than 0.5 can be ascribed to the presence of pin-holes and defects. The flow mechanisms responsible for this phenomenon can be attributed to either Knudsen or Pouiselle flow, resulting in exponents greater than 0.5 [33,34]. In addition to this, it is worth noting that the pressure exponent may be less than 0.5 when dealing with extremely thin membranes operating under low-temperature conditions. Nevertheless, variations can still be observed even in cases where thick membranes are present [34,35]. The pressure exponent is highly sensitive to the accurate measurement of the permeate H_2 flow rate. The process of diffusion through bulk Pd exhibits a relatively low activation energy, measuring less than 30 kJ mol^{-1}. Conversely, the activation energy associated with the adsorption and desorption processes is considerably greater, ranging from 54 to 146 kJ mol^{-1} [10].

$$J = - D \times (\partial C/\partial x) \quad 2.2$$

$$C_{Gas} = S \times P_{Gas} \quad 2.3$$

$$S = [C_{H_2}]/ [P_{H_2}]^{0.5} \quad 2.4$$

$$J_{H_2} = D.S \times \frac{\partial {P_{H_2}}^{0.5}}{\partial x} = D.S \times \frac{\Delta {P_{H_2}}^{0.5}}{\Delta x} \quad 2.5$$

$$P_e = D \times S \quad 2.6$$

$$J_{H_2} = P_e \frac{\Delta {P_{H_2}}^{0.5}}{\Delta x} = P_e \frac{\left({P_{H_{2,r}}}^{0.5}\right) - \left({P_{H_{2,p}}}^{0.5}\right)}{L} \text{ or } P_e \frac{\left({P_{H_{2,r}}}^{n}\right) - \left({P_{H_{2,p}}}^{n}\right)}{L} \quad 2.7$$

$$P = \frac{P_e}{L} \quad 2.8$$

$$J_{H_2} = P\left[\left({P_{H_{2,r}}}^{0.5}\right) - \left({P_{H_{2,p}}}^{0.5}\right)\right] \quad 2.9$$

Where J (mol m^{-1} s^{-1}) = molar flux of diffusing species, P_e (mol m^{-1} s^{-1} Pa^{-1}) = permeability, D (m^2 s^{-1}) = diffusivity, S (mol m^{-3} Pa^{-1}) = solubility, $\partial C/\partial x$ (mol m^{-4}) = concentration gradient, C (mol m^{-3}) = concentration, S_H (mol m^{-3} atm^{-1}) = Henry's law constant, P_{Gas} (atm) = vapor pressure, ${C_{H_2}}$ (mol m^{-3}) = hydrogen concentration, n = pressure exponent, $\Delta {P_{H_2}}^{0.5}$ = square root of the pressure difference between the feed and permeate sides of the membrane, Δx or L (μm) = membrane thickness, $P_{H_{2,r}}$ = H_2 partial pressure in retentate, $P_{H_{2,p}}$ = H_2 partial pressure in permeate, and P (mol m^{-2} s^{-1} Pa^{-1}) = permeance.

Other than that, the diffusivity, solubility, and permeability as given in Equation 2.10, Equation 2.11, and Equation 2.12 respectively exhibit a dependence on temperature-dependent characteristics that are represented by the Arrhenius-type relationship. The activation energy associated with hydrogen permeation is determined by the combined activation energies for diffusivity and solubility, as represented in Equation 2.13.

$$D = D_o \exp\left[\frac{-E_D}{RT}\right] \quad 2.10$$

$$S = S_o \exp\left[\frac{-E_S}{RT}\right] \quad 2.11$$

$$P_e = P_o \exp\left[\frac{-E_{Pe}}{RT}\right] \quad 2.12$$

$$E_{Pe} = E_S + E_D \quad 2.13$$

Where P_o, S_o, and D_o are the permeability, solubility, and diffusivity of hydrogen at infinite high temperatures. Similarly E_{Pe}, E_S, and E_D are the activation energy (J mol^{-1}) for hydrogen permeation, enthalpy of solution of hydrogen, and activation energy for hydrogen diffusion respectively. R is the universal gas constant (J mol^{-1} K^{-1}) and T is the absolute temperature (K).

The selectivity of a membrane is a key determinant of its capacity to effectively separate gases. The concept of ideal selectivity, also known as the separation factor, is characterized by the ratio between the permeability of the specific penetrants that are of interest. Equation 2.14 can be used to characterize the ideal perm-selectivity of hydrogen over nitrogen [12].

$$\text{Selectivity} = (\alpha_{H_2/i}) = \frac{J_{H_2}}{J_i} \qquad 2.14$$

where $\alpha_{H_2/i}$ is the ideal perm-selectivity of the hydrogen to the other gas, J_{H_2} is the hydrogen molar flux, and J_i is the molar flux of other gases such as N_2, Ar, H_2, CO_2, etc.

However, in the unfortunate circumstance that the Pd membrane exhibits pinholes or flaws, the exclusive reliance on the solution diffusion mechanism for H_2 permeation through the membrane is no longer applicable. The transport of H_2 via pinholes or defects is characterized by two mechanisms: Knudsen diffusion and viscous flow. These mechanisms can be effectively represented using the dusty-gas model. The overall permeate H_2 flux ($J^T_{H_2}$) for nonabsorbable gases can be mathematically represented as the sum of the Knudsen flow ($J^K_{H_2}$) and the viscous flow ($J^V_{H_2}$), as stated in Equation 2.15 [5].

$$J^T_{H_2} = J^K_{H_2} + J^V_{H_2} = \left[\frac{2}{3} \cdot \sqrt{\frac{8}{\pi}} \cdot \frac{\epsilon\, \mu_K\, d}{L\sqrt{RTM}}\right]\left(P_{H_{2,r}} - P_{H_{2,p}}\right) + \left[\frac{1}{8} \cdot \frac{\epsilon\, \mu_V\, d^2\, P_{avg}}{L\eta RT}\right]\left(P_{H_{2,r}} - P_{H_{2,p}}\right) \qquad 2.15$$

η = gas viscosity (Pa s), M = gas molecular weight (g mol^{-1}), d = pore diameter (m), ε = porosity, P_{avg} = average pressure of retentate and permeate (bar), μ_K and μ_V = Knudsen and Viscous geometric factor coefficient respectively. The ideal H_2/N_2 perm-selectivity decreased with an increase in the trans-membrane pressure. This is due to the permeation mechanism of N_2 which is governed by the Knudsen diffusion or viscous flow through the defects and/or pin-holes. The permeate N_2 flux increases almost linearly with the trans-membrane pressure whereas the permeate H_2 flux depends on the difference of the square root of the H_2 partial pressure [5,36]. Hence, by increasing the pressure the permeate N_2 flux increases with higher order compared to the permeate H_2 flux, and consequently, the ideal H_2/N_2 perm-selectivity decreased. However, with the increase in temperature, the H_2/N_2 perm-selectivity increased which is a characteristic feature of a Pd-based membrane. The N_2 permeation through defects and/or pin-holes is proportional to $T^{-0.5}$ and T^{-1} for Knudsen and Poissuile flow respectively, i.e. it decreases with an increase in the temperature. A study conducted by Guazzone et al. [32] observed a decrease in the pressure exponent (n) as the H_2/He selectivity increased. They found that when the selectivity exceeded 400, the pressure exponent approached 0.5. The pressure

exponent is likely to approach unity when considering a Pd membrane with a selectivity much below 400.

Traditionally, the predominant methods for producing H_2 have been steam reforming of natural gas, coal gasification, and oil and naphtha reforming, accounting for over 95% of the total production [37,38]. Nevertheless, these thermochemical processes result in the production of a mixture of gases that is rich in hydrogen yet additionally contains N_2, CO_2, CO, CH_4, and other gases with low concentrations. However, the majority of industrial applications and proton exchange membrane fuel cells (PEMFCs) require high-purity H_2 (>99.99%), which further necessitates downstream H_2 purification. Moreover, PEMFCs require ultra-pure hydrogen with a CO concentration of less than 10 ppm, as CO poisons the Pt-catalyst at the anode and subsequently degrades the performance over time [39]. In order to attain a state of high purity, it is imperative that the membrane being manufactured must be free of any defects or pin-holes. The significance of support and its selection is crucial in attaining this objective. Several parameters, including pore size distribution, size of the largest pore, nature of the support, cost, and viability, must be considered prior to proceeding with Pd membrane preparation. Therefore, the next section of this chapter discusses the role of support and measures to be taken to prepare a defect free Pd membrane.

2.1.4. Factors Affecting H_2 Permeation in Pd-Membrane

The rate of H_2 penetration is significantly influenced by any parameters that directly or indirectly affect the stages involved in hydrogen transfer through the membrane via the solution diffusion mechanism. Additionally, the H_2 permeation rate can be determined by several parameters such as operating temperature, pressure, and H_2 concentration, as stated by Sieverts' law.

- **Effect of poisonous contaminant:** The feed gas obtained from various sources may contain a range of contaminants, such as carbon monoxide, chlorine, ammonia, sulfur compounds, hydrocarbons, and carbon particles [40]. The adsorption of contaminants onto the surface of the membrane leads to the inhibition of active sites responsible for hydrogen dissociation, consequently causing a reduction in hydrogen permeation [41]. Multiple active sites can be obstructed by a single contaminant. Species that are adsorbed, such as carbon monoxide and hydrocarbons, increase the activation energy required for hydrogen dissociation, resulting in a decrease in the permeation of H_2. Hydrocarbons can undergo a reaction that results in the formation of a carbonaceous layer on the membrane, which has a negative effect

on the penetration of H_2. Likewise, a significant amount of sulfur and H_2S undergoes a reaction with palladium, resulting in the formation of metal sulfide on the surface of the membrane. This metal sulfide further hinders the H_2 permeation [42–44]. In addition to this, the existence of metallic contaminants and chlorine compounds permanently reduces the membrane's ability to permeate hydrogen. These metal hydrides have different hydrogen solubility and diffusivity compared to pure palladium, affecting the membrane's performance [2].

- **Effect of temperature, pressure, and H_2 concentration:** The solubility and diffusivity of hydrogen have a significant impact on the penetration of hydrogen through the metal/alloy. However, these two parameters are largely affected by the change in the temperature. One aspect to consider is that when temperature increases, the solubility of H_2 drops, while its diffusivity increases. The magnitude of the temperature-dependent rise in diffusivity is significantly greater than that of solubility, thereby increasing the overall permeation capacity of the metal/alloy [10,28]. Higher temperatures lower the activation energy barrier, making it easier for hydrogen atoms to overcome energy barriers and diffuse through the membrane. The temperature dependency of hydrogen penetration via palladium membranes exhibits an Arrhenius-type relationship as expressed in Equation 2.12. As temperature rises, more hydrogen atoms dissolve into the palladium lattice, contributing to higher hydrogen permeation rates. However, this effect saturates at elevated temperatures, as the solubility limit of hydrogen in palladium is reached [2]. Expansion or contraction of the membrane as a result of the change in the temperature can influence the membrane's microstructure and surface morphology, potentially impacting its permeation properties. Additionally, it is essential to consider the trade-offs between permeation rate, selectivity, mechanical integrity, and the potential for hydrogen embrittlement when determining the optimal operating temperature for a given application [45,46].

Pressure significantly influences the permeation of hydrogen through palladium membranes. With the increase in pressure, the hydrogen solubility increases in the palladium membrane. According to Fick's law of diffusion, the flux of hydrogen through the membrane is directly proportional to the pressure difference across the membrane [27,47]. As pressure increases, the system approaches thermodynamic equilibrium, where the rate of hydrogen permeation through the membrane becomes balanced with the rate of hydrogen absorption and desorption within the membrane material. This phenomenon is more prevalent, particularly at high pressure where pressure polarization effects can occur which is referred to the buildup of pressure on the permeate side of the membrane, which can reduce the effective driving force

for hydrogen permeation and limit the overall permeation rate. Consequently, non-ideal behavior under high-pressure conditions may be encountered [48]. In addition to this, the permeation rates of other gases present in the feed stream may also increase, potentially reducing the membrane's selectivity for hydrogen. Therefore, optimizing operating pressure is crucial for maximizing the performance of palladium membranes in hydrogen separation applications. Similarly, the hydrogen concentration determines the hydrogen partial pressure at a particular pressure difference. The higher the hydrogen concentration in the feed mixture gas greater the hydrogen partial pressure resulting in higher hydrogen permeation.

- **Effect of change in the micro-structure of the membrane:** The microstructure of palladium membranes plays a crucial role in determining their hydrogen permeation. Several key aspects of microstructure influence hydrogen permeation including grain boundaries, lattice defects, voids in the lattice, dislocations, phase composition, surface morphology, metal deposition technique, and annealing [49–52]. Traps such as lattice defects, grain boundaries, and voids impede hydrogen permeation by increasing the activation energy required for diffusion. Increased permeability is commonly observed in smaller grain sizes as a consequence of the reduced diffusion routes available for hydrogen atoms. The utilization of fine-grained membranes results in an increased surface area and grain boundary density, hence promoting accelerated hydrogen diffusion across the membrane [53]. In comparison to pure palladium, phase composition may demonstrate increased hydrogen solubility or diffusivity, leading to improved permeability. Nevertheless, the performance of membranes may be negatively impacted over time due to phase instability or phase changes that occur at elevated temperatures [54]. The hydrogen permeation process can be considerably influenced by the surface morphology of the palladium membrane, encompassing factors such as roughness, texture, and surface area. Rougher surfaces have the potential to offer additional locations for the adsorption and desorption of hydrogen, hence augmenting hydrogen permeation [5,55]. Different deposition techniques form films of different microstructures having variations in lattice defects and grain boundaries. In addition, the choice of deposition technique plays a crucial role in determining the shape, texture, and alignment of the atomic planes inside the film. These factors have a substantial impact on the adsorption enthalpy and diffusion of hydrogen across the palladium membrane [56]. Apart from the aforementioned reasons, the annealing and hydrogen absorption cycle results in the rearrangements of the planes and crystal lattice. Therefore, a steady increase or decrease in hydrogen permeation during the initial period may be observed [57,58]. In order to achieve maximum hydrogen flux it is important to

meticulously control these parameters by utilizing advanced manufacturing techniques and material processing procedures to customize the microstructure of palladium membrane, while also maintaining their mechanical strength and long-term resistance to degradation.

- **Effect of feed load:** It is well established that the presence of other gases significantly influences the hydrogen permeation through the palladium membrane as a result of the feed dilution and mass transfer limitations. Rapid permeation of hydrogen from the feed side further reduces the driving force [59,60]. Another phenomenon commonly known as concentration polarization is also observed due to the accumulation of non-permeable gases on the surface of the membrane which in turn offers additional mass transfer resistance to the hydrogen transport from the bulk of the retentate to the surface, a necessary step involved in the solution diffusion mechanism [61]. If the feed flow rate is too low, mass transfer limitations may occur. This means that the rate at which hydrogen molecules are transported to the membrane surface may become the limiting factor, reducing the overall permeation rate. Higher feed flow rates can result in thinner boundary layers, reducing the resistance to hydrogen transport from the bulk feed stream to the membrane surface. This can enhance the mass transfer rate and increase hydrogen permeation albeit at the expense of reduced hydrogen recovery [62,63]. Therefore, any changes in the feed flow rate can influence the hydrodynamics within the membrane module or separator system. Flow patterns, turbulence, and residence time distribution can all impact the distribution of hydrogen molecules within the system, affecting their interaction with the membrane surface and subsequent permeation behavior. Balancing factors such as mass transfer limitations, boundary layer thickness, and hydrodynamic considerations is essential to achieve efficient and consistent hydrogen separation.

- **Effect of membrane module or separator geometry:** The design of the membrane module or separator geometry is of great importance to maximize the utilization of available membrane surface area for enhanced hydrogen permeation. Moreover, the module design should support the uniform distribution of the feed along the membrane surface with proper residence time to diffuse. By doing so, the mass transfer limitations and localized concentration gradients can be avoided to enhance the permeation efficiency [64]. Optimizing hydrodynamic conditions is also essential to promote effective mixing and minimize stagnant zones inside the separator. When scaling up membrane-based hydrogen separation systems, careful consideration must be given to the design of larger-scale membrane modules or separators. Scaling effects such as changes in flow dynamics, pressure drop, and heat transfer characteristics should be addressed to ensure the scalability and performance of the system

[65]. Recent studies have demonstrated that the incorporation of baffles on the retentate side has the potential to reduce concentration polarization. By doing so a more uniform distribution of H_2 partial pressure is achieved throughout the separator, both radially and axially, while maintaining a constant feed flow rate [66–69]. The presence of baffles induces a disturbance in the gas flow field and the boundary layer adjacent to the membrane, which causes extra hydrogen to be forced toward the surface of the membrane [64,65,70,71]. In addition, baffles enhance the contact between the feed and the membrane by directing the flow pattern of the feed and promoting recirculation within the separator [72].

2.1.5. Porous Support and Modification for Composite Membrane

Pd and Pd-alloy-based membranes can be categorized into two main groups depending on the sort of support they utilize: unsupported and supported. Unsupported membranes are typically manufactured as foil or film and tubes, lacking any supplementary structure to impart the mechanical strength necessary for sustaining the top metallic film. Furthermore, it is vital that these films lacking support possess a thickness ranging from 20 to 100 μm to ensure an adequate degree of mechanical strength [4,73]. Despite the membranes' ability to generate hydrogen with a high level of purity (>99.9999%), the cost involved in the preparation procedure, along with a relatively low H_2 permeation flux (1.4×10^{-8} to 9.3×10^{-7} mol m^{-2} s^{-1} Pa^{-1}), limits its extensive utilization for commercial purposes [74,75]. Furthermore, the utilization of these membranes is predominantly constrained to sophisticated applications, such as the fabrication of semiconductors and the retrieval of H_2 isotopes within nuclear plants [2]. Therefore, it is desirable to have a balance between the permeate H_2 flux, the cost of preparation, and mechanical stability, while also ensuring an appropriate level of hydrogen perm-selectivity.

In contrast, the supported membrane is comprised of a porous material such as porous alumina [26,76–78], PSS [5,79–81], porous vycor glass [6,82,83], ceramic hollow fibers [84–87], and Inconel or Hastelloy [88–91], which serves to offer mechanical reinforcement for the top metallic layer. These membranes are usually referred to as composite membranes. Composite membranes have been in very high demand due to the thin palladium layer required and hence a reduced cost. The careful choice of porous support is crucial for the successful fabrication of a thin, high-quality palladium-based membrane without any defects. Before depositing the Pd selective layer, it is essential to consider many characteristics of the porous support, including pore size distribution or media grade (pore-mouth and pore-throat), surface smoothness,

thermal expansion coefficient, and chemical compatibility. It is widely acknowledged that the morphology and continuity of the selective layer are predominantly influenced by both pore size and roughness. Based on the findings of Mardilovich et al. [5], it has been shown that in order to attain a dense membrane, the thickness of the Pd layer must be approximately three times more than the maximum pore size present on the support material. Subsequently, Uemiya [92] documented the deposition of varying thicknesses of a Pd layer over support materials of varied media grades to achieve a dense membrane, as outlined in Table 2.2.

Table 2. 2. The thickness of the Pd-layer adequately covers supports featuring varying media grades or pore sizes (reproduced from [92]).

Media grade of support (µm)	Thickness of deposited layer (µm)
0.005	0.8
0.1	2.2
0.2	4.5
0.3	13

Alumina is a support that is most commonly employed due to its lower thermal expansion coefficient compared to Pd and controllable pore size ranging from 5 to 200 nm. Alumina supports are particularly appealing because of their favorable surface characteristics and chemical compatibility with Pd-layers. In addition, the ability to deposit a defect-free ultra-thin layer of Pd on an alumina support is facilitated by the narrow pore size of the support material. Unfortunately, the integration of alumina into a membrane reactor poses a significant obstacle owing to its fragile structure and poor mechanical strength in comparison to metallic support systems. To overcome this issue, researchers have suggested the utilization of graphite ferrules as a sealing medium for the purpose of connecting the alumina tube with metallic fittings. Furthermore, it is possible to connect porous alumina tubes with dense ones by utilizing a glass sealant that exhibits excellent thermal resistance [93,94]. Recently, asymmetric tubular alumina supports have been preferred because of their larger surface/volume ratio compared with disk-shaped substrates. Typically, asymmetric supports are comprised of a porous substrate with large pores, onto which a ceramic layer with small pores and low roughness is deposited. However, the difference in the thermal expansion coefficient of the various support and intermediate layers in the case of asymmetric support is crucial as given in Table 2.3 [10,95,96]. In relation to this issue, Okazaki et al. [97] observed a significant interaction

between the palladium layer and the alumina support at elevated temperatures, specifically over 873 K. At these temperatures, the alumina undergoes a reaction with Pd, resulting in the formation of a Pd-Al alloy. This alloy demonstrates a reduced hydrogen permeation flux. This phenomenon exhibits a rapid progression at elevated temperatures, specifically above 1123 K. Paglieri et al. [98] have also shown this phenomenon, wherein an irreversible decline in the flux of H_2 is observed at temperatures exceeding 1023 K, even after subjecting the membrane to thermal treatment including air and hydrogen. To address this concern, it is possible to apply an additional intermediary layer consisting of ZrO_2 and YSZ, which exhibits no reactivity with Pd at temperatures up to 923 K [99,100].

Table 2. 3. The linear thermal expansion coefficient of support material used for Pd-based membrane preparation (adapted from [10,95,96,101]).

Material	Linear thermal expansion coefficient (10^{-6} K^{-1})
Al_2O_3	6.5-7.6
YSZ	10
ZrO_2	10
CeO_2	11
TiO_2	9.2
316L PSS	16
Borosilicate glass	3.3
Vycor glass	7.5
Hastelloy-c22	12.4
Inconel-625	13.1
Pd	11.8
Ag	18.9-19.7
Au	14.2
Cu	16.5-17
Ni	11.8-13.3
Nb	7.3
Ti	8.6
Fe	12
Cr	4.1

In the context of membrane reactors, it has been observed that metallic supports exhibit more robustness compared to ceramic supports in terms of their integration with the reactor. Nevertheless, the support available in the market has significant drawbacks such as the presence of large pores, an uneven distribution of pore sizes, and a high degree of surface roughness. Furthermore, it is common practice to employ supports at high temperatures,

typically surpassing the Tamman temperature, which is equivalent to half the melting point of the alloying metal, for both the selective layer and metallic support. The Tamman temperature and melting values for commonly utilized materials for membrane preparation are presented in Table 2.4 and are calculated using the empirical relation in Equation 2.15. As a consequence of this factor, there exists a perpetual potential for the interdiffusion of Pd and the metallic support, leading to a drastic decrease in the perm-selectivity of the membrane. Additionally, the incorporation of porous sintered metal components into the compact Pd and Pd-alloy layer, which selectively allows the passage of hydrogen, would result in a drop in hydrogen permeability. This reduction can be attributed to the contraction of the Pd lattice, leading to a decrease in both hydrogen solubility and diffusivity [5,102,103]. Furthermore, a thick layer of the Pd is required to make a defect-free membrane. To address this issue, a variety of intermetallic diffusion barriers are deposited onto the support. These barriers include α-Al_2O_3 [104], γ-Al_2O_3 [105], YSZ [106], ZrO_2 [107,108], TiO_2 [109], CeO_2 [110], zeolite [111], graphite [112], and the oxide layer (Fe_2O_3-Cr_2O_3) [113,114]. Dip coating, powder suspension deposition, and atmospheric plasma spraying are the prevailing methods employed for the deposition of intermetallic diffusion barriers [10,115]. However, an extra mass transfer resistance is induced. The incorporation of these intermediary layers leads to a notable decrease in both the distribution of pore sizes and the roughness of the support surface. Consequently, a thin Pd layer is required in order to attain a completely dense membrane. Various approaches are available for the deposition of a dense Pd layer. The selection of a particular fabrication technique is contingent upon various factors that dictate the rationale behind choosing one approach over another. A more comprehensive description of each technique is provided in the subsequent section.

$$T_{tamman} = 0.5 \times T_{melting}\ (K) \qquad 2.15$$

Table 2. 4. Melting temperature, T_{tamman} temperature, and density of commonly used materials for Pd-alloy, and support preparation (reproduced from [101]).

Element	Melting temperature (K)	T_{tamman} Temperature (K)	Density (g cm^{-3})
Pd	1828	914	12
Ag	1235	618	10.5
Cu	1358	679	8.92
Au	1337	669	19.3
Fe	1811	906	7.87
Ni	1728	864	8.91
Cr	2180	1090	7.14
Mo	2896	1448	10.3
W	3695	1848	19.3
Rh	2237	1119	12.5
Ir	2739	1370	22.7
Ru	2607	1304	12.4
Pt	2041	1021	21.1
Al	934	467	2.7

2.1.6. Palladium Membrane Fabrication Technique

To achieve improved H_2 permeance and selectivity, the membrane fabrication technique must possess particular features. These attributes encompass a high deposition rate, uniform deposition, better control over deposition rate, effective composition control in the case of alloy deposition, high purity of the deposited materials, ease of scale-up, and cost-effectiveness of the deposition process [116]. Other than unsupporting membranes prepared by cold rolling, the majority of Pd-based membranes are now being fabricated on porous substrates. A Pd-based membrane is typically deemed successful when it meets the following criteria: (a) exhibiting selectivity exclusively for hydrogen, (b) high permeate H_2 flux, (c) possessing good thermal stability suitable for prolonged industrial use, (d) maintaining stability under thermal cycling conditions, (e) displaying resistance to the detrimental effects of H_2S, CO, NH_3, C, and impurities present in the inlet feed gas, (f) ability to operate even at low temperature (< 573 K) without structural failure, (g) good regenerative properties after deactivation, and (h) exhibiting reduced thickness, thereby reducing overall manufacturing costs [117]. Several approaches have been suggested for the deposition of dense Pd and Pd-alloy layers onto a substrate composed of either porous ceramic or porous metallic material. In this respect, the techniques most frequently employed include cold rolling,

electroplating, spray pyrolysis, chemical vapor deposition (CVD), physical vapor deposition (PVD), and electroless plating (ELP).

2.1.6.1. Cold Rolling and Diffusion Welding (CRDW)

Historically, membranes composed of Pd and Pd alloys have been fabricated as self-supported foils or thin tubes through the utilization of arc-melting and cold-rolling methodologies. This process involves the passage of a metal sheet between a pair of rolls below the recrystallization temperature, intending to produce a thin sheet that exhibits enhanced uniformity [1,17]. In order to provide mechanical strength, these foils are welded over the porous alumina and PSS tubes, thereby forming a composite membrane [4]. Tosti et al. [4,73] prepared Pd and Pd-Ag (23-25% Ag) membranes with a thickness of 50 μm. Several steps of cold rolling, annealing (1473 K, 2-3 h), and welding were carried out to get thin foil. Despite its well-established and straightforward nature, the low permeability of H_2 and the substantial costs associated with its fabrication have presented challenges in terms of its extensive adoption in commercial environments. Furthermore, the membrane fabricated employing this technique has a higher susceptibility to fracture because of the presence of induced defects and less ductility, leading to disruption in the crystal lattice. The processes of rolling and annealing in succession are time-consuming.

2.1.6.2. Chemical Vapor Deposition (CVD)

The deposition of volatile metal-organic compounds onto a pre-existing substrate is performed within the confines of an enclosed chamber using this particular technique. CVD involves two significant stages: the diffusion of metal-organic species from the precursor to the surface of the substrate, and the subsequent breakdown of the target element on the substrate's surface. The reaction occurs on the heated substrate while the leftover chemicals exit the chamber in the form of various gaseous compounds. In this regard, Yan et al. [118] deposited Pd on the porous α-alumina support with the metal-organic chemical vapor deposition (MOCVD) technique of palladium acetate as the precursor. They reported an H_2 permeance of 10×10^{-7} mol m^{-2} s^{-1} $Pa^{-0.5}$ with an H_2/N_2 selectivity of 1000 on a 2 μm thick Pd membrane. Further, Itoh et al. [119] modified the CVD setup and prepared a 2-4 μm Pd membrane on the tubular alumina support with forced flow CVD. A pressure difference is applied between the chamber and substrate tube wall to deposit Pd on the walls of support. This helped in pinhole minimization. The membrane exhibited an H_2 permeance of 33.4×10^{-7} mol m^{-2} s^{-1}

$Pa^{-0.5}$, and H_2/N_2 selectivity of 5000 at 573 K. Several factors need to be considered when conducting the experiment, including the gas flux (flux of H_2 and N_2), precise control of temperature during the sublimation of the metal precursor, the expensive nature of the Pd precursor, and the requirement of a high vacuum level (< 0.1 mmHg) [120]. However, these considerations render this technique unsuitable for industrial applications. Additionally, the technique necessitates the utilization of highly volatile and thermally stable Pd precursors, which are crucial for achieving efficient processing durations and maximizing output. The utilization of this approach is restricted due to the requirement of high-purity ingredients, lack of alloy precursor, and stringent process conditions. Furthermore, it is worth noting that the presence of residual carbon has the potential to cause contamination in the palladium membranes.

2.1.6.3. Physical Vapor Deposition (PVD)

The desired coating material, which constitutes the target, undergoes atomization through the collision of argon ions excited by the action plasma. This atomized material is then deposited onto a substrate in a vacuum environment (< 5 millitorrs). The neutrally charged sputtered atoms, with an energy range of 4-6 eV, undergo collisions with the substrates intended for coating. This collision process results in the formation of a highly adherent coating, characterized by a virtually unbreakable bond between the film and its substrate. This bond is established at the molecular level, as the neutrally charged sputter atoms and the substrate atoms engage in bonding interactions [10,101]. A similar technique is also used for film deposition known as physical vapor deposition (PVD) involves the vaporization of a solid material from a target within a vacuum environment, followed by the condensation of the vapor onto a substrate, resulting in the formation of a thin layer. The process of vaporization coating refers to the transfer of material at the atomic level through the bombardment of a solid precursor, known as a target, using an extremely powerful source ion beam [121]. A study conducted by Jayaraman and Lin [122] demonstrated the exploitation of the radio frequency magnetron sputtering technique for the synthesis of ultrathin (200-500 nm) Pd-Ag (25% Ag) alloy layers α-Al_2O_3 support modified with a γ-Al_2O_3 sol-gel layer. An H_2 permeance of 2.60×10^{-7} mol m^{-2} s^{-1} Pa^{-1} with an extremely low H_2/N_2 separation factor of only 5.7 is achieved at 523 K. Further, Ryi et al. [123] synthesized a Pd-Cu-Ni (4.5% Cu and 6.5% Ni) pin-hole free membrane on a porous Ni support (55 mm thickness). They achieved a membrane thickness of 4 µm using the

sputtering technique with copper reflow. The Cu-reflow process is considered effective in addressing flaws and membrane delamination on the surface of the substrate. At the temperature of 773 K, they achieved an infinite selectivity with a permeance of 2.3×10^{-7} mol m^{-2} s^{-1} $Pa^{-0.6}$. The membrane exhibited a consistent shape throughout a 10-day testing period, whereby it was subjected to cyclic variations in operating temperature and transmembrane pressure difference. No intermetallic diffusion has been observed during this testing. Recently Fernandez et al. [124] fabricated a PdAg (23% Ag) membrane on a silicon wafer with a thickness of 0.5-2 μm and N_2 permeance of 14×10^{-7} mol m^{-2} s^{-1} Pa^{-1} at 298 K. But at the same time, they reported very low H_2/N_2 selectivity. Although magnetron sputtering offers better control over the microstructure and composition of the Pd-alloy, the challenge of effectively managing the directional flow of atoms during this process remains a significant obstacle. This limitation hinders the feasibility of utilizing sputtering for mass manufacturing and large-scale commercial applications. However, advancements resulting from the application of high-powered magnets have contributed to the emergence of "magnetron sputtering", a technique that also faces challenges in terms of economic viability. Additional limitations involve the considerable cost of equipment, which arises from the necessity of maintaining a high vacuum and achieving a substantial power density to facilitate the evaporation of the target material. The practical applications of support geometry are significantly constrained due to its limitation on a two-dimensional substrate. Moreover, the preparation of highly selective membranes over irregular surfaces of the support with this technique is still a challenge.

2.1.6.4. Electroplating Deposition (EPD)

During this particular process, the metallic ions carrying a positive charge move toward the cathode (also known as the substrate) from the solution. The movement occurs due to the existence of an applied electric potential between the electrodes. The thickness and qualities of the film are primarily influenced by various factors, including the electrolyte composition, temperature, pH level, current density, deposition time, migration and diffusion velocity of metal ions, and the level of electrolyte agitation. One notable benefit of employing this approach is its compatibility with basic apparatus. Additionally, it offers the convenience of depositing films of desired thickness by effectively regulating electroplating duration and current density [125,126]. The rate of deposition and homogeneity is controlled by maintaining

the electrical potential. Nevertheless, it should be noted that this particular approach is constrained in its applicability, as it is only suitable for the utilization of support materials that possess conductivity, such as PSS and Hastelloy. Moreover, surface modification is also not possible with a ceramic-based intermetallic diffusion barrier. Consequently, it cannot be universally employed for ceramic and non-conductive materials which can be densified at relatively low Pd-layer thickness [10].

2.1.6.5. Spray Pyrolysis (SP)

During this particular procedure, a thin layer is applied onto the surface of the heated substrate, whereby the material used for coating undergoes decomposition on the heated surface. However, the shape, texture, crystallinity, and other physical properties of the deposited film are significantly influenced by various factors, including the temperature of the substrate surface, the temperature during deposition, the chemistry of the precursor solution, and the presence of additives in the precursor solution. Furthermore, the complicated nature and the challenges associated with controlling the experimental parameters of the spray pyrolysis process impose constraints on its utilization in membrane-based separation technologies. In a previous study conducted by Li et al. [127], a thin film of Pd-Ag (24% Ag) was fabricated on a surface modified with γ-Al_2O_3 as a support through the utilization of spray pyrolysis. The membrane that was constructed had an H_2/N_2 selectivity of 24, indicating a relatively low level of selectivity. Additionally, the membrane demonstrated a permeance of around 8×10^{-7} mol m^{-2} s^{-1} Pa^{-1} at a temperature of 773 K. The mechanical strength of this membrane was insufficient, leading to its propensity to easily detach from the support.

2.1.6.6. Electroless Plating (ELP)

Electroless plating is an autocatalytic process (deposited metal catalyzes the further deposition) that involves the deposition of continuous metal film onto a substrate through immersion in a solution containing metal complex ions, first developed by Rhoda et al. [128] for Pd deposition. The metallic complex, which is in a meta-stable state (i.e. stable salt unless it is not disturbed by any external agent) and contains the desired metal ions, undergoes chemical reduction on the target substrate as depicted in Equation 2.16. The usual electroless plating bath is composed of an electrolyte solution that contains metallic ions, reductants, complexing agents (to stabilize the solution), and other minor components. The metal particles thereafter undergo growth

on metal nuclei that have been previously introduced onto the substrate surface via a series of activation and sensitization steps. These metal nuclei also serve as catalysts for the reduction of further metal ions. This phenomenon gives rise to the autocatalytic mechanism of electroless plating. Due to the absence of an external electric source, the metal deposition process takes place on a wide range of substrates, including both conductive and nonconductive surfaces like ceramics and polymers. The electroless plating process possesses various advantages in comparison to alternative methods. These include the ability to achieve a homogeneous coating on surfaces with uneven shapes, the absence of a need for external energy, a low cost, and the utilization of simple equipment [10,101].

$$\text{Metal ion} + \text{Reducing agent} \longrightarrow \text{Metal} + \text{Oxidized product} \qquad 2.16$$

Although ELP offers notable advantages, it is important to acknowledge its associated drawbacks. These include the need for frequent refilling of the plating bath, challenges in controlling plating conditions and achieving reproducible results, a relatively slower rate of deposition, as well as the generation of toxic waste chemicals and hazardous liquid waste [129]. However, proper activation and careful control of the plating bath composition can accelerate the plating rate. In order to address this issue, Sanz et al. [130] made modifications to the conventional electroless plating method. They achieved this by introducing both the plating solution and reducing agent from opposite directions of the support. This modification enabled the development of membranes that are entirely selective to hydrogen while consuming a considerably reduced amount of Pd. The reaction between the Pd complex and the reducing agent occurs inside the walls of the pores, resulting in the deposition of metallic Pd at the site of contact and subsequent filling of the pores. This approach effectively enhances the stability of the membrane by effectively preventing delamination of the Pd layer. Nevertheless, the introduction of Pd into the pores led to an additional mass transfer resistance. In addition to this, it is inevitable to stop the formation of micro pinholes during the Pd-layer deposition using ELP. To overcome this challenge, it is suggested to apply a vacuum from inside the lumen of the support for some time [86]. Table 2.5 presents the relative overall rating of membrane preparation based on many factors including performance, stability, production cost, ease of production, raw material cost, impact on the environment, and potential for development in the near future [131]. Therefore, ELP is considered as the most effective methodology for the Pd-based membrane preparation. Furthermore, Gugliuzza et al. [121] conducted a comprehensive

analysis of different approaches to the fabrication of metallic membranes, highlighting the advantages and limitations of each method as briefly shown in Table 2.6.

Table 2. 5. Relative overall ranking of evaluation of membrane manufacturing technique (reproduced from [131]).

Membrane manufacturing technique	Ranking
Electroless plating	1.00
Pore-plugging-interfacial reaction	0.77
Pore-plugging-micro emulsion	0.72
Physical vapor deposition	0.63
Laser deposition	0.52
Chemical vapor deposition	0.46

Table 2. 6. Advantages and limitations of the methods of palladium-based membrane manufacturing technique (adapted from [101,121,129]).

Method	Advantages	Limitations
Cold rolling	Good material characteristics, good electronic properties, corrosion resistance, and high catalytic activities	Enhanced H_2 solubility in palladium and its alloys owing to the accumulation of H_2 excess in the stress field around dislocations
Electroplating	Deposit is extremely hard and wear-resistant, thick deposits can be machined for repair/tolerance applications, simple, well-understood technology, a wide range of applications, and offer good corrosion resistance	Slow deposition rate, multiple coats often needed, machining needed to get uniform thickness, susceptible to H_2 embrittlement, exhibit brittleness, leading to micro-cracking and reduced corrosion resistance, and decontamination of plating solutions is difficult
Spray pyrolysis	Very simple technique	Shows a quite low separation factor, and complicated experimental parameters
Chemical vapor deposition	Controlled thickness, better film quality, and thin membrane preparation	Expensive Pd precursor, high vacuum (< 0.1 mm Hg), no alloy precursor available, complex operating conditions, and contamination by carbon residue
Magnetron sputtering	Better adhesion to the substrates, composition controlled by evaporation rates, growth surface is constantly under electron bombardment and thus is highly energetic	Decrease in the substrate ion current when increasing the substrate-to-target distance, difficult deposition of alloys, and evaporation rates from the melting of the components
Physical vapor deposition	Materials can be deposited with improved properties compared to the substrate material, and almost any type of inorganic material can be used as well as some kinds of organic materials	Difficult to coat irregular surfaces, high capital cost, high vacuums, and temperatures require skilled operators, processes requiring large amounts of heat require appropriate cooling systems, rate of coating deposition is usually quite slow
Electroless plating deposition	Uniformity of deposits on complex shapes, no external energy required, low cost, and simple equipment	Difficult thickness controls costly losses of palladium in the bath, reproducibility problems, slow deposition rate, and the purity of the deposit is not guaranteed

2.1.7. Industrial Application and Challenges for Commercial Deployment

Palladium membranes have found diverse applications in various industrial sectors where hydrogen separation is critical. Palladium membranes offer unparalleled selectivity and purity for hydrogen separation, making them ideal for applications requiring high-purity hydrogen. However, the commercial deployment of palladium membranes for hydrogen separation presents both opportunities and challenges.

- **Industrial applications and opportunities*:*** In various industrial applications, such as steam reforming of methane, water gas shift reaction, chemical processing, electronics manufacturing, catalytic reforming, steel making, and industrial waste stream, palladium membranes are predominantly utilized for the purpose of hydrogen separation or purification from gas mixtures. The utilization of palladium membranes enables the targeted extraction of hydrogen from gas mixtures that contain impurities, including methane, carbon monoxide, and hydrogen sulfide [2,10]. This process results in the production of high-purity hydrogen, which is well-suited for various applications. After undergoing purification, the hydrogen that has been recovered is then utilized for many purposes, including the synthesis of ammonia, hydrogenation reactions within the petrochemical sector, and the generation of power through fuel cells. Furthermore, the Pd membrane is utilized in hydrogenation and dehydrogenation processes to selectively introduce or eliminate hydrogen from reaction mixtures. Precise control of hydrogen partial pressure plays a critical role in optimizing reaction kinetics and product quality in the production of fine chemicals, medicines, and specialty polymers [132]. Palladium membranes also find application in nuclear power facilities to purify hydrogen and recover tritium from reactor coolant and moderator systems. The targeted elimination of hydrogen isotopes, such as tritium, from heavy water or other streams containing hydrogen significantly contributes to the domains of nuclear safety and waste hazard management [17,133]. Palladium membrane systems can be retrofitted into refineries, chemical plants, and other industrial facilities to extract and purify hydrogen from waste streams or enhance product streams. The efficient separation of hydrogen at lower working temperatures and pressures is facilitated by the high permeability and selectivity of palladium membranes, resulting in reduced energy consumption and operating costs. The continuous progress in membrane materials, fabrication techniques, and system design is facilitating enhancements in the performance, reliability, and cost-efficiency of palladium membrane technology. The current research and development endeavors are primarily directed at addressing technical obstacles

and enhancing membrane-based separation methodologies, hence creating novel prospects for their commercial implementation.

- **Challenges for scale-up and commercial deployment:** A major obstacle to the widespread use of palladium, a valuable metal, is its exorbitant price. The degradation of palladium membranes can occur over time as a result of various circumstances, including hydrogen embrittlement, heat cycling, and exposure to contaminants. The economic viability of palladium membranes heavily relies on the assurance of their resilience and lifespan under real-time industrial operating conditions [134–136]. Additionally, the process of scaling palladium membrane systems from small-scale prototypes in the laboratory to large-scale units in commercial settings has significant technological and logistical obstacles. In order to achieve dependable and economically viable operation on a larger scale, it is important to tackle concerns pertaining to the consistency of membrane manufacture, optimization of module design, and integration of systems [137]. The process of scaling up for commercial applications necessitates meticulous examination of mass transfer constraints, since bigger modules may encounter significant concentration polarization phenomena, particularly when subjected to increased flow rates and higher membrane surface areas [138]. In scaling up membrane separators, it is crucial to thoroughly evaluate module design characteristics, including flow distribution and membrane support structures. The optimization of module design and configuration is crucial to provide a consistent distribution of flow, minimize the occurrence of pressure drop, and maximize the exploitation of membrane surface area [95,139,140]. Increasing the size of membrane separator modules may result in higher pressure drop across the module as a consequence of heightened flow resistance and fluid dynamics. To prevent excessive energy consumption and uphold system efficiency, it is imperative to strike a balance between pressure drop considerations and membrane performance needs [65]. The commercial use of palladium membranes may be contingent upon adherence to regulatory mandates and safety protocols pertaining to the handling of materials, ensuring process safety, and mitigating environmental consequences. By overcoming these challenges, palladium membrane technology can realize its full potential for hydrogen separation in various industrial applications, contributing to energy efficiency, sustainability, and economic competitiveness.

2.2. Literature Review on Methanol Steam Reforming (MSR)

This section presents an extensive literature review comprising diverse facets pertaining to methanol reforming, encompassing a comparative analysis of the numerous approaches employed in the reforming process. Furthermore, a comprehensive examination of several catalysts and reaction mechanisms utilized for MSR is presented. The MSR is affected by various elements, including temperature, pressure, steam-to-carbon ratio, feed flow rate, and reactor system. Finally, a thorough review of different approaches for catalyst preparation is provided to select the most appropriate procedure.

2.2.1. Comparison of Methanol Reforming Techniques

Hydrogen production through methanol can be accomplished through various reforming processes, such as methanol decomposition, partial oxidation of methanol, oxidative steam reforming of methanol, and methanol steam reforming [141]. The process referred to as methanol decomposition, or methanol cracking, involves the direct conversion of methanol into H_2 and CO, as represented by Equation 2.17. On the other hand, the process of partial oxidation of methanol requires a controlled amount of oxygen or air to facilitate the conversion of methanol into hydrogen and carbon monoxide, as illustrated in Equation 2.18. Typically, partial oxidation occurs at high temperatures between 473 K and 773 K. Nevertheless, the management of process conditions poses significant challenges. Oxidative steam reforming is a process that entails the concurrent reaction of methanol, steam, and oxygen, resulting in the production of H_2, CO, and CO_2, as seen in Equation 2.19 and Equation 2.20. Finally, methanol steam reforming involves the transformation of methanol and steam into H_2, CO, and CO_2. The process of MSR is characterized by its complete endothermic nature, encompassing three concurrent reactions: MSR, water gas shift reaction, and methanol decomposition as given in Equations 2.21, Equations 2.22, and Equations 2.23. In the methanolysis reaction, methanol is initially broken down into carbon monoxide and hydrogen, followed by the water gas shift (WGS) reaction, where CO combines with steam to produce CO_2 and H_2.

Methanol decomposition or methanol cracking

$$CH_3OH \rightarrow CO + 2H_2 \qquad \Delta H = 90.2 \text{ kJ mol}^{-1} \qquad (2.17)$$

Partial oxidation of methanol

$$2CH_3OH + O_2 \rightarrow 2CO + 4H_2 \qquad \Delta H = 256.4 \text{ kJ mol}^{-1} \qquad (2.18)$$

Oxidative steam reforming of methanol

$CH_3OH + H_2O + ½ O_2 \rightarrow CO + 2H_2$ $\Delta H = 370.0$ kJ mol^{-1} (2.19)

$CO + H_2O \rightarrow CO_2 + H_2$ $\Delta H = -41.2$ kJ mol^{-1} (2.20)

Methanol steam reforming

$CH_3OH + H_2O \rightleftarrows CO_2 + 3H_2$ $\Delta H = 49.7$ kJ mol^{-1} (2.21)

$CH_3OH \rightleftarrows CO + 2H_2$ $\Delta H = 90.2$ kJ mol^{-1} (2.22)

$CO + H_2O \rightleftarrows CO_2 + H_2$ $\Delta H = -41.2$ kJ mol^{-1} (2.23)

Table 2.7 outlines the benefits and drawbacks of each of these techniques [142]. Out of the aforementioned technologies, methanol steam reforming is considered the most favorable option for hydrogen production due to its ability to yield the maximum amount of hydrogen. The steam reforming method is highly efficient and unique in its ability to generate three hydrogen molecules for each mole of methanol, with water contributing one mole of H_2 [143].

Table 2. 7. Comparison of methanol-reforming methods (reproduced from [142]).

Methods	Advantages	Disadvantages
Methanol decomposition	• H_2 can be produced directly from methanol • No additional reactants (water/ steam or oxygen) are required	• Highly selective towards CO • High concentrations of CO necessitate further clean-up for use in fuel cells • Requires external energy source
Partial oxidation of methanol	• Exothermic • No additional heating source is required	• Low H_2 yield • High CO content • High reaction temperature
Oxidative steam reforming of methanol	• Thermally neutral process • No external heating is required	• Requires sophisticated oxygen separation unit to feed pure oxygen • Expensive
Methanol steam reforming	• Mild reaction conditions • High conversion rate • High hydrogen content • Low CO generation	• Endothermic • Requires external heat supply

2.2.2. Catalyst Preparation, Composition, and Active Sites

In the context of methanol steam reforming, active sites in catalysts refer to specific areas on the catalyst surface that facilitate chemical reactions. These reactions primarily involve the conversion of methanol and water into hydrogen, carbon monoxide, and carbon dioxide. The active sites on the surface of the catalysts are comprised of metal particles such as Cu, Ni, Pd, Pt, and others. The primary function of these active sites is to adsorb, activate, and convert reactant molecules into desired products. Moreover, the composition of the catalyst i.e. the amount of metal loading over the support plays a critical role in determining the number of active sites and therefore the overall performance of the catalyst. However, different methodologies adopted for doping the metal particle over the support significantly influence the catalyst's structure, morphology, surface area, dispersion of active sites, and catalytic activity.

Several techniques for catalyst synthesis have been reported in the literature, including co-precipitation [144], wet impregnation [145], hydrothermal treatment [146], oxalate gel coprecipitation [147], soft reactive grinding techniques [148], solid-state reaction [149] and other similar techniques with minor variation in the preparation methodology. The traditional coprecipitation and wet impregnation methods are widely employed for catalyst preparation. The study conducted by Shen et al. [150] examined the effect of various preparation techniques on the catalyst's performance for MSR. Cu/Zn/Al catalysts were synthesized using different methods including co-precipitation, impregnation, and hydrothermal. They observed that the utilization of a co-precipitated catalyst yields a higher surface area and exhibits enhanced activity with almost 100% conversion. The catalytic activity of Cu/Zn/Zr/Al for MSR, prepared using two distinct methods including wet impregnation and co-precipitation was investigated by Patel et al. The Cu/Zn/Zr/Al catalyst, when co-precipitated, exhibited the best methanol conversion and a low concentration of CO ranging from 0.04 to 0.8 mol %. In contrast, the catalyst synthesized using wet impregnation resulted in a CO concentration ranging from 0.7 to 2.5 mol %. Bagherzadeh et al. [146] compared the effect of the plasma treatment of $Cu/ZnO/Al_2O_3$ catalyst synthesized via two different techniques namely the hydrothermal method and co-precipitation method. The plasma-treated catalyst prepared through co-precipitation performed better compared to the untreated sample. They observed a methanol conversion of 95% and selectivity to CO of 0.24% at 240 °C for plasma-treated catalyst whereas the untreated catalyst exhibited a reduced conversion of 93% and CO selectivity of 0.28%. Another study by Shishido et al. [151] showed that Cu/ZnO and $Cu/ZnO/Al_2O_3$

catalysts prepared through homogeneous precipitation using urea hydrolysis have better activity compared to the same catalyst prepared through the co-precipitation technique. Ahmadi et al. [152] compared the performance of ZrO_2/CeO_2 doped $CuO/ZnO/Al_2O_3$ catalysts prepared via sono-chemical co-precipitation with same catalyst prepared through conventional co-precipitation method. The catalyst exhibited excellent uniformity and decreased particle size when subjected to ultrasonic treatment. As a result, they were able to increase the specific surface area and improve the conversion of methanol, while also achieving low selectivity for CO. The application of plasma and microwave techniques has been commonly employed in conventional preparation methods, resulting in enhanced dispersion and uniformity of active metal particle. Purnama et al. [153] developed a nanostructured CuO/ZrO_2 catalyst with controlled morphology and porosity of zirconia by employing a polymer template approach. In comparison to commercial $CuO/ZnO/Al_2O_3$ catalysts, CuO/ZrO_2 exhibited a significant reduction in CO production by almost 50 times, while also demonstrating improved stability for the same methanol conversion.

Since metal particles are typically thought of as the catalyst's active ingredient, the morphology and composition of doped metal particles have a significant influence on the catalytic properties. Nevertheless, the presence of higher metal loading in catalysts does not necessarily employ enhanced activity and selectivity. Therefore, the optimal performance is significantly influenced by the synergy of metal particles with the support. For instance, Cu is the active metal particle in the commercially available MSR catalyst ($Cu/ZnO/Al_2O_3$). ZnO is believed to enhance the surface catalytic characteristics by facilitating the reducibility of Cu, which is crucial for the reforming process. Meanwhile, the utilization of porous alumina works as a support with substantial surface area support, hence enhancing the dispersion of copper. This, in turn, leads to increased loading capacity and reduced particle size. Yang and Liao [154] conducted a study in which they synthesized a range of Cu/ZnO catalysts supported on carbon nanotubes, with varying metal loadings. The performance of these catalysts was then evaluated. It was found that as the total metal loading increased, the catalytic activity exhibited an increase until reaching a value of 30 wt. %, beyond which it decreased. The observed phenomenon can be ascribed to the partial degradation of the structure or the aggregation of metals due to the higher metal concentration. Furthermore, a minimum quantity of ZnO (20 wt. %) was necessary to ensure that the concentration of CO remained below 1%. In a separate investigation, three different catalysts were synthesized, specifically a Ni-Cu alloy supported on carbon nanotubes, a bimetal catalyst consisting of Ni and Cu supported on carbon

nanotubes, and a Ni-Cu catalyst supported on activated carbon. The experimental findings indicate that the Ni-Cu alloy, when supported on carbon nanotubes, has superior performance in comparison to the other catalysts. In addition, the performance of the Ni-Cu alloy supported on carbon nanotubes is improved by reducing the Ni content. The optimal value for the overall loading of Ni-Cu is calculated to be 20 wt. %, resulting in a total conversion of 98% [155]. According to Alejo et al. [156], the catalytic activity and interaction are influenced by the chemical composition of the catalyst. A range of copper-zinc catalysts was employed, with the copper content varying from 20% to 70%. The catalyst with a composition of 40% copper and 60% zinc exhibited the highest level of activity.

The identity of the active sites in Cu-based catalysts for MSR is a topic of ongoing research and debate due to no general agreement on the mechanism underlying active sites and surface reactions involved. In the past, metallic copper (Cu^0) has been widely regarded as the principal active site for MSR. The process of H_2O dissociation on Cu^0 is considered a pivotal stage in the reaction pathway since it produces surface hydrogen that aids in the cleavage of C-H bonds in methanol. Several studies indicate that Cu plays a crucial function in a partially oxidized state as well, namely in the presence of Cu^+, Cu^0 with Cu^{2+}, and a combination of all. This is particularly important at the Cu-support contact, as it facilitates the activation of methanol or the promotion of water dissociation. Additionally, the presence of CuO on the catalyst surface can serve as an active site that could participate in the dehydrogenation processes during the conversion of methanol [142,157,158]. At last, the importance of support materials and promoters, such as Al_2O_3, CeO_2, and ZrO_2, lies in their ability to interact with Cu, hence potentially facilitating the creation of active sites. Hirunsit and Faungnawakij [159] prepared multiple Cu-based spinel-oxide catalysts, including $CuFe_2O_4$, $CuMn_2O_4$, and $CuCr_2O_4$. The catalysts were then compared with the commercial $Cu/ZnO/Al_2O_3$. Reduced $CuFe_2O_4$ and $CuMn_2O_4$ exhibited a high concentration of Cu^+ ions on the catalyst surface, while the reduced $CuCr_2O_4$ and $Cu/ZnO/Al_2O_3$ displayed a relatively low concentration of Cu^+ ions on the catalyst surface. Zhang et al. [160] reported that the encapsulation of copper nanoparticles by ZnO resulted in the formation of numerous synergistic Cu_2O/ZnO sites, as well as an increased concentration of Cu^+ ions on the catalyst surface. The presence of a high concentration of Cu^+ ions increased the hydrogen output from 54.6 % to 63.5 %. Das et al. [161] found that a greater Cu^+/Cu^0 ratio is associated with increased MSR activity and decreased CO selectivity. The inclusion of Cu^+ ions on the catalyst surface facilitates the reaction between CO and surface oxygen, resulting in the production of CO_2. This chemical reaction leads to a decrease in CO

selectivity when compared to metallic copper species since it hinders the RWGS reaction. Therefore, to ensure a low selectivity of CO during the MSR, it is vital to possess a specific range of the Cu^{+}/Cu^{0} ratio on the surface, alongside the mere existence of reduced copper phases (Cu^{0} and Cu^{+}). The active sites and their spatial arrangement in Cu-modified molybdenum carbide (Cu-Mo_xC_y) catalysts were established by Ma et al. [162]. Their finding revealed the presence of a robust metal-support interaction between Cu and molybdenum carbide. The surface of the molybdenum carbide was found to contain both Cu^{I} and Cu^{II} species, as determined using X-ray photoelectron spectroscopy. Furthermore, the active site of Cu^{I} is situated along the periphery of the Cu particle, positioned between the support and the surface of the metal. To summarize, the primary active sites observed in Cu-based catalysts for methanol steam reforming are Cu^{0}, Cu^{+}, and other partially oxidized sites. These sites have the ability to efficiently activate and convert the reaction intermediates. The properties and performance of the active sites are significantly influenced by the support material as well.

2.2.3. Catalyst Deactivation

In the context of MSR, catalyst deactivation pertains to the gradual decline in catalytic activity and selectivity caused by a range of variables that include coking, sintering, poisoning due to foreign material (e.g. chlorine, sulfur, heavy metals, etc.), change in oxidation state, and mechanical degradation. These effects collectively have a detrimental impact on the overall performance of the catalyst [163–165].

The methanol decomposition and the occurrence of side reactions result in the formation of carbonaceous intermediates, which then degrade and accumulate on the surface of the catalyst. The key factors that facilitate coking include elevated temperatures, low steam-to-carbon (S/C) ratios, and extended reaction durations [165,166]. However, Valdés-Sols et al. [167] suggest that the deactivation is probably not influenced by the process used to synthesize the catalyst. Instead, it is linked to the composition of the feed and the space velocity, which leads to the deposition of coke and the sintering of the catalyst. It was also suggested that increasing the S/C ratio and injecting oxygen in the intermediate of the reaction has the ability to suppress the coke formation. In another work by Fasanya et al. [168], it was observed that the S/C significantly affects the selectivity of the side reactions. For instance, an excess of methanol results in higher CO and CH_4 selectivity whereas the equimolar ratio of the S/C produced the least amount of CO even at 573 K. Fortunately the deactivation of catalysts caused by the deposition of coke is a reversible phenomenon that can be mitigated by exposing the catalyst

to air-flow (coke burning) at a temperature of 623 K, resulting in a near restoration of its initial catalytic activity [169,170].

The process of sintering, which entails the coalescence and growth of metal nanoparticles to create agglomerate on the catalyst surface, typically occurs due to elevated temperatures, pressure, and thermal cycling. This leads to a decrease in the active surface area and catalytic sites [165,166]. Consequently, the collapse of the catalyst structure leads to an irreversible loss of catalytic activity. Kurtz et al. [165] revealed that elevated levels of carbon monoxide resulted in an augmented process of sintering for the metallic copper particles. Hence, it is imperative to consistently observe the alteration in the composition of the active metal phase prior to and following the reaction. The use of moderate temperatures (e.g., 473 K to 673 K) and pressures during the operation of the MSR has been found to have a substantial impact in mitigating the occurrence of sintering. Research has shown that the utilization of high surface area support materials (e.g., alumina, silica, ceria, nanomaterials), incorporation of promoters or dopants (e.g., oxides and alloys), use of bimetallic or multi-metallic catalysts, can effectively mitigate the occurrence of sintering. Catalysts with tailored morphology, pore structure, and surface chemistry can mitigate the sintering effects. To improve mass transfer, mitigate diffusion constraints, and minimize pore blockage caused by sintering, it is suggested to employ catalyst supports that include hierarchical or mesoporous architectures [171,172].

On the other hand, impurities in the feed stream can cause catalyst poisoning by inhibiting active sites or modifying the electronic structure of the catalyst. Irreversible binding of contaminants to metal-active sites results in the inhibition of catalytic activity [173]. The effect of impurities or poisonous substances such as chlorine and sulfur was thoroughly examined by Lindstrom et al. [164]. According to their findings, the poisonous effect of sulfur was shown to be more pronounced in comparison to that of chlorine. Furthermore, the decline in catalyst activity occurred gradually rather than suddenly. High temperatures and low S/C ratio exacerbate sulfur poisoning effects, as sulfur adsorption and desorption kinetics are influenced by reaction conditions. In a separate investigation conducted by Twigg et al. [171] it was observed that the presence of even a trace amount of chlorides can greatly expedite the process of surface migration, leading to the thermal sintering of the catalyst. To eliminate sulfur and chlorine contaminants from the feed stream, it is recommended to employ pre-treatment techniques, such as desulfurization or chlorination. In addition to this, employing catalyst supports that are resistant to sulfur and chlorine, such as alumina or ceria can be beneficial in order to reduce the occurrence of adsorption and poisoning.

Under oxidizing conditions, such as the presence of oxygen and steam at elevated temperatures, metal nanoparticles have the ability to undergo oxidation-reduction cycles. This process leads to the creation of inactive metal oxides and the electronic structure of the active site [174]. Phase alterations or lattice rearrangements can occur in metal oxides when subjected to reaction conditions, resulting in modifications to their catalytic activity and stability. In order to restore catalytic activity and reduce deactivation resulting from oxidation, in situ regeneration approaches, such as reduction treatments or gas-phase processes, can be utilized.

Mechanical degradation arises when catalyst particles experience physical alterations, such as attrition, disintegration, or reduction in surface area, throughout the processes of handling, operation, or regeneration. The catalyst particles may experience mechanical stress and subsequent breakdown or deterioration in structure when subjected to harsh reaction conditions, such as high pressures or flow velocities [175]. The process of mechanical degradation has the potential to cause a decrease in the surface area and porosity of catalyst particles, leading to a subsequent reduction in active site density and catalytic activity. The reduction of mechanical deterioration of catalysts can be achieved by optimizing reactor design and operating conditions to limit flow velocities and turbulence. In addition, the utilization of particle size control methods, such as granulation or palletization, can enhance the stability of the catalyst bed and minimize attrition, thereby decelerating the degradation process, even under challenging operating conditions.

2.2.4. MSR Reaction Mechanism

The reaction mechanism of MSR over Cu-based catalysts is generally considered to take place via the following routes: (a) methanol decomposition followed by WGS reaction, (b) direct MSR reaction, (c) methanol decomposition followed by RWGS reaction, and (d) methyl formate reaction. However, additional evidence supports the notion that alternative pathways may be involved, such as the intermediate formation of formate and methyl formate, formaldehyde, dioxymethylene, and methoxy species [170,176]. It is challenging to reach a consensus regarding the most accurate approach among these options. Previously, there has been a prevailing belief that the reaction process involves the decomposition of methanol, which is subsequently followed by the WGS reaction as given in Equation 2.22 and Equation 2.23 respectively. Nevertheless, for this to occur, the concentration of CO must exceed the equilibrium value, which contradicts the experimental observation [177]. Therefore, Chein et al. [178] and Peppley et al. [179,180] proposed a different reaction mechanism route as given in Equation 2.21, Equation 2.22, and Equation 2.23. It can be deduced that the WGS reaction

plays a crucial role by either facilitating the conversion of CO to CO_2 or by restoring the equilibrium between CO and CO_2 through a single-step process.

The formation of methyl formate as an intermediate product was proposed by Takahashi et al. [181] as shown in Equation 2.24, Equation 2.25, and Equation 2.26. Jiang et al. [182,183] proposed that the dehydrogenation of methanol leads to the formation of methyl formate in conjunction with hydrogen. Furthermore, it has been suggested that MSR has only a single sort of active site based on Langmuir-Hinshelwood rate expression. Subsequently, the hydrolysis of methyl formate leads to the production of formic acid and methanol, which is then followed by the generation of CO_2. Since the formation of CO_2 is not attributed to the decomposition of methanol, therefore the RWGS reaction is considered the sole reason for CO_2 formation as described in Equation 2.27. The reaction mechanism of MSR was further elucidated by Peppley et al. [179] The authors proposed two distinct categories of active sites: one designed to facilitate MSR and the water-gas shift reactions, and another solely intended to help the decomposition reaction. Furthermore, the authors made the assumption that hydrogen adsorption did not compete for the active sites specifically occupied by oxygen-containing species.

$$2CH_3OH \rightarrow HCOOCH_3 + 2H_2 \qquad \Delta H = +64.4 \text{ kJ mol}^{-1} \qquad (2.24)$$

$$HCOOCH_3 + H_2O \rightarrow CH_3OH + HCOOH \qquad \Delta H = -31.2 \text{ kJ mol}^{-1} \qquad (2.25)$$

$$HCOOH \rightarrow H_2 + CO_2 \qquad \Delta H = +31.2 \text{ kJ mol}^{-1} \qquad (2.26)$$

$$CO_2 + H_2 \leftrightarrow CO + H_2O \qquad \Delta H = +41.0 \text{ kJ mol}^{-1} \qquad (2.27)$$

A distinct reaction mechanism was postulated in an independent investigation conducted by Takezawa and Iwasa [184], wherein the intermediate formation of formaldehyde and formic acid was observed during MSR on a Cu-based catalyst. Following the dehydrogenation of CH_3OH to HCHO as given in Equation 2.28, H_2O nucleophilically reacts with HCHO to produce HCOOH as shown in Equation 2.29, which decomposes to H_2 and CO_2 described in Equation 2.30. The rate-limiting step in the reaction is the dehydrogenation of methanol to produce formaldehyde. Furthermore, the RWGS reaction is once again ascribed to the production of CO. One could contend that adsorbed HCHO underwent direct decomposition to H_2 and CO, which were subsequently utilized in the WGS reaction. The rate-limiting step, in this case, will be methanol decomposition, which should be accounted for in kinetic modeling due to the greater influence of the endothermic decomposition reaction at relatively high temperatures in the presence of water [170].

$CH_3OH \rightarrow HCHO + H_2$ $\Delta H = +92.1\ kJ\ mol^{-1}$ (2.28)

$HCHO + H_2O \rightarrow HCOOH + H_2$ $\Delta H = +74.3\ kJ\ mol^{-1}$ (2.29)

$HCOOH \rightarrow CO_2 + H_2$ $\Delta H = +31.2\ kJ\ mol^{-1}$ (2.30)

Frank et al. [185] provided a comprehensive summary of the reaction mechanisms pertaining to catalysts in the literature for MSR. The initiation of the catalytic cycle involves the dissociative adsorption of methanol onto the surface of the catalyst. The assumption was made that active site A is responsible for the adsorption of hydrogen, while active site B serves for the adsorption of all other intermediates. One mechanism outlined in the cycle entails the generation of dioxomethylene through the interaction between surface hydroxyl groups and formaldehyde. The dioxomethylene undergoes dehydrogenation to generate a formate group, which subsequently undergoes further dehydrogenation, resulting in the release of carbon dioxide and hydrogen. Another mechanism reported by Zhang et al. [186] was also proposed in the catalytic cycle, in which the formaldehyde produced from the dehydrogenation of methanol is subjected to a chemical attack by a methoxy group, leading to the formation of the intermediate methyl formate. The hydroxyl groups of the later intermediate can undergo decomposition, resulting in the formation of methoxy and formate groups. Following the previously proposed mechanism, Papavasiliou et al. [187] conducted a study examining three distinct copper catalysts, including Cu−Mn-O, Cu-Ce-O, and Cu-ZnO-Al_2O_3. Their findings indicated that the Cu-Mn-O catalyst resulted in the formation of methyl formate as the intermediate, while the Cu-Ce-O and Cu-ZnO-Al_2O_3 catalysts led to the formation of dioxomethylene as the intermediate. The influence of reaction temperature on the formation of formic acid and methyl formate as intermediates has been observed by Cao et al. [188]. The prevalence of the formic acid intermediate pathway is observed at temperatures below 453 K, but the methyl formate intermediate pathway is observed at reaction temperatures beyond 453 K.

2.2.5. Effect of Catalyst Microstructure

In addition to the active metal's surface area, factors such as metal dispersion, particle size, and defects in the bulk structure (such as microstrain and structural disorder) have a substantial impact on catalytic activity according to Kniep et al. [189]. They examined the correlation between the activity of copper catalysts and their copper phase structure. The catalysts were synthesized using the co-precipitation approach, in which the precipitates were allowed to mature in the mother liquor at a particular temperature. During the process of aging, it was

noted that the disordered precipitates underwent a transformation into ordered crystalline structures. The process of aging resulted in an enhancement of the copper surface area, leading to a more uniform microstructure with smaller crystalline sizes of both copper and ZnO. Additionally, the aging process strengthened the interface between the copper and zinc oxide materials. The nanostructured Cu particles exhibited a higher level of microstrain, which was the primary reason contributing to their enhanced catalytic activity. Further, Wang et al. [148] examined the effect of extended grinding and observed that microstructural properties are affected by the grinding process. The thermal decomposition of oxalate precursors obtained by grinding enables the creation of higher dispersion of copper and more robust contacts between the metal and the support in the oxide predecessors. Furthermore, it was reported that an elevated microstrain in the nanostructured copper particles was due to both structural disorder and an increase in the copper surface area resulting during the grinding period. In another study by Wang et al. [190] conducted a study to examine the impact of calcination temperature on copper oxide catalysts supported by zirconia. Several Zr catalysts supported on CuO were synthesized by decomposing the oxalate precursors generated using oxalate gel coprecipitation in an alcoholic solution. These catalysts were then investigated for their performance in the MSR process. The catalytic activity was shown to be improved as the calcination temperature increased, reaching its peak at 823 K. The primary crystalline phase seen in the catalyst after being calcined at 823 K was tetragonal ZrO_2, while the predominant surface layer of the support material was monoclinic ZrO_2.

2.2.6. Catalyst for Methanol Steam Reforming

In order to fully utilize the potential of hydrogen, it must be separated from methanol due to its lower heating value (119.9 MJ kg^{-1}) which is roughly 6.5 times higher than methanol's (18.1 MJ kg^{-1}) [38]. The price of reforming methanol is nearly one-third that of reforming natural gas. Its low reforming temperature (523-623 K) due to the absence of a C-C bond also lowers the possibility of coke production over the catalyst at high temperatures. The presence of the –OH functional group is also a good attribute, as it reduces the amount of water consumed in the steam reforming reaction to produce hydrogen, hence reducing the steam reforming temperature. Moreover, there is no requirement for auxiliary units such as the desulphurization unit and the pre-reforming process to obtain the H_2-rich stream after reforming over the catalyst [191]. Therefore, the selection of a catalyst that is commercially viable with long-term performance is the key component for MSR. Generally, the catalyst for MSR is categorized into copper-based catalysts and Group-VIII metal-based catalysts also known as novel metal-

based catalysts (Pd, Pt, Ni, Ru, and Rh). Recently, nanomaterial-based catalysts attracted the attention of researchers due to their exceptional performance compared to conventional catalysts. Nanomaterial-based catalysts are currently in the early stage of development and are gaining attention due to their exceptional performance compared to conventional catalysts. Nanocatalysts need intricate synthesis techniques and come with a high cost to exhibit exceptional performance, rendering them impractical for widespread use [192]. Nevertheless, it is crucial to consider the restricted rate of heat transfer to the reactants when addressing endothermic steam reforming reactions. Therefore, structured catalysts including monoliths, porous metal fiber, 3D-solid foam, and 3D-printed catalysts have interconnected void frameworks, particularly SiC-based foam, which intensifies heat transfer and reduces the radial variation in temperature. In addition to this, it improves conversion by supplying a large surface area and turbulent mixing within an interconnected three-dimensional framework. The catalyst-coated foam structure can further reduce the quantity of catalyst required for a specific output, allowing for the design of compact reactors such as membrane reactors (MR) [193–195]. The subsequent section provides a more in-depth examination of the literature pertaining to these catalysts.

2.2.6.1. Copper-based Catalyst and Effect of Promoters

While there have been investigations into catalytic systems utilizing copper, noble metals, and other group 8–10 metals for MSR, copper-based catalysts have been the predominant focus in MSR studies due to their notable attributes of high activity and selectivity, as well as their relative affordability [142]. Zinc, in conjunction with copper, was initially employed in the synthesis of catalysts for MSR owing to its favorable reaction conditions within the temperature range of 523 K to 573 K. In general, ZnO is utilized as a spacer to isolate copper particles to prevent the sintering during high-temperature operation. Moreover, copper-zinc catalysts are afflicted with several drawbacks, including the potential for pyrophoric behavior upon exposure to air, and sensitivity to even minute concentrations of sulfur. Therefore, Fasanya et al. [168] employed hydrothermally synthesized zinc oxide nanorods on the surface of cordierite, which were subsequently loaded with copper. In the temperature range of 453 K to 503 K, the reaction exhibited a selectivity of 98% towards H_2 and a selectivity of 0% towards CO. However, coke production and catalytic deactivation were observed after 573 K. Nevertheless, the primary disadvantages of copper-based catalysts are their deactivation caused by agglomeration and migration, as well as sintering resulting from high-temperature heating. To address these challenges, researchers have explored catalytic supports, promoters, and other

synthesis methods to improve the catalyst's performance [196,197]. Various promoters and supports, such as Al_2O_3 [198], ZnO [160], CeO_2 [147], ZrO_2 [199], Ga_2O_3 [200], MgO [201], In_2O_3 [202], Fe [203], Ni [196], Ti [204], Sc_2O_3 [205], Y_2O_3 [202], La [206], Sm [207], and Gd [208], are utilized to enhance the catalytic activity and selectivity. Furthermore, promoters have brought attention to its feasibility of addressing additional challenges, including heat sintering, agglomeration, and coke formation. The selection of an appropriate promoter and its composition is critical for hydrogen production during MSR, especially to achieve stable physiochemical properties and improved metal dispersion, along with small particle sizes and high surface area [142]. Al_2O_3, ZnO, CeO_2, and ZrO_2 are extensively documented in the literature for their exceptional ability to enhance catalyst performance through various means. All promoters or support, except for Sm, have exhibited a positive effect on the catalytic activity. The presence of Sm hindered the ability of Cu species to be reduced and led to the clustering of Cu particles, resulting in a decrease in the overall amount of Cu on the catalytic surface. Consequently, negatively affects the performance of the catalyst. Several techniques for catalyst synthesis have been reported in the literature, including coprecipitation [144], wet impregnation [145], hydrothermal treatment [146], oxalate gel coprecipitation [147], soft reactive grinding techniques [148], and other similar techniques with minor variation in the preparation methodology. The traditional coprecipitation and wet impregnation methods are widely employed for catalyst preparation. Alumina is commonly employed as a support material due to its high surface area, which facilitates enhanced dispersion of the active metal. Alumina also functions to decelerate the process of catalyst sintering and enhance its stability. Alumina exhibits a modest level of acidity and basicity, which can impact the processes of reactions and the selectivity of products in MSR. The presence of acidic sites on the alumina support can enhance the process of adsorption and activation of reactant molecules, whereas the presence of basic sites can ease the desorption of reaction intermediates, thus improving the overall catalytic performance [156,209].

ZnO is of significant importance in augmenting the efficacy and longevity of copper-based catalysts utilized in MSR. This is achieved through the better dispersion of Cu particles, prevention of sintering, and facilitation of key reaction steps. The interaction between ZnO and Cu species exhibits a robust metal-support interaction, which effectively stabilizes tiny Cu particles and inhibits their agglomeration or sintering during the reaction. In comparison to pure copper particles, the presence of copper-zinc alloy phases or mixed metal oxide structures offers enhanced resistance to sintering. In addition, ZnO offers Lewis acid sites that facilitate

the adsorption and dissociation of methanol on the surface of the catalyst, resulting in enhanced catalytic activity. ZnO also demonstrates enhanced CO conversion via the WGS reaction. In addition, the inclusion of ZnO promotes the reduction of Cu^{2+} to Cu^{+} and Cu^{0}, which are the primary species involved in the MSR process [210,211]. Zhang et al. [160] conducted a study on the encapsulation of copper nanoparticles by ZnO. This encapsulation process resulted in the formation of numerous synergistic Cu_2O/ZnO sites, as well as an increased concentration of Cu^{+} ions on the catalyst surface. Consequently, the activation energy barrier of the rate determining step (methoxy dehydrogenation) is significantly reduced. Additionally, Cu^{+} decreased the self-activation response time of the catalyst.

Zirconia plays a vital role in enhancing the performance and stability of Cu-based catalysts by increasing the metal dispersion, increasing stability, and inhibiting sintering and carbon deposition. ZrO_2 offers a stable and high surface-area support structure, which promotes the even dispersion of Cu particles. The sintering of Cu particles is also impeded by zirconia due to its ability to establish a solid anchoring surface through strong metal-support interactions [199]. For instance, Chen et al. [212] observed the formation of interfacial sites between Cu^{0}/Cu^{+}-ZrO_xH_y when ZrO_2 was introduced as a promoter. The reaction mechanism described in this study proposed the promotion of methanol and intermediate degradation by Cu^{0}/Cu^{+} species. Additionally, the Cu^{0}/Cu^{+}-ZrO_xH_y interface sites play a crucial role in the constant availability of –OH groups by steam activation by hydroxylated Zr species. The combined effects facilitated the oxidation of intermediate compounds and the water-gas shift reaction, leading to increased production of hydrogen and carbon dioxide. A similar study performed by Ritzkopf et al. [213] also demonstrated the formation of less CO in CuO/ZrO_2-based catalyst compared to the commercial CuO/ZnO/Al_2O_3 catalyst. The study conducted by Jeong et al. [214] examined the performance of three catalysts, namely Cu/ZnO, Cu/ZnO/Al_2O_3, and Cu/ZnO/ZrO_2/Al_2O_3. The authors observed that the Cu/ZnO/ZrO_2/Al_2O_3 catalyst exhibited a 16% higher methanol conversion rate while exhibiting a 7.3 times lower proportion of CO in the product gas. This behavior was attributed to the presence of a ZrO_2 promoter which is responsible for the better dispersion of Cu within the catalyst. The incorporation of zirconia into Cu-based catalysts facilitates the alteration of their surface characteristics, including acidity, basicity, and redox properties. ZrO_2 modifies the electronic configuration and surface properties of Cu active sites, hence affecting the reaction mechanism and kinetics. In addition, ZrO_2 has improved surface oxygen mobility and activation, which aids in the adsorption and activation of methanol and water molecules during MSR. For example, the influence of ZrO_2

structure support, specifically monoclinic and cubic was examined by Azenha et al. [152] The Cu-Pd/ZrO_2-monoclinic catalyst exhibited much higher activity and selectivity compared to the Cu-Pd/ZrO_2-cubic catalyst, owing to an improved dispersion of the metal phase. Furthermore, the incorporation of zirconia into the standard CuO/ZnO/Al_2O_3 catalyst resulted in enhanced stability. This improvement is possibly due to the availability of surface oxygen sites on zirconia clusters, which enhances their ability to adsorb methanol.

Ceria demonstrates a positive influence on copper-based catalysts, leading to increased methanol conversion, reduced CO production, and enhanced stability. CeO_2 possesses a distinctive ability to retain oxygen. The fluorite cubic structure of CeO_2 facilitates the migration of oxygen ions toward the surface even under low-temperature conditions. The oxidation state of cerium in cerium oxide exhibits oscillatory behavior between Ce^{4+} and Ce^{3+}. Consequently, the surface of the catalyst is susceptible to surface imperfections, thereby facilitating the storage and supply of oxygen. Consequently, the use of CeO_2 facilitates the WGS reaction thereby reducing the concentration of CO in the reforming gas. In a reducing environment such as SRM, the catalyst undergoes partial reduction of ceria, resulting in the formation of oxygen-containing sites. These oxygen-forming sites then react with carbon, facilitating the gasification of coke instead of its deposition. The presence of ceria facilitates the cleavage of C-H bonds and the formation of intermediate species, promoting steam reforming. Furthermore, the addition of CeO_2 to ZrO_2 results in a solid solution of CeO_2–ZrO_2, which exhibits surface methanol dehydrogenation capabilities and a greater capacity for oxygen storage compared to CeO_2 [147,215]. In a study conducted by Patel et al. [145], it was observed that Cu-Zn-Ce-Al-oxide catalysts, when supported by cerium, exhibited enhanced catalytic activity and hydrogen selectivity, while effectively reducing CO within the reformate gas. The Cu-Zn-Ce-Al oxide catalyst exhibited stable performance over a long period, demonstrating no decline in activity in comparison to catalysts promoted with zinc. Yang et al. [216] investigated the effect of ceria morphology on the catalyst performance for MSR. Nano-rod, nano-particle, and sponginess of ceria samples are compared, amongst them the nanorod exhibited the most elevated concentration of surface Ce^{3+} and active species Cu^{+}, hence enhancing its surface reducibility and overall activity. Ceria is also believed to enhance thermal stability and exhibit resistance to sintering.

In addition to the extensively reported ZnO, ZrO_2, and CeO_2 oxides, researchers have also explored the utilization of Ga, Mg, Sc, Y, In, Fe, Ti, La, Gd, and Sm oxides as promoters to enhance the catalytic activity. Toyir et al. [200] reported that the addition of Ga to Cu/ZnO

catalysts enhanced the methanol conversion and hydrogen yield. Almost 100% methanol conversion was achieved at 593 K. This behavior was mostly due to the large number of active copper clusters which resulted in increased methanol conversion at low temperatures. Another study by Tong et al. [217] over the mixed oxide $CuZnGaO_x$ catalyst revealed no CO formation till 323 K and almost complete conversion at 493 K. By introducing Ga^{3+} into $CuZnO_x$, the physical surface areas of Cu can be significantly increased as a result of the formation of a non-stoichiometric cubic spinel structure. Zhang et al. [218] reported that the $CuFeMg/Al_2O_3$ catalyst demonstrated a 2.5-fold enhancement in H_2 production when compared to a commercially available catalyst. The catalyst exhibited stable performance for 200 hours and sustained a methanol conversion rate of 85%. In addition, the catalyst demonstrated a reduced start-up time of only 18 minutes, which is considerably 1–2 hours required for activating Cu-based catalysts. The incorporation of Fe resulted in greater dispersion of Cu, reduced particle agglomeration, and improved adsorption and activation of H_2O. Pu et al. [205] examined the role of Sc in Cu/Sc_2O_3-ZnO catalysts, where they observed that incorporating Sc^{3+} doping into the ZnO lattice enhanced the interaction between Cu and the support, leading to improved dispersion of the metal and increased resistance to sintering of Cu. However, the presence of Sc favored the formation of CO as a result of RWGS reaction in the temperature range of 573 K to 873 K. Further study conducted by Matsumura [202] regarding the effect of Y_2O_3 in the $Cu/ZnO/ZrO_2/In_2O_3$, revealed that the presence of Y_2O_3 increased the number of Cu particle on the surface of the catalyst i.e. better metal dispersion. Nevertheless, the coprecipitated particles undergo gradual agglomeration during the reaction, primarily at a temperature of 773 K. As a result, the activity of the reaction approaches that of the reaction without yttrium oxide, mostly due to the reduction in the quantity of Cu surface area. The effect of Ti as a promoter was investigated by Zhao et al. [204], where they optimized the catalyst composition to $CuTi_{1.9}/\gamma$-Al_2O_3/Al which achieved nearly 100% conversion at 548 K. The simultaneous presence of Ti^{4+} and Ti^{3+} facilitates the transfer of charge between Cu and Ti, hence enhancing the redox efficiency of copper. The density functional theory (DFT) simulations demonstrate that titanium also augments the adsorption capacity of water and methanol on the catalysts' surface. Additionally, the presence of Ti in catalysts can effectively decrease the acid sites by diminishing the quantity of hydroxyl groups. Consequently, this reduction in the occurrence of side reactions, such as methanol dehydration, proves advantageous in diminishing the selectivity towards dimethyl ether and enhancing the production of hydrogen. Therefore, the incorporation of promoters into catalyst formulations offers significant potential for optimizing

hydrogen production processes and advancing the development of efficient and sustainable catalytic systems for MSR.

2.2.6.2. Other Group VIII to XII-based Catalyst

In addition to copper, several metals from Group VIII to XII, such as Ni, Pd, Pt, Fe, Ru, and Au, are utilized as active metals in MSR, particularly at lower temperatures. In the context of steam reforming methanol, catalysts composed of metals in Groups VIII–XII demonstrate inadequate selectivity, while the reaction proceeds with remarkable selectivity on copper catalysts. Methanol is decomposed to CO and H_2 over Group VIII–XII metal catalysts except for Pd-based catalysts, where the reaction mechanism is similar to copper-based catalysts, whereas it is dehydrogenated to $HCOOCH_3$ over copper catalysts [219,220]. The variation in the reactivity of formaldehyde was identified as the cause of this distinction in the reaction mechanism. When formaldehyde was exposed to water, palladium alloy-based catalysts converted it to CO_2 and H_2O; conversely, palladium-based catalysts decomposed formaldehyde back into CO and H_2O [184]. In addition, Ranganathan et al. [221] hypothesized that the support material influences the behavior of the catalyst. According to their findings, acidic environments facilitate progress through the formation of HCOOH, whereas basic environments do so through the decomposition of HCHO. However, in the case of Ni-based catalysts, Takezawa et al. [184] proposed a different reaction mechanism route for methanol decomposition. This behavior was attributed to the strong electron back donation from the metals to πCO* antibonding orbital of the HCHO, as a result of which C–H bonds break and the HCHO adsorbed over the catalyst through C and O immediately decompose to CO and H_2 without reacting with nucleophiles to form CO_2. Pd-based and Ni-based catalysts are the most studied catalysts after Cu-based catalysts.

The extraordinary activity and selectivity of Pd supported on ZnO for CO_2 and H_2 was initially reported by Iwasa et al. [219]. They examined the effect of several catalytic supports, such as SiO_2, La_2O_3, Nb_2O_5, Nd_2O_3, ZnO, Al_2O_3, and ZrO_2, which had a substantial influence on the performance of the catalyst. The experiment revealed that palladium when supported on ZnO, had the highest selectivity for carbon dioxide in the context of MSR. Additionally, the Pd catalyst without support exhibited a significant degree of selectivity towards the decomposition reaction, while ZnO by itself did not exhibit any reaction [219,220,222,223]. The catalytic performance of Pd/ZnO is enhanced by the development of a Pd–Zn alloy. Additionally, it is necessary to subject Pd/ZnO catalysts to a reduction in the H_2 atmosphere at temperatures exceeding 573 K. When the reduction temperature is increased, a Pd nanoparticle combines

with Zn to form an alloy, which allows the catalyst to be stable across a wide range of temperatures during operation [224]. In their further investigation, high catalytic activity favoring steam reforming was observed for the Pt/ZnO-based catalyst, which was again attributed to the formation of Pd-ZnO alloy. However, ZnO-supported Ni, Co, Ru, and Ir actually favored methanol decomposition [219]. Chin et al. [225] found that the degree of mixing between Zn^{2+} and Pd^{2+} cations had a substantial impact on the production of Pd-Zn alloy, which in turn affected the catalytic activity. Liu et al. [226] in their study found that a high Pd loading is essential to achieve a more active, selective, and stable catalyst. Conant et al. [227] found that the $Pd/ZnO/Al_2O_3$ catalyst for MSR has greater activity and stability in comparison to the commercially available $Cu/ZnO/Al_2O_3$ catalyst. Ranganathan et al. [221] conducted a comparison between Pd/ZnO and Pd/CeO_2 catalysts. They revealed that Pd/ZnO catalysts promoted the production of CO_2 due to the presence of more acidic sites. On the other hand, Pd/CeO_2 catalysts favored the synthesis of CO due to the higher concentration of basic sites. In addition to this, Pd/ZnO-based catalysts are more prone to catalyst deactivation. The deactivation process is proposed to occur through two primary mechanisms: carbon deposition and oxidation of the Pd−Zn alloy.

Nickel, being among the least expensive metals in its category, is the subject of extensive research regarding MSR. Nickel-based catalysts are commonly employed due to their increased surface area, excellent dispersion, and reduced particle size. The different supports employed for catalysts modify the physicochemical properties and the efficacy of the catalyst. For instance, Lu et al. [206] observed that the metal-support interaction and low-temperature reduction were essential variables in determining the catalytic activity in the context of a La-loaded Ni-based catalyst, rather than the overall surface area. Upon analyzing the impact of adding La to Ni-based catalysts with various supports, it was shown that the addition of La resulted in a drop in CO selectivity and an increase in H_2 selectivity, following a certain order. The order of reactivity is as follows: $10La–10Ni/Al_2O_3 > 10La–10Ni/SiO_2 > 10La–10Ni/MgO$. Another study by Lu et al. [228] showed that the addition of Praseodymium oxide (Pr_6O_{11}) enhanced the catalytic activity even at low temperatures. Pr_6O_{11} decreased the contact between Ni and the support, resulting in the stabilization of the Ni^0/NiO structure and the formation of a robust geometrical and electrical interaction, thereby reducing the risk of Ni particles. Khzouz et al. [229] studied the effect of the addition of Ni in Cu-based catalysts. Ni eventually led to an increase in the CO selectivity and decreased coke formation. They compared the $5\%Ni–5\%Cu/Al_2O_3$, Ni/Al_2O_3 and $Cu/ZnO/Al_2O_3$ catalysts for MSR. The addition of Ni increased the

Cu dispersion over the support which resulted in the enhanced WGS reaction, thereby reducing the CO formation. Moreover, a reduction in the coke formation is observed in the Ni–Cu/Al_2O_3 catalyst. The reason for this behavior was ascribed to the formation of Ni-Cu alloy. At 598 K a methanol conversion of 99% and H_2 selectivity of 89% were reported for Ni–Cu/Al_2O_3 compared to the 99% methanol conversion and 86% H_2 selectivity for Cu/ZnO/Al_2O_3. Another study performed by Khzouz et al. [230] showed that increasing the Ni content from 3 wt% to 7 wt% in Ni–Cu/Al_2O_3 decreased the methanol conversion, H_2 selectivity, and CO_2 selectivity, but increased the CO selectivity at the same time. This behavior was attributed to the direct methanol decomposition in the presence of the Ni-Cu bimetallic phase. In addition to this, the WGS reaction equilibrium shifts toward the RWGS reaction resulting in the formation of more CO, particularly at the copper active phase.

Liu et al. [231] investigated the performance of Pt (1 wt. %)/In_2O_3 (3 wt. %)/MO_x in the temperature range of 523 K to 673 K. The catalyst achieved a conversion rate of around 98.7%, with a CO selectivity of 2.6%. Shanmugam et al. [232] evaluated the effect of CeO_2, Al_2O_3, ZrO_2, and In_2O_3 as supports for Pt catalysts in the context of MSR. The supports CeO_2, Al_2O_3, and ZrO_2 were prepared using the sol-gel process, whereas In_2O_3 was doped prior to the addition of Pt using the wet impregnation technique. The presence of In_2O_3 enhanced both the dispersion and concentration of Pt on the support material. The catalyst containing 15 wt. % of Pt on cerium dioxide (Pt/CeO_2) showed the most effective catalytic performance, achieving full conversion of methanol. However, it also resulted in a high concentration of carbon monoxide, which was subsequently lowered upon the introduction of In_2O_3. The decreased specificity for carbon monoxide was ascribed to the formation of more oxygen vacancies caused by a smaller particle size, as well as a more dispersed distribution of platinum. The CeO_2-supported Pt/In_2O_3 catalyst demonstrated superior stability compared to other catalysts, with the lowest CO selectivity during steam reforming for a duration of up to 100 hours. The significant connection between Pt and In_2O_3 resulted in a synergistic impact that played an important part in activating H_2O effectively. This interaction reduced the CO selectivity and improved the long-term stability of the catalysts. Shtyka et al. investigated the catalytic efficacy of Ru, Au, and Pt catalysts based on carbon nanotubes (CNTs). Prior to testing, the CNTs underwent functionalization in a solution of acidified potassium permanganate. The methanol conversion showed a significant increase of 26-fold when using the 2%Ru/CNT-$KMnO_4$ catalyst at a temperature of 533 K. In comparison, the Au-based catalyst demonstrated improvements of 4.4-fold at 523 K and 4.8-fold at 573 K. In addition, the catalyst based on Ru

exhibited the lowest selectivity towards CO compared to the other catalysts. Catalysts based on metals of the 8-10 group have been acknowledged for their exceptional thermal and long-term durability. The catalysts based on noble metals such as platinum and palladium exhibit exceptional performance. However, their prohibitively expensive cost prevents their widespread usage in commercial applications. Efforts have been concentrated on lowering the amount of noble metal used in the catalyst while simultaneously improving methanol conversion and hydrogen selectivity. While Pd alloy catalysts serve as a viable substitute, there is still room for improvement in their level of activity. Certain benefits of the 8–10 group catalysts, such as heat stability and stability over time, might be emphasized in comparison to copper-based catalysts. Ultimately, future investigations in this field should prioritize addressing these issues to ensure that methanol becomes a viable hydrogen carrier.

2.2.6.3. Nanomaterial based Catalyst

Nanomaterial-based catalysts are superior to conventional catalysts because of their improved catalytic activity, stability, and CO selectivity. The synergetic integration of nanotechnology with catalyst preparation methodology can improve catalyst performance. The biggest advantage of the nanomaterial-based catalyst is its exceptionally high surface area, which is a crucial factor in choosing MSR catalysts [192]. For instance, Valdes-Solis et al. [167] prepared a nano-catalyst using nano-casting techniques for H_2 production via MSR. A series of catalysts were prepared where $CuMn_2O_4$ and CuO/CeO_2 catalysts showed the best activity with BET surface area of 144 m^2 g^{-1} and 153 m^2 g^{-1} respectively. Mierczynski et al. [233] synthesized the bimetallic Au-Cu and Au-Ni-based MSR catalyst on the multi-walled carbon nanotube (MWCNTs) using the wet impregnation technique where Au was introduced on monometallic copper or nickel catalyst surface by deposition–precipitation method. Au-Cu/MWCNTs and Au-Ni/MWCNTs exhibited a very high BET surface area of 272 m^2 g^{-1} and 311 m^2 g^{-1} respectively. Another study by Lytkina et al. [234] reported extremely high BET surface areas for bimetallic (Ru–Rh, Ni–Cu) catalysts synthesized on a surface of different carbon supports: detonation nano-diamonds (DND), infrared pyrolyzed polyacrylonitrile (PAN), carbon black Vulcan-XC-72. An exceptionally high surface area of 289 m^2 g^{-1}, 230 m^2 g^{-1}, 206 m^2 g^{-1}, and 1600 m^2 g^{-1} were observed for Ru-Rh/DND, Ni-Cu/DND, Ru-Rh/Vulcan, and Ru-Rh/PAN respectively. Recently Tajrishi et al. [235] prepared different Cu/SBA-15-based nano-catalysts using the wet impregnation method for MSR. Multiple catalysts including Cu/ZnO/SBA-15, $Cu/ZnO/CeO_2$/SBA-15, $Cu/ZnO/ZrO_2$/SBA-15, and $Cu/ZnO/CeO_2/ZrO_2$/SBA-15 were synthesized with BET surface area of 463.7 m^2 g^{-1}, 441.7 m^2 g^{-1}, 498.7 m^2 g^{-1}, 557.3 m^2 g^{-1},

523.6 m^2 g^{-1} accordingly. Mostly the metal particle is doped over the different nanoscale support materials with high surface area and thermal stability, serving as effective supports for metal nanoparticles. However, nanomaterial-based catalysts are currently in the early stage of development and are gaining attention due to their exceptional performance. Nano-catalysts need intricate synthesis techniques and come with a high cost to exhibit exceptional performance. A long milestone needs to be achieved for catalyst modification technology to reduce the cost and simplicity of manufacturing processes in order to facilitate the large-scale generation of high-purity hydrogen. It is important to mention that although catalysts based on noble metals exhibit excellent performance, their high cost renders large-scale commercial usage impractical. Moreover, the issue of catalyst deactivation and sintering continues to remain a major challenge. As a result, the focus has always been concentrated on enhancing the activity of copper-based catalysts.

2.2.6.4. Various Structured Catalyst

Three-dimensional (3D) structured catalysts provide benefits compared to conventional catalyst forms because of their superior mass and heat transfer capacities, enhanced mechanical strength, and increased catalytic efficiency. Although the field of 3D structured catalysts for MSR is still in its early stages, there have been notable breakthroughs in this domain. For instance, the use of structured support materials with large surface areas and porosity, such as foams, monoliths, and honeycombs, serves as a framework/scaffold for catalyst deposition and facilitates uniform dispersion of active catalytic particles [192]. Developing catalysts with organized pore networks at multiple levels to enhance the mass transfer and the diffusion of reactants. The presence of hierarchical pore architectures enhances the accessibility of reactant molecules to active sites and improves the functionality of the catalyst in MSR. Additionally, the utilization of 3D structured catalysts, such as interconnected networks, fractal-like structures, or specifically designed shapes, aids in enhancing the dispersion of flow, reducing pressure loss, and maximizing the catalytic surface area [170]. Nevertheless, to fully exploit the advantages of 3D structured catalysts in MSR applications, it is imperative to conduct research and innovation in the areas of materials design, deposition processes, and reactor engineering. These structured catalysts are an attractive choice for compact reactor systems for hydrogen production such as membrane reactors. Metallic 3D structures are susceptible to corrosion and thermal expansion when exposed to reaction conditions for an extended duration. Hence, ceramic materials with excellent chemical stability, a low coefficient of thermal expansion, low cost, and strong corrosion resistance are considered highly promising for use

as catalyst supports [236]. Liao et al. [237] developed a porous SiC ceramic material that has a hierarchical structure consisting of pores within pores. This material serves as a support for a catalyst, which is coated with a porous layer made of $CuO/ZnO/CeO_2/ZrO_2$. They successfully achieved a methanol conversion rate of 100% at a temperature of 553 K and were able to sustain a consistent conversion rate of 95% even after 30 hours of reaction time. Zhou et al. [238] prepared a Cu/Zn/Al/Zr-based catalyst supported over Cu foam (100 pores per inch) and compared its performance with a Ni foam-based catalyst. It was observed that the Cu-foam performed better than Ni foam in a microreactor. In addition to porosity and gradient, the cascading structure, having no clearance but a broader width at the inlet and a narrower width at the outlet, demonstrated superior performance in terms of hydrogen production, methanol conversion (80%), and stability (10 hours). Wang et al. [236] prepared four different pore size regular shaped porous SiC scaffolds. It was noted that the SiC structure catalyst support with narrower pore size exhibited the maximum hydrogen production rate, albeit had unsatisfactory fluid flow properties. Falco et al. [239] performed the experimental analysis of steam reforming of natural gas over $Rh\text{-}Pt/Al_2O_3$ coated SiC foam-based catalyst. The study was conducted for almost 1000 operating hours with a heating/cooling cycle above 70 cycles. They achieved a conversion of 57.3% which is 26% more than the same traditional reformer at 873 K. SiC foam helped to improve the thermal transport property of the catalyst bed. Patrascu and Sheintuch et al. [193] used Pt(3 wt. %)Ni(10 wt. %)/CeO_2 catalyst coated over SiC foam scaffold (30 PPI and 85% porosity) in a Pd-Ag membrane-based membrane reactor. One dimensional mathematical model was used to predict the performance of the membrane reactor, temperature profile, gas composition, and permeate flow rate. Giaconia et al. [194] coated the Ni(10 wt. %)Pt (3 wt. %)/$CeZrLaO_x$ over SiC foam-based monolith using wash coating methods. The characteristics in terms of void fraction, size, and surface properties were optimized to achieve high conversion. The catalyst and membrane were then assembled inside the molten salt ($NaNO_3/KNO_3$ liquid mixture (60/40 w/w) heated pilot scale membrane reformer having ten distinct chambers. More than 60% of methane conversion was observed at 823 K with less than 10 ppm CO on the permeated side. Recently Yan and Cheng [195] investigated the performance of the 2.0 wt. % Ru/α-Al_2O_3 catalyst wash coated over the 3D SiC continuous skeleton in a membrane reactor. They observed that the membrane reactor with SiC-foam significantly improved the radial heat and mass transfer compared to the same traditional packed bed reactor. An increase of 293 K in the temperature was seen along with a high H_2 concentration near the membrane surface. Moreover, they were able to save more than 78% of the catalyst while achieving almost 100% catalyst utilization efficiency.

Hence, to optimize the reactor's efficiency, it is crucial to build it in a manner that significantly enhances radial heat and mass flow, while also ensuring the system remains compact. This is particularly important for endothermic reactions when scaling up in a membrane reactor system, as catalytic reaction and membrane separation are extremely sensitive to temperature. Furthermore, a significant percentage of the overall cost is attributed to the catalyst and reactor design. In order to establish a balance in the cost, it is crucial to ensure efficient catalyst utilization and well-designed reactors while simultaneously producing hydrogen at different scales. Therefore, it is both valuable and essential to investigate the capabilities of solid foam in membrane reactors and ultimately address the current challenges.

2.3. Literature Review on Membrane Reformer for MSR

This section provides a comprehensive assessment of the existing literature on palladium-based membrane reactors used in the process of methanol steam reforming. Firstly, a detailed review of the latest developments in the reactor related to the MSR is examined to determine the current obstacles and research opportunities. Various reactor systems are analyzed to determine the most practical reactor design and innovations for improving the overall efficiency of the entire system. Additionally, the use of MSR in the Pd-based membrane reactor is outlined to establish a synergy between the process condition for the reaction and separation. Furthermore, the literature review is specifically centered on the effective integration of the membrane with the catalyst to improve hydrogen recovery. Finally, a techno-economic analysis of the membrane reactor MSR is conducted to determine the viability and potential of this current technology.

2.3.1. Recent Advancements in Reactors for MSR

The traditional tubular packed bed reactor architecture is extensively utilized in MSR for hydrogen production because of its simplicity, cost-effectiveness, repeatability, and well-established understanding of catalyst functioning. The effectiveness of a packed bed reactor is influenced by numerous variables, including the temperature variation inside the reactor, pressure gradient, heat distribution, reactor design, and the feed flow rate [145,173,240]. Nevertheless, packed bed reactors have encountered numerous difficulties during operations, particularly when handling endothermic reactions. These challenges encompass a significant decrease in pressure, proper design of the reactor geometry, as well as unfavorable heat transfer properties, including both axial and radial temperature variations across the catalyst bed [241,242]. Reducing the size of the reactor often leads to lower temperature differences,

although it is noted that there is a significant increase in pressure drop within the catalyst bed. Therefore reactor geometry and size play a critical role in determining the performance of the catalyst. For example, Peng et al. [243] examined the effect of geometrical construction on the performance of the catalyst. Their result illustrated that reducing the diameter-to-length ratio and increasing the thickness of the catalyst bed increased both methanol conversion and H_2 production. The maximum methanol conversion of 85.49% and H_2 concentration of 48% (wet base) was achieved at 573 K when the catalyst bed thickness of 15 mm and a diameter-to-length ratio of 0.08 was maintained. Also increasing the fuel temperatures at the inlet of the catalyst bed helped to increase the H_2 production, resulting in an H_2 concentration of 55% (wet base) at an inlet temperature of 413 K. Moreover, the methanol conversion can be greatly enhanced by introducing a heated rod into the center of the catalyst bed, as demonstrated by Nehe et al. [244]. In another study, Shi et al. [245] demonstrated the effect of reactor length and space velocity on methanol conversion. Increasing the space velocity, the methanol conversion increased by 4% at the outlet of the reactor. In the 80 mm long reactor, following the 30 mm long entrance section, the degree of methanol conversion dropped due to a sudden decrease in temperature. Moreover, it became increasingly evident that the reaction predominantly takes place in the central region of the reactor, rather than along the reactor wall. Catalyst utilization along the reactor wall is poor compared to the center of the reactor. In order to enhance the uniformity of the temperature inside the reactor Zhang et al. [246] analyzed the simultaneous heating system from both sides of the reactor i.e. internally and externally. To achieve internal heating the helical fins surrounding an interior heating pipe were designed and simulated using a 3D model. It was observed that the helical fins surrounding an interior heating pipe improved the temperature uniformity by 48.9% across the catalyst bed. Helical fins helped to improve the convective heat transfer as well as the reactant distribution across the reactor. Chein et al. [247] designed another type of reactor consisting of the liquid methanol/water vaporizer, methanol/steam reformer, and methanol/air combustor in a single unit, similar to the tube-and-shell heat exchanger. The numerical simulation demonstrated that the reactor design with the combustor positioned as the shell side demonstrates superior performance compared to the reactor design with the combustor as the tube side, due to the more efficient heat transfer characteristics in the vaporizer, while maintained under same conditions. The reactor can be initiated at ambient temperature by providing a sufficient flow rate of methanol/air in the the combustion chamber, relative to the flow rate of methanol/water in the reformer chamber. Despite the proposal of different structural and design modifications for packed-bed reactors, certain limitations continue to exist. Some of the challenges include

elevated operating temperatures, uneven temperature distribution, cold spots, and substantial pressure reduction. Non-uniform flow distribution within the packed bed can result in channeling, characterized by the formation of preferential flow pathways, which diminishes the interaction between the reactants and catalyst. This can lead to an inconsistent conversion and inequitable distribution of temperature. Packed bed reactors, despite its favorable surface area-to-volume ratio, are susceptible to challenges in terms of heat and mass transfer, especially when dealing with high reactant concentrations or reaction rate. Scaling up packed bed reactors by extending the reactor diameter or length may present additional issues in terms of heat and mass transfer, flow distribution, and pressure drop management. Thorough planning and fine-tuning are necessary to guarantee a successful increase in size or capacity. In order to overcome these issues, it is necessary to implement techniques and developments in reactor design, materials, and process control. Therefore, researchers are increasingly investigating alternatives to conventional fixed-bed reactors in order to address these challenges. In this regard microchannel or micro-reactors are proposed to achieve enhanced reactor performance.

In order to address the difficulties associated with packed-bed reactors, scientists have suggested the use of a fluidized bed reactor (FBR), which presents various benefits including effective heat transmission, even temperature distribution, a large surface-to-volume ratio, and extended contact time [248]. The process of fluidizing the particles guarantees a comprehensive intermixing of the reactants, resulting in more consistent concentration profiles. When comparing packed bed reactors to FBR, it is often observed that FBRs have a lower pressure drop. This characteristic can lead to reduced energy consumption and operational expenses. Consequently, an FBR can provide enhanced reactor efficiency in comparison to a packed bed reactor. Additionally, the MSR reaction exhibits fast reaction kinetics, necessitating the employment of small catalyst particles to minimize internal mass transfer restrictions in FBR [249,250]. For instance, Shi et al. [248] compared the performance of FBR and packed bed reactors for MSR using $Cu/ZnO/Al_2O_3$. They observed that the methanol conversion for FBR was 20% higher compared to the packed bed at 623 K due to the even temperature distribution, a large surface-to-volume ratio, and extended contact time. Zhang et al. [250] utilized the dual rate kinetics model to analyze the reaction kinetics of MSR in FBR, utilizing experimental data. It was noted that the reaction rate per unit mass of the catalyst depends on the partial pressure of the components. Furthermore, the activation energy required for steam reforming was greater than that for the decomposition reaction. This can account for the prior finding that the selectivity of CO_2 dropped as the temperature increased. Nevertheless, the FBR has certain

drawbacks, such as the gradual erosion of the reactor wall and the creation of small particles through attrition, which could potentially impact the fluidization process and overall effectiveness. Gas-solid reactions are more efficient when using fluidized beds, but liquid-phase reactions face difficulties in maintaining good fluidization, making them less suitable for this type of reaction. Furthermore, ensuring consistent isothermal conditions throughout the reactor can be difficult, particularly in large-scale operations. To overcome some of the challenges of packed bed and fluidized bed reactors attempts have been made in the design of microchannel reactors that offer more flexibility compared to the aforementioned reactor system.

Microchannel reactors are reactors that employ small-scale channels, usually with dimensions in the micrometer range (often less than 1 mm in width), for conducting chemical reactions. Microchannel reactors have numerous benefits compared to packed-bed reactors as a result of their distinctive design and operational principles. The channels' narrow dimensions yield excellent surface area-to-volume ratios, enabling swift heat and mass transfer and precise regulation of reaction conditions [251]. As a result, accelerated reaction kinetics, increased conversion rates, and higher product selectivity can be achieved. Furthermore, microchannel reactors possess a compact and lightweight structure, rendering them appropriate for portable or space-limited applications. Microchannel reactors, despite being small, can achieve high throughput due to their ability to process large amounts of reactants, thereby high H_2 yield [142,173]. Most of the previous studies primarily focused on the structure of microchannels, fabrication techniques, catalyst support, and integrated design. For instance, Pan et al. [252] investigated the microchannel structure and distribution for MSR. The microchannel structure with equal distribution in the Left-Right direction (ELR) and a rectangular cross-section exhibited superior reaction performance in MSR compared to all other examined microchannel structures, regardless of whether they had a rectangular or tooth cross-section. Du et al. [253] in their study found that the non-parallel microchannels exhibit superior capabilities in terms of uniform feed flow and temperature distribution compared to the parallel microchannels, thereby showing enhanced performance for MSR. In addition to the fabrication of microchannels, research has been conducted on integrated design and catalyst support to enhance the performance of MSR in microreactors. For example, Won et al. [254] designed a microchannel reactor integrated with a combustor. They utilized a commercial $Cu/ZnO/Al_2O_3$ catalyst for the MSR and a Pt/ZrO_2 catalyst for the combustion of methanol. They attained a hydrogen flow rate of 3.9 L h^{-1} at a temperature of 543 K and a feed flow rate of 3.65 ml h^{-1}.

In another study, Chein et al. [255] designed a microchannel reactor for MSR combining a vaporizer, combustor, and steam reformer into a single unit. Three distinct microchannels including patterned microchannel, single plain channel, and inserted stainless mesh layer were examined and it was observed that the patterned microchannel had the best performance. Wang et al. [256] fabricated a microreactor using a SiC honeycomb structure with an additional combustion chamber loaded with Pt/Al_2O_3 catalyst. In just 9 minutes, the reaction chamber achieved the optimum operating temperature for MSR due to the exceptional thermal conductivity of SiC, which facilitated efficient heat transfer from the combustion chamber to the reaction chamber. Their findings, derived from the 3D numerical model, demonstrated improved heat transfer and fluid flow properties, along with a notable reduction in pressure drop and a more evenly distributed temperature within the SiC honeycomb support. Nevertheless, the process of designing microchannel reactors with accurate geometries and dimensions can be intricate and expensive, particularly for manufacturing on a commercial scale. Fouling is a common issue in microchannels because of their small size and large surface area-to-volume ratio. Contaminants or reaction by-products can cause fouling, which can block flow channels, decrease reactor performance, and require frequent cleaning or maintenance.

In all the previously discussed reactor designs for methanol steam reforming, it is necessary to further purify the reformatted gas to remove hydrogen from the gas mixture. Consequently, the entire process necessitates the use of a distinct separation unit, resulting in high energy consumption and significant expenses. In order to address this problem, membrane reformers have been developed to combine the processes of reforming and separation within a single unit. This improvement not only eliminates the need for an additional separation device but also renders the entire system compact and portable. Furthermore, the concurrent extraction of hydrogen promotes the progression of the reaction towards the desired product in accordance with Le Chatelier's principle. Selectively removing H_2 from mixtures of gas shifts the thermodynamic equilibrium in favor of the product side, allowing for a high conversion rate to be achieved at a lower temperature. Indeed several attempts have been made to reduce the level of CO content in MSR reactions by modifying the catalyst composition and optimizing the process condition but they are still not able to ensure a consistent CO-free H_2 supply.

2.3.2. MSR in Palladium-based Membrane Reformer

An important limitation of the MSR reaction is the production of CO at high temperatures. It is crucial to minimize the generation of CO because it can have a negative impact on the performance of the anodic catalyst in PEMFCs and the H_2 permeability of the Pd-based

membrane. Hence, it is imperative to minimize the generation of CO not only during the reforming reaction but also during the separation process using membranes. On one hand, the temperature increase enhances both the catalytic activity and membrane performance, whereas it also leads to an increase in the formation of CO at elevated temperatures as well as a reduced catalyst-specific activity because of coking. The conflicting behavior of MSR and hydrogen separation poses a significant challenge to their integration into a single device [257]. In a study conducted by Israni and Harold [258], it was discovered that the presence of CO_x and CH_3OH has a substantial impact on reducing the H_2 flux of a single-fiber Pd-Ag (3.9 μm) membrane reactor. This reduction is attributed to the surface adsorption effect. Under the working conditions of 523 K and 1000 kPa, they successfully achieved complete conversion of methanol, with a hydrogen recovery rate of 95% and a hydrogen purity of almost 100% in the permeate. Moreover, their computational simulation data was also in agreement with the experimental data. Therefore, it is imperative to thoroughly examine the performance of the membrane reactor to optimize the entire process condition and achieve maximum efficiency. In a recent study, Iulianelli et al. [175] conducted a comparison of data on MSR between a membrane reformer and a traditional catalytic reactor. The authors found that the majority of methanol conversions exceeding 50% reported for the membrane reformer fell within the temperature range of 473 K to 573 K. However, the majority of methanol conversions in catalytic reactors exceeding 50% have been found within the temperature range of 573 K to 673 K. In regards to the cost of hydrogen generation, Kim et al. [259] discovered in their study that the cost of producing hydrogen using a packed bed reactor is $9.37 per kg of H_2, whereas using a membrane reactor costs $7.24 per kg of H_2. This represents a cost saving of around 23%. In order to determine the effect of temperature, pressure, sweep gas, and steam-to-carbon ratio, Saidi [260] performed the simulation study using a two-dimensional non-isothermal stationary model on MSR using the commercial $Cu/ZnO/Al_2O_3$ catalyst and Pd-Ag membrane. They observed that the selective removal of H_2 shifted the reaction equilibrium toward the H_2, thereby increasing the methanol conversion and higher H_2 production. Their findings indicate that the generation of H_2 is more favorable at elevated temperatures and pressures and with increased amounts of sweep gas and steam-to-carbon ratio. Moreover, membranes with high H_2 permeability help to recover more hydrogen from the mixture of gas and consequently improve the methanol conversion rate. Recently Sharma et al. [261] compared the performance of the membrane reactor and reformer combined with the separator in a series. Efficient operation of the entire system necessitates meticulous optimization of the pressure, temperature, and feed flow rate, as there is no need for any subsequent gas processing. On the

other hand, when a reforming reactor is paired with a membrane separator in series, it allows for the ability to operate both systems under separate process conditions. Nevertheless, the need for distinct separation units results in an expansion of the system's size and consequently, an escalation in the total expenses. Fortunately, their research demonstrated that operating the reactor and separator separately can greatly decrease the inhibition of the membrane caused by CO and steam at the ideal temperature of 673 K and pressure of 300 kPaG. Liguori et al. [262] experimentally determined the performance of the composite Pd membrane (7 μm) supported over Al_2O_3 for MSR using a commercial Cu/Zn-based catalyst. They achieved a high-grade permeate purity of H_2 suitable for PEMFCs having CO content less than 10 ppm at 603 K and 250 kPa. At a space velocity of 18500 h^{-1}, they obtained a methanol conversion of 85% with H_2 recovery of 40% and H_2 yield 80%. Additionally, the Pd-membrane demonstrated sustained performance for up to 1000 hours. However, its ideal perm-selectivity was considerably diminished due to repeated thermal heat cycles. Prior to the process, the ideal selectivity for H_2/N_2 was 6000 which reduced to 4300 after 1000 hours of testing. This was ascribed to the occurrence of defects and the creation of pinholes resulting from the expansion of the lattice during the test.

The current progress of MSR reactors falls short of meeting the requirements for industrialization. The majority of reformers are constrained to a small-scale experimental setting. Microreactors are also unable to sustain their superior performance due to heat and mass transfer losses during scale-up. Ultimately, the utilization of microreactors in industrial settings is impractical due to the exorbitant expenses associated with their precise fabrication, rendering large-scale production impracticable. On the other hand, membrane reactors have a limited presence in the industrial sector due to their high cost. However, researchers have been investigating methods to expand the practical utilization of membrane reactors. An unresolved challenge in the field of membrane reactors using MSR reactions is the inability to compare the performance in terms of conversion, hydrogen yield, and hydrogen recovery of different scientific studies due to variations in the experimental methodology employed by each author. The expensive cost of membrane reactors now limits their widespread use. However, this issue is projected to be resolved with the implementation of large-scale production and technological advancements. Furthermore, conducting further research on the techno-economic analysis of MSR in MR, design optimization, and life cycle evaluation would contribute to a more precise delineation of the subsequent actions required to develop a cost-effective and sustainable

technology for hydrogen production. As a result, the process has a significant possibility of being exploited for localized H_2 production.

2.3.3. Techno-Economic Analysis of MSR in MR

Several studies have provided evidence supporting the viability of hydrogen production using MSR via membrane reactors in comparison to conventional reactors. Prior to proceeding with commercial deployment or scaling up, it is crucial to comprehend the techno-economic analysis of the membrane reactor. An examination of the techno-economic aspects of methanol steam reforming in palladium-based membrane reactors encompasses several parameters that can impact the process's performance and efficiency. Multiple parameters contribute to the reaction process, including the choice of catalyst, specific operating conditions, reactor design, the thickness of the palladium membrane, measures taken to avoid hydrogen back-permeation, CAPEX/OPEX, and levelized cost of hydrogen (calculated by dividing the total annual cost of hydrogen production by the annual hydrogen production) [263–265]. In terms of volumetric energy density (based on LHV), liquid methanol (15.8 MJ L^{-1}, atm) outperforms other substitutes like liquid H_2 (8 MJ L^{-1}, 20 K), H_2 compressed cylinder (~ 4.5 MJ L^{-1}, 70000 kPa), and CH_4 compressed cylinder (~ 16.5 MJ $L^{-}1$, 70000 kPa) [266]. Accounting for the cost per kilogram of hydrogen storage, methanol (3.57 USD) once again has an advantage compared to compressed hydrogen (> 12 USD, 70000 kPa) and liquid H_2 (~ 8 USD, 20 K). To fully utilize hydrogen's potential, it must be separated from methanol due to its lower heating value (119.9 MJ kg^{-1}) which is roughly 6.5 times higher than methanol's (18.1 MJ kg^{-1}) [38]. Kim et al., [259] investigated the techno-economic analysis of the PSA-based PB reactor and MR for 1.33 kg h^{-1} of H_2 production via MSR. Based on process simulation results, a unit H_2 production cost was calculated by dividing the annual cost by the annual H_2 production yield for a PB reactor and the MR. They claimed that the capital expenditures (CAPEX) for the MR reactor are only 3%, compared to 17% for the PB reactor, primarily as a result of the abolition of PSA. The authors employed the Hysys simulation program to analyze the data, which revealed that MR exhibited reduced overall expenses mostly attributed to the absence of additional H_2 separation units, such as the PSA required in catalytic reactors. The aggregate yearly expenditures for MR and catalytic reactors amounted to $72,305 and $93,401, respectively. Based on the itemized cost estimation for a unit of H_2 production, the MR (7.24 $ per kg of H_2) reactor is 23% less expensive than the PB reactor (9.37 $ per kg of H_2). The study conducted by Buyn et al. [267] examined the cost of hydrogen production using MSR at various capacities, specifically 30, 100, 300, and 700 $m^3\,h^{-1}$, in both catalytic reactors and MR. It is

observed that when the production capacity increases, there is a decrease in the cost of hydrogen production in both MR and catalytic reactors. As an illustration, the cost of producing H_2 is \$10.41 per kg of H_2 and \$8.82 per kg of H_2 for the catalytic reactor and MR at a flow rate of 30 $m^3 h^{-1}$, respectively. However, at a flow rate of 700 $m^3 h^{-1}$, the cost is \$7.24 per kg of H_2 and \$6.43 per kg of H_2 for the catalytic reactor and MR. Furthermore, MR exhibited reduced expenses in comparison to catalytic reactors across all the examined H_2 production capacities. According to the life cycle assessment, the MR exhibited a CO_2 emission rate of 0.3680 kmol h^{-1}, which is 20% lower compared to the catalytic reactor, which emitted 0.4645 kmol h^{-1} of CO_2. Despite the fact that the minimal estimated cost of H_2 production found in the economic analysis conducted in this paper, which is \$2.78 per kg of H_2, remains greater than the cost associated with methane steam reforming, which is \$2.30 per kg of H_2. In an MR, a methanol conversion of greater than 50% is achievable at temperatures between 473-573 K, whereas in a TR, more than 50% of methanol conversion is only possible at temperatures between 573-673 K. However, at elevated temperatures, the CO selectivity increases, and several studies have reported a serious problem with a decrease in catalyst activity owing to coking [175]. The first MR was commercialized by Johnson Matthey in 1964. They fabricated different modules ranging from 166 L min^{-1} to 833 L min^{-1} of hydrogen production with purity levels up to 99.9999%. Further, they developed a methanol-water-based H_2 generator with 416 L min^{-1} of capacity. However, a small unit of 33 L min^{-1} of H_2 production was successfully installed for the British Antarctica Survey in 1974 [268,269]. The methanol-based membrane reformer developed by Element1 Powering Innovation (Oregon, United States) generates hydrogen with an efficiency of over 70%. In addition, they offer a variety of hydrogen generators with production rates ranging from 1 L min^{-1} to 1300 L min^{-1} (purity = 99.95%) [270]. The cost of the membrane prepared using Pd again adds to the overall cost. The 2015 target set by the Department of Energy, United States (DOE, US) for the hydrogen flux is 1.13 mol m^{-2} s^{-1} with a purity of 99.99% (selectivity > 9,999), even in gas mixture conditions. The requirement must be satisfied at a differential partial pressure of H_2 of 138 kPa, temperature of 673 K, durability of 5 years, recovery of above 90%, and a cost of less than \$4400 per meter square. With this objective, the requisite membrane thickness to meet the objective is on the order of 0.1 μm (ultra-thin membrane) [271]. Unit costs for Pd-based membrane reformers can range from a few thousand to tens of thousands of dollars. Utilizing an ultra-thin Pd membrane is anticipated to result in a significant reduction in membrane-related capital expenditures. However, the thermal heat cycle stability of the ultra-thin membrane for long-term hydrogen production under industrial condition is difficult to achieve. Evidence has demonstrated that MRs offer

numerous advantages compared to CRs. Further research and investigation are necessary to improve the characteristics of the membrane, decrease expenses, and facilitate the commercialization of MSR in MRs. Furthermore, further examination of the techno-economic analysis of MSR in MRs, along with design optimization and life cycle assessment, will contribute to the development of a more cost-effective and sustainable technology for hydrogen production.

2.4. Summary

Membrane reformer is established as the efficient way for hydrogen production at the decentralized level because of its compactness and cost competitiveness compared to other parallel technologies. Moreover, palladium membrane is the best choice for the separation of hydrogen at lower working temperatures and pressures are facilitated by the high permeability and selectivity of palladium membranes, resulting in reduced energy consumption and operating costs. The preparation of this dense palladium membrane through the ELP technique is cost-effective and simple. Utilizing an ultra-thin Pd membrane is anticipated to result in a significant reduction in membrane-related capital expenditures. However, the thermal heat cycle stability of the ultra-thin membrane for long-term hydrogen production under industrial conditions is difficult to achieve. Integration of these membranes with methanol steam reforming for simultaneous hydrogen production and separation can solve the challenge associated with hydrogen storage and transport. The use of a structured catalyst such as SiC-foam can significantly reduce the heat and mass transfer issue in endothermic MSR. Moreover, continuous separation of hydrogen through the membrane drives the overall reaction toward the desired product according to Le Chateliers' principle. Both the membrane and MSR are compatible in the temperature range of 573 K to 673 K and pressure range of 100-400 kPa. However, the efficient hydrogen separation from the reaction mixture is crucial to achieve maximum H_2 recovery. The researchers have been investigating methods to expand the practical utilization of membrane reactors. The issue is projected to be resolved with the implementation of large-scale production and technological advancements. Furthermore, conducting further research on the techno-economic analysis of MSR in MR, design optimization, and life cycle evaluation would contribute to a more precise delineation of the subsequent actions required to develop a cost-effective and sustainable technology for hydrogen production. As a result, the process has a significant possibility of being exploited for localized H_2 production. Evidence has demonstrated that MR offers numerous advantages compared to CRs. Further research and investigation are necessary to improve the

characteristics of the membrane, decrease expenses, and facilitate the commercialization of MSR in MR. Additionally, further examination of the techno-economic analysis of MSR in MR, along with design optimization and life cycle assessment, will contribute to the development of a more cost-effective and sustainable technology for hydrogen production.

References

[1] T. Grahm, On the absorption and dialytic separation of gases by colloid septa, Philosophical Transactions of the Royal Society of London, 156 (1866), pp. 399–439.

[2] S.N. Paglieri, J.D. Way, Innovations in palladium membrane research, Separation and Purification Methods, 31 (2002), pp. 1–169.

[3] J. Shu, B.P.A. Grandjean, E. Ghali, S. Kaliaguine, Autocatalytic Effects in Electroless Deposition of Palladium, Journal of The Electrochemical Society, 140 (1993), pp. 3175.

[4] S. Tosti, L. Bettinali, V. Violante, Rolled thin Pd and Pd-Ag membranes for hydrogen separation and production, International Journal of Hydrogen Energy, 25 (2000), pp. 319–325.

[5] P.P. Mardilovich, Y. She, Y.H. Ma, M.H. Rei, Defect-Free Palladium Membranes on Porous Stainless-Steel Support, AIChE Journal, 44 (1998), pp. 310–322.

[6] S. Uemiya, N. Sato, H. Ando, Y. Kude, T. Matsuda, E. Kikuchi, Separation of hydrogen through palladium thin film supported on a porous glass tube, Journal of Membrane Science, 56 (1991), pp. 303–313.

[7] J.P. Collins, J.D. Way, Preparation and Characterization of a Composite Palladium-Ceramic Membrane, Industrial and Engineering Chemistry Research, 32 (1993), pp. 3006–3013.

[8] A.G. Knapton, Palladium Alloys for Hydrogen Diffusion Membranes., Platinum Metals Review, 21 (1977), pp. 44–50.

[9] F.A. Lewis, The Palladium-Hydrogen System: A survey of hydride formation and the effects, Platinum Metals Review, 26 (1982), pp. 20–27.

[10] S. Yun, S. Ted Oyama, Correlations in palladium membranes for hydrogen separation: A review, Journal of Membrane Science, 375 (2011), pp. 28–45.

[11] A. Basile, F. Gallucci, S. Tosti, Synthesis, Characterization, and Applications of Palladium Membranes, Membrane Science and Technology, 13 (2008), pp. 255–323.

[12] S. Adhikari, S. Fernando, Hydrogen membrane separation techniques, Industrial and Engineering Chemistry Research, 45 (2006), pp. 875–881.

[13] L.J. Gillespie, L.S. Galstaun, The Palladium-Hydrogen Equilibrium and New Palladium

Hydrides, Journal of the American Chemical Society, 58 (2005), pp. 2565–2573.

[14] J. Shu, B.E.W. Bongondo, B.P.A. Grandjean, S. Kaliaguine, Morphological changes of Pd-Ag membranes upon hydrogen permeation, Journal of Materials Science Letters, 16 (1997), pp. 294–297.

[15] A.K.M. Fazle Kibria, Y. Sakamoto, Effect of alloying of palladium with silver and rhodium on the hydrogen solubility, miscibility gap and hysteresis, International Journal of Hydrogen Energy, 25 (2000), pp. 853–859.

[16] F.A.L. J. C. Barton, J. A. S. Green, Changes of Electrode Potential and Electrical Resistance as a Function of the Hydrogen Content of some Pd+Ni and Pd+Rh Alloys BY, Chemistry Dept., The Queen's University of Belfast, 1 (1965), pp. 960–970.

[17] V. Gryaznov, Metal containing membranes for the production of ultrapure hydrogen and the recovery of hydrogen isotopes, Separation and Purification Methods, 29 (2000), pp. 171–187.

[18] D.L. McKinley, Metal alloy for hydrogen separation and purification, 3350845, 1967.

[19] Y. Sakamoto, T. Ohishi, E. Kumashiro, K. Takao, Diffusivity and solubility of hydrogen in Pd-Fe and Pd-V alloys, Journal of The Less Common Metals, 88 (1982), pp. 379–385.

[20] M. Kajiwara, S. Uemiya, T. Kojima, E. Kikuchi, Rhodium- and iridium-dispersed porous alumina membranes and their hydrogen permeation properties, Catalysis Today, 56 (2000), pp. 83–87.

[21] K.J. Bryden, J.Y. Ying, Nanostructured palladium-iron membranes for hydrogen separation and membrane hydrogenation reactions, Journal of Membrane Science, 203 (2002), pp. 29–42.

[22] H. Yoshida, K. Okuno, Y. Naruse, T. Kashiwai, Metallurgical Considerations on Pd, Pd-Alloy and Their Metal-Hydrogen Systems, Fusion Technology, 8 (1985), pp. 2388–2394.

[23] Y. Sakamoto, F.L. Chen, M. Furukawa, K. Mine, The (α + β) hydrogen miscibility gaps in hydrogenated palladium-rich Pd-Y(Gd)-Ag ternary alloys, Journal of The Less-Common Metals, 166 (1990), pp. 45–56.

[24] G.L. Holleck, Diffusion and solubility of hydrogen in palladium and palladium-silver

alloys, Journal of Physical Chemistry, 74 (1970), pp. 503–511.

[25] A.C. Makrides, Absorption of hydrogen by silver-palladium alloys, Journal of Physical Chemistry, 68 (1964), pp. 2160–2169.

[26] S. Uemiya, T. Matsuda, E. Kikuchi, Hydrogen permeable palladium-silver alloy membrane supported on porous ceramics, Journal of Membrane Science, 56 (1991), pp. 315–325.

[27] N.A. Al-Mufachi, N. V. Rees, R. Steinberger-Wilkens, Hydrogen selective membranes: A review of palladium-based dense metal membranes, Renewable and Sustainable Energy Reviews, 47 (2015), pp. 540–551.

[28] T.L. Ward, T. Dao, Model of hydrogen permeation behavior in palladium membranes, 153 (1999), pp. 211–231.

[29] K.W. Kehr, Theory of the diffusion of hydrogen in metals BT- Hydrogen in Metals I: Basic Properties, in: G. Alefeld, J. Völkl (Eds.), Springer Berlin Heidelberg, Berlin, Heidelberg, 1978: pp. 197–226.

[30] M.D. Dolan, Non-Pd BCC alloy membranes for industrial hydrogen separation, Journal of Membrane Science, 362 (2010), pp. 12–28.

[31] J. Melendez, E. Fernandez, F. Gallucci, M. van Sint Annaland, P.L. Arias, D.A. Pacheco Tanaka, Preparation and characterization of ceramic supported ultra-thin (~1 μm) Pd-Ag membranes, Journal of Membrane Science, 528 (2017), pp. 12–23.

[32] F. Guazzone, E.E. Engwall, Y.H. Ma, Effects of surface activity, defects and mass transfer on hydrogen permeance and n-value in composite palladium-porous stainless steel membranes, Catalysis Today, 118 (2006), pp. 24–31.

[33] X. Li, T.M. Liu, D. Huang, Y.Q. Fan, N.P. Xu, Preparation and characterization of ultrathin palladium membranes, Industrial and Engineering Chemistry Research, 48 (2009), pp. 2061–2065.

[34] A. Caravella, F. Scura, G. Barbieri, E. Drioli, Sieverts law empirical exponent for Pd-based membranes: Critical analysis in pure H2 permeation, Journal of Physical Chemistry B, 114 (2010), pp. 6033–6047.

[35] S. Hara, M. Ishitsuka, H. Suda, M. Mukaida, K. Haraya, Pressure-dependent hydrogen permeability extended for metal membranes not obeying the square-root law, Journal of

Physical Chemistry B, 113 (2009), pp. 9795–9801.

[36] R.J.R. Uhlhorn, K. Keizer, A.J. Burggraaf, Gas and surface diffusion in modified γ-alumina systems, Journal of Membrane Science, 46 (1989), pp. 225–241.

[37] C. Koroneos, A. Dompros, G. Roumbas, N. Moussiopoulos, Life cycle assessment of hydrogen fuel production processes, International Journal of Hydrogen Energy, 29 (2004), pp. 1443–1450.

[38] I. Dincer, C. Acar, Review and evaluation of hydrogen production methods for better sustainability, International Journal of Hydrogen Energy, 40 (2014), pp. 11094–11111.

[39] X. Cheng, Z. Shi, N. Glass, L. Zhang, J. Zhang, D. Song, Z.S. Liu, H. Wang, J. Shen, A review of PEM hydrogen fuel cell contamination: Impacts, mechanisms, and mitigation, Journal of Power Sources, 165 (2007), pp. 739–756.

[40] R.G. Musket, Effects of contamination on the interaction of hydrogen gas with palladium: A review, Journal of The Less-Common Metals, 45 (1976), pp. 173–183.

[41] M. Eriksson, L.G. Ekedahl, Real time measurements of hydrogen desorption and absorption during CO exposures of Pd: Hydrogen sticking and dissolution, Applied Surface Science, 133 (1998), pp. 89–97.

[42] C.H. Chen, Y.H. Ma, The effect of H2S on the performance of Pd and Pd/Au composite membrane, Journal of Membrane Science, 362 (2010), pp. 535–544.

[43] A. Dalla Fontana, N. Sirini, L.M. Cornaglia, A.M. Tarditi, Hydrogen permeation and surface properties of PdAu and PdAgAu membranes in the presence of CO, CO2 and H2S, Journal of Membrane Science, 563 (2018), pp. 351–359.

[44] S.H. Jung, K. Kusakabe, S. Morooka, S.D. Kim, Effects of co-existing hydrocarbons on hydrogen permeation through a palladium membrane, Journal of Membrane Science, 170 (2000), pp. 53–60.

[45] G. Zeng, A. Goldbach, L. Shi, H. Xu, On alloying and low-temperature stability of thin, supported PdAg membranes, International Journal of Hydrogen Energy, 37 (2012), pp. 6012–6019.

[46] J. Okazaki, T. Ikeda, D.A. Pacheco Tanaka, T.M. Suzuki, F. Mizukami, In situ high-temperature X-ray diffraction study of thin palladium/α-alumina composite membranes and their hydrogen permeation properties, Journal of Membrane Science, 335 (2009),

pp. 126–132.

[47] A. Suzuki, H. Yukawa, A review for consistent analysis of hydrogen permeability through dense metallic membranes, Membranes, 10 (2020), pp. 1–22.

[48] A. Caravella, N. Hara, H. Negishi, S. Hara, Quantitative contribution of non-ideal permeability under diffusion-controlled hydrogen permeation through Pd-membranes, International Journal of Hydrogen Energy, 39 (2014), pp. 4676–4682.

[49] K.L. Yeung, S.C. Christiansen, A. Varma, Palladium composite membranes by electroless plating technique. Relationships between plating kinetics, film microstructure and membrane performance, Journal of Membrane Science, 159 (1999), pp. 107–122.

[50] G. Zeng, L. Shi, Y. Liu, Y. Zhang, Y. Sun, A simple approach to uniform PdAg alloy membranes: Comparative study of conventional and silver concentration-controlled co-plating, International Journal of Hydrogen Energy, 39 (2014), pp. 4427–4436.

[51] E. Hadjixenophontos, M. Mahmoudizadeh, M. Rubin, D. Ullmer, F. Razmjooei, A.C. Hanf, J. Brien, R. Dittmeyer, A. Ansar, M.K. Hassan, M. Khraisheh, E. Hadjixenophontos, M. Mahmoudizadeh, M. Rubin, D. Ullmer, F. Razmjooei, A.C. Hanf, J. Brien, R. Dittmeyer, A. Ansar, Palladium Membrane with High Density of Large-Angle Grain Boundaries to Promote Hydrogen Diffusivity, Membranes, 12 (2022), pp. 1–14.

[52] T.A. Peters, P.A. Carvalho, M. Stange, R. Bredesen, Formation of hydrogen bubbles in Pd-Ag membranes during H2 permeation, International Journal of Hydrogen Energy, 45 (2019), pp. 7488–7496.

[53] J.M. Polfus, O.M. Løvvik, R. Bredesen, T. Peters, Hydrogen induced vacancy clustering and void formation mechanisms at grain boundaries in palladium, Acta Materialia, 195 (2020), pp. 708–719.

[54] S.G. Kang, K.E. Coulter, S.K. Gade, J.D. Way, D.S. Sholl, Identifying metal alloys with high hydrogen permeability using high throughput theory and experimental testing, Journal of Physical Chemistry Letters, 2 (2011), pp. 3040–3044.

[55] G. Zeng, A. Goldbach, H. Xu, Defect sealing in Pd membranes via point plating, Journal of Membrane Science, 328 (2009), pp. 6–10.

[56] S.K. Gade, E.A. Payzant, H.J. Park, P.M. Thoen, J.D. Way, The effects of fabrication

and annealing on the structure and hydrogen permeation of Pd-Au binary alloy membranes, Journal of Membrane Science, 340 (2009), pp. 227–233.

[57] N. Verma, R. Delhez, N.M. van der Pers, F.D. Tichelaar, A.J. Böttger, The role of the substrate on the mechanical and thermal stability of Pd thin films during hydrogen (de)sorption, International Journal of Hydrogen Energy, 46 (2021), pp. 4137–4153.

[58] R. Kirchheim, Hydrogen solubility and diffusivity in defective and amorphous metals, Progress in Materials Science, 32 (1988), pp. 261–325.

[59] M.M. Barreiro, M. Maroño, J.M. Sánchez, Hydrogen separation studies in a membrane reactor system: Influence of feed gas flow rate, temperature and concentration of the feed gases on hydrogen permeation, Applied Thermal Engineering, 74 (2015), pp. 186–193.

[60] M.M. Barreiro, M. Maroño, J.M. Sánchez, Hydrogen permeation through a Pd-based membrane and RWGS conversion in H2/CO2, H2/N2/CO2 and H2/H2O/CO2 mixtures, International Journal of Hydrogen Energy, 39 (2014), pp. 4710–4716.

[61] T.A. Peters, M. Stange, H. Klette, R. Bredesen, High pressure performance of thin Pd-23%Ag/stainless steel composite membranes in water gas shift gas mixtures; influence of dilution, mass transfer and surface effects on the hydrogen flux, Journal of Membrane Science, 316 (2008), pp. 119–127.

[62] W. Wang, X. Pan, X. Zhang, W. Yang, G. Xiong, The effect of co-existing nitrogen on hydrogen permeation through thin Pd composite membranes, Separation and Purification Technology, 54 (2007), pp. 262–271.

[63] W.H. Chen, M.H. Hsia, Y.L. Lin, Y.H. Chi, C.C. Yang, Hydrogen permeation and recovery from H2-N2 gas mixtures by Pd membranes with high permeance, International Journal of Hydrogen Energy, 38 (2013), pp. 14730–14742.

[64] R. Sharma, A. Kumar, R.K. Upadhyay, Characteristics of a multi-pass membrane reactor to improve hydrogen recovery, International Journal of Hydrogen Energy, 46 (2021), pp. 14429–14440.

[65] R. Ma, B. Castro-Dominguez, A.G. Dixon, Y.H. Ma, Scalability of multitube membrane modules for hydrogen separation: Technical considerations, issues and solutions, Journal of Membrane Science, 564 (2018), pp. 887–896.

[66] W.H. Chen, C.H. Lin, Y.L. Lin, Flow-field design for improving hydrogen recovery in

a palladium membrane tube, Journal of Membrane Science, 472 (2014), pp. 45–54.

[67] M. Jafarkhani, M.K. Moraveji, R. Davarnejad, F. Moztarzadeh, M. Mozafari, Three-dimensional simulation of turbulent flow in a membrane tube filled with semi-circular baffles, Desalination, 294 (2012), pp. 8–16.

[68] W.H. Chen, W.Z. Syu, C.I. Hung, Y.L. Lin, C.C. Yang, Influences of geometry and flow pattern on hydrogen separation in a Pd-based membrane tube, International Journal of Hydrogen Energy, 38 (2013), pp. 1145–1156.

[69] N. Mori, T. Nakamura, K.I. Noda, O. Sakai, A. Takahashi, N. Ogawa, H. Sakai, Y. Iwamoto, T. Hattori, Reactor configuration and concentration polarization in methane steam reforming by a membrane reactor with a highly hydrogen-permeable membrane, Industrial and Engineering Chemistry Research, 46 (2007), pp. 1952–1958.

[70] W.H. Chen, C.W. Tsai, Y.L. Lin, Numerical studies of the influences of bypass on hydrogen separation in a multichannel Pd membrane system, Renewable Energy, 104 (2017), pp. 259–270.

[71] R. Sharma, A. Kumar, R.K. Upadhyay, Characteristic of a multi-pass membrane separator for hydrogen separation through self-supported Pd–Ag membranes, International Journal of Hydrogen Energy, 43 (2018), pp. 5019–5032.

[72] J. Zhu, S.S. Araya, X. Cui, S.L. Sahlin, S.K. Kær, Zhu, Araya, Cui, S.L. Sahlin, Kær, Modeling and design of a multi-tubular packed-bed reactor for methanol steam reforming over a Cu/ZnO/Al2O3 catalyst, Energies, 13 (2020), pp. 610.

[73] S. Tosti, A. Adrover, A. Basile, V. Camilli, G. Chiappetta, V. Violante, Characterization of thin wall Pd-Ag rolled membranes, International Journal of Hydrogen Energy, 28 (2003), pp. 105–112.

[74] D.L. McKinley, Method for hydrogen separation and purification, 3,439,474, 1969.

[75] A. Santucci, F. Borgognoni, M. Vadrucci, S. Tosti, Testing of dense Pd-Ag tubes: Effect of pressure and membrane thickness on the hydrogen permeability, Journal of Membrane Science, 444 (2013), pp. 378–383.

[76] F. Roa, J. Douglas Way, R.L. McCormick, S.N. Paglieri, Preparation and characterization of Pd-Cu composite membranes for hydrogen separation, Chemical Engineering Journal, 93 (2003), pp. 11–22.

[77] X. Hu, W. Chen, Y. Huang, Fabrication of Pd/ceramic membranes for hydrogen separation based on low-cost macroporous ceramics with pencil coating, International Journal of Hydrogen Energy, 35 (2010), pp. 7803–7808.

[78] B. Anzelmo, S. Liguori, I. Mardilovich, A. Iulianelli, Y.H. Ma, J. Wilcox, A. Basile, Fabrication & performance study of a palladium on alumina supported membrane reactor: Natural gas steam reforming, a case study, International Journal of Hydrogen Energy, 43 (2018), pp. 7713–7721.

[79] J. Shu, A. Adnot, B.P.A. Grandjean, S. Kaliaguine, Structurally stable composite Pd-Ag alloy membranes: Introduction of a diffusion barrier, Thin Solid Films, 286 (1996), pp. 72–79.

[80] V. Höllein, M. Thornton, P. Quicker, R. Dittmeyer, Preparation and characterization of palladium composite membranes for hydrogen removal in hydrocarbon dehydrogenation membrane reactors, Catalysis Today, 67 (2001), pp. 33–42.

[81] D. Martinez-Diaz, R. Sanz, A. Carrero, J.A. Calles, D. Alique, Effective H2 separation through electroless pore-plated pd membranes containing graphite lead barriers, Membranes, 10 (2020), pp. 1–17.

[82] Y.S. Cheng, K.L. Yeung, Palladium-silver composite membranes by electroless plating technique, Journal of Membrane Science, 158 (1999), pp. 127–141.

[83] K. Kuraoka, H. Zhao, T. Yazawa, Pore-filled palladium-glass composite membranes for hydrogen separation by novel electroless plating technique, Journal of Materials Science, 39 (2004), pp. 1879–1881.

[84] N.M. Terra, L.P. Bessa, V.L. Cardoso, M.H.M. Reis, Graphite coating on alumina substrate for the fabrication of hydrogen selective membranes, International Journal of Hydrogen Energy, 43 (2018), pp. 1534–1544.

[85] B.K.R. Nair, J. Choi, M.P. Harold, Electroless plating and permeation features of Pd and Pd/Ag hollow fiber composite membranes, Journal of Membrane Science, 288 (2007), pp. 67–84.

[86] Y. Ji, H. Sun, X. Wang, T. Yang, Z. Xue, C. Li, N. Yang, J. Sunarso, S. Liu, Vacuum-assisted continuous flow electroless plating approach for high performance Pd membrane deposition on ceramic hollow fiber lumen, Journal of Membrane Science, 645 (2022), pp. 120207.

[87] S.K. Thawatchai Maneerung, Kus Hidajat, Ultra-thin 1 μm) internally-coated Pd–Ag alloy hollow fiber membrane with superior thermal stability and d.pdf, Journal of Membrane Science, 452 (2014), pp. 127–142.

[88] E. Tosto, D. Martinez-Diaz, R. Sanz, G. Azzato, J.A. Calles, J.A. Medrano, E. Fernandez, D.A. Pacheco Tanaka, F. Gallucci, D. Alique, A. Caravella, Systematic experimental assessment of concentration polarization and inhibition in Pd-based membranes for hydrogen purification, Fuel Processing Technology, 213 (2021), pp. 106661.

[89] S.K. Ryi, N. Xu, A. Li, C.J. Lim, J.R. Grace, Electroless Pd membrane deposition on alumina modified porous Hastelloy substrate with EDTA-free bath, International Journal of Hydrogen Energy, 35 (2010), pp. 2328–2335.

[90] Y.H. Ma, C.H. Chen, J. Catalano, F. Guazzone, E.A. Payzant, Synthesis, annealing, and performances of Pd-Au asymmetric composite membranes for hydrogen purification, Industrial and Engineering Chemistry Research, 52 (2013), pp. 8732–8744.

[91] A. Arratibel, J.A. Medrano, J. Melendez, D.A. Pacheco Tanaka, M. van Sint Annaland, F. Gallucci, Attrition-resistant membranes for fluidized-bed membrane reactors: Double-skin membranes, Journal of Membrane Science, 563 (2018), pp. 419–426.

[92] S. Uemiya, State-of-the-art of supported metal membranes for gas separation, Separation and Purification Methods, 28 (1999), pp. 51–85.

[93] W. Chen, X. Hu, R. Wang, Y. Huang, On the assembling of Pd/ceramic composite membranes for hydrogen separation, Separation and Purification Technology, 72 (2010), pp. 92–97.

[94] E. Fernandez, A. Helmi, K. Coenen, J. Melendez, J.L. Viviente, D.A. Pacheco Tanaka, M. Van Sint Annaland, F. Gallucci, Development of thin Pd-Ag supported membranes for fluidized bed membrane reactors including WGS related gases, International Journal of Hydrogen Energy, 40 (2015), pp. 3506–3519.

[95] A. Arratibel Plazaola, D.A. Pacheco Tanaka, M. Van Sint Annaland, F. Gallucci, Recent Advances in Pd-Based Membranes for Membrane Reactors, Molecules (Basel, Switzerland), 22 (2017), pp. 1–53.

[96] S.K. Ryi, H.S. Ahn, J.S. Park, D.W. Kim, Pd-Cu alloy membrane deposited on CeO2 modified porous nickel support for hydrogen separation, International Journal of

Hydrogen Energy, 39 (2014), pp. 4698–4703.

[97] J. Okazaki, T. Ikeda, D.A.P. Tanaka, M.A. Llosa Tanco, Y. Wakui, K. Sato, F. Mizukami, T.M. Suzuki, Strong interaction at the palladium/alumina interface of membrane during hydrogen permeation at elevated temperature, Chemistry Letters, 37 (2008), pp. 1004–1005.

[98] S.N. Paglieri, K.Y. Foo, J.D. Way, J.P. Collins, D.L. Harper-Nixon, A new preparation technique for Pd/alumina membranes with enhanced high- temperature stability, Industrial and Engineering Chemistry Research, 38 (1999), pp. 1925–1936.

[99] J. Okazaki, T. Ikeda, D.A. Pacheco Tanaka, M.A. Llosa Tanco, Y. Wakui, K. Sato, F. Mizukami, T.M. Suzuki, Importance of the support material in thin palladium composite membranes for steady hydrogen permeation at elevated temperatures, Physical Chemistry Chemical Physics, 11 (2009), pp. 8632–8638.

[100] J. Okazaki, T. Ikeda, D.A.P. Tanaka, K. Sato, T.M. Suzuki, F. Mizukami, An investigation of thermal stability of thin palladium-silver alloy membranes for high temperature hydrogen separation, Journal of Membrane Science, 366 (2011), pp. 212–219.

[101] M.E. Ayturk, Synthesis, Annealing Strategies and in-situ Characterization of Thermally Stable Composite Thin Pd-Ag Alloy Membranes for H2 Separation, Worcester Polutechnic Institute, 2007.

[102] M.E. Ayturk, I.P. Mardilovich, E.E. Engwall, Y.H. Ma, Synthesis of composite Pd-porous stainless steel (PSS) membranes with a Pd/Ag intermetallic diffusion barrier, Journal of Membrane Science, 285 (2006), pp. 385–394.

[103] Y.H. Ma, B.C. Akis, M.E. Ayturk, F. Guazzone, E.E. Engwall, I.P. Mardilovich, Characterization of Intermetallic Diffusion Barrier and Alloy Formation for Pd/Cu and Pd/Ag Porous Stainless Steel Composite Membranes, Industrial & Engineering Chemistry Research, 43 (2004), pp. 2936–2945.

[104] M.L. Bosko, J.B. Miller, E.A. Lombardo, A.J. Gellman, L.M. Cornaglia, Surface characterization of Pd-Ag composite membranes after annealing at various temperatures, Journal of Membrane Science, 369 (2011), pp. 267–276.

[105] H.B. Zhao, K. Pflanz, J.H. Gu, A.W. Li, N. Stroh, H. Brunner, G.X. Xiong, Preparation of palladium composite membranes by modified electroless plating procedure, Journal

of Membrane Science, 142 (1998), pp. 147–157.

[106] R. Sanz, J.A. Calles, D. Alique, L. Furones, S. Ordóñez, P. Marín, P. Corengia, E. Fernandez, Preparation, testing and modelling of a hydrogen selective Pd/YSZ/SS composite membrane, International Journal of Hydrogen Energy, 36 (2011), pp. 15783–15793.

[107] A. Tarditi, C. Gerboni, L. Cornaglia, PdAu membranes supported on top of vacuum-assisted ZrO2-modified porous stainless steel substrates, Journal of Membrane Science, 428 (2013), pp. 1–10.

[108] H. Gao, J.Y.S. Lin, Y. Li, B. Zhang, Electroless plating synthesis, characterization and permeation properties of Pd-Cu membranes supported on ZrO2 modified porous stainless steel, Journal of Membrane Science, 265 (2005), pp. 142–152.

[109] L. Wei, J. Yu, X. Hu, Y. Huang, Facile surface modification of porous stainless steel substrate with TiO2 intermediate layer for fabrication of H2-permeable composite palladium membranes, Separation Science and Technology (Philadelphia), 51 (2016), pp. 998–1006.

[110] A. Qiao, K. Zhang, Y. Tian, L. Xie, H. Luo, Y.S. Lin, Y. Li, Hydrogen separation through palladium-copper membranes on porous stainless steel with sol-gel derived ceria as diffusion barrier, Fuel, 89 (2010), pp. 1274–1279.

[111] M.L. Bosko, F.Ojeda, E.A. Lombardo, L.M. Cornaglia, NaA zeolite as an effective diffusion barrier in composite Pd/PSS membranes, Journal of Membrane Science, 331 (2009), pp. 57–65.

[112] L. Wei, J. Yu, X. Hu, Y. Huang, Fabrication of H2-permeable palladium membranes based on pencil-coated porous stainless steel substrate, International Journal of Hydrogen Energy, 37 (2012), pp. 13007–13012.

[113] M. Maroño, G. ĎAlessandro, A. Morales, D. Martinez-Diaz, D. Alique, J.M. Sánchez, Influence of Si and Fe/Cr oxides as intermediate layers in the fabrication of supported Pd membranes, Separation and Purification Technology, 234 (2020), pp. 116091.

[114] S. Samingprai, S. Tantayanon, Y.H. Ma, Chromium oxide intermetallic diffusion barrier for palladium membrane supported on porous stainless steel, Journal of Membrane Science, 347 (2010), pp. 8–16.

[115] E. Fernandez, Palladium-based supported membranes for membrane reactors for

hydrogen production, Eindhoven University of Technology, 2016.

[116] R. Bhandari, The synthesis of Pd-Ag composite membranes for H2 separation using electroless plating method, Worcester Polytechnic Institute, 2010.

[117] T.A. Peters, R. Bredesen, H.J. Venvik, Pd-based Membranes in Hydrogen Production: Long-term Stability and Contaminant Effects, in: Enrico Drioli; Giuseppe Barbieri; Adele Brunetti (Ed.), Membrane Engineering for the Treatment of Gases: Volume 2: Gas-Separation Issues Combined with Membrane Reactors, The Royal Society of Chemistry, 2017: pp. 177–211.

[118] S. Yan, H. Maeda, K. Kusakabe, S. Morooka, Thin Palladium Membrane Formed in Support Pores by Metal-Organic Chemical Vapor Deposition Method and Application to Hydrogen Separation, Industrial and Engineering Chemistry Research, 33 (1994), pp. 616–622.

[119] N. Itoh, T. Akiha, T. Sato, Preparation of thin palladium composite membrane tube by a CVD technique and its hydrogen permselectivity, Catalysis Today, 104 (2005), pp. 231–237.

[120] J.R. Creighton, P. Ho, Introduction to Chemical Vapor Deposition (CVD), in: Chemical Vapor Deposition, ASM International, 2001: pp. 1–13.

[121] A. Gugliuzza, A. Iulianelli, A. Basile, Membranes for hydrocarbon fuel processing and separation, in: Advanced Membrane Science and Technology for Sustainable Energy and Environmental Applications, Woodhead Publishing Limited, 2011, 2011: pp. 295–338.

[122] V. Jayaraman, Y.S. Lin, Synthesis and hydrogen permeation properties of ultrathin palladium-silver alloy membranes, Journal of Membrane Science, 104 (1995), pp. 251–262.

[123] S.K. Ryi, J.S. Park, S.H. Kim, S.H. Cho, D.W. Kim, K.Y. Um, Characterization of Pd-Cu-Ni ternary alloy membrane prepared by magnetron sputtering and Cu-reflow on porous nickel support for hydrogen separation, Separation and Purification Technology, 50 (2006), pp. 82–91.

[124] E. Fernandez, J.A. Sanchez-Garcia, J.L. Viviente, M. Van Sint Annaland, F. Gallucci, D.A.P.P. Tanaka, Morphology and N2 Permeance of Sputtered Pd-Ag Ultra-Thin Film Membranes, Molecules, 21 (2016), pp. 1–13.

[125] S.E. Nam, K.H. Lee, A study on the palladium/nickel composite membrane by vacuum electrodeposition, Journal of Membrane Science, 170 (2000), pp. 91–99.

[126] S.E. Nam, S.H. Lee, K.H. Lee, Preparation of a palladium alloy composite membrane supported in a porous stainless steel by vacuum electrodeposition, Journal of Membrane Science, 153 (1999), pp. 163–173.

[127] Z.Y. Li, H. Maeda, K. Kusakabe, S. Morooka, H. Anzai, S. Akiyama, Preparation of palladium-silver alloy membranes for hydrogen separation by the spray pyrolysis method, Journal of Membrane Science, 78 (1993), pp. 247–254.

[128] N.J.W. and A.-M.M. Rhoda, R. N., Palladium plating by chemical reduction, 2,915,406, 1959.

[129] M.R. Rahimpour, F. Samimi, A. Babapoor, T. Tohidian, S. Mohebi, Palladium membranes applications in reaction systems for hydrogen separation and purification: A review, Chemical Engineering and Processing: Process Intensification, 121 (2017), pp. 24–49.

[130] R. Sanz, J.A. Calles, D. Alique, L. Furones, New synthesis method of Pd membranes over tubular PSS supports via “pore-plating” for hydrogen separation processes, International Journal of Hydrogen Energy, 37 (2012), pp. 18476–18485.

[131] J.W. Pex, P P.A.C., Van Delft, Y C, Correia, L A, Van Veen, H M, Jansen, D, and Dijkstra, Palladium alloy membranes for energy efficient membrane reactors, Netherlands, 2004.

[132] M.S. Salehi, M. Askarishahi, F. Gallucci, H.R. Godini, Selective CO2-Hydrogenation using a membrane reactor, Chemical Engineering and Processing - Process Intensification, 160 (2021), pp. 108264.

[133] Y. Huang, G. Lu, Y. Zeng, N. Qian, X. Chu, G. Wang, S. Wu, W. Liu, Experimental and Simulation Analysis of Hydrogen Permeation Performance of Pd/Ag Permeator Used for Tritium Processing, Nuclear Technology, 206 (2020), pp. 458–466.

[134] S. Singla, N.P. Shetti, S. Basu, K. Mondal, T.M. Aminabhavi, Hydrogen production technologies - Membrane based separation, storage and challenges, Journal of Environmental Management, 302 (2022), pp. 113963.

[135] P.K. Seelam, B. Rathnayake, S. Pitkäaho, E. Turpeinen, R.L. Keiski, Overview on recent developments on hydrogen energy: Production, catalysis, and sustainability, Current

Trends and Future Developments on (Bio-) Membranes, (2020), pp. 3–32.

[136] S. Liguori, K. Kian, N. Buggy, B.H. Anzelmo, J. Wilcox, Opportunities and Challenges of Low-Carbon Hydrogen via Metallic Membranes, Progress in Energy and Combustion Science, 80 (2020), pp. 100851.

[137] B.D.L. Ag, E. Division, Development of a compact steam reformer using a palladium membrane for the production of hydrogen, Energy, 78 (2010), pp. 1–6.

[138] D. Barba, M. Capocelli, M. De Falco, G. Franchi, V. Piemonte, Mass transfer coefficient in multi-stage reformer/membrane modules for hydrogen production, Membranes, 8 (2018), pp. 1–17.

[139] B. Castro-Dominguez, I.P. Mardilovich, R. Ma, N.K. Kazantzis, A.G. Dixon, Y.H. Ma, Performance of a pilot-scale multitube membrane module under coal-derived syngas for hydrogen production and separation, Journal of Membrane Science, 523 (2017), pp. 515–523.

[140] A. Helmi, F. Gallucci, M. Van Sint Annaland, Resource scarcity in palladium membrane applications for carbon capture in integrated gasification combined cycle units, International Journal of Hydrogen Energy, 39 (2014), pp. 10498–10506.

[141] M. Rostami, A.H. Farajollahi, R. Amirkhani, M.E. Farshchi, A review study on methanol steam reforming catalysts: Evaluation of the catalytic performance, characterizations, and operational parameters, AIP Advances, 13 (2023), pp. 030701.

[142] A.H. Mohammed Abbas, K.K. Cheralathan, E. Porpatham, S.K. Arumugam, Hydrogen generation using methanol steam reforming – catalysts, reactors, and thermo-chemical recuperation, Renewable and Sustainable Energy Reviews, 191 (2024), pp. 114147.

[143] P. Nikolaidis, A. Poullikkas, A comparative overview of hydrogen production processes, Renewable and Sustainable Energy Reviews, 67 (2017), pp. 597–611.

[144] J. Agrell, H. Birgersson, M. Boutonnet, I. Melián-Cabrera, R.M. Navarro, J.L.G. Fierro, Production of hydrogen from methanol over Cu/ZnO catalysts promoted by ZrO2 and Al2O3, Journal of Catalysis, 219 (2003), pp. 389–403.

[145] S. Patel, K.K. Pant, Activity and stability enhancement of copper-alumina catalysts using cerium and zinc promoters for the selective production of hydrogen via steam reforming of methanol, Journal of Power Sources, 159 (2006), pp. 139–143.

[146] S.B. Bagherzadeh, M. Haghighi, Plasma-enhanced comparative hydrothermal and coprecipitation preparation of CuO/ZnO/Al2O3 nanocatalyst used in hydrogen production via methanol steam reforming, Energy Conversion and Management, 142 (2017), pp. 452–465.

[147] S.B. Bagherzadeh, M. Haghighi, N. Rahemi, Novel oxalate gel coprecipitation synthesis of ZrO2-CeO2-promoted CuO-ZnO-Al2O3nanocatalyst for fuel cell-grade hydrogen production from methanol: Influence of ceria-zirconia loading, Energy Conversion and Management, 134 (2017), pp. 88–102.

[148] L.C. Wang, Y.M. Liu, M. Chen, Y. Cao, H.Y. He, G.S. Wu, W.L. Dai, K.N. Fan, Production of hydrogen by steam reforming of methanol over Cu/ZnO catalysts prepared via a practical soft reactive grinding route based on dry oxalate-precursor synthesis, Journal of Catalysis, 246 (2007), pp. 193–204.

[149] Y.H. Huang, S.F. Wang, A.P. Tsai, S. Kameoka, Reduction behaviors and catalytic properties for methanol steam reforming of Cu-based spinel compounds CuX2O4 (X=Fe, Mn, Al, La), Ceramics International, 40 (2014), pp. 4541–4551.

[150] J.P. Shen, C. Song, Influence of preparation method on performance of Cu/Zn-based catalysts for low-temperature steam reforming and oxidative steam reforming of methanol for H2 production for fuel cells, Catalysis Today, 77 (2002), pp. 89–98.

[151] T. Shishido, Y. Yamamoto, H. Morioka, K. Takaki, K. Takehira, Active Cu/ZnO and Cu/ZnO/Al2O3 catalysts prepared by homogeneous precipitation method in steam reforming of methanol, Applied Catalysis A: General, 263 (2004), pp. 249–253.

[152] F. Ahmadi, M. Haghighi, H. Ajamein, Sonochemically coprecipitation synthesis of CuO/ZnO/ZrO2/Al2O3 nanocatalyst for fuel cell grade hydrogen production via steam methanol reforming, Journal of Molecular Catalysis A: Chemical, 421 (2016), pp. 196–208.

[153] H. Purnama, F. Girgsdies, T. Ressler, J.H. Schattka, R.A. Caruso, R. Schomäcker, R. Schlögl, Activity and selectivity of a nanostructured CuO/ZrO2 catalyst in the steam reforming of methanol, Catalysis Letters, 94 (2004), pp. 61 – 68.

[154] H.M. Yang, P.H. Liao, Preparation and activity of Cu/ZnO-CNTs nano-catalyst on steam reforming of methanol, Applied Catalysis A: General, 317 (2007), pp. 226–233.

[155] P.H. Liao, H.M. Yang, Preparation of catalyst Ni-Cu/CNTs by chemical reduction with

formaldehyde for steam reforming of methanol, Catalysis Letters, 121 (2008), pp. 274–282.

[156] L. Alejo, R. Lago, M.A. Peña, J.L.G. Fierro, Partial oxidation of methanol to produce hydrogen over Cu-Zn-based catalysts, Applied Catalysis A: General, 162 (1997), pp. 281–297.

[157] X. Xu, K. Shuai, B. Xu, Review on copper and palladium based catalysts for methanol steam reforming to produce hydrogen, Catalysts, 7 (2017), pp. 1–15.

[158] H. Meng, Y. Yang, T. Shen, Z. Yin, L. Wang, W. Liu, P. Yin, Z. Ren, L. Zheng, J. Zhang, F.S. Xiao, M. Wei, Designing Cu0−Cu+ dual sites for improved C−H bond fracture towards methanol steam reforming, Nature Communications, 14 (2023), pp. 1–12.

[159] P. Hirunsit, K. Faungnawakij, Cu − Cr , Cu − Mn , and Cu − Fe Spinel-Oxide-Type Catalysts for Reforming of Oxygenated Hydrocarbons, The Journal of Physical Chemistry C, 117 (2013), pp. 23757−23765.

[160] G. Zhang, J. Zhao, T. Yang, Q. Zhang, L. Zhang, In-situ self-assembled Cu2O/ZnO core-shell catalysts synergistically enhance the durability of methanol steam reforming, Applied Catalysis A: General, 616 (2021), pp. 118072.

[161] D. Das, J. Llorca, M. Dominguez, A. Gayen, Single step combustion synthesized Cu/Ce0.8Zr0.2O2 for methanol steam reforming: structural insights from in situ XPS and HRTEM studies, Catalysis, Structure and Reactivity, 1 (2015), pp. 174–182.

[162] Y. Ma, G. Guan, X. Hao, Z. Zuo, W. Huang, P. Phanthong, K. Kusakabe, A. Abudula, Highly-efficient steam reforming of methanol over copper modified molybdenum carbide, RSC Advances, 4 (2014), pp. 44175–44184.

[163] S. Sá, H. Silva, L. Brandão, J.M. Sousa, A. Mendes, Catalysts for methanol steam reforming-A review, Applied Catalysis B: Environmental, 99 (2010), pp. 43–57.

[164] B. Lindström, L.J. Pettersson, Deactivation of copper-based catalysts for fuel cell applications, Catalysis Letters, 74 (2001), pp. 27–30.

[165] M. Kurtz, H. Wilmer, T. Genger, O. Hinrichsen, M. Muhler, Deactivation of supported copper catalysts for methanol synthesis, Catalysis Letters, 86 (2003), pp. 77–80.

[166] X. Chen, X. Li, Q. Yang, C. Li, Methanol Steam Reforming for Hydrogen Production

over CuZnZrOx: Promotion Effect of Cu, ACS Applied Energy Materials, 6 (2023), pp. 10061–10069.

[167] T. Valdés-Solís, G. Marbán, A.B. Fuertes, Nanosized catalysts for the production of hydrogen by methanol steam reforming, Catalysis Today, 116 (2006), pp. 354–360.

[168] O.O. Fasanya, R. Al-Hajri, O.U. Ahmed, M.T.Z. Myint, A.Y. Atta, B.Y. Jibril, J. Dutta, Copper zinc oxide nanocatalysts grown on cordierite substrate for hydrogen production using methanol steam reforming, International Journal of Hydrogen Energy, 44 (2019), pp. 22936–22946.

[169] F. Tonelli, O. Gorriz, A. Tarditi, L. Cornaglia, L. Arrúa, M. Cristina Abello, Activity and stability of a CuO/CeO2 catalyst for methanol steam reforming, International Journal of Hydrogen Energy, 40 (2015), pp. 13379–13387.

[170] H. Li, C. Ma, X. Zou, A. Li, Z. Huang, L. Zhu, On-board methanol catalytic reforming for hydrogen Production-A review, International Journal of Hydrogen Energy, 46 (2021), pp. 22303–22327.

[171] M. V. Twigg, M.S. Spencer, Deactivation of copper metal catalysts for methanol decomposition, methanol steam reforming and methanol synthesis, Topics in Catalysis, 22 (2003), pp. 191–203.

[172] R. Thattarathody, M. Artoul, R.M. Digilov, M. Sheintuch, Pressure, Diffusion, and S/M Ratio Effects in Methanol Steam Reforming Kinetics, Industrial and Engineering Chemistry Research, 57 (2018), pp. 3175–3186.

[173] M.A. Achomo, A. Kumar, N.R. Peela, P. Muthukumar, Hydrogen production from steam reforming of methanol: A comprehensive review on thermodynamics, catalysts, reactors, and kinetic studies, International Journal of Hydrogen Energy, 58 (2024), pp. 1640–1672.

[174] M.M. Günter, T. Ressler, R.E. Jentoft, B. Bems, Redox behavior of copper oxide/zinc oxide catalysts in the steam reforming of methanol studied by in situ X-ray diffraction and absorption spectroscopy, Journal of Catalysis, 203 (2001), pp. 133–149.

[175] A. Iulianelli, P. Ribeirinha, A. Mendes, A. Basile, Methanol steam reforming for hydrogen generation via conventional and membrane reactors: A review, Renewable and Sustainable Energy Reviews, 29 (2014), pp. 355–368.

[176] A.M. Ranjekar, G.D. Yadav, Steam Reforming of Methanol for Hydrogen Production:

A Critical Analysis of Catalysis, Processes, and Scope, Industrial and Engineering Chemistry Research, 60 (2021), pp. 89–113.

[177] E. Santacesaria, S. Carrá, Kinetics of catalytic steam reforming of methanol in a cstr reactor, Applied Catalysis, 5 (1983), pp. 345–358.

[178] R.Y. Chein, Y.C. Chen, J.N. Chung, Thermal resistance effect on methanol-steam reforming performance in micro-scale reformers, International Journal of Hydrogen Energy, 37 (2012), pp. 250–262.

[179] B.A. Peppley, J.C. Amphlett, L.M. Kearns, R.F. Mann, Methanol-steam reforming on Cu/ZnO/Al2O3 catalysts. Part 2. A comprehensive kinetic model, Applied Catalysis A: General, 179 (1999), pp. 31–49.

[180] B.A. Peppley, J.C. Amphlett, L.M. Kearns, R.F. Mann, Methanol-steam reforming on Cu/Zno/Al2O3. Part 1: The reaction network, Applied Catalysis A: General, 179 (1999), pp. 21–29.

[181] K. Takahashi, N. Takezawa, H. Kobayashi, The mechanism of steam reforming of methanol over a copper-silica catalyst, Applied Catalysis, 2 (1982), pp. 363–366.

[182] C.J. Jiang, D.L. Trimm, M.S. Wainwright, N.W. Cant, Kinetic study of steam reforming of methanol over copper-based catalysts, Applied Catalysis A, General, 93 (1993), pp. 245–255.

[183] C.J. Jiang, D.L. Trimm, M.S. Wainwright, N.W. Cant, Kinetic mechanism for the reaction between methanol and water over a Cu-ZnO-Al2O3 catalyst, Applied Catalysis A, General, 97 (1993), pp. 145–158.

[184] N. Takezawa, N. Iwasa, Steam reforming and dehydrogenation of methanol: Difference in the catalytic functions of copper and group VIII metals, Catalysis Today, 36 (1997), pp. 45–56.

[185] B. Frank, F.C. Jentoft, H. Soerijanto, J. Kröhnert, R. Schlögl, R. Schomäcker, Steam reforming of methanol over copper-containing catalysts: Influence of support material on microkinetics, Journal of Catalysis, 246 (2007), pp. 177–192.

[186] R. Zhang, Y. Sun, S. Peng, In situ FTIR studies of methanol adsorption and dehydrogenation over Cu/SiO2 catalyst, Fuel, 81 (2002), pp. 1619–1624.

[187] J. Papavasiliou, G. Avgouropoulos, T. Ioannides, Steady-state isotopic transient kinetic

analysis of steam reforming of methanol over Cu-based catalysts, Applied Catalysis B: Environmental, 88 (2009), pp. 490–496.

[188] J. Cao, Y. Ma, G. Guan, X. Hao, X. Ma, Z. Wang, K. Kusakabe, A. Abudula, Reaction intermediate species during the steam reforming of methanol over metal modified molybdenum carbide catalysts, Applied Catalysis B: Environmental, 189 (2016), pp. 12–18.

[189] B.L. Kniep, F. Girgsdies, T. Ressler, Effect of precipitate aging on the microstructural characteristics of Cu/ZnO catalysts for methanol steam reforming, Journal of Catalysis, 236 (2005), pp. 34–44.

[190] L.C. Wang, Q. Liu, M. Chen, Y.M. Liu, Y. Cao, H.Y. He, K.N. Fan, Structural evolution and catalytic properties of nanostructured Cu/ZrO 2 catalysts prepared by oxalate gel-coprecipitation technique, Journal of Physical Chemistry C, 111 (2007), pp. 16549–16557.

[191] A. Goeppert, M. Czaun, J.P. Jones, G.K. Surya Prakash, G.A. Olah, Recycling of carbon dioxide to methanol and derived products-closing the loop, Chemical Society Reviews, 43 (2014), pp. 7995–8048.

[192] H. Yu, Y. Li, C. Xu, F. Jin, F. Ye, X. Li, Distinct facets to enhance the process of hydrogen production via methanol steam reforming — a review, Energy Storage and Saving, 1 (2022), pp. 53–69.

[193] M. Patrascu, M. Sheintuch, On-site pure hydrogen production by methane steam reforming in high flux membrane reactor: Experimental validation, model predictions and membrane inhibition, Chemical Engineering Journal, 262 (2015), pp. 862–874.

[194] A. Giaconia, G. Iaquaniello, G. Caputo, B. Morico, A. Salladini, L. Turchetti, G. Monteleone, A. Giannini, E. Palo, Experimental validation of a pilot membrane reactor for hydrogen production by solar steam reforming of methane at maximum 550 °C using molten salts as heat transfer fluid, International Journal of Hydrogen Energy, 45 (2020), pp. 33088–33101.

[195] P. Yan, Y. Cheng, Foam structured membrane reactor for distributed hydrogen production, Journal of Membrane Science, 661 (2022), pp. 120927.

[196] A.A. Lytkina, N.A. Zhilyaeva, M.M. Ermilova, N. V. Orekhova, A.B. Yaroslavtsev, Influence of the support structure and composition of Ni-Cu-based catalysts on

hydrogen production by methanol steam reforming, International Journal of Hydrogen Energy, 40 (2015), pp. 9677–9684.

[197] Y. Matsumura, H. Ishibe, High temperature steam reforming of methanol over Cu/ZnO/ZrO2 catalysts, Applied Catalysis B: Environmental, 91 (2009), pp. 524–532.

[198] M. Khanchi, S.M.A. Mousavian, S. Soltanali, Methanol steam reforming over Cu supported on SiO2, amorphous SiO2-Al2O3, and Al2O3 catalysts: Influence of support nature, International Journal of Energy Research, 46 (2022), pp. 3057–3071.

[199] J.E. Park, S.D. Yim, C.S. Kim, E.D. Park, Steam reforming of methanol over Cu/ZnO/ZrO2/Al 2O3 catalyst, International Journal of Hydrogen Energy, 39 (2014), pp. 11517–11527.

[200] J. Toyir, P. Ramírez De La Piscina, N. Homs, Ga-promoted copper-based catalysts highly selective for methanol steam reforming to hydrogen; Relation with the hydrogenation of CO2 to methanol, International Journal of Hydrogen Energy, 40 (2015), pp. 11261–11266.

[201] X. Hou, S. Qing, Y. Liu, L. Li, Z. Gao, Y. Qin, Enhancing effect of MgO modification of Cu–Al spinel oxide catalyst for methanol steam reforming, International Journal of Hydrogen Energy, 45 (2020), pp. 477–489.

[202] Y. Matsumura, Development of durable copper catalyst for hydrogen production by high temperature methanol steam reforming, International Journal of Hydrogen Energy, 38 (2013), pp. 13950–13960.

[203] R. Sharma, A. Kumar, R.K. Upadhyay, Bimetallic Fe-Promoted Catalyst for CO-Free Hydrogen Production in High-Temperature-Methanol Steam Reforming, ChemCatChem, 11 (2019), pp. 4568–4580.

[204] J. Zhao, G. Zhang, H. Liu, Q. Shu, Q. Zhang, Improved charge transfer and morphology on Ti-modified Cu/γ-Al2O3/Al catalyst enhance the activity for methanol steam reforming, International Journal of Hydrogen Energy, 47 (2022), pp. 18294–18304.

[205] Y.C. Pu, S.R. Li, S. Yan, X. Huang, D. Wang, Y.Y. Ye, Y.Q. Liu, An improved Cu/ZnO catalyst promoted by Sc2O3 for hydrogen production from methanol reforming, Fuel, 241 (2019), pp. 607–615.

[206] J. Lu, X. Li, S. He, C. Han, G. Wan, Y. Lei, R. Chen, P. Liu, K. Chen, L. Zhang, Y. Luo, Hydrogen production via methanol steam reforming over Ni-based catalysts: Influences

of Lanthanum (La) addition and supports, International Journal of Hydrogen Energy, 42 (2017), pp. 3647–3657.

[207] Y. Lei, Y. Luo, X. Li, J. Lu, Z. Mei, W. Peng, R. Chen, K. Chen, D. Chen, D. He, The role of samarium on Cu/Al2O3 catalyst in the methanol steam reforming for hydrogen production, Catalysis Today, 307 (2018), pp. 162–168.

[208] S.Q. Yang, J.P. He, N. Zhang, X.W. Sui, L. Zhang, Z.X. Yang, Effect of rare-earth element modification on the performance of Cu/ZnAl catalysts derived from hydrotalcite precursor in methanol steam reforming, Ranliao Huaxue Xuebao/Journal of Fuel Chemistry and Technology, 46 (2018), pp. 179–188.

[209] C.P. Thurgood, J.C. Amphlett, R.F. Mann, B.A. Peppley, Deactivation of Cu/ZnO/Al2O3 catalyst: Evolution of site concentrations with time, Topics in Catalysis, 22 (2003), pp. 253–259.

[210] M. Mrad, D. Hammoud, C. Gennequin, A. Aboukaïs, E. Abi-Aad, A comparative study on the effect of Zn addition to Cu/Ce and Cu/Ce-Al catalysts in the steam reforming of methanol, Applied Catalysis A: General, 471 (2014), pp. 84–90.

[211] A. Wang, Y. Zhang, P. Fu, Q. Zheng, Q. Fan, P. Wei, L. Zheng, Achieving strong thermal stability in catalytic reforming of methanol over in-situ self-activated nano Cu2O/ZnO catalyst with dual-sites of Cu species, Journal of Environmental Chemical Engineering, 10 (2022), pp. 107676.

[212] M. Chen, G. Sun, Y. Wang, D. Liang, C. Li, J. Wang, Q. Liu, Steam reforming of methanol for hydrogen production over attapulgite-based zeolite-supported Cu-Zr catalyst, Fuel, 314 (2022), pp. 122733.

[213] I. Ritzkopf, S. Vukojević, C. Weidenthaler, J.D. Grunwaldt, F. Schüth, Decreased CO production in methanol steam reforming over Cu/ZrO2 catalysts prepared by the microemulsion technique, Applied Catalysis A: General, 302 (2006), pp. 215–223.

[214] H. Jeong, K.I. Kim, T.H. Kim, C.H. Ko, H.C. Park, I.K. Song, Hydrogen production by steam reforming of methanol in a micro-channel reactor coated with Cu/ZnO/ZrO2/Al2O3 catalyst, Journal of Power Sources, 159 (2006), pp. 1296–1299.

[215] F. Liang, Y. Yu, W. Zhou, X. Xu, Z. Zhu, Highly defective CeO2 as a promoter for efficient and stable water oxidation, Journal of Materials Chemistry A, 3 (2015), pp. 634–640.

[216] S. Yang, F. Zhou, Y. Liu, L. Zhang, Y. Chen, H. Wang, Y. Tian, C. Zhang, D. Liu, Morphology effect of ceria on the performance of CuO/CeO2 catalysts for hydrogen production by methanol steam reforming, International Journal of Hydrogen Energy, 44 (2019), pp. 7252–7261.

[217] W. Tong, K. Cheung, A. West, K.M. Yu, S.C.E. Tsang, Direct methanol steam reforming to hydrogen over CuZnGaOx catalysts without CO post-treatment: Mechanistic considerations, Physical Chemistry Chemical Physics, 15 (2013), pp. 7240–7248.

[218] G. Zhang, J. Zhao, Q. Wang, T. Yang, Q. Zhang, L. Zhang, Fast start-up structured CuFeMg/Al2O3 catalyst applied in microreactor for efficient hydrogen production in methanol steam reforming, Chemical Engineering Journal, 426 (2021), pp. 130644.

[219] N. Iwasa, S. Masuda, N. Takezawa, Steam reforming of methanol over Ni, Co, Pd and Pt supported on ZnO, Reaction Kinetics & Catalysis Letters, 55 (1995), pp. 349–353.

[220] N. Iwasa, T. Mayanagi, N. Ogawa, K. Sakata, N. Takezawa, New catalytic functions of Pd–Zn, Pd–Ga, Pd–In, Pt–Zn, Pt–Ga.pdf, Catalysis Letters, 54 (1998), pp. 119–123.

[221] E.S. Ranganathan, S.K. Bej, L.T. Thompson, Methanol steam reforming over Pd/ZnO and Pd/CeO2 catalysts, Applied Catalysis A: General, 289 (2005), pp. 153–162.

[222] N. Iwasa, N. Takezawa, New supported Pd and Pt alloy catalysts for steam reforming and dehydrogenation of methanol, Topics in Catalysis, 22 (2003), pp. 215–224.

[223] N. Iwasa, S. Kudo, H. Takahashi, S. Masuda, N. Takezawa, Highly selective supported Pd catalysts for steam reforming of methanol, Catalysis Letters, 19 (1993), pp. 211–216.

[224] N. Iwasa, S. Masuda, N. Ogawa, N. Takezawa, Steam reforming of methanol over Pd/ZnO: Effect of the formation of PdZn alloys upon the reaction, Applied Catalysis A, General, 125 (1995), pp. 145–157.

[225] Y.H. Chin, Y. Wang, R.A. Dagle, X.S. Li, Methanol steam reforming over Pd/ZnO: Catalyst preparation and pretreatment studies, Fuel Processing Technology, 83 (2003), pp. 193–201.

[226] S. Liu, K. Takahashi, M. Ayabe, Hydrogen production by oxidative methanol reforming on Pd/ZnO catalyst: Effects of Pd loading, Catalysis Today, 87 (2003), pp. 247–253.

[227] T. Conant, A.M. Karim, V. Lebarbier, Y. Wang, F. Girgsdies, R. Schlögl, A. Datye,

Stability of bimetallic Pd-Zn catalysts for the steam reforming of methanol, Journal of Catalysis, 257 (2008), pp. 64–70.

[228] J. Lu, Y. Lei, G. Wan, Z. Mei, J. Yu, Y. Zhao, S. He, Y. Luo, Weakening the metal-support strong interaction to enhance catalytic performances of alumina supported Ni-based catalysts for producing hydrogen, Applied Catalysis B: Environmental, 263 (2020), pp. 118177.

[229] M. Khzouz, J. Wood, B. Pollet, W. Bujalski, Characterization and activity test of commercial Ni/Al2O3, Cu/ZnO/Al2O3 and prepared Ni-Cu/Al2O3 catalysts for hydrogen production from methane and methanol fuels, International Journal of Hydrogen Energy, 38 (2013), pp. 1664–1675.

[230] M. Khzouz, E.I. Gkanas, S. Du, J. Wood, Catalytic performance of Ni-Cu/Al2O3 for effective syngas production by methanol steam reforming, Fuel, 232 (2018), pp. 672–683.

[231] X. Liu, Y. Men, J. Wang, R. He, Y. Wang, Remarkable support effect on the reactivity of Pt/In2O3/MOx catalysts for methanol steam reforming, Journal of Power Sources, 364 (2017), pp. 341–350.

[232] V. Shanmugam, S. Neuberg, R. Zapf, H. Pennemann, G. Kolb, Hydrogen production over highly active Pt based catalyst coatings by steam reforming of methanol: Effect of support and co-support, International Journal of Hydrogen Energy, 45 (2020), pp. 1658–1670.

[233] P. Mierczynski, K. Vasilev, A. Mierczynska, W. Maniukiewicz, M.I. Szynkowska, T.P. Maniecki, Bimetallic Au-Cu, Au-Ni catalysts supported on MWCNTs for oxy-steam reforming of methanol, Applied Catalysis B: Environmental, 185 (2016), pp. 281–294.

[234] A.A. Lytkina, N. V. Orekhova, M.M. Ermilova, S. V. Belenov, V.E. Guterman, M.N. Efimov, A.B. Yaroslavtsev, Bimetallic carbon nanocatalysts for methanol steam reforming in conventional and membrane reactors, Catalysis Today, 268 (2016), pp. 60–67.

[235] O.Z. Tajrishi, M. Taghizadeh, A.D. Kiadehi, Methanol steam reforming in a microchannel reactor by Zn-, Ce- and Zr- modified mesoporous Cu/SBA-15 nanocatalyst, International Journal of Hydrogen Energy, 43 (2018), pp. 14103–14120.

[236] Y. Wang, H. Liu, D. Mei, S. Yu, Direct ink writing of 3D SiC scaffold as catalyst support

for thermally autonomous methanol steam reforming microreactor, Renewable Energy, 187 (2022), pp. 923–932.

[237] M. Liao, C. Guo, W. Guo, T. Hu, H. Qin, P. Gao, H. Xiao, Hydrogen production in microreactor using porous SiC ceramic with a pore-in-pore hierarchical structure as catalyst support, International Journal of Hydrogen Energy, 45 (2020), pp. 20922–20932.

[238] W. Zhou, Y. Ke, Q. Wang, S. Wan, J. Lin, J. Zhang, K.S. Hui, Development of cylindrical laminated methanol steam reforming microreactor with cascading metal foams as catalyst support, Fuel, 191 (2017), pp. 46–53.

[239] M. De Falco, G. Iaquaniello, A. Salladini, Experimental tests on steam reforming of natural gas in a reformer and membrane modules (RMM) plant, Journal of Membrane Science, 368 (2011), pp. 264–274.

[240] J. Agrell, H. Birgersson, M. Boutonnet, Steam reforming of methanol over a Cu/ZnO/Al2O3 catalyst: A kinetic analysis and strategies for suppression of CO formation, Journal of Power Sources, 106 (2002), pp. 249–257.

[241] G. Wang, F. Wang, L. Li, G. Zhang, Experiment of catalyst activity distribution effect on methanol steam reforming performance in the packed bed plate-type reactor, Energy, 51 (2013), pp. 267–272.

[242] J. Kang, Y. Song, T. Kim, S. Kim, Recent trends in the development of reactor systems for hydrogen production via methanol steam reforming, International Journal of Hydrogen Energy, 47 (2022), pp. 3587–3610.

[243] S.W. Perng, R.F. Horng, H.W. Ku, Effects of reaction chamber geometry on the performance and heat/mass transport phenomenon for a cylindrical methanol steam reformer, Applied Energy, 103 (2013), pp. 317–327.

[244] P. Nehe, V.M. Reddy, S. Kumar, Investigations on a new internally-heated tubular packed-bed methanol-steam reformer, International Journal of Hydrogen Energy, 40 (2015), pp. 5715–5725.

[245] H. Shi, H. Ibrahim, M.M. Elamin, R. Idem, P. Tontiwachwuthikul, Kinetics and Reactor Modeling of the Steam Reforming of Methanol over a Mn-Promoted Cu/Al Catalyst, Chemical Engineering and Technology, 38 (2015), pp. 2305–2315.

[246] H. Zhang, C. Xu, H. Yu, H. Wu, F. Jin, F. Xiao, Z. Liao, Enhancement of methanol

steam reforming in a tubular fixed-bed reactor with simultaneous heating inside and outside, Energy, 254 (2022), pp. 124330.

[247] R. Chein, Y.C. Chen, J.N. Chung, Numerical study of methanol-steam reforming and methanol-air catalytic combustion in annulus reactors for hydrogen production, Applied Energy, 102 (2013), pp. 1022–1034.

[248] Y. Shi, X. Du, L. Yang, Y. Sun, Y. Yang, Experiments on hydrogen production from methanol steam reforming in fluidized bed reactor, International Journal of Hydrogen Energy, 38 (2013), pp. 13974–13981.

[249] Z. Chen, J.R. Grace, C. Jim Lim, A. Li, Experimental studies of pure hydrogen production in a commercialized fluidized-bed membrane reactor with SMR and ATR catalysts, International Journal of Hydrogen Energy, 32 (2007), pp. 2359–2366.

[250] F. Zhang, Y. Shi, L. Yang, X. Du, Kinetics for hydrogen production by methanol steam reforming in fluidized bed reactor, Science Bulletin, 61 (2016), pp. 401–405.

[251] O. Sanz, I. Velasco, I. Pérez-Miqueo, R. Poyato, J.A. Odriozola, M. Montes, Intensification of hydrogen production by methanol steam reforming, International Journal of Hydrogen Energy, 41 (2016), pp. 5250–5259.

[252] M. Pan, Q. Wu, L. Jiang, D. Zeng, Effect of microchannel structure on the reaction performance of methanol steam reforming, Applied Energy, 154 (2015), pp. 416–427.

[253] X. Du, Y. Shen, L. Yang, Y. Shi, Y. Yang, Experiments on hydrogen production from methanol steam reforming in the microchannel reactor, International Journal of Hydrogen Energy, 37 (2012), pp. 12271–12280.

[254] J.Y. Won, H.K. Jun, M.K. Jeon, S.I. Woo, Performance of microchannel reactor combined with combustor for methanol steam reforming, Catalysis Today, 111 (2006), pp. 158–163.

[255] R.Y. Chein, Y.C. Chen, Y.S. Lin, J.N. Chung, Experimental study on the hydrogen production of integrated methanol-steam reforming reactors for PEM fuel cells, International Journal of Thermal Sciences, 50 (2011), pp. 1253–1262.

[256] Y. Wang, H. Liu, D. Mei, Q. Wu, H. Zhou, A novel thermally autonomous methanol steam reforming microreactor using SiC honeycomb ceramic as catalyst support for hydrogen production, International Journal of Hydrogen Energy, 46 (2021), pp. 25878–25892.

[257] S. Sá, J.M. Sousa, A. Mendes, Methanol steam reforming in a dual-bed membrane reactor for producing PEMFC grade hydrogen, Catalysis Today, 156 (2010), pp. 254–260.

[258] S.H. Israni, M.P. Harold, Methanol steam reforming in single-fiber packed bed Pd-Ag membrane reactor: Experiments and modeling, Journal of Membrane Science, 369 (2011), pp. 375–387.

[259] S. Kim, S.W. Yun, B. Lee, J. Heo, K. Kim, Y.T. Kim, H. Lim, Steam reforming of methanol for ultra-pure H2 production in a membrane reactor: Techno-economic analysis, International Journal of Hydrogen Energy, 44 (2019), pp. 2330–2339.

[260] M. Saidi, Performance assessment and evaluation of catalytic membrane reactor for pure hydrogen production via steam reforming of methanol, International Journal of Hydrogen Energy, 42 (2017), pp. 16170–16185.

[261] R. Sharma, A. Kumar, R.K. Upadhyay, Performance comparison of methanol steam reforming integrated to Pd-Ag membrane: Membrane reformer vs. membrane separator, Separation and Purification Technology, 183 (2017), pp. 194–203.

[262] S. Liguori, A. Iulianelli, F. Dalena, V. Piemonte, Y. Huang, A. Basile, Methanol steam reforming in an Al2O3 supported thin Pd-layer membrane reactor over Cu/ZnO/Al2O3catalyst, International Journal of Hydrogen Energy, 39 (2014), pp. 18702–18710.

[263] A. Iulianelli, K. Ghasemzadeh, A. Basile, Progress in methanol steam reforming modelling via membrane reactors technology, Membranes, 8 (2018), pp. 1–22.

[264] N. Itoh, Y. Kaneko, A. Igarashi, Efficient hydrogen production via methanol steam reforming by preventing back-permeation of hydrogen in a palladium membrane reactor, Industrial and Engineering Chemistry Research, 41 (2002), pp. 4702–4706.

[265] O. Jazani, J. Bennett, S. Liguori, Carbon-low, renewable hydrogen production from methanol steam reforming in membrane reactors – a review, Chemical Engineering and Processing - Process Intensification, 189 (2023), pp. 109382.

[266] Suhaib Muhammed Ali, Solar-Hydrogen Systems for Remote Area Power Supply, RMIT University, 2007.

[267] M. Byun, B. Lee, H. Lee, S. Jung, H. Ji, H. Lim, Techno-economic and environmental assessment of methanol steam reforming for H2 production at various scales,

International Journal of Hydrogen Energy, 45 (2020), pp. 24146–24158.

[268] M.J. Cole, The generator of pure hydrogen for industrial applications, Platinum Metals Review, 25 (1981), pp. 12–13.

[269] J.E. Philpott, Hydrogen Diffusion Technology., Platinum Metals Review, 29 (1985), pp. 12–16.

[270] Element1, Affordable Hydrogen Generation, Element 1, (2022), pp. 1–3. https://www.e1na.com/resource/affordable-hydrogen-generation (accessed April 15, 2023).

[271] U.S. Department of Energy, Report of the DOE Workshop on Hydrogen Separations and Purification, U.S. Department of Energy Office of Hydrogen, Fuel Cells & Infrastructure Technologies, US, Arlington, VA, 2004.

CHAPTER 3: Pd-Ag Membrane: Preparation, Characterization, and Testing

Abstract

This chapter provides an overview of the key attributes shown by Pd-Ag membranes in the context of hydrogen separation. A concise overview of hydrogen separation through the Pd-Ag membrane with specific emphasis on recent advancements in various support types and materials employed for surface modification. Following the overview a composite Pd-Ag membrane is prepared using ELP technique over the alumina support. The surface pore-mouth of the support is modified using a 2B-graphite lead owing to its enhanced ductility, thermo-electrical conductivity, and exceptional resistance to thermal shocks, all at a relatively economical price. Multiple cycles of deposition are performed to obtain a dense Pd-Ag membrane till 400 kPaG. Ten similar membranes are prepared following the same methodology. The surface morphology and elemental composition are further monitored using a scanning electron microscope (SEM) and energy dispersive spectroscopy (EDS) respectively. After the preliminary leak test using the rising water bubble point technique, the permeation properties of the membrane are examined by subjecting it to pure H_2 and N_2 under varying temperatures (573 K to 773 K) and pressure (100 kPaG to 300 kPaG) conditions. The investigation also encompasses the examination of the effect of mixture gases, such as H_2/N_2, H_2/CO_2, H_2/CH_4, and H_2/CO, on the performance of the membrane. In addition to this, the long-term thermal heat cycle stability of the membrane is performed to assess its potential for commercial exploitation followed by surface characterization after testing. Lastly, the effect of feed load is investigated with pure H_2 as well as H_2/N_2 mixture gas with varying compositions to assess its separation ability for enhanced hydrogen separation.

3.1. Introduction

Palladium membranes have been the subject of increasing interest for hydrogen purification, particularly in membrane reactors for process intensification, owing to their exceptionally high permeability and ideally infinite selectivity for H_2. The majority of commercially accessible Pd-alloy-based membranes have a significant thickness, typically exceeding 20 μm, resulting in high costs and limited H_2 permeability [1]. Consequently, their widespread usage is constrained. Prior to advancing toward large-scale implementation, it is necessary to optimize the trade-off among membrane thickness, cost, permeability, and selectivity. The commercial Pd-based membrane is expected to have a supported structure, consisting of a thin selective layer on top of a porous support, to ensure sufficient mechanical durability. However, according to Theon et al. [2] the cost of support constitutes a majority part of the entire membrane module in the case of the very thin membrane (< 2 μm). As a result, the choice of the support becomes vital. The asymmetric porous ceramic support with a steady decrease in pore size is commonly used for depositing a thin layer of Pd due to its excellent surface quality and narrow pore size distribution. Before depositing the Pd selective layer, it is essential to consider many characteristics of the porous support, including pore size distribution or media grade (pore-mouth and pore-throat), surface smoothness, thermal expansion coefficient, and chemical compatibility. It is widely acknowledged that the morphology and continuity of the selective layer are predominantly influenced by both pore size and roughness [3–6]. Unfortunately, the integration of alumina into a membrane reactor poses a significant obstacle owing to its fragile structure and poor mechanical strength in comparison to metallic support systems. To overcome this issue, researchers have suggested the utilization of graphite ferrules as a sealing medium for the purpose of connecting the alumina tube with metallic fittings. Furthermore, it is possible to connect porous alumina tubes with dense ones by utilizing a glass sealant that exhibits excellent thermal resistance [7,8]. Metallic supports exhibit more robustness compared to ceramic supports in terms of their integration with the reactor. Nevertheless, the support available in the market has significant drawbacks such as the presence of large pores, an uneven distribution of pore sizes, and a high degree of surface roughness. The interdiffusion of Pd and the metallic support results in a drastic decrease in the perm-selectivity of the membrane. To address this challenge, a variety of intermetallic diffusion barriers are deposited onto the support. These barriers include α-Al_2O_3 [9], γ-Al_2O_3 [10], YSZ [11], ZrO_2 [12,13], TiO_2 [14], CeO_2 [15], zeolite [16], graphite [17], and the oxide layer (Fe_2O_3-Cr_2O_3) [18,19]. Dip coating, powder suspension deposition, and atmospheric

plasma spraying are the prevailing methods employed for the deposition of intermetallic diffusion barriers [1,20]. However, an extra mass transfer resistance is induced. Moreover, careful composition control, multiple rounds of deposition, and repeated sintering are required which adds to the overall cost of membrane preparation.

Often the pure Pd-based membranes experience hydrogen embrittlement below the critical temperature (571 K) and pressure (2000 kPaG) due to the phase transition of the Pd-H system from α to β phase [21]. The coexistence of both phases is observed in a pure Pd membrane, which displays a face-centered cubic (FCC) lattice structure. In the case of an H_2-free Pd membrane, the lattice parameters of the crystal unit cell exhibit an increase from 0.3890 nm to 0.3895 nm (H/Pd < 0.03) in the α-phase, while in the β-phase, the increase is up to 0.410 nm (H/Pd < 0.6). During the process of temperature cycling, the transformation from the α phase to the β phase is anticipated to cause a volumetric expansion of approximately 10%. This significant expansion has the potential to induce substantial deformation, hence increasing the risk of membrane failure. Researchers have proposed the incorporation of several metals, such as Ag, Cu, Au, Pt, Ni, Fe, Y, Ce, Ru, etc., into Pd alloys as a potential solution to address the difficulties associated with phase change and H_2 embrittlement [22–28]. The α to β-phase transition exhibits a notable decrease in both the critical temperature and average bond distance. This decrease has the effect of lowering the extent of crystal lattice distortion caused by the cyclic absorption and desorption of H_2. For instance, the critical temperature is even lowered to 298 K for Pd-Cu (8% Cu), Pd-Pt (19% Pt), and Pd-Ni (19% Ni), whereas it is 323 K when more than 20-30 wt.% of Ag is alloyed with Pd [29,30]. When the silver content reaches 23 wt.% Ag, the maximum permeability of H_2 is obtained, which is 1.6-1.8 times higher compared to the permeability of pure Pd. Furthermore, it has been shown that silver has a similar electron-donating effect to that of hydrogen in palladium. Consequently, both silver and hydrogen engage in a competitive process to occupy the electron vacancies in the 4d band of palladium. Later on, Makrides [31] reported that the Pd-Ag alloy exhibits two notable effects on solubility. Firstly, at low pressures (below the critical pressure for the α-β phase transition), the solubility of hydrogen increases up to a silver content of 25 atomic percent. This increase can be attributed to an interaction between an interstitial hydrogen atom and a silver ion. Secondly, as the silver content exceeds 30 atomic percent, the maximum solubility of hydrogen decreases. This decrease is likely due to alterations in the electronic structure of the Pd-Ag resulting from the introduction of silver into the palladium lattice. Moreover, the crystal

structure variation from FCC to body-centered cubic (BCC) with changing temperature also contributes toward enhanced H_2 permeability.

Several approaches have been suggested for the deposition of dense Pd and Pd-alloy layers onto a substrate composed of either porous ceramic or porous metallic material. In this respect, the techniques most frequently employed include cold rolling electroplating, spray pyrolysis, chemical vapor deposition (CVD), magnetron sputtering (MS), and electroless plating (ELP). Amongst them most widely used is ELP owing to its ability to achieve a uniform coating even on non-conductive material with complex geometry, the absence of a need for external energy, its low cost, better adhesion characteristics, and the utilization of simple equipment [1,32]. Previously, several studies have been conducted to prepare Pd-Ag membranes using ELP on different supports. In the following part, a succinct literature overview of the preparation of Pd-Ag membranes is presented.

3.1.1. Literature Review on Pd-Ag Membrane

Rhoda et al. [33] first proposed the ELP bath composition for Pd plating using hydrazine as a reducing agent. A linear correlation is observed between the plating rate and temperature in the range of 311 K to 353 K. However, the bath suffered precipitation above 347 K when Ethylenediaminetetraacetic acid (EDTA) was not present. Furthermore, it is seen that the plating experiences a rapid decline over time as a result of the exhaustion of both Pd^{2+} ions and N_2H_4. In the context of bi-metallic alloys, such as Pd-Ag, ELP is performed using either sequential or co-deposition techniques. Equations 3.1, 3.2, and 3.3 describe the redox reaction involved in the process of Pd deposition. Similarly, Equations 3.4, 3.5, and 3.6 represent the redox reaction involved in the process of Ag deposition. However, the process of alloying the metal layer formed using a sequential deposition approach may necessitate prolonged thermal treatment (> 12 hr) at elevated temperatures (773-1173 K). Consequently, the Pd-Ag layer can develop pinholes, cracks, and delamination from the support material as a result of inadequate adhesion and variations in thermal expansion coefficients. Insufficient alloying may lead to a decrease in the permeate H_2 flux. For instance, Uemiya et al. [3] observed a significant decrease in permeate H_2 flux following heat treatment at 773 K in comparison to 1173 K. An Energy Dispersive Spectroscopy (EDS) examination conducted on the cross-section demonstrated the homogeneous dispersion of Pd-Ag when thermally treated at 1173 K. However, multi-layer deposition of very thin Pd and Ag layers can reduce the alloying temperature and time [34]. On the contrary, co-deposition necessitates a comparatively reduced duration and lower

temperatures to achieve full alloy formation between the Pd-Ag particles. In this scenario, the competitive deposition of the Ag^{+} ion onto the Pd^{0} nuclei hinders the deposition of the Pd^{2+} ion. This behavior is mainly attributed to the lower standard hydrogen electrode (SHE) potential (a measure of the tendency of a chemical species to acquire electrons and thereby be reduced) of Ag^{+} ion (SHE = +0.799 V) compared to Pd^{2+} ion (SHE = +0.987 V). Additionally, the SHE of the Pd and Ag in the bath is reduced by the addition of complexing agents such as NH_3 and ethylenediaminetetraacetic acid (EDTA). The reported stability constants for the complexation processes of NH_3 and EDTA with Pd are 10^{32} and 10^{18}, respectively. Similarly, the equivalent values for Ag are reported to be $10^{7.2}$ and $10^{7.3}$, respectively [35]. Hence, it is imperative to meticulously tune the composition of the plating bath. It is crucial that the support surface possesses a sufficient amount of Pd-nuclei to effectively allow the deposition of Pd-Ag [36]. To mitigate the selective deposition of Ag on the freshly activated support, Shu et al. [37] proposed the application of a thin Pd layer prior to commencing the co-deposition process. To achieve the simultaneous deposition of Pd-Ag, Tanaka et al. [38] conducted optimization experiments of Pd-Ag co-deposition on the amounts of hydrazine (which promotes Ag deposition) and ammonia (which inhibits Ag deposition). This was done to effectively manage the deposition rate of both Pd and Ag. It has been observed that the utilization of a 5 M ammonia solution is appropriate when the Ag concentration surpasses 20% (% by wt.). Conversely, a 4 M ammonia solution is deemed enough for Ag content below 20% (% by wt.). Therefore, in order to produce a membrane with a high silver content, it is recommended to use a plating bath that has a high concentration of ammonia and a low concentration of hydrazine (< 5 mM). Similarly, Fernandez et al., [8] deposited a 3.6 µm thickness Pd-Ag layer over alumina support using co-deposition. However, to increase the Ag content (13-15 wt. %) in the membrane, they added a booster silver nitrate solution (12.5 mM) periodically at the rate of 0.117 ml min^{-1}. This way they successfully managed to maintain a high Ag content. They achieved an H_2/N_2 ideal perm-selectivity of 8000-10000 at 673 K and 200 kPaG. In a further development, Melendez et al. [39] used co-deposition to successfully prepare an ultra-thin Pd-Ag membrane over asymmetric tubular alumina support by tuning the chemical composition of the plating bath. The thickness ranged from 200 nm to 1.3 µm by regulating the time of plating, whereas the Ag content varied from 7% to 8.2% (wt. %). Mejdell et al. [40] prepared a 1.4 µm ultra-thin self-supported Pd-Ag (wt. %) membrane in a microchannel-based configuration. Permeance of 1.7×10^{-2} mol m^{-2} s^{-1} $Pa^{-0.5}$ was achieved at 573 K. However, the H_2/N_2 selectivity reduced to 390 from 5700 at 300 kPaG after 7 days of testing and thermal cycling with H_2/N_2 mixture gas. Peter et al. [41] successfully developed a

Pd-Ag (23 wt. %) membrane with 1.9-3.8 µm thickness using magnetron sputtering. H_2/N_2 perm-selectivity of 2900 was obtained at 2500 kPaG having a permeance of 1.5×10^{-2} mol m^{-2} s^{-1} $Pa^{-0.5}$ at 673 K. Recently, Agnolin et al. [42] developed a methodology to reduce the pore size of the metallic Hastelloy filters systematically using the α-Al_2O_3 filler particle having particle size of 18 µm, 5 µm, and 1.5 µm. Lastly an intermetallic diffusion barrier of a mesoporous γ-Al_2O_3 layer about 540 nm thick was deposited which finally reduced the pore size distribution to 200 nm. Multiple cycle of filler was coated to achieve sufficient surface smoothness. Membrane having asymmetric filling of the pores showed maximum H_2/N_2 selectivity of ~40000 at 673 K and 100 kPaG with H_2 permeance of 7×10^{-7} mol m^{-2} s^{-1} Pa.

For palladium:

$$\text{Overall: } 2Pd(NH_3)_4^{+2} + N_2H_4 + 4OH^- \longrightarrow 2Pd + N_2\uparrow + 4H_2O + 8NH_3 \quad (3.1)$$

$$\text{Anodic: } N_2H_4 + 4OH^- \longrightarrow N_2\uparrow + 4H_2O + 4e \quad (3.2)$$

$$\text{Cathodic: } 2Pd(NH_3)_4^{+2} + 4e \longrightarrow 2Pd + 8NH_3 \quad (3.3)$$

For silver:

$$\text{Overall: } 4Ag(NH_3)_2^{+} + N_2H_4 + 4OH^- \longrightarrow 4Ag + N_2\uparrow + 4H_2O + 8NH_3 \quad (3.4)$$

$$\text{Anodic: } N_2H_4 + 4OH^- \longrightarrow N_2\uparrow + 4H_2O + 4e \quad (3.5)$$

$$\text{Cathodic: } 4Ag(NH_3)_2^{+} + 4e \longrightarrow 4Ag + 8NH_3 \quad (3.6)$$

Therefore, it is essential to tune the plating bath composition, and time of plating to achieve the desired membrane thickness and composition. These processes necessitate the deposition of many layers and subsequent heat sintering at high temperatures. This eventually leads to an increase in the overall cost of the membrane. In addition, the chemicals necessary for synthesizing the asymmetric support give rise to significant environmental concerns. Hence, to mitigate the expenses associated with support modification the utilization of 2B-graphite lead pencil coating has been proposed by Hu et al. [5]. In comparison to alternative materials employed for surface modification or even as the intermediate layer, 2B-graphite lead exhibits superior ductility, thermo-electrical conductivity, and exceptional resistance to thermal shocks, all at a relatively affordable price point. Moreover, the graphite lead has sufficient slit-type pores which further facilitates the gas diffusion. They successfully prepared a membrane of 5 µm thickness using ELP with the H_2/N_2 selectivity of 3700 and permeate H_2 flux of 25 m^3 m^{-2} h^{-1} at 100 kPa and 723 K. Moreover, the membrane showed excellent thermal stability for 330 h at 723 K. In a separate study, Hu et al. [43] deposited NiO (2.8 wt. % Ni) over alumina

support via impregnation to minimize the CO content on the permeate side. The NiO-impregnated alumina is further modified using 2B-graphite lead over which 5 µm Pd-layer is deposited using ELP called a by-functional membrane. It is observed that the Ni impregnation effectively catalyzes the methanation of CO and CO_2 making the permeate stream ideal for PEMFCs. The levels of CO and CO_2 experience a decrease of at least tenfold compared to membranes without NiO coating. Similarly, Wei et al. [17] applied the 2B-graphite lead on PSS support and deposited Pd using ELP (Pd thickness = 7 µm). Nevertheless, they observed delamination of the palladium (Pd) layer, which was afterward rectified by the application of vacuum suction during the plating process. Despite the implementation of a vacuum, the attained perm-selectivity of H_2/N_2 remained below 150. Terra et al. [44] used alumina hollow fiber and reduced the surface roughness from 120 nm to 37 nm by a graphite coating. It required 2 rounds of Pd plating after graphite coating (Pd thickness = 1.81 µm) to attain a completely dense membrane which is 3 rounds without graphite coating (Pd thickness = 2.41 µm). Recently Martinez-Diaz et al. [45] prepared a 17 µm thick Pd membrane using the electroless pore plating (ELPP) technique over 2B-graphite lead-modified PSS support. The membrane demonstrated excellent mechanical strength despite changing the direction of the permeate flux from in-out to out-in condition. The H_2 permeance ranges from 3.24×10^{-4} to 4.33×10^{-4} mol m^{-2} s^{-1} $Pa^{-0.5}$ with H_2/N_2 perm-selectivity above 10,000 under out–in mode at temperatures ranging from 623 K to 723 K.

It is also important to note that the strong interaction between the Pd layer and the alumina support (Pd-Al alloy) significantly reduces the hydrogen permeation at temperatures above 873 K as reported by Okazaki et al. [46]. Based on their findings, Okazaki et al. [36] proposed the utilization of a ZrO_2 and YSZ layer at elevated temperatures (up to 923 K) to prevent any interaction with Pd. Furthermore, Straczewski et al. [47] noted that TiO_2 layers exhibit instability when subjected to thermal cycling. In addition to this, the Pd-Ag membrane exhibits the migration of Ag on its surface when subjected to prolonged exposure to H_2, owing to the lower surface tension of Ag in comparison to Pd. Nevertheless, this occurrence can be reduced at higher temperatures [48]. For long-term operation, the Pd-Ag membrane may experience grain development and the production of pin-holes, particularly when the temperature exceeds 723 K. This can be primarily due to the localized changes in the topography of the macro-porous support [49]. Zang et al. [50] observed that the Pd-Ag layer experienced leak growth as a result of the sublimation of Ag at temperatures over 873 K during continuous operation. Furthermore, the H_2 flux decreased at temperatures of 873 K and higher for membranes having

a thickness less than 10 µm. This is caused by the formation of crystallites depleted in silver on the surface of the membrane. Nevertheless, the precise understanding of the textural and stoichiometric inhomogeneity remains incomplete due to the unidentified activity within the Pd-Ag hydride system. Impurities induced during the preparation of the membrane also contribute to the formation of pin-holes during long-term operation. According to Abu El Hawa et al. [51], at a temperature of 823 K, both Pd-Pt and Pd-Ru alloys exhibit decreased rates of leak evolution compared to pure Pd. Additionally, both alloys maintain a consistent H_2 permeation flux up to a temperature of 873 K.

3.2. Experimental Methodology

From the above discussion, it can be inferred that the capability to produce a Pd-based membrane in a controlled way enhances the appeal of the ELP technique over others for depositing dense layers of Pd and Pd-alloys onto a porous support. The porous alumina tubular support (O.D. = 10 mm, I.D. = 7 mm, and 150 mm long) with 23% porosity is provided by M/s Kumar Ceramics Pvt Ltd., India, over which the $Pd_{85}Ag_{15}$ (85 wt.% Pd and 15 wt.% Ag) metallic selective layer is deposited. The average pore size distribution of the support is approximately 0.2 µm where some of the largest pores are in the range of 5-8 µm as determined using the 'Rising Water Bubble Point Technique'. Ten identical membranes have been prepared using the same approach. The details of the membrane preparation, characterization, and performance testing are discussed in the subsequent sub-section.

3.2.1. Support Cleaning, Modification, and Activation

Surface cleaning is a necessary procedure to achieve a deposit that is adherent, consistent, and free from defects. The process of cleaning involves the utilization of various cleaning agents, including alkaline solutions, detergents, and diluted acids [52]. The potential impurities present on the porous substrate include ceramic powders, typically originating from post-sintering activities such as cutting processes. Additionally, organic substances from fingerprints and handling, as well as grease, oil, and dirt, may also be encountered [53,54]. A typical composition of the cleaning solution is given in Table 3.1. The basic solution eliminates fats, oils, and other organic substances. Ultrasound irradiation is employed to enhance the reactivity of soluble organic solvents, facilitating their dissolution within the solvent medium. Additionally, the application of sonication is effective in the removal of residual clay and dust particles from the inside of the pores. Before the cleaning process, the alumina support undergoes gritting with 1000 SiC sandpaper to eliminate any additional ceramic patches that may have formed during the production stage. Then the tube is submerged in an alkaline solution (pH > 10), which is formulated using the chemical composition specified in Table 3.1. Subsequently, the support is subjected to ultrasonic irradiation for a duration of 60 minutes at a temperature of 333 K. Additionally, the support underwent a thorough washing process using de-ionized (DI) water to eliminate any residual basic solution that may be present within the pores of the support material. This washing step is carried out for 10 minutes at 333 K. To determine the pH of the liquid retained within the pores, a strip of pH paper was applied to the moist surface of the samples. The DI water rinse stage stopped when achieving a pH of 7,

typically necessitating 4 to 5 cycles of washing. The support is further immersed in isopropanol for 40 minutes at 333 K to facilitate the fast drying of the support. At last, the support is dried at 393 K for 4 to 5 hours [53,54].

Table 3. 1. Typical chemical composition for cleaning PSS and alumina supports.

	Chemicals	Alumina	PSS
Alkaline	Sodium phosphate	45 g L^{-1}	45 g L^{-1}
	Sodium carbonate	65 g L^{-1}	65 g L^{-1}
	Sodium hydroxide	45 g L^{-1}	45 g L^{-1}
	Detergent	5 mL	5 mL
Acidic	HCl	NA	0.1M
Neutral	2-propanol (91%)	Yes	Yes

In order to attain a defect-free palladium membrane, it is necessary to process porous alumina support in a manner that reduces surface roughness and narrows the distribution of pore sizes. The conventional approach of modifying support surfaces typically entails the application of various materials such as YSZ, ZrO_2, Al_2O_3, and CeO_2, among others. These processes necessitate the deposition of many layers and subsequent heat sintering at high temperatures. This eventually leads to an increase in the overall cost of the membrane. In addition, the chemicals necessary for synthesizing the asymmetric support give rise to significant environmental concerns. Hence, to mitigate the expenses associated with support modification The utilization of 2B-graphite lead pencil coating has been proposed by Hu et al. [5]. In comparison to alternative materials employed for surface modification or even as the intermediate layer in the case of PSS, 2B-graphite lead exhibits superior ductility, thermo-electrical conductivity, and exceptional resistance to thermal shocks, all at a relatively affordable price point. Moreover, the graphite lead has sufficient slit-type pores which further facilitates gas diffusion with very minimum mass transfer resistance. Ten similar porous alumina supports are scrapped with 2B-graphite lead till the entire surface assumes a homogeneous black color according to the method described by Hu et al. [5]. To eliminate any surplus loose graphite, the support is subjected to a meticulous cleaning process involving repeated gentle rubbing with a textile cloth. The cleaning process is considered to be finished when there is no longer any visible presence of graphite powder on the surface of the textile

cloth. The support is subjected to calcination at a temperature of 773 K for 5 hours to eliminate organic volatile impurities, including clay, binders, and waxes. Depending on the variation in capillary mouth size of the support surface, the amount of 2B-graphite loading per tube ranges from 1 mg cm^{-2} to 1.3 mg cm^{-2} as measured gravimetrically using a microelectronic weighing machine (MxRady Lab Solutions Pvt Ltd., India, Model: KERRO, BL-P7/2204 (INT), Capacity: 0.0001 g to 60 g). However, most of the 2B-graphite particles remained inside the pore mouth of the support. By employing this approach, the support's average pore size and surface roughness are effectively reduced in order to facilitate the deposition of continuous thin membrane layer.

Before the deposition of the Pd-Ag layer over the support it is important to activate the cleaned support with Pd-nuclei to accelerate the autocatalytic nature of the electroless plating process. To achieve a uniform distribution of Pd seeding on the support, the support is consecutively immersed in acidic $SnCl_2$ (sensitization), acidic $PdCl_2$ (activation), 0.01 M HCl, and deionized water as per the methodology described by Mardilovich et al. [53]. Typically, a dark brown color is visible within 8-10 cycles. If not visible, it may be necessary to conduct further cycles. Table 3.2 and Equation 3.7 depict the composition of the activation bath and the chemistry involved respectively. After activation, the support is gently washed with DI water and dried at 393 K for 4 to 5 hours. This process for activation is largely acknowledged as the most prevalent and acceptable approach for surface activation of the support.

$$Sn^{2+} + Pd^{2+} \rightarrow Sn^{4+} + Pd^{0} \qquad 3.7$$

Table 3. 2. Typical composition of the sensitization/activation solution.

Chemicals	Sn solution	Pd solution
$SnCl_2.2H_2O$ (g L^{-1})	1.0	--
$PdCl_2$ (g L^{-1})	--	0.1
HCl (~ 37 %) (ml L^{-1})	1	1
Temperature (K)	293	293
Duration (minutes)	5	3-5
pH	~2	~2

3.2.2. Pd-Ag Deposition using ELP Technique

After the successful activation of the support, the Pd-Ag metallic layer is co-deposited over the support using the ELP technique. To achieve the appropriate composition of the metallic layer,

the chemical composition of the plating bath is further adjusted as shown in Table 3.3. Hydrazine is added from time to time to avoid the bulk precipitation of the plating bath. The membrane is thoroughly washed with de-ionized water at intervals of 30 minutes throughout the plating process, which took a total of 300 minutes. The constant vacuum of -50 kPaG is applied from the lumen side of the tube after 90 minutes of plating for 150 minutes to seal the tiny membrane defects. Excess of hydrazine is added at the end of each plating cycle. This is done with the purpose of facilitating the deposition of residual palladium and silver ions, hence mitigating the potential loss of valuable palladium content present in the plating solution. Three rounds of deposition are performed to achieve a completely dense membrane. The difference in weight is calculated using a microelectronic weighing machine. The overall membrane thickness has been estimated gravimetrically using Equation 3.8.

$$\text{Thickness } (\mu m) = \frac{\text{Final weight (g)} - \text{Initial weight(g)}}{\text{Plated area } (cm^2) \times \text{Density of deposited metal } (g\ cm^{-3})} \quad 3.8$$

Table 3. 3. Chemical composition of Pd-Ag ELP plating bath used for membrane preparation.

Solution	Chemicals	Quantity
Plating bath	Palladium chloride (mmol L^{-1})	8.5
	Silver nitrate (mmol L^{-1})	1.5
	Ammonia (mol L^{-1})	5
	Na_2EDTA (mol L^{-1})	0.15
	Hydrazine (mmol L^{-1})	13-15
	pH	11-12
	Temperature (K)	328-333

3.2.3. Membrane Annealing, Polishing, and Fitting

To attain a consistently uniform Pd-Ag alloy layer and ensure its stability, it is important to place the membrane in a thermal treatment process known as annealing. Typically, annealing is conducted at temperatures beyond the Tamman temperature of the metal precursor. This temperature represents the point at which the metal undergoes alloy formation or the initiation of diffusion inside the metal lattice, typically occurring at around half of the metal's melting point [55]. Therefore, the membrane is annealed at 773 K in a 10% H_2 / 90% N_2 (total flow rate = 0.5 L min^{-1}) environment for 300 minutes with a heating rate of 3 K min^{-1}. The membrane is cooled to ambient temperature under a nitrogen atmosphere (total flow rate = 0.5 L min^{-1}).

Following the annealing process, residual inorganic contaminants persist on the surface of the membrane. The presence of contaminants has the potential to impede the permeance of the membrane or the catalytic dissociation of hydrogen molecules into atoms on an active Pd-site. Therefore, to address this particular challenge, membrane polishing is performed. This technique not only effectively eliminates impurities from the surface, but also serves to fill any existing pinhole defects [56]. However, it may reduce the membrane thickness but increase the H_2 selectivity [35]. Therefore, the membrane undergoes a gentle polishing process using 1500 SiC sandpaper, followed by cleaning with DI water and ethanol to effectively eliminate any contaminants that may have accumulated on the membrane surface during polishing. The completion of the polishing process is often indicated by the presence of a lustrous shiny metallic surface finish.

Once the membrane is ready for further permeation testing it is important to connect the membrane with the metal fitting to facilitate its assembly with the separator. The membrane is further assembled to the SS-fitting using an in-house graphite ferrule as shown in Figure 3.1 (a). Before assembling the membrane, the ferrule is conditioned at 773 K inside the fitting with an SS-rod (O.D. = 10 mm) using the compression fitting technique to shape the ferrule as shown in Figure 3.1 (b) and (c). One advantage of utilizing a graphite ferrule is its high compressibility, which allows for easy compression. This property helps to prevent scratching and enables the ferrule to distribute the tightening load more effectively across a larger surface area of the membrane [7,8]. Nevertheless, a reduction in membrane surface area occurs within the fitting. Furthermore, it is imperative to use caution when tightening the fitting to prevent frequent breaking. Table 3.4 shows the characteristics information on ten similar membranes prepared following the procedure described above with active lengths of 100 mm each as shown in Figure 3.1 (d).

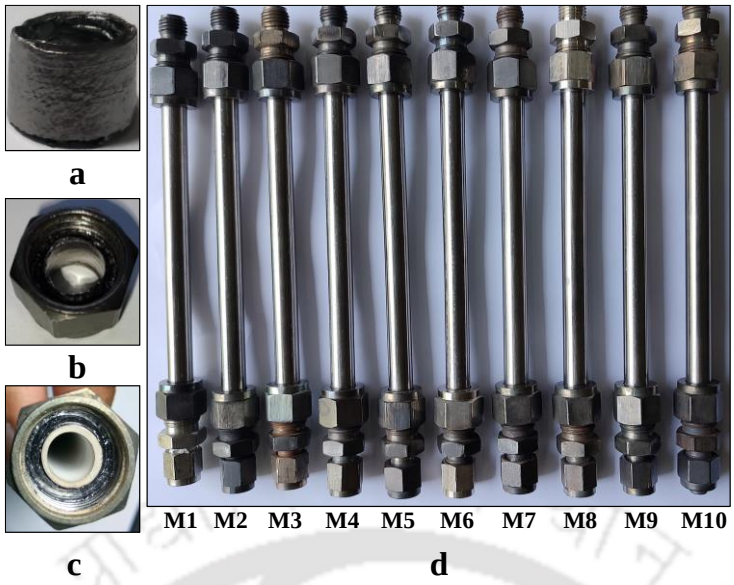

Figure 3. 1. Membrane assembling using graphite ferrule (a) graphite ferrule, (b) after conditioning with SS-rod, (c) membrane inside the fitting, (d) membranes prepared for testing with an approximate active length of 100 mm each.

Table 3. 4. Characteristics information of the membranes prepared for testing.

Name of membrane /Position inside the separator	Membrane layer	2B-graphite loading (mg cm^{-2})	Gravimetric membrane thickness (µm)
M1/P1	PdAg/2B graphite	1.064	10.08
M2/P2	PdAg/2B graphite	1.068	9.95
M3/P3	PdAg/2B graphite	1.140	9.38
M4/P4	PdAg/2B graphite	1.095	10.11
M5/P5	PdAg/2B graphite	1.142	9.52
M6/P6	PdAg/2B graphite	1.197	9.23
M7/P7	PdAg/2B graphite	1.114	9.55
M8/P8	PdAg/2B graphite	1.272	10.25
M9/P9	PdAg/2B graphite	1.005	9.39
M10/P10	PdAg/2B graphite	1.056	9.84

3.2.4. Rising Water-Bubble Point Testing for Leak Detection

A customized bubble point test apparatus is designed in-house to visualize the defects and pin-holes present on the surface of the membrane as shown in Figure 3.2. This method is highly reliable for directly visualizing the exact position of the defects and pin-holes. Before doing the permeation study, a leakage test of each membrane using the Rising Water Bubble Technique is performed in ethanol with nitrogen gas fed inside the lumen of the membrane till 400 kPaG. The pressure line is cut off and the drop in the pressure is noticed for half an hour. The membrane is considered to be defect free only when there is no pressure drop. The membrane is considered for further permeation testing only when there is no visible leakage from the fitting and the membrane surface.

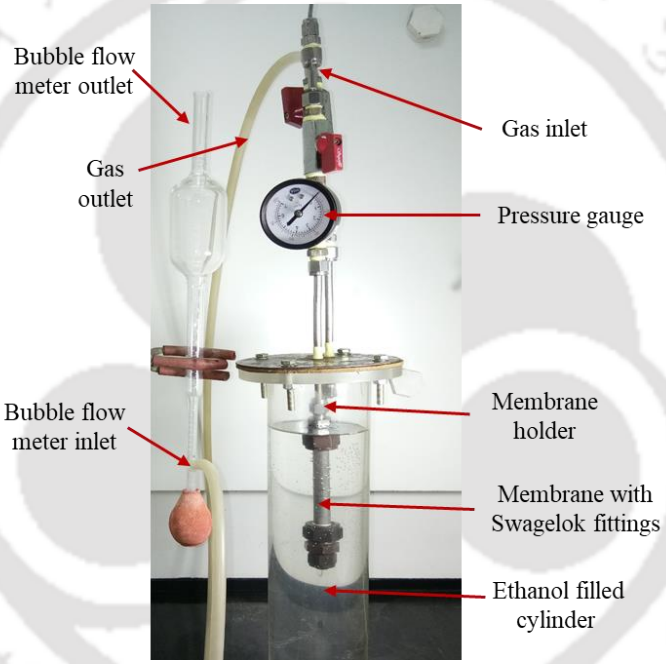

Figure 3. 2. In-house set-up to check leakage in the membrane before testing.

3.2.5. SEM and EDS Analysis of Membrane

In order to observe the surface morphology of the Pd-Ag membrane prepared field emission scanning electron microscope (FESEM, FESEM with OXFORD EDS, Make: Zeiss, Model: Sigma) analysis is performed at various stages of preparation including fresh support, 2B-graphite modified support, Pd-Ag deposited support, annealed membrane, and polished surface. Additionally, the thickness of the membrane is evaluated through cross-sectional investigation utilizing the SEM. An average thickness of at least three points in the cross-section is calculated to cross-examine the same with the gravimetrically calculated thickness. Energy-dispersive X-ray spectroscopy (EDS, FESEM with OXFORD EDS, Make: Zeiss,

Model: Sigma) technique has been used to determine the elemental composition of the Pd-Ag membrane. Additionally, the mapping of the elements over the support is performed to ensure a uniform distribution of Pd and Ag.

3.2.6. Permeance Testing with Pure H_2 and N_2

A process flow diagram of the experimental setup is outlined in Figure 3.3. The desired gas composition and the feed flow rate are maintained using the mass flow controller (MFC) provided by Aalborg Instruments & Controls, Inc. USA. The membrane is hung within the Inconel-800 tube from the upper flange to permit operation at high temperatures. The separator is subjected to heating using a 2-zone split electrical furnace with independent temperature control, which enables the regulation of the required temperature. The feed stream is introduced into the separator through the bottom section, while the retentate is extracted by an outlet located in proximity to the upper flange. A thermocouple is placed inside the separator near the membrane surface to monitor the temperature. Two additional thermocouples are also placed at the bottom and upper section of the furnace. To achieve the desired transmembrane pressure difference a back-pressure regulator is used at the outlet of the retentate. The pressure is monitored using the pressure gauge at the outlet of the retentate as well as the permeate. The H_2 flow rate and gas composition are regularly monitored using a soap bubble flow meter and GC (Centurion Scientific, India, Model: CS-5770) respectively. Both the retentate and permeate sections can be analyzed independently. In order to evaluate the H_2 permeation flux, activation energy, and H_2/N_2 ideal perm-selectivity one of the membranes (M1) is tested using the pure H_2, and the N_2 at various temperatures (from 573 to 773 K) and pressures (from 50 to 300 kPaG). For the entire study, the permeate side is maintained at the atmospheric pressure and no sweep gas is used. The membrane is heated to the required temperature under an N_2 atmosphere at a fixed flow rate of 1 L min^{-1} and ramping rate of 3 K min^{-1}. The membrane surface is activated before the permeation test by eliminating carbonaceous contaminants using an oxidation reaction with air (1 L min^{-1}) at 773 K for 5 minutes, followed by a purge with N_2 (1 L min^{-1}) for 5 minutes at the same temperature [8]. Before conducting the hydrogen permeation experiment, the membrane is subjected to activation by employing pure hydrogen gas at a temperature of 773 K and 100 kPaG. The completion of activation is inferred when a consistent and enduring permeate H_2 flux is achieved. Thereafter, the permeation testing is performed to determine the permeate H_2 flux at the aforementioned temperature and pressure range. Once the testing with H_2 is finished, the permeate N_2 flux is also measured at the same condition to evaluate the H_2/N_2 ideal perm-selectivity. The calculated selectivity in this study

represents the ideal selectivity for the purpose of comparing it with similar membranes mentioned in the literature. The overall feed flow rate is consistently maintained at 2 L min^{-1} during the permeation experiment for both H_2 and N_2. Following the completion of the permeation testing, the membrane is put through a cooling procedure in an N_2 environment (500 ml min^{-1}) until it reaches the ambient temperature.

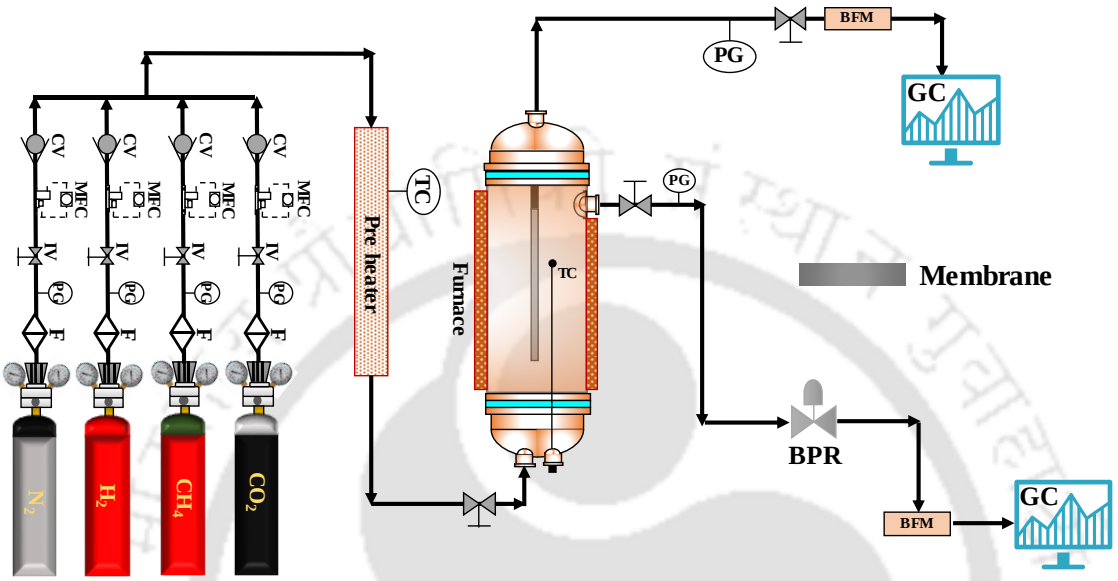

CV = Check Valve, **BFM** = Bubble Flow Meter, **BPR** = Back Pressure Regulator, **TC** = Thermocouple (K-type), **IV** = Isolation valve, **PG** = Pressure Gauge, **MFC** = Mass Flow Controller , **F** = Filter, **GC** = Gas Chromatography

Figure 3. 3. A process flow diagram of the experimental setup used for permeation testing of the membrane.

3.2.7. Permeation Testing with Mixture Gases

The H_2 permeation behavior of the membrane is influenced by various parameters, such as H_2 concentration in the inlet feed, rate of hydrogen depletion, formation of boundary layer due to concentration polarization, and surface inhibition [57–60]. Hence, a comprehensive investigation is undertaken to examine the effect of a mixture gas including N_2, CO_2, CO, and CH_4. These gases are often present with various degrees of concentration during the production of H_2 industrially. Before performing the test with the mixture gas, the membrane (M1) is activated at a temperature of 773 K and 100 kPaG using pure H_2 until a maximum stable permeate H_2 flux is achieved. The performance with feed mixture H_2/N_2 is evaluated with increasing temperature (from 573 K to 673 K), and pressure (from 50 kPaG to 300 kPaG). The H_2 concentration is varied from 100% to 70% by vol. while the remaining quantity is supplemented with N_2. A similar study is performed with a mixture of gas H_2/CO_2 as per the

aforementioned methodology. At last, the effect of H_2/N_2, H_2/CO_2, H_2/CO, and H_2/CH_4 is determined with increasing concentration (from 0% to 80% by vol.) of impurity gases at 673 K and 300 kPaG. The feed flow rate is maintained at 1 L min^{-1} (feed load i.e feed flow rate per unit membrane area as given in Equation 3.9 is maintained at 320 L min^{-1} $m^{-2}_{membrane}$) while the permeate side is kept at atmospheric pressure. No sweep gas and vacuum are applied on the permeate side.

$$F_{in}/A \text{ (L min}^{-1} \text{ m}^{-2}_{membrane}) = \frac{\text{Feed flow rate}}{\text{Active membrane area}} \quad 3.9$$

The influence of CO on the membrane performance is investigated using the M3 membrane. The adsorption inhibition effect of CO is studied at a CO concentration varying from 1% to 20% (by vol.) and a temperature range of 573 K to 673 K. Two different pressure conditions of 100 kPaG and 300 kPaG are studied to evaluate the effect of H_2 partial pressure across the membrane. The experimental result of increasing CO concentration is further compared with the predicted value of the Sieverts-Langmuir Model (SL Model) proposed by Barbieri et al. [61] as given in Equation 3.10. SL Model considers Sieverts' Law and Langmuir isotherm together to predict the permeate H_2 flux in the presence of CO. In the case of CO, the decrease in H_2 flux is due to the effect of concentration polarization as well as the competitive adsorption of CO. Therefore, to evaluate the comprehensive inhibiting effect, additional permeation studies are done employing a mixture of H_2, N_2, and CO gases. The decrease in the permeate H_2 flux resulting from the introduction of N_2 can be solely attributable to the phenomenon of concentration polarization, whereas the introduction of CO has an inhibitory effect. Therefore, to investigate the inhibitory impact, a certain quantity of N_2 (from 5% to 10% by vol.) is substituted with an equivalent quantity of CO (0% to 5% by vol.). Given that the binary diffusion coefficient of H_2/N_2 is comparable to that of H_2/CO, the substitution of N_2 with an equivalent quantity of CO would not result in a substantial alteration in the concentration polarization. The observed decrease in H_2 flux in the $H_2/N_2/CO$ system, compared to the H_2/N_2 system, is only attributed to the competitive adsorption of CO. The effect of CO is further quantified in terms of the effective average concentration polarization (EACPC), overall inhibition coefficient (OIC), and adsorption inhibition coefficient (AIC) as described by Equations 3.11, Equations 3.12, and Equations 3.13 respectively.

$$\frac{J_{H_2/CO}}{J_{H_2}} = 1 - \alpha(T)\frac{K_{CO}P_{CO}}{1+K_{CO}P_{CO}} \text{ (Sieverts-Langmuir Model)} \quad 3.10$$

$$EACPC_{H_2/i} = 1 - \frac{J_{H_2/i}}{J_{H_2}},\ i = N_2,\ CO_2,\ CH_4, \text{ and CO} \quad 3.11$$

$$OIC_{H_2/N_2/CO} = 1 - \frac{J_{H_2/N_2/CO}}{J_{H_2}} \quad 3.12$$

$$AIC_{H_2/CO} = OIC_{H_2/N_2/CO} - EACPC_{H_2/N_2} \quad 3.13$$

where J_{H_2}, $J_{H_2/i}$, and $J_{H_2/N_2/CO}$ are the permeate hydrogen flux in the presence of pure H_2, the mixture of H_2 with i (= N_2, CO_2, CH_4, and CO) and the mixture of H_2, N_2, and CO. P_{CO} is the partial pressure of CO, K_{CO} is the adsorption equilibrium constant, and α is the reduction factor. The reduction factor α is a result of the presumed linear relationship between the decrease in permeate H_2 flux and the surface covering by CO. The parameter $K_{CO}P_{CO}/(1 + K_{CO}P_{CO})$ is derived from the Langmuir isotherm, representing the effective surface coverage by CO. While α is only determined by temperature, the parameter $K_{CO}P_{CO}/(1 + K_{CO}P_{CO})$ is influenced by both temperature and the partial pressure of CO.

3.2.8. Membrane Performance at Varying Feed Load

By augmenting the feed load, an additional amount of hydrogen is introduced into the separator, thus leading to an increase in the permeate hydrogen flux until a state of saturation plateau is attained. Simultaneously, the hydrogen recovery will exhibit a decline, contingent upon the feed load and many operational parameters involving temperature, pressure, and H_2 concentration in the gas mixture. Therefore, to investigate the effect of feed load the performance of the membrane is evaluated by varying the feed flow rate from 260 to 1600 L min^{-1} $m^{-2}_{membrane}$. Initially, the performance is evaluated using pure H_2 at 300 kPaG for three different temperatures including 573 K, 623 K, and 673 K. The effect of feed load on the permeate H_2 flux and H_2 recovery (defined as the ratio of the amount of hydrogen permeating through the membrane to the amount of H_2 supplied to the separator is shown in Equation 3.13) is determined.

$$\text{Hydrogen recovery (\%)} = \frac{F_{H_2,permeate}}{F_{H_2,feed}} \times 100 \quad 3.13$$

A similar permeation study is also investigated using 70% H_2 / 30% N_2 mixture gas to evaluate the effect of feed dilution. The permeate H_2 flux and H_2 recovery is determined at 673 K for three different pressures 100, 200, and 300 kPaG. Following the result another study is performed to determine the permeation behavior for varying hydrogen concentrations in the feed mixture gas at 300 kPaG and 673 K. Three different feed mixture compositions are studied including 90% H_2 / 10% N_2, 70% H_2 / 70% N_2, and 50% H_2 / 50% N_2 with varying feed load ranging from 260 to 1600 L min^{-1} $m^{-2}_{membrane}$. After the completion of the permeation testing,

the membrane is put through a cooling procedure in an N_2 environment (500 ml min^{-1}) until it reaches the ambient temperature.

3.2.9. Long-Term Thermal Heat Cycle Stability

Other than the permeation testing of the membrane, ten thermal heat cycles lasting six hours each are performed to assess the thermal stability of the membrane M2. The long-term thermal heat cycle stability of the membrane is another key parameter for their practical commercial application. The membrane is subjected to heating till 673 K under N_2 followed by air oxidation. Thereafter, H_2 is introduced and pressure is maintained at 100 kPaG. For the first (573 K), second (623 K), and third (673 K) heat cycles, pure H_2 is utilized, followed by 70% H_2 / 30% N_2 (% by vol.) for the rest of the cycle at 673 K. In each case, the total feed feed load is maintained at 320 L min^{-1} $m^{-2}_{membrane}$. The permeate H_2 flow rate and gas composition are regularly monitored using a soap bubble flow meter and GC (Centurion Scientific, India, Model: CS-5770) respectively. H_2/N_2 perm-selectivity is determined and plotted for each heat cycle throughout the testing period. Following each heat cycle, the membrane is cooled under the N_2 environment (500 ml min^{-1}) until it reaches room temperature. For the next cycle, the desired temperature is achieved under a pure N_2 environment. Thereafter, the pressure is maintained using pure H_2 and H_2/N_2 mixture gas wherever desired as per the thermal testing aforementioned. Whenever there is a decrease in the selectivity of H_2/N_2, the membrane is removed and examined using the rising water bubble set-up to detect the possible formation of pin-holes on the membrane surface or any other potential leaks from the fittings. After identifying the potential reason responsible for the drop in hydrogen selectivity, the membrane is fixed and subsequently retested under identical conditions to determine its performance.

3.3. Results and Discussion

The performance of the membrane is investigated at different parameters including temperature, pressure, and feed load using pure H_2 and N_2. Additionally, the effect of a mixture gas such as H_2/N_2, H_2/CO_2, H_2/CO, and H_2/CH_4 having varying concentrations of H_2 is examined. Finally, the membrane's thermal heat cycle stability is examined at various temperatures using both pure H_2 and H_2/N_2 mixture gas. Simultaneously, the purity of H_2 is monitored. Following the thermal heat cycle stability testing, the surface morphology of the membrane is analyzed using SEM to identify any potential development of micro pin-holes that may have occurred due to long-term thermal applications.

3.3.1. SEM and EDS Analysis

A section of the M1 membrane is carefully cut at different stages of the preparation for characterization purposes. Figure 3.4 (a) illustrates the characteristics of the fresh Al_2O_3 support, which is comprised of big pores-mouth exhibiting an uneven surface with a very high level of surface roughness. Nevertheless, it is imperative to minimize surface roughness to prepare a thin defect-free membrane. The direct deposition of Pd-Ag onto the pristine Al_2O_3 support may necessitate the application of a rather thick Pd-Ag layer to adequately fill the pore openings. As a consequence, it is expected that there would be a reduction in the permeate H_2 flux and an accompanying rise in costs. Hence, to decrease the average pore size and surface roughness, the support is meticulously scrapped using a 2B graphite lead. In Figure 3.4 (b) it can be observed that most of the pore mouth is covered after scrapping with the 2B graphite lead. However, most of the graphite remains inside the pore mouth, thereby partially blocking the pores. It is crucial to acknowledge that the SEM effectively shows the surface features, specifically limited to the visible pore-mouth regions. There is a potential for the pore mouth to have a significantly bigger size in comparison to the pore throat. To block through-through pores, it is essential to completely fill the pore mouth. Several slit types of pores are available in the graphite layer which facilitates gas diffusion as shown in the small box of Figure 3.4 (b). The membrane surface following the deposition of the Pd-Ag onto the modified support is depicted in Figure 3.4 (c). A uniform layer is evident across the entire support, characterized by a radial growth pattern of the dense Pd-Ag cluster consisting of the small Pd-Ag particles. After annealing and polishing of the membrane, no visible pin-holes are detected in the SEM image as can be seen in Figure 3.4 (d) and (e). Subsequently, no pin-holes are present on the surface as evident in the rising water bubble experiment as well. Moreover, the Pd-Ag cluster

sinter to form a densely arranged continuous structure and becomes stable. Upon undergoing the process of polishing, the membrane has a glossy and lustrous appearance, characterized by a metallic finish. The morphology of the other membranes listed in Table 2.10 are also uniform similar to the M1 membrane. Figure 3.4 (f) shows the cross-section of the Pd-Ag layer deposited over the support. The average thickness of the membrane is estimated to be 10.01 µm which is approximately close to the thickness measured gravimetrically i.e. 10.08 µm. The deposition of Pd-Ag within the pores through vacuum suction enhances the mechanical integrity of the membrane. EDS analysis of the M1 membrane is shown in Figure 3.5 (a). It can be observed that the Pd and Ag composition is estimated to be 83.5% and 15.8% (wt. %) respectively. No major peak other than Pd and Ag is observed which confirms that the entire surface is covered with the Pd-Ag particle. The Pd and Ag particles exhibit a notable level of compactness and display uniformity across the surface. Figure 3.5 (b) shows the cross-section analysis of the Pd-Ag layer. It is observed that a uniform Ag distribution across the cross-section is observed due to the co-deposition of Pd and Ag. Even across the cross-section, there are no significant changes in the Pd (86.5 wt. %) and Ag (wt. %) composition.

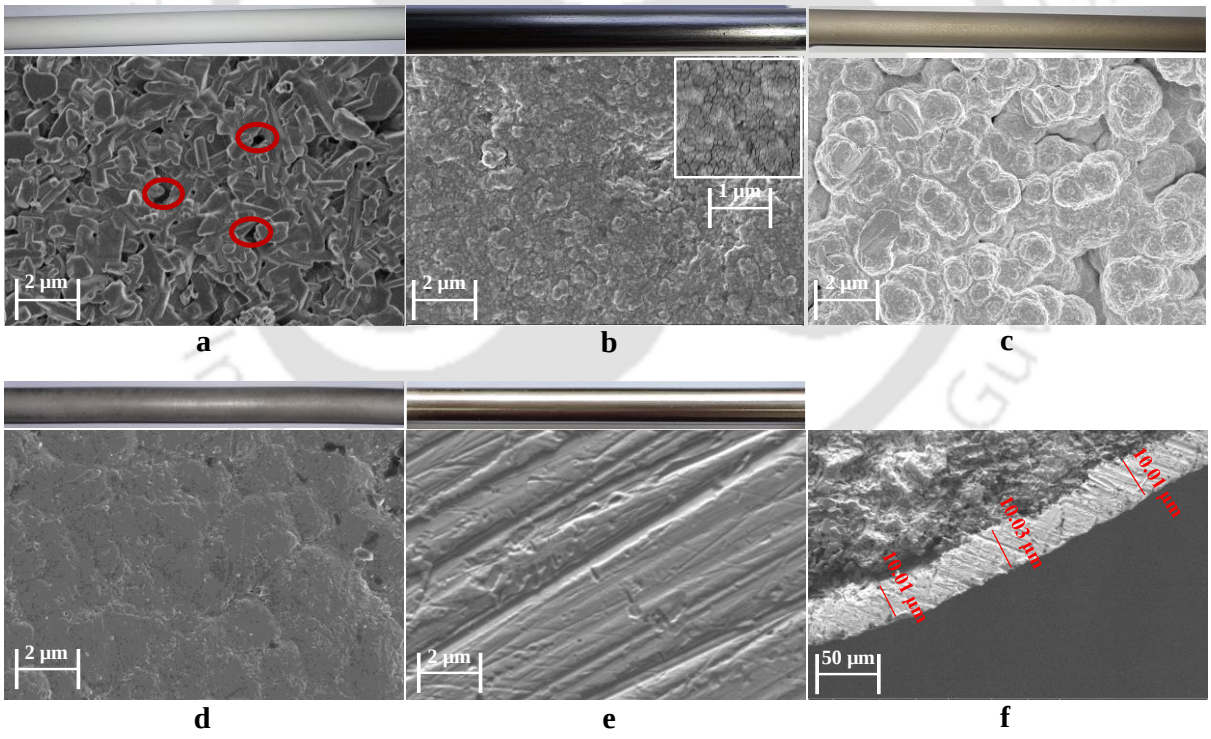

Figure 3. 4. SEM analysis of M1 membrane at a different stage of preparation (a) after cleaning and drying the support at 393 K, (b) after surface modification with 2B graphite lead coating (slit type pores in a small box), (c) after the Pd-Ag deposition, (d) after annealing of the membrane, (e) after polishing, and (f) cross-section of the deposited layer.

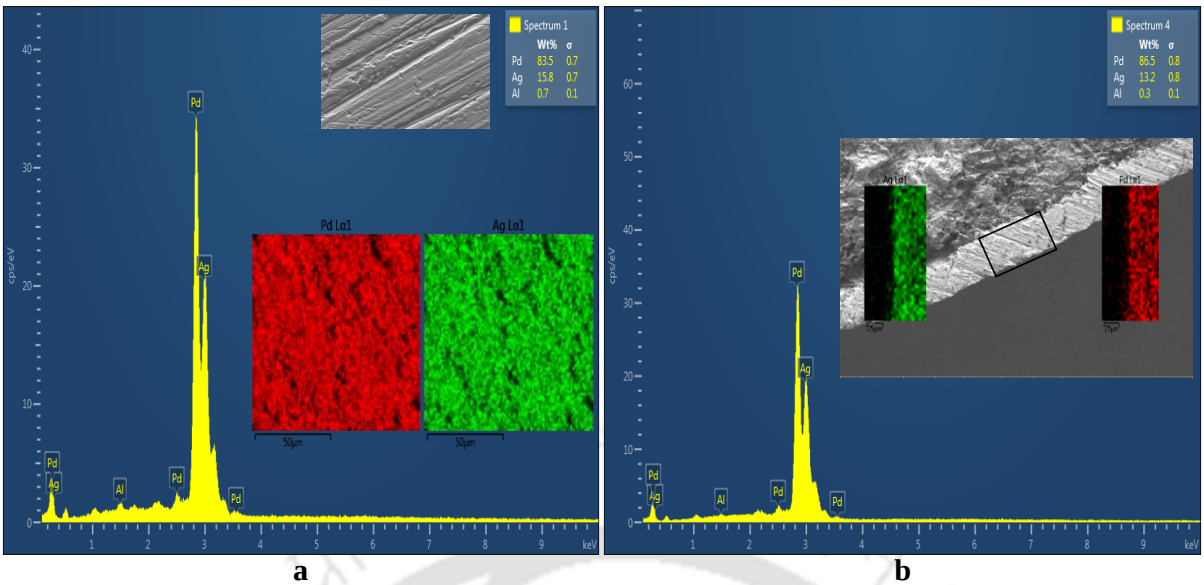

a **b**

Figure 3. 5. EDS analysis of the M1 membrane (a) surface area and (b) cross-section.

3.3.2. Rising Water-Bubble Point Testing

The entire membrane undergoes testing for potential pinholes and leaks using the Rising Water Bubble Technique. The membrane is immersed in ethanol while nitrogen gas is introduced into the lumen of the membrane until it reaches a pressure of 400 kPaG. If there is still a pinhole on the surface of the membrane, the membrane is once again coated only at the location of the defect. The membrane is subjected to additional permeation analysis at various temperatures and pressures using only N_2 and H_2 gases, but only after confirming the absence of any pinholes or leaks in the membrane.

3.3.3. Pure H_2 and N_2 Permeance Testing

The membrane M1 is selected for the pure gas permeation testing. The membrane is initially exposed to a cleaning process whereby the residual carbonaceous material, including organic compounds, is eliminated through the application of the air oxidation technique. By releasing the active sites for H_2 dissociation, the surface area is increased, and thereby the H_2 permeation without affecting the integrity of the Pd-Ag membrane. However, the process of air oxidation leads to an elevation in surface roughness due to the development of surface grains and thereby the hidden grain boundary. The rate of hydrogen diffusion along the grain boundary is approximately 100 times greater than the rate of diffusion within the lattice [62,63]. Upon the introduction of hydrogen, it is found that the permeate H_2 flux exhibited an initial increase over time, eventually reaching a steady state after a duration of 35 minutes as shown in Figure 3.6.

The phenomenon is a distinctive characteristic of the Pd-based membrane system, commonly known as "permeation stabilization". The observed behavior can be mostly attributable to the rapid infiltration of H-atoms into the palladium-silver lattice, which subsequently occupy the lattice sites, hence promoting additional permeation. Nevertheless, the continuous H_2 permeation results in the saturation of lattice sites with H-atoms, eventually reaching a state of equilibrium. At this stage, the hydrogen concentration remains generally consistent across both the upstream and downstream regions of the membrane, resulting in the stabilization of the permeate H_2 flux. Over a prolonged duration, the presence of hydrogen can induce alterations in the structure of the Pd-based membrane, including the phenomena of grain growth and lattice expansion. Furthermore, the surface of the Pd-Ag layer can effectively eliminate the presence of pinholes caused by the convergence of Pd and Ag grains after undergoing H_2 treatment [64,65]. Continuous exposure to H_2 has been seen to decrease the formation of surface oxides (Pd-O) that occur during air activation. After achieving flux stabilization, subsequent permeation testing is conducted under varying temperatures and pressures.

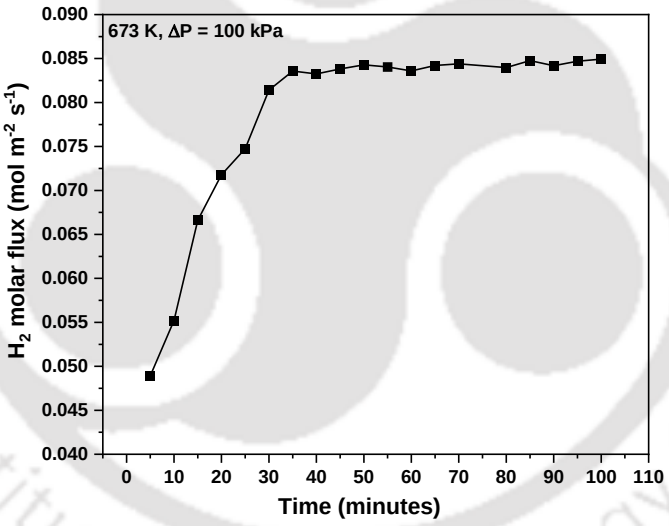

Figure 3. 6. Permeate H_2 flux of membrane M1 as a function of time during activation with hydrogen.

The hydrogen permeation characteristics of the Pd-Ag membrane are evaluated within a temperature range of 523 K to 773 K, and a hydrogen partial pressure range of 50 kPaG to 300 kPaG. A marginal variation of 5% is seen over the full set of experiments conducted under similar conditions, which is considered to be reasonably acceptable. For each set of data points, an average of at least five readings is taken. Hydrogen permeation through the Pd-Ag membrane is facilitated by the solution-diffusion mechanism, wherein the behavior of permeation is regulated by Sievert's Law. Figure 3.7 (a) shows the permeate H_2 flux as the

function of the H_2 partial pressure difference at n = 0.5. It should be noted that a good linear fitting with a coefficient of determination (COD or R^2) above 0.999 is obtained at these conditions. This indicates that H_2 diffusion through the bulk of the Pd-Ag layer is the rate-limiting step. If, on the other hand, the Knudsen diffusion or Poissuile mechanism governs H_2 diffusion through the membrane, then the n-value deviates from 0.5 and shifts towards 1.0 in order to achieve adequate linear fitting with R^2 close to 1.0. This phenomenon is ascribed to the fact that some H_2 diffuses through the defects and/or pinholes on the membrane surface, making associative and/or dissociative chemisorption the rate-limiting step, especially in the case of thicker membranes (> 5 μm) [1]. A steady increase in the permeate H_2 flux is also observed with the increase in temperature as illustrated in Figure 3.7 (b) as per the Arrhenius Law. This behavior is mostly ascribed to the Arrhenius-type temperature dependency of H_2 solubility and diffusivity. Diffusivity, solubility, and permeability as given in Equation 2.10, Equation 2.11, and Equation 2.12 respectively exhibit a dependence on temperature-dependent characteristics that are represented by the Arrhenius-type relationship. The activation energy associated with hydrogen permeation is determined by the combined activation energies for diffusivity and solubility, as represented in Equation 2.13. Subsequently, the molar H_2 flux through a dense Pd-Ag membrane is governed by the Sieverts' law as given in Equation 2.9. Thus, with the increase in temperature both the diffusivity (atoms move faster through lattice) and solubility (more hydrogen dissolves into membrane) increases ultimately resulting in the increase in the H_2 permeability and hence the molar H_2 flux though the Pd-Ag membrane. A maximum of 0.26 mol m^{-2} s^{-1} of permeate H_2 is achieved at 773 K and 300 kPaG.

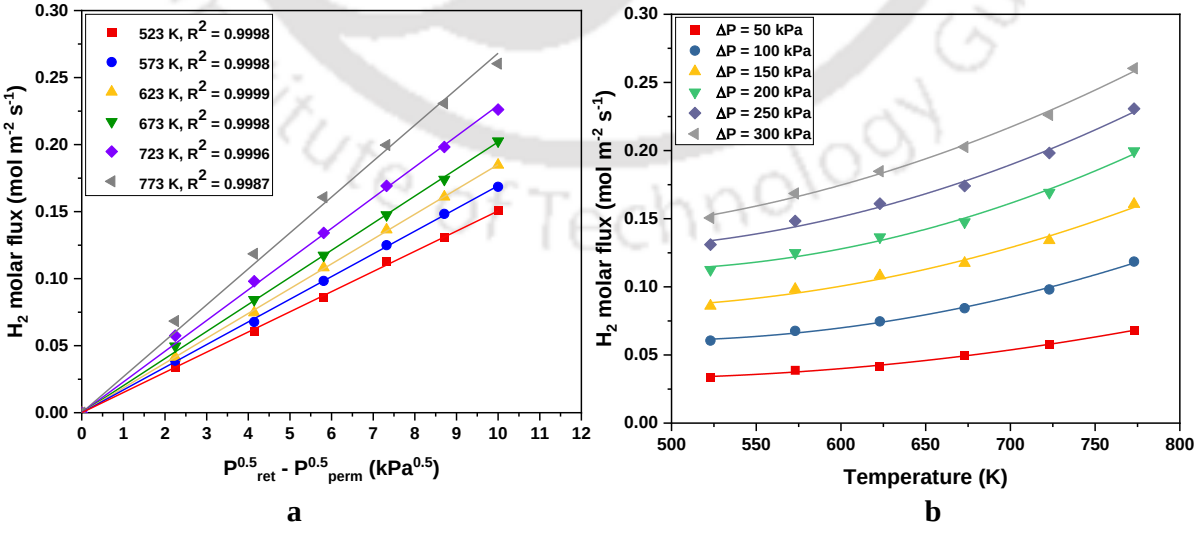

Figure 3. 7. Permeate H_2 molar flux of membrane M1 as a function of the (a) difference of the square root of the hydrogen partial pressure, and (b) increasing temperature.

The N_2 leak test of the M1 membrane under dry conditions is conducted at ambient temperature. The permeate N_2 flux is observed while gradually raising the trans-membrane pressure at various stages of preparation. The purpose of this study is to investigate the impact of 2B-graphite coating and membrane thickness on the permeate N_2 flux. Additionally, multiple bubble point testing may partially erode the 2B-graphite layer and particles adhered near the pore-mouth of the support. Figure 3.8 shows that the N_2 flux after the 2B-graphite coating is decreased by roughly 2.1 times compared to the bare support at 300 kPaG. The N_2 flux experienced a reduction of two orders after the first and second rounds of Pd-Ag deposition. After the first round of coating, the N_2 flux was 0.069 mol m^{-2} s^{-1} at 300 kPaG whereas it was 0.031 mol m^{-2} s^{-1} after the second round. Although the N_2 flux dropped to a greater extent, it was not sufficient to achieve a completely dense membrane. Therefore, another round of coating was performed which reduced the N_2 flux to an order of 10^4 compared to the bare tube. At this stage, the membrane may be assumed completely dense and ready for further permeation testing. In order to assess the selectivity of the membrane, it is important to measure the permeate N_2 flow under varying temperatures and trans-membrane pressures. Figure 3.9 (a) and (b) depict the dependency of N_2 molar flux on temperature and pressure. It is observed that the N_2 flux increased with the increase in pressure whereas it decreased with the increase in temperature. This behavior is mostly attributed to the permeation mechanism of N_2 which is governed by the Knudsen diffusion or Poiseuille flow through the defects and/or pin-holes as described in Equation 2.15. The permeate N_2 flux increases almost linearly with the trans-membrane pressure. The N_2 permeation through defects and/or pin-holes is proportional to $T^{-0.5}$ and T^{-1} for Knudsen and Poiseuille flow respectively, therefore it decreases with an increase in the temperature [53,66]. Additionally, no abrupt changes in the N_2 flux were observed which suggests that the membrane is stable under the testing conditions. The aforementioned phenomena have a significant influence on the perm-selectivity, thus underscoring the necessity of precise measurement of the N_2 flow rate. A slight difference in the N_2 flow rate can lead to a substantial variation in the perm-selectivity.

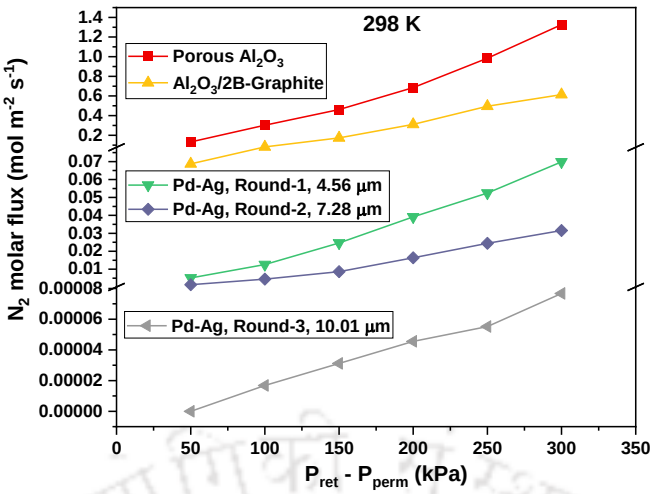

Figure 3. 8. Nitrogen flux as a function of the pressure difference at different stages of membrane M1 preparation at room temperature.

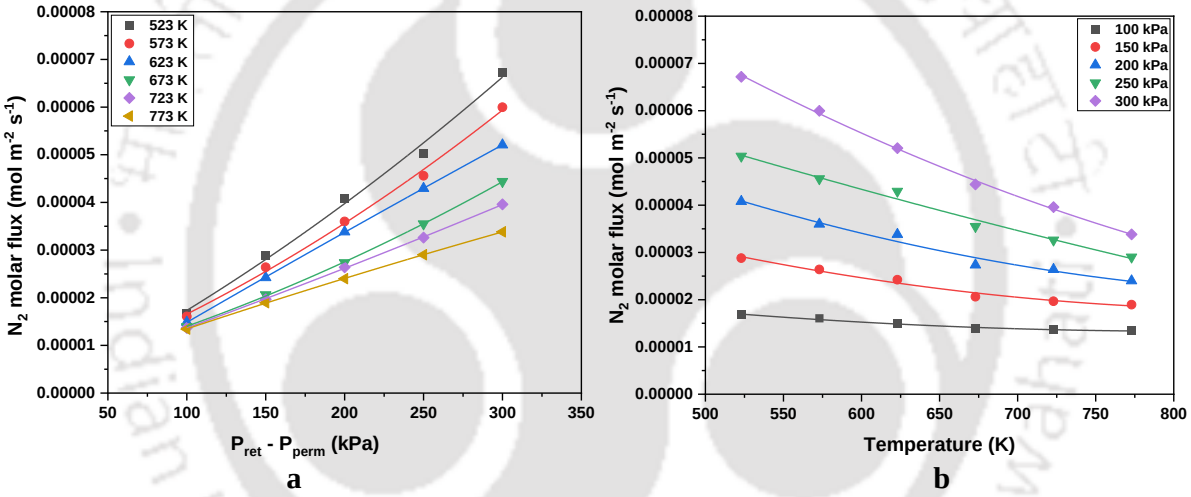

Figure 3. 9. Influence of (a) pressure and (b) temperature on the permeate N_2 flux of membrane M1.

3.3.4. Sieverts' Law Validation at Various Temperatures and Pressure

To validate Sievert's Law, permeate H_2 flux is plotted against the H_2 partial pressure at different pressure exponents varying from n = 0.5 to n = 1 at different temperatures as shown in Figure 3.10. It can be observed that the R^2 value is highest at n = 0.5 (R^2 = 0.9998) and constantly decreases as the n-value shifts toward 1.0 (R^2 = 0.9959) at 573 K. Therefore, at this temperature, bulk diffusion of H_2 through the Pd-Ag layer is the rate-limiting step [67]. A comparable pattern is observed for other studied temperatures as shown in Figure 3.11 (a) and (b). However, it should be noted that the R^2 value is highly sensitive to the precision of the permeate H_2 flow rate measurement. Consequently, a consistent pattern in the R^2 value is not

discernible when the temperature increases at the same pressure exponent. Other than the adsorption and desorption kinetics, several factors including surface modification, coating methodology, grain size, and microstructural characteristics also play a critical role [68]. Furthermore, the selectivity of the membrane has a significant effect on the pressure exponent, since it serves as the primary parameter in defining the magnitude of defects. Therefore, the membrane is subjected to an assessment of its permeation behavior by exposing it to pure nitrogen at identical temperature and pressure conditions to ascertain the ideal H_2/N_2 permselectivity.

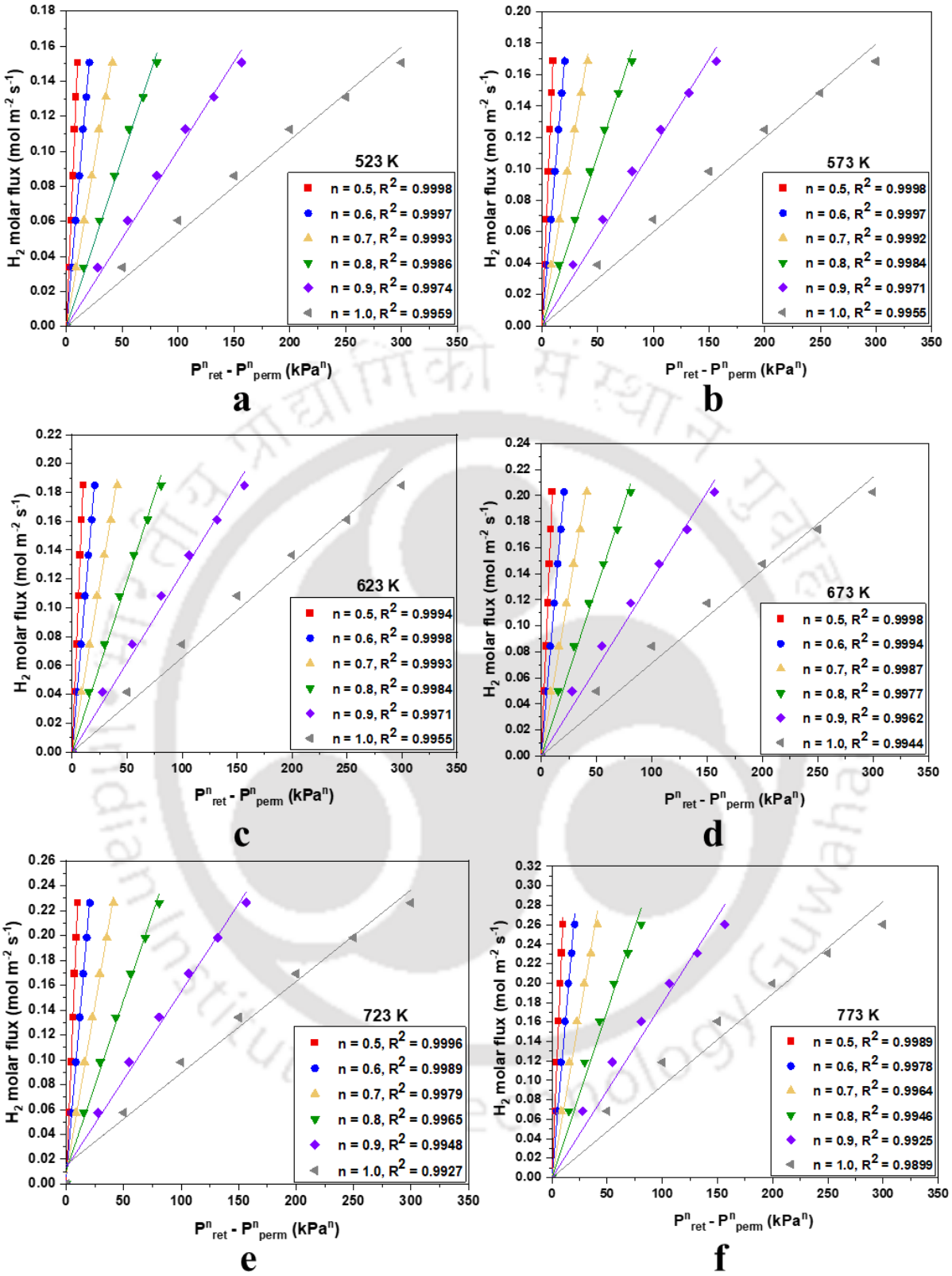

Figure 3. 10. Permeate H_2 molar flux of membrane M1 as a function of the difference of the hydrogen partial pressure at various n-values varying from 0.5 to 1.0 at various temperatures (a) 523 K, (b) 573 K, (c) 623 K, (d) 673 K, (e) 723 K, and (f) 773 K.

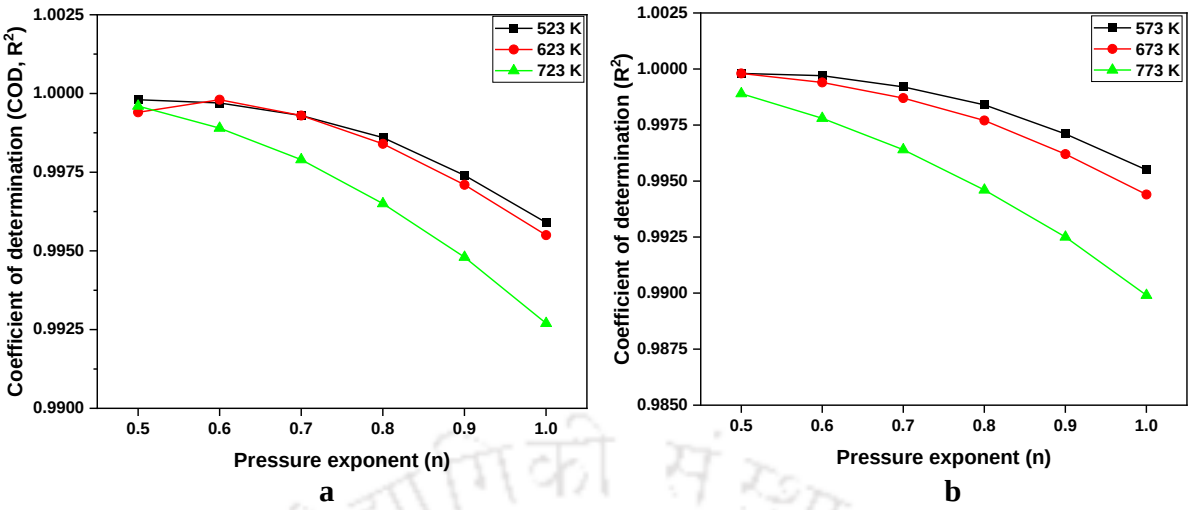

Figure 3. 11. Coefficient of determination as a function of pressure exponent at different temperatures (a) 523, 623, 723 K, and (b) 573, 673, 773 K for membrane M1.

3.3.5. Selectivity and Activation Energy of the Membrane

The ideal H_2/N_2 perm-selectivity is determined at different temperatures and transmembrane pressures as shown in Figure 3.12 (a). The ideal H_2/N_2 perm-selectivity decreased with an increase in the trans-membrane pressure. This is due to the permeation mechanism of N_2 which increases almost linearly with the trans-membrane pressure whereas the permeate H_2 flux depends on the difference of the square root of the H_2 partial pressure [53,66]. Hence, by increasing the pressure the permeate N_2 flux increases with higher order compared to the permeate H_2 flux, and consequently, the ideal H_2/N_2 perm-selectivity decreased. However, with the increase in temperature, the H_2/N_2 perm-selectivity increased which is a characteristic feature of a Pd-based membrane. The observed trend can be attributed to the decrease in N_2 penetration through defects and/or pin-holes as the temperature increases. Irrespective of the condition the perm-selectivity however remained above 2000 which is sufficient for the bulk diffusion of atomic H_2 through the Pd-Ag layer [68]. The experiment is conducted at a temperature below 773 K to maintain the structural integrity of the membrane. Furthermore, it is worth noting that researchers have suggested a significant rise in the permeate N_2 flow as temperatures increase above 773 K. This is related to the change in the microstructure of the Pd-Ag layer, leading to the formation of defects and/or pin-holes [53,69]. Therefore, the selectivity is not tested at temperatures above 773 K to maintain the structural integrity of the membrane for subsequent testing. The activation energy at ΔP = 100 kPa is estimated by plotting the Arrhenius-type dependence of the logarithm of the hydrogen permeance as a function of the reciprocal of the temperature, as shown in Figure 3.12 (b). A linear relation is

obtained and the activation energy of 8.66 kJ mol^{-1} is calculated directly from the slope. The E_a values are in agreement with those reported by Barison et al. [70] (7.3 kJ mol^{-1}), Zeng et al. [71] (7.4 kJ mol^{-1}), Fernandez et al. [8] (7.8 kJ mol^{-1}), Uemiya et al. [3] (8.3 kJ mol^{-1}), and Bosko et al. [72] (7.8 kJ mol^{-1}) having similar membrane properties. Activation energy below 30 kJ mol^{-1} suggests that dissociative adsorption and associative desorption have minimal influence on the permeation process, whereas higher activation energy above 54 kJ mol^{-1} indicates that the permeation behavior is governed by these surface phenomena. The fluctuation occurs due to the occupation of sites with high adsorption energy at low surface coverages of H_2. As a result, the adsorbed hydrogen becomes tightly bound and its mobility is constrained. Increasing the amount of H_2 on the surface leads to the occupation of surface sites with lower binding energies, which in turn enhances the mobility of H_2 [73,74]. However, variations in E_a can be caused by a number of factors including membrane thickness, various proportions of Ag content, mass transfer properties of support, microstructure due to preparation technique, and testing conditions.

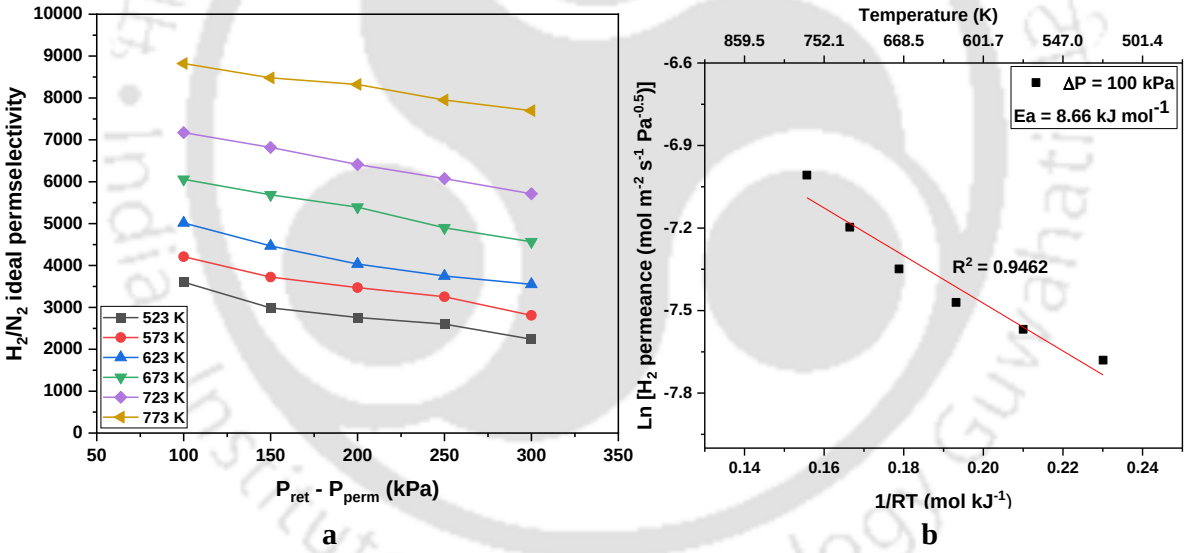

Figure 3. 12. (a) Ideal H_2/N_2 perm-selectivity as a function of transmembrane pressure at different temperatures, and (b) Arrhenius plot of ln[H_2 permeance] Vs 1/RT to calculate the activation energy of M1 membrane.

Hu et al. [5] first used the 2B-graphite lead pencil coating over alumina support to prepare Pd-based membrane. They successfully prepared a membrane of 5 µm thickness using ELP with the H_2/N_2 selectivity of 3700 and permeate H_2 flux of 25 $m^3\ m^{-2}\ h^{-1}$ at 100 kPa and 723 K. In a separate study, Hu et al. [43] deposited NiO (2.8 wt. % Ni) over alumina support via impregnation to minimize the CO content on the permeate side. The NiO-impregnated alumina

is further modified using 2B-graphite lead over which 5 µm Pd-layer is deposited using ELP called a by-functional membrane. At 723 K the Pd/Pencil/Ni/Al_2O_3 membrane exhibited a H_2/N_2 selectivity of <1000 and hydrogen permeability of 150 m^3 m^{-2} h^{-1} $MPa^{-0.5}$. Similarly, Wei et al. [17] applied the 2B-graphite lead on PSS support and deposited Pd using ELP (Pd thickness = 7 µm). Nevertheless, they observed delamination of the palladium (Pd) layer, which was afterward rectified by the application of vacuum suction during the plating process. Despite the implementation of a vacuum, the attained perm-selectivity of H_2/N_2 remained below 150 and the hydrogen permeability of 4.43 m^3 m^{-2} h^{-1} $KPa^{-0.5}$. Terra et al. [44] used alumina hollow fiber and reduced the surface roughness from 120 nm to 37 nm by a graphite coating. It required 2 rounds of Pd plating after graphite coating (Pd thickness = 1.81 µm) to attain a completely dense membrane which is 3 rounds without graphite coating (Pd thickness = 2.41 µm). After 2 rounds of Pd coating with graphite layer they were able to obtain a permeance value of 1.02×10^{-2} mol m^{-2} s^{-1} $kPa^{-0.5}$ and infinite H_2/N_2 selectivity. Recently Martinez-Diaz et al. [45] prepared a 17 µm thick Pd membrane using the electroless pore plating (ELPP) technique over 2B-graphite lead-modified PSS support. The membrane demonstrated excellent mechanical strength despite changing the direction of the permeate flux from in-out to out-in condition. The H_2 permeance ranges from 3.24×10^{-4} to 4.33×10^{-4} mol m^{-2} s^{-1} $Pa^{-0.5}$ with H_2/N_2 perm-selectivity above 10,000 under out–in mode at temperatures ranging from 623 K to 723 K. Nevertheless, in the present investigation a maximum of 0.26 mol m^{-2} s^{-1} of permeate H_2 flux and H_2/N_2 selectivity of > 5500 is achieved at 773 K and 300 kPaG for M1 membrane. These performance characteristics of the Pd-Ag membrane (~10 µm of thickness) are comparable to literature discussed.

3.3.6. Membrane Performance Under H_2/N_2 Mixture Gas

H_2 permeation through the Pd-Ag membrane is detrimentally affected by the presence of an additional gas component in the H_2-containing feed stream. Overall, three distinct explanations are provided related to the presence of each gas on the membrane performance: (i) the dilution of feed substantially reducing the partial pressure of H_2, thereby reducing the actual driving force behind H_2 permeation [75]; (ii) the active Pd-sites undergo competitive adsorption of poisoning gases such as CO, CO_2, H_2O vapor, and CH_4, which partially blocks the available sites for H_2 adsorption [8,39,76]; and (iii) the formation of a mass transfer boundary layer consisting of non-permeable gases in close proximity to the membrane surface which as a result restrict the transport of H_2 from the bulk of feed to the membrane surface [77]. Furthermore, the activation energy barrier for the dissociative adsorption and associative desorption of H_2

molecules on both sides of the membrane becomes higher in the presence of these gases [78]. In the case of H_2/N_2 mixture gas, nitrogen is regarded as the inert gas exhibiting no poisoning or inhibition effect on the H_2 permeation through the Pd-Ag membrane. However, Wang et al. [79] reported the interaction between N_2 and H_2 during the long-term co-existence which results in the formation NH_x (x = 0-2). These species block the active sites for H_2 diffusion on the membrane surface. The effect of binary H_2/N_2 feed mixture gas is plotted to represent the permeate H_2 flux as a function of the transmembrane pressure difference at 573 K, 623 K, and 673 K as shown in Figure 3.13 (a), (b), and (c) respectively. Different mixture of feed gas including 90% H_2 / 10% N_2, 80% H_2 / 20% N_2, and 70% H_2 / 30% N_2 is compared to the corresponding value with pure H_2. Feed dilution with nitrogen decreased the hydrogen partial pressure difference across the membrane resulting in lower permeate H_2 flux. The permeate H_2 flux decreased to a greater extent as temperature increased while maintaining the same pressure and N_2 content. The extent of the decrease in H_2 flux becomes even more severe at higher pressure. This is largely attributed to the formation of concentration polarization or build-up of the hydrogen-depleted layer adjacent to the membrane surface. At higher pressure, the rate of H_2 permeation is high, thereby more N_2 near the membrane surface on the retentate side effectively reduces the actual permeation driving force [75,80,81]. Moreover, a deviation from the linear trend is observed showing the presence of additional resistance to mass transport in the gas phase. This deviation may also be the result of the H_2 concentration gradient along the axial direction of the membrane which makes it almost impossible to calculate the actual partial pressure (driving force) at the end of the membrane. Calles et al. [82] observed a decrease in H_2 content of 10-15% toward the end of the membrane compared to the initial section. Additionally, the concentration of H_2 might decrease by as much as 25% in conditions of elevated temperature and pressure. This phenomenon is prominently noticeable in membranes with high permeate H_2 flux, specifically thin membranes (< 5 μm). Melendez et al. [39] reported a significant deviation in the permeate H_2 flux from Sieverts' law at higher pressure which appears to follow the same at lower pressure. Their study shows downward convexity of permeate H_2 flux toward the pressure axis at higher pressure when plotted against the square root of the H_2 partial pressure difference between retentate and permeate. It is crucial when dealing with the membrane with high permeate H_2 flux and high H_2/N_2 selectivity. In our work, we did not see this trend depicted in Figure 3.14 (a) and (b) because of the low operational H_2 partial pressure and the considerably thicker membrane. A lower permeation value helps to keep a suitable concentration of H_2 on the membrane surface even when a gas phase mass transport boundary layer is present. Hence the trend appears to follow Sieverts' law. However,

when the partial pressure of H_2 is increased beyond a certain point, a noticeable divergence from the linear pattern can be seen, as depicted in Figure 3.14 (c). This behavior indicates the presence of concentration polarization as an extra barrier to hydrogen transport, in addition to that offered by the Pd-Ag membrane [80]. Therefore, any method of increasing hydrogen permeation through the membrane helps further strengthen the influence of concentration polarization. Furthermore, it is crucial to manage the steady growth of the H_2 concentration gradient along the axial direction of the membrane. This occurrence provides a distinct indication of the corrective measures that must be implemented to counteract the concentration polarization to enhance the performance of the membrane.

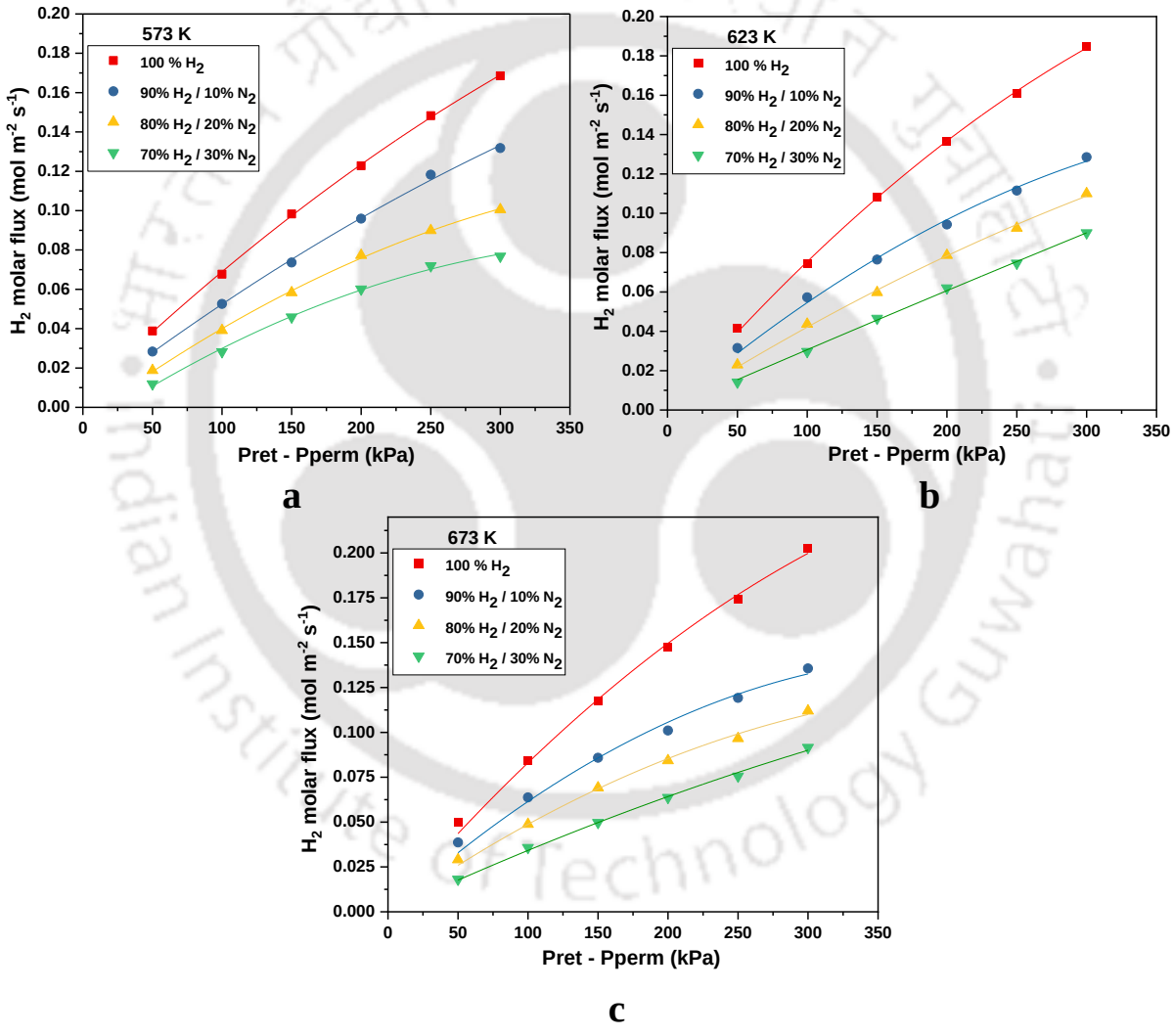

Figure 3. 12. Permeate H_2 flux for H_2/N_2 binary mixture as a function of the transmembrane pressure difference at (a) 573 K, (b) 623 K, and (c) 673 K for membrane M1.

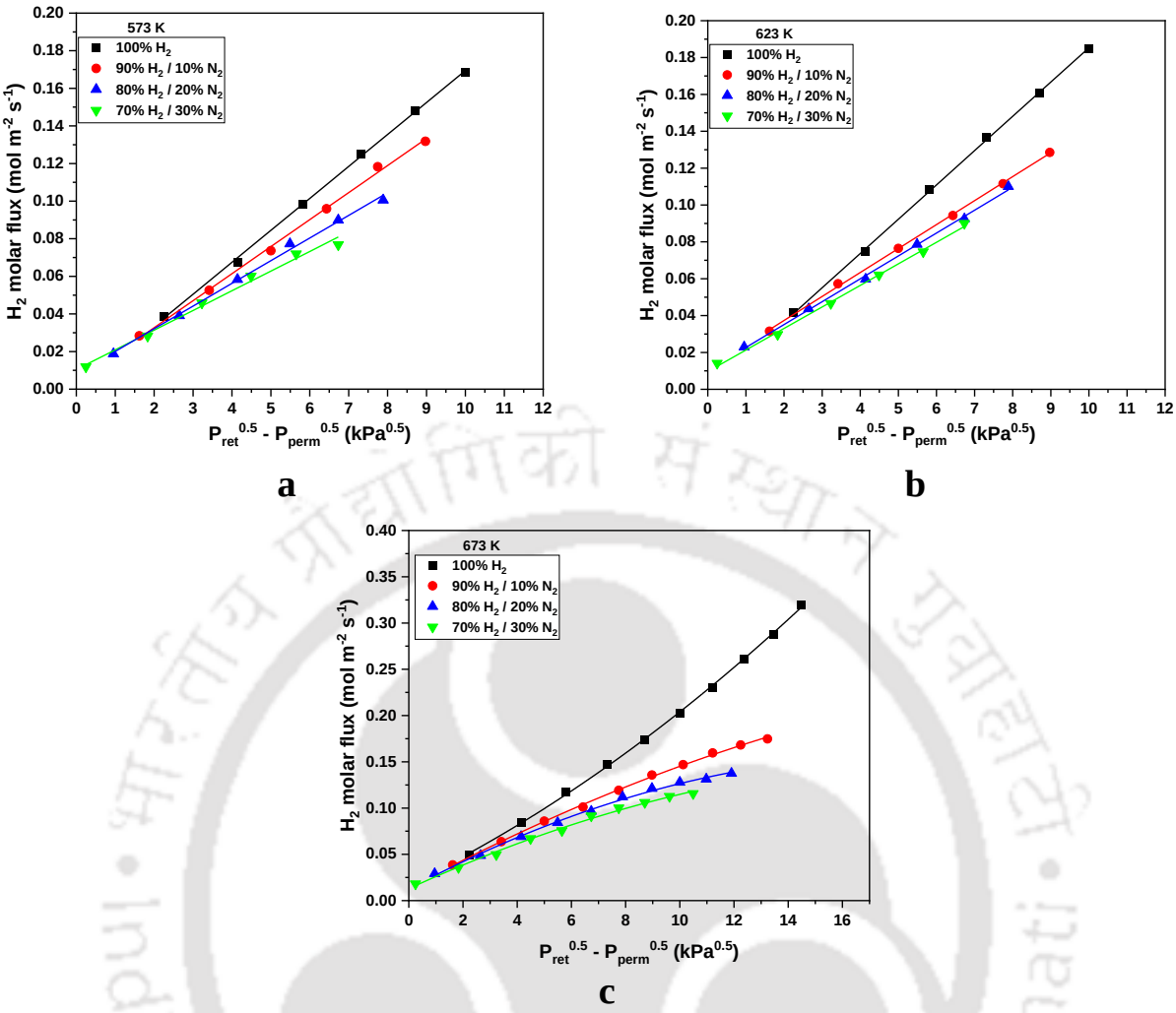

Figure 3. 13. Permeate H_2 flux for H_2/N_2 binary mixture as a function of the square root of the H_2 partial pressure at (a) 573 K, (b) 623 K, and (c) 673 K for membrane M1.

3.3.7. Membrane Performance Under H_2/CO_2 Mixture Gas

To establish a correlation between the effect of CO_2 and its interactions with the Pd-Ag membrane, the permeation test with H_2/CO_2 binary mixture gas is conducted under the same conditions as was previously described for H_2/N_2 mixture gas. Increasing the CO_2 content decreased the hydrogen partial pressure (i.e. driving force) across the membrane resulting in lower hydrogen permeation as shown in Figure 3.15 (a), (b), and (c) performed at 573 K, 623 K, and 673 K respectively. Different mixtures of feed gas including 90% H_2 / 10% CO_2, 80% H_2 / 20% CO_2, and 70% H_2 / 30% CO_2 compared to the corresponding value with pure H_2. The variation in the permeate H_2 flux is similar to that of the H_2/N_2 mixture gas at different temperatures, pressures, and mixture gas composition. According to the literature, CO_2 does not undergo any chemical reactions on the Pd membrane surface at temperatures below 723 K.

At temperatures greater than 723 K chemical reactions of CO_2 such as Reverse water-gas-shift (RWGS) play a critical role in reducing the permeate H_2 flux by a higher degree ($CO_2+H_2 \rightarrow CO+H_2O$, $CO_2+4H_2 \rightarrow CH_4+2H_2O$, and $CO_2+2H_2 \rightarrow C+H_2O$). The Pd membrane itself acts as a catalyst for the RWGS reaction. Moreover, with the increase in temperature, the effect of these chemical reactions becomes stronger [75,83,84]. Li et al. [84] reported the growth of nanoscopic carbon on the Pd membrane when exposed to CO_2 above 723 K. Carbon deposited can be slowly removed over time by switching back to pure hydrogen. However, in our study, the trend of the plot is similar to H_2/N_2 indicating that there is no surface adsorption and reaction. High-temperature testing is avoided to prevent membrane failure or any microscopic alterations for future usage in other investigations.

To examine the effect of various gas mixtures such as H_2/N_2, H_2/CO_2, H_2/CH_4, and H_2/CO on the permeation behavior of the Pd-Ag membrane, the concentration of H_2 in the mixture is altered between 90% and 20% (vol.%), with the remainder being replaced with other gases present in the mixture. Figure 3.16 shows the decrease in the permeate H_2 flux as a function of the H_2 concentration (vol. %) at 673 K and 300 kPaG. The decline in various mixture gases shows a consistent linear pattern. The permeate hydrogen flux for H_2/N_2 and H_2/CH_4 is almost the same, whereas, for H_2/CO_2 and H_2/CO gas mixtures, the hydrogen flux is slightly lower. However, according to Gallucci et al. [75], the impact of CO_2 is expected to be quite comparable to that of N_2. This deviation is thought to be caused by the potential surface interaction between CO_2 and the Pd-Ag membrane. Melendez et al. [39] also reported a similar observation where the formation of the steam and CO as a result of RWGS reaction inhibited the membrane surface even at 673 K and 300 kPaG. Additionally, the effect of H_2/CO mixture gas shows a further decrease in the permeate H_2 flux due to its significant inhibitory effect toward hydrogen permeation. As a result of the surface inhibition, it is expected that permeate H_2 flux will follow a non-linear behavior due to the strong interaction between the CO and Pd membrane. However, the influence of CO is more pronounced at lower temperatures (< 623 K). With the increase in temperature, the permeate H_2 flux starts approaching the trend quite similar to H_2/N_2 mixture gas [75]. Therefore, in our case at 673 K non-linear trend for permeate H_2 flux is not observed. While the behavior of H_2/CO is similar to H_2/N_2, the lower slope indicates that the detrimental impact of CO has not been completely eliminated. The surface inhibition of a Pd-based membrane decreases as the temperature increases [57,85]. The overall effect of CO is the result of two phenomena combined together i.e. the inhibition by CO and the decrease in the H_2 partial pressure. The subsequent section will provide a detailed

discussion of how CO affects membrane performance in relation to variations in concentration, temperature, and pressure.

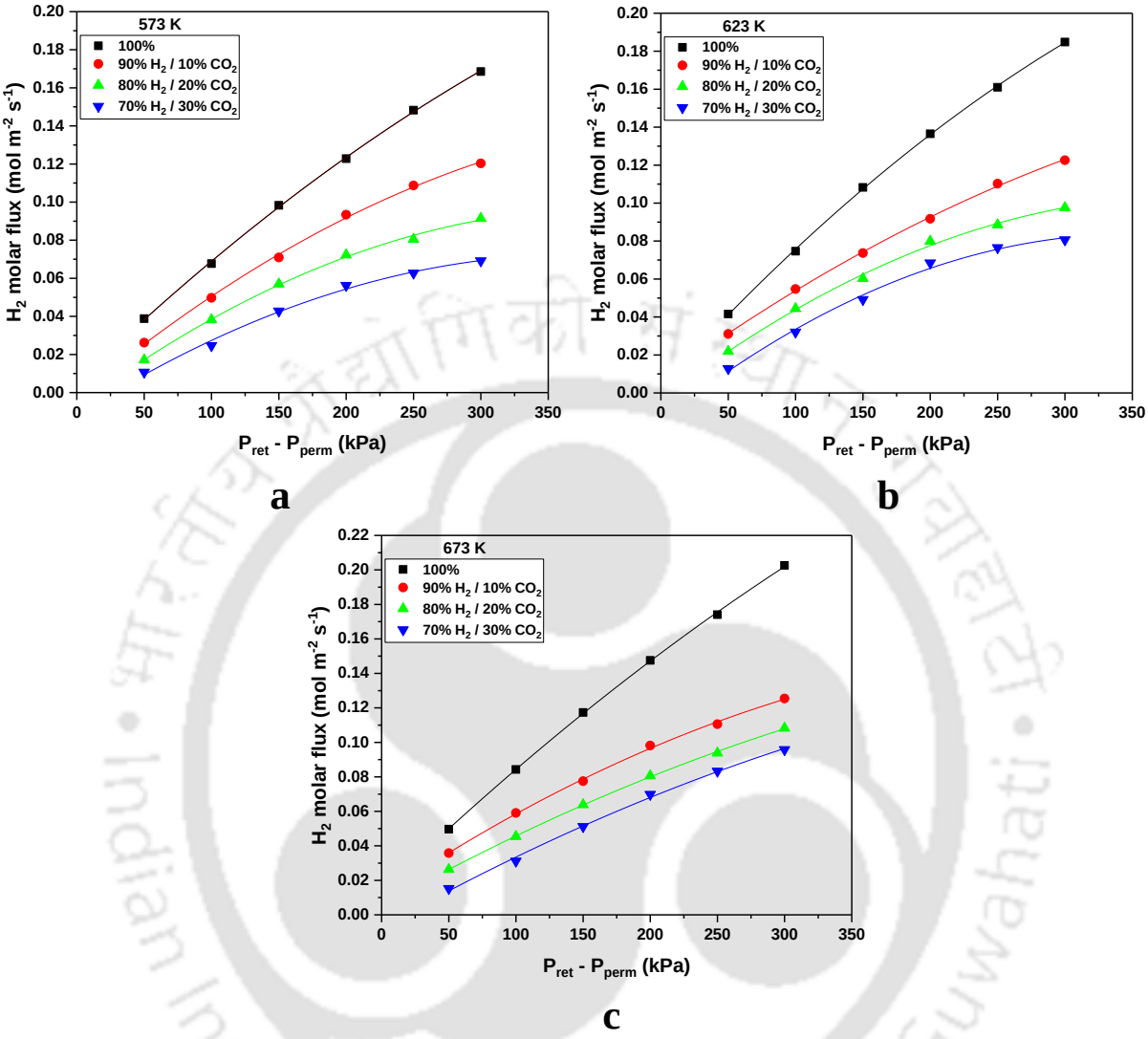

Figure 3. 14. Permeate H_2 flux for H_2/CO_2 binary mixture as a function of the transmembrane pressure difference at (a) 573 K, (b) 623 K, and (c) 673 K for membrane M1.

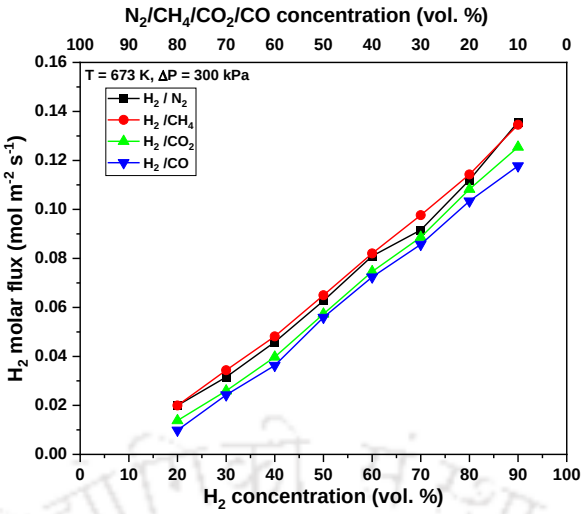

Figure 3. 15. Permeate H_2 flux as a function of H_2 concentration (vol. %) under H_2/N_2, H_2/CO_2, H_2/CH_4, and H_2/CO mixture gas at 673 K and 300 kPaG for membrane M1.

3.3.8. Membrane Performance Under H_2/CO Mixture Gas

When dealing with a feed stream that contains CO, it is crucial to consider the extra competitive adsorption of CO on the Pd-Ag membrane creating a CO-Pd surface bond via a physical adsorption process. It is necessary to consider the impact of concentration polarization as well as the coverage of the membrane surface by CO when analyzing the deviation in the permeate H_2 flux from Sieverts' law. A single CO molecule typically restricts many hydrogen dissociation sites, thereby raising the energy required for H_2 desorption by introducing an additional activation energy barrier for H_2 dissociation [86]. In addition to this, Mejdell et al. [59,87] observed microscopic alterations on the membrane surface due to a chemical reaction. This reaction led to a considerable variation in the membrane's performance by altering the number of active sites on the surface responsible for H_2 adsorption. The degree of inhibition is directly influenced by the gas composition, temperature, pressure, and thickness of the membrane [88]. The CO inhibition effect generally diminishes as the thickness of the membrane increases. The H_2 permeation through a thinner membrane is primarily dependent on the surface phenomena, for instance, the H_2 dissociation process on the active sites over the membrane. These sites the more susceptible to inhibition through competitive CO adsorption. Conversely, hydrogen permeation through a thicker membrane is predominately facilitated by bulk-phase hydrogen diffusion. Hence, it is imperative to minimize the effect of CO as much as is practical [89].

The influence of CO on the membrane performance is investigated using the M3 membrane. In order to account for the influence of CO adsorption on the membrane surface, Barbieri et al.

[61] introduced a modified version of Sieverts' law as given in Equation 3.10 that incorporates a Langmuir isotherm to quantify the decrease in the permeate H_2 flux. The modified equation is referred to as Sieverts' Langmuir Model (SL Model). The dimensionless factor $K_{CO}P_{CO}/1 + K_{CO}P_{CO}$ defines the membrane surface covered with CO due to adsorption or the amount of membrane inactive in hydrogen separation. The revised model considers the overall effect of CO adsorption i.e. inhibition due to adsorption, hydrogen dissociation, and desorption energy. A linear relation between the permeate H_2 flux and the surface coverage is assumed in this model. When the P_{CO} is greater than or equal to the saturation partial pressure of carbon monoxide i.e. the entire membrane surface is completely covered with the CO, the dimensionless factor is one. Conversely, if P_{CO} is zero then the dimensionless factor is zero and then the permeation behavior of the membrane is characterized by Sieverts' law. As a consequence, the permeate H_2 flux in relation to the driving force in Sieverts' law will exhibit a non-linear pattern until the saturation limit of carbon monoxide is reached, after the saturation limit is achieved a linear trend can be anticipated solely due to feed dilution. The effect of CO on the Pd-Ag membrane is investigated and the experimental data is compared with the values predicted by the SL Model. To accomplish this, Equation 3.10 is transformed into Equation 3.14, where a linear correlation is developed between $1/(1- (J_{H_2/CO}/J_{H_2}))$ and $1/P_{CO}$ as shown in Figure 3.17 to determine the value of α and K_{CO} two critical parameters involved in the SL Model.

$$\frac{1}{\left(1 - \frac{J_{H_2/CO}}{J_{H_2}}\right)} = \frac{1}{\alpha K_{CO}}\left(\frac{1}{P_{CO}}\right) + \frac{1}{\alpha} \qquad 3.14$$

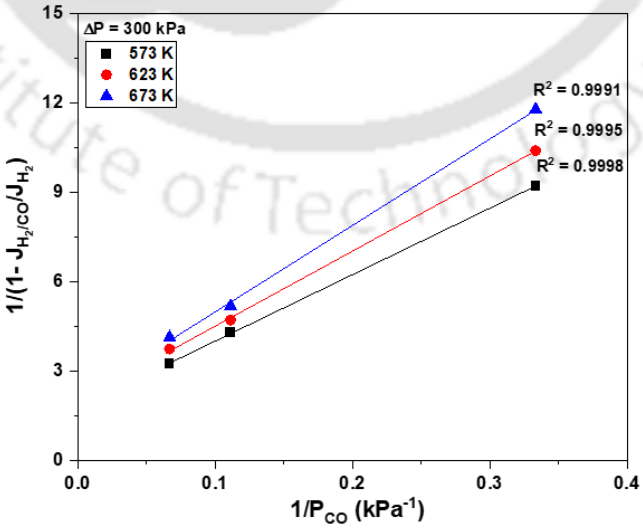

Figure 3. 16. Linear correlation between $1/(1- (J_{H2/CO} / J_{H2}))$ Vs $1/P_{co}$ at 300 kPaG and three different temperatures including 573 K, 623 K, and 673 K for membrane M3.

The parameters involved in the SL Model are directly estimated from the slope and intercept obtained from the linear fitting of the values at three different CO partial pressures (1%, 2%, and 3%). The values of parameters K_{CO} (kPa^{-1}) and α at 573 K, 623 K, and 673 K are listed in Table 3.5. The SL model can be employed to assess the reduction in permeate H_2 flux in relation to the CO partial pressures by utilizing the α and K_{CO} values. It is observed that these parameters decrease with the increase in temperature which is in agreement with Barbieri et al. [61], Yue et al. [89], and Caravella et al. [90]. The value of α is a function of temperature and it is closer to unity at lower temperature. This indicates the additional effect of the adsorbed gases, for instance, the increased dissociation of the H_2 molecules on the membrane surface, as a result of which the hydrogen permeation increases at higher temperatures.

Table 3. 5. Different parameters as obtained after fitting experimental data in the SL Model at 300 kPaG given in Equation 3.10.

Temperature (K)	α	K_{CO} (kPa^{-1})
573	0.5586	0.0801
623	0.5263	0.0753
673	0.4807	0.0716

The relative H_2 flux is calculated by dividing the permeate H_2 flux in the presence of CO by the pure H_2 permeate flux as given in Equation 3.15. The data are graphed as a relative H_2 flux to provide an easy assessment of the CO inhibitory effect performed at various temperatures. As the concentration of CO in the feed stream increases, the relative hydrogen flux approaches the saturation point, which is defined as the point at which the majority of the membrane's surface is covered with CO [61]. The SL Model is used to predict the H_2 permeation behavior in the presence of CO and compared with the data obtained experimentally. A comparison of the relative H_2 flux is presented in Figure 3.18 (a) between the experimental data and the values predicted by the SL Model, with respect to the CO concentration (vol. %) at 300 kPaG. The comparison is performed at three different temperatures including 573 K, 623 K, and 673 K. It is observed that the experimental data is in good agreement with the values predicted by the SL Model. Increasing the CO content in the feed to 20% results in a non-linear drop in the permeate H_2 flux, indicating the presence of an inhibitory effect on the membrane surface. Subsequently, a linear trend shows a drop in the permeate H_2 flux primarily caused by a reduction in the H_2 partial pressure. For instance, the relative H_2 flux is reduced to 0.53 at 573

K when the CO content is maintained at 20% showing a sharp decrease as observed from the slope of the plot. On the other hand, the relative H_2 flux dropped to only 0.42 when the CO content was increased to 80% while maintaining a linear trend. The same phenomenon is seen at temperatures of 623 K and 673 K. The observed temperature dependence may be attributed to an alteration in the equilibrium of CO adsorption, which shifts towards a greater value in comparison to hydrogen at lower temperatures. Yet, the degree of inhibition caused by CO decreases at higher temperatures. Furthermore, the value of the dimensionless factor $(K_{CO}P_{CO}/(1 + K_{CO}P_{CO}))$ increases consistently as the concentration of CO in the feed mixture is increased and ultimately approaches the unit, following the Langmuir isotherm as shown in Figure 3.18 (b) [59]. As anticipated, the value of the dimensionless factor is higher at lower temperatures as a result of the high degree of membrane surface coverage with CO. This indicates that the surface coverage by CO decreases and the global effect of CO due to inhibition and feed dilution is minimized. At higher CO partial pressure the value of a dimensionless factor approaches unity, whereas at a lower value of CO partial pressure dimensionless factor approaches zero. The primary cause of this behavior can be ascribed to the decrease in the value of the CO adsorption equilibrium relative to the hydrogen at elevated temperatures. This behavior is more clear in the plot of the extent of overall concentration polarization defined in terms of EACPC as given in Equation 3.11. $EACPC_{H_2/CO}$ considers the effect of concentration polarization and the inhibition by CO as a whole. It is observed that the value of $EACPC_{H_2/CO}$ increases with the increase in the CO concentration in the feed at 300 kPaG as shown in Figure 3.18 (c). However, a decrease in the extent of polarization is seen with the increase in temperature. This behavior is contrary to the established theory that increasing the temperature will enhance the hydrogen permeation through the membrane resulting in the accumulation of more CO near the membrane surface and hence the extent of polarization should eventually increase. These phenomena lead us to think that surface inhibition due to CO adsorption must have decreased considerably at elevated temperatures. Consequently, a decrease in the overall value of $EACPC_{H_2/CO}$ is seen at 623 K and 673 K compared to 573 K. In addition to this, $EACPC_{H_2/CO}$ starts approaching saturation at high CO concentration in the feed. Nevertheless, this study predicts the overall effect of CO on the Pd-Ag membrane, but it is not possible to separately estimate the inhibition and concentration polarization due to CO. To further investigate the inhibition effect of CO, additional permeation studies are done employing a mixture of H_2, N_2, and CO gases.

$$\text{Relative } H_2 \text{ flux} = \frac{\text{Permeate } H_2 \text{ flux with mixture gas (J)}}{\text{Permeate } H_2 \text{ flux with pure hydrogen } (J_o)} \quad 3.15$$

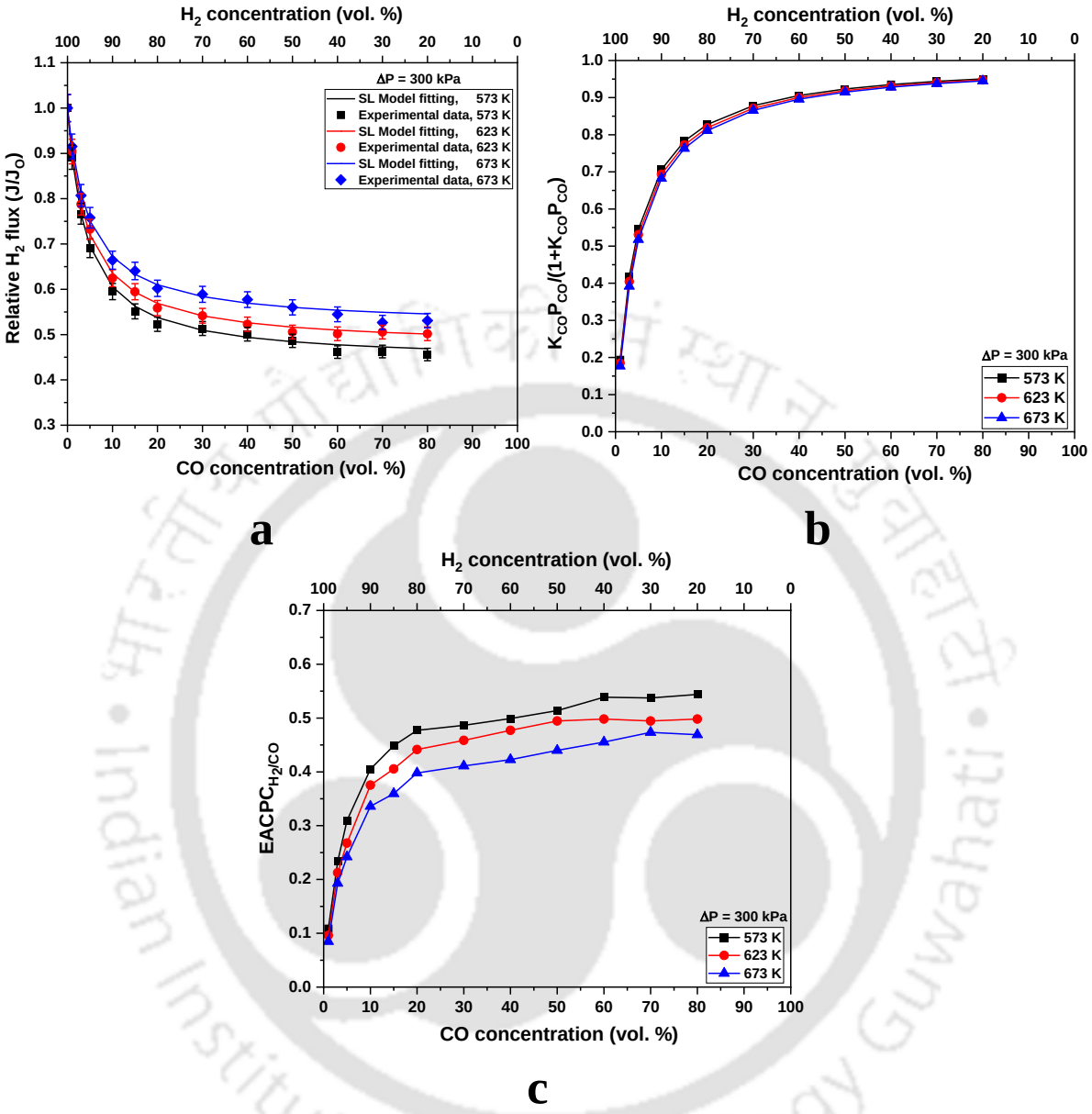

Figure 3. 17. (a) Comparison of relative H_2 flux (J/J_o) experimental data with SL model fitting between 573 K to 673 K, (b) dimensionless factor, and (c) EACPC (H_2/CO) as a function of CO concentrations (vol. %) at 300 kPaG for membrane M3.

The decrease in the permeate H_2 flux resulting from the introduction of N_2 can be solely attributable to the phenomenon of concentration polarization, whereas the introduction of CO has an inhibitory effect. Given that the binary diffusion coefficient of H_2/N_2 (0.774 cm^2 sec^{-1}) is comparable to that of H_2/CO (0.669 cm^2 sec^{-1}) [91], the substitution of N_2 with an equivalent quantity of CO would not result in a substantial alteration in the concentration polarization.

The observed decrease in H_2 flux in the $H_2/N_2/CO$ system, compared to the H_2/N_2 system, is only attributed to the competitive adsorption of CO. The effect of CO is quantified in terms of $EACPC_{H_2/N_2}$, $OIC_{H_2/N_2/CO}$, and $AIC_{H_2/CO}$ as described by Equations 3.11, 3.12, and 3.13 respectively. The permeation study is performed at three different temperatures including 573 K, 623 K, and 673 K. Table 3.6 shows the operating conditions of the experiments performed involving $H_2/N_2/CO$ mixture gas at 300 kPaG.

Table 3. 6. Operating conditions of the experiments performed involving $H_2/N_2/CO$ mixture gas at 300 kPaG.

Temperature (K)	H_2 (vol. %)	N_2 (vol. %)	CO (vol. %)
573-673	80	20	00
573-673	80	19	01
573-673	80	17	03
573-673	80	15	05
573-673	80	10	10

The inhibition coefficient, comprising EACPC and OIC, is plotted versus temperature at different concentrations of CO in the feed mixture as shown in Figure 3.19 (a) to analyze the effect of temperature on permeation behavior, both with and without CO. It is observed that the extent of concentration polarization without CO i.e. $EACPC_{H_2/N_2}$ increased with the increase in the temperature as a result of the improved hydrogen permeation at elevated temperatures. Nevertheless, the overall inhibition coefficient i.e. $OIC_{H_2/N_2/CO}$, exhibited a reduction at elevated temperatures when an equivalent quantity of N_2 was substituted with CO. This finding contradicts the observed trend in the EACPC since it can be attributed to the rise in the diffusion coefficient, which subsequently amplifies mass transfer with increasing temperature [92]. In order to understand the phenomena leading to this behavior additional parameter $AIC_{H_2/CO}$ is calculated. It is seen that increasing the temperature eventually leads to a significant decrease in the adsorption effect of CO as shown in Figure 3.19 (b). As a result, the OIC exhibited a decline, despite the presence of a contradictory trend between the EACPC and AIC. Figure 3.20 provides more evidence of this result, displaying the ratio of EACPC and AIC in OIC at 300 kPaG and varying CO content in the feed mixture. As the temperature

increased, the proportion of AIC to the total inhibition reduced, but EACPC increased. Similar behavior is also reported by Yue et al. [89].

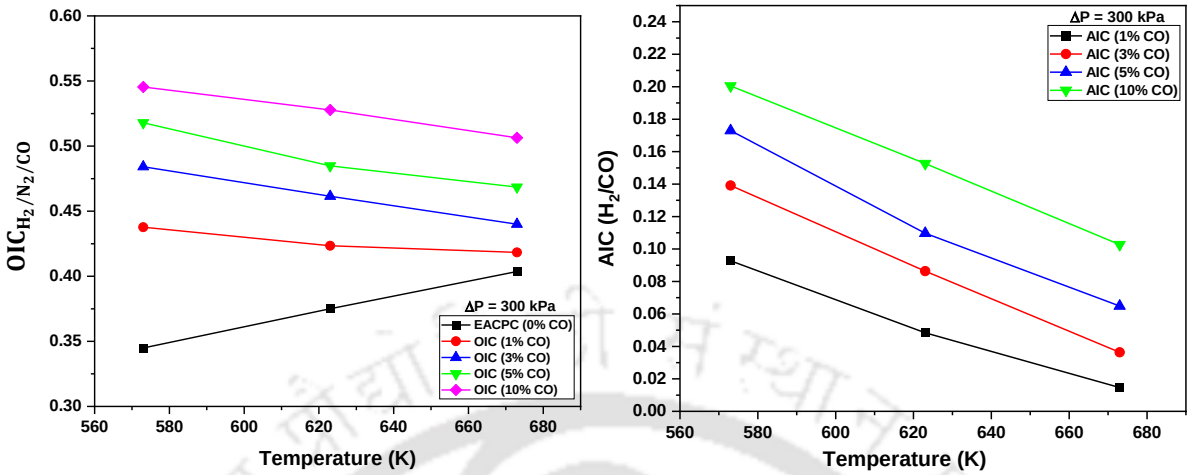

Figure 3. 18. (a) Inhibition coefficient (EACPC and OIC) and (b) AIC as a function of temperature at 300 kPaG for membrane M3.

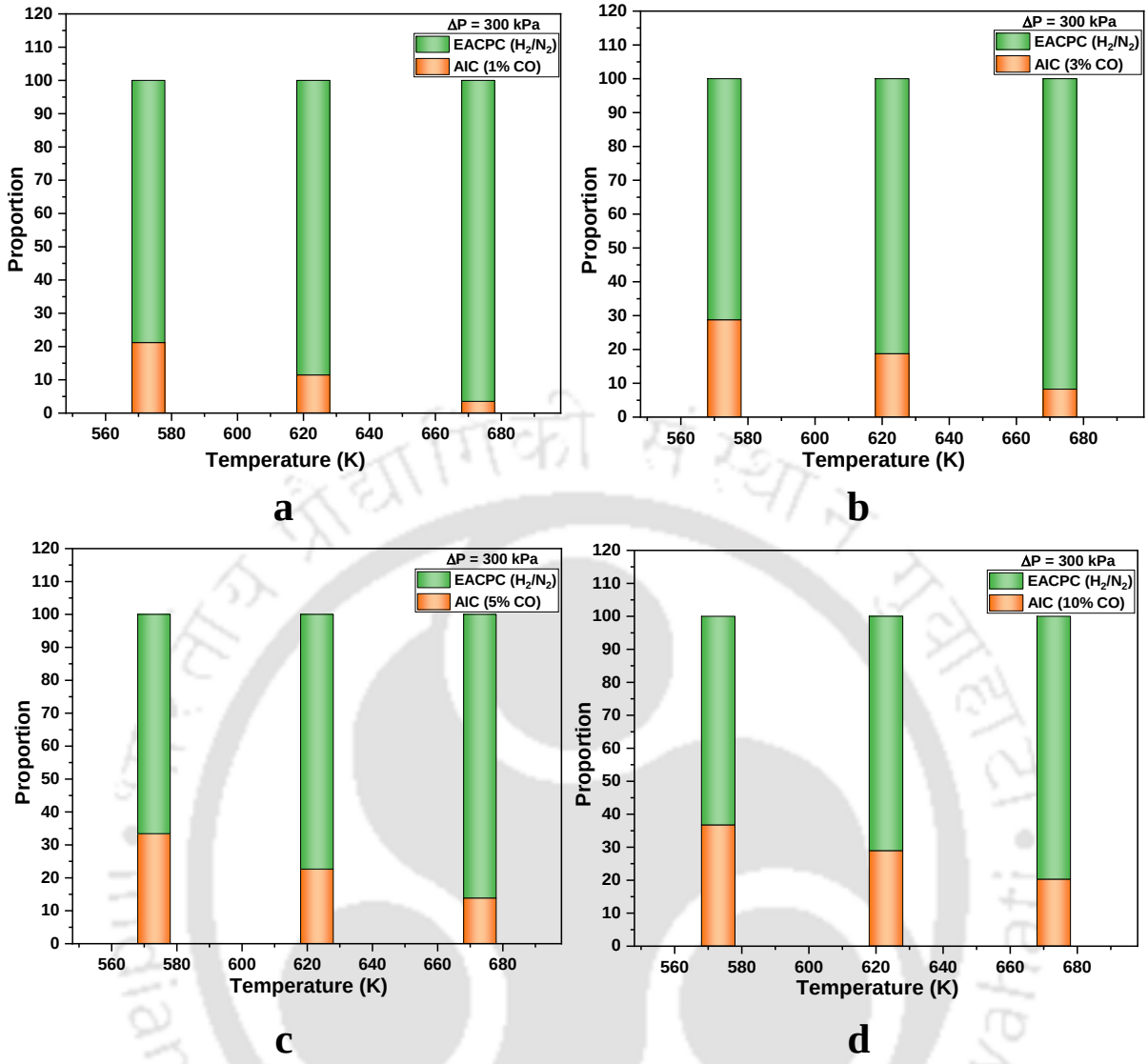

Figure 3. 19. Proportion of EACPC and AIC in OIC as a function of temperature at 300 kPaG: (a) 1% CO, (b) 3% CO, (c) 5% CO, and (d) 10% CO for membrane M3.

3.3.9. Effect of Feed Load on Membrane Performance

The initial study is performed using pure H_2 gas at varying feed loads ranging from 195 to 1600 L min^{-1} $m^{-2}_{membrane}$ at 300 kPaG of feed pressure for three different temperatures involving 573 K, 623 K, and 673 K. The permeate hydrogen flux and hydrogen recovery are plotted against the feed load for all the aforementioned temperatures as shown in Figure 3.21 (a), (b), and (c). The findings indicate that there is a positive correlation between the permeate H_2 flux and the feed load, with the latter finally reaching a maximum saturation plateau at a specific feed load. Furthermore, an H_2 recovery of 100% is observed for low feed load, indicating that the membrane retains the ability to permeate more hydrogen. Once the permeate H_2 flux

reaches saturation, there is a considerable drop in H_2 recovery. This phenomenon can be ascribed to the observation that a significant portion of the hydrogen delivered to the separator is being directed towards the retentate due to the membrane's attainment of its maximum capacity. In addition, it is necessary to increase the feed load to achieve saturation threshold at higher temperatures. The observed phenomenon aligns with the principles of the Arrhenius law, which states that the H_2 permeation through the membrane is enhanced at elevated temperatures. For instance, the permeate H_2 flux achieved saturation at 258, 322, and 483 L min^{-1} $m^{-2}_{membrane}$ of feed load for 573 K, 623 K, and 673 K respectively. Thus, one can contend that enhancing the membrane's permeation capacity necessitates a higher feed load to reach the saturation point in the permeate H_2 flux [49].

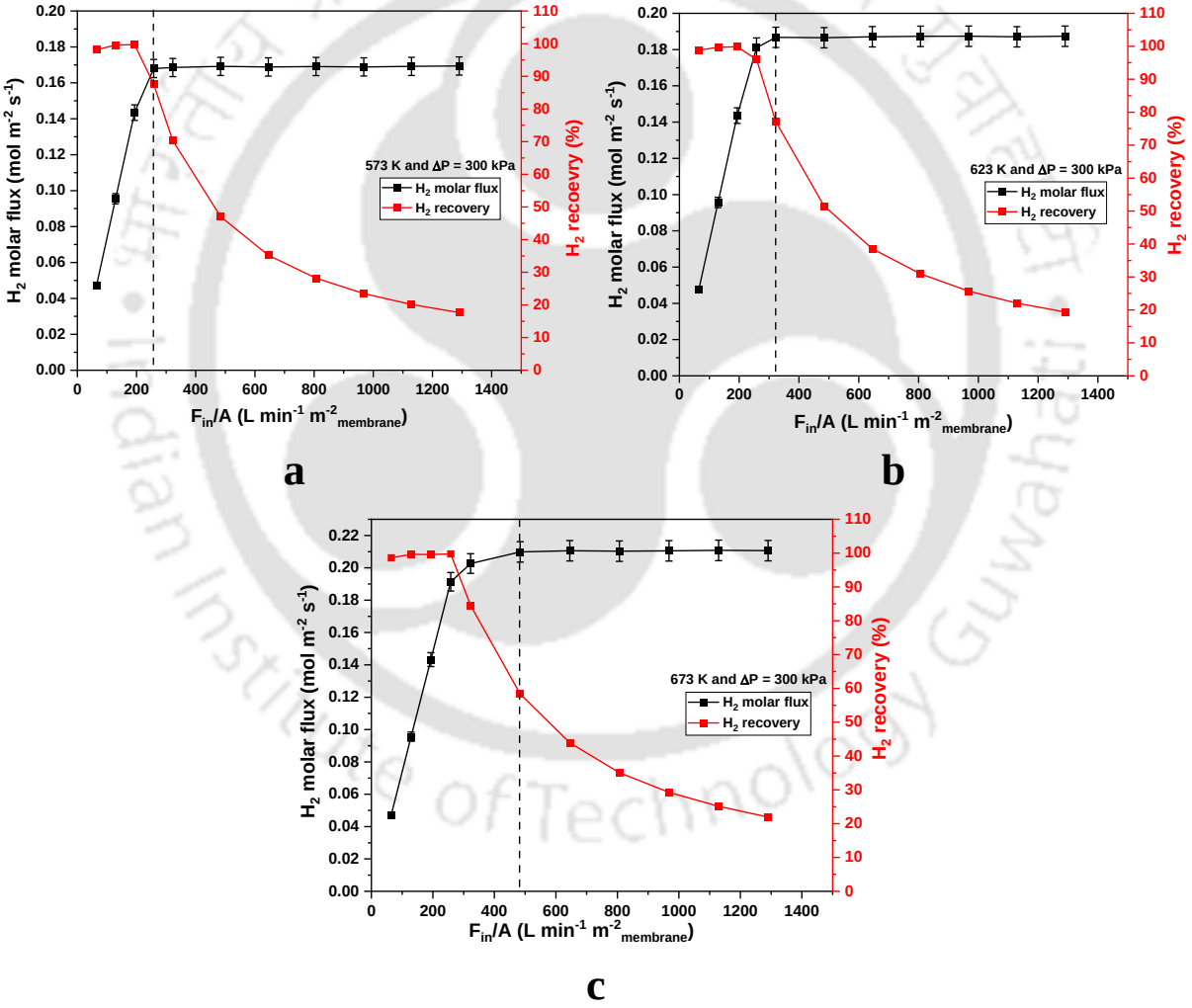

Figure 3. 20. Effect of feed load on the permeate H_2 flux and H_2 recovery at (a) 573 K, (b) 623 K, and (c) 673 K using pure H_2 at 300 kPaG for membrane M3.

Another set permeation study is also investigated using 70% H_2 / 30% N_2 mixture gas to evaluate the effect of feed dilution. The permeate H_2 flux and H_2 recovery are determined at 673 K for three different pressures 100, 200, and 300 kPaG. Figure 3.22 (a) and (b) illustrate the permeate hydrogen flux and H_2 recovery as a function of feed load for different feed pressures at 673 K and 70% H_2 / 30% N_2 binary mixture. It is observed that increasing the feed pressure, it is necessary to increase the feed load to achieve a saturation threshold at higher pressure. The observed behavior is attributed to the increase in the permeate H_2 flux at elevated pressure according to Sieverts' law. For instance, the permeate H_2 flux achieved saturation at approximately 258, 645, and 1130 L min^{-1} $m^{-2}_{membrane}$ of feed load for 100 kPaG, 200 kPaG, and 300 kPaG respectively. In the case of mixture gas, it is important to note that the concentration polarization plays a critical role and increases with the increases in the partial pressure of H_2. However, by increasing the feed load it is anticipated that the extent of concentration polarization will be reduced. Even though the concentration polarization is reduced a constant decline in the H_2 recovery is observed as shown in Figure 3.23 (b). In addition, it has been noticed that by changing the concentration of H_2 in the feed mixture gas, while keeping the feed pressure constant at 300 kPaG and the temperature at 673 K, the saturation value is obtained at a lower feed load for mixture gas with a higher H_2 concentration as shown in Figure 3.23 (a). On the other hand, the H_2 recovery decreased and began to approach a steady value when the feed load was significantly increased as illustrated in Figure 3.23 (b). This phenomenon is primarily caused by the saturation of the membrane surface with nitrogen molecules, resulting in the formation of a thin layer. Consequently, the concentration polarization exhibits minimal reduction with subsequent increases in the feed load [93,94]. The obtained outcome holds significant importance in the optimization of the membrane separator with a changing feed load, as it enables the adjustment of process conditions to attain the maximum possible recovery of H_2. Furthermore, this will aid in the development of either a membrane separator or a catalytic membrane reactor featuring multiple membranes, to demonstrate the correlation between the amount of hydrogen generation and permeation through the membrane.

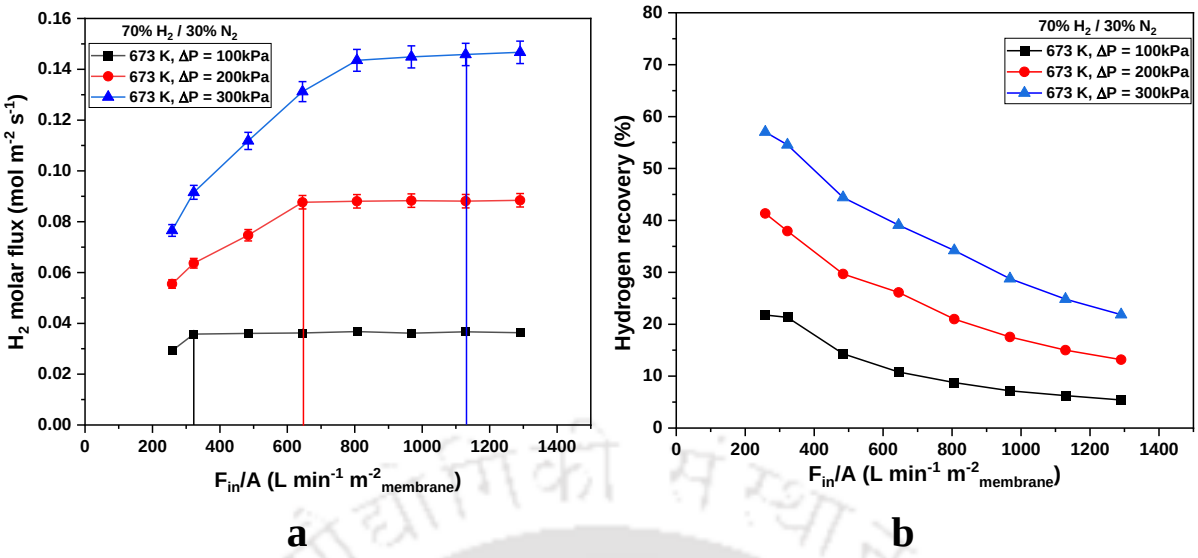

Figure 3. 21. (a) Permeate hydrogen flux and (b) H_2 recovery as a function of feed load for different feed pressures at 673 K and 70% H_2 / 30% N_2 binary mixture for membrane M3.

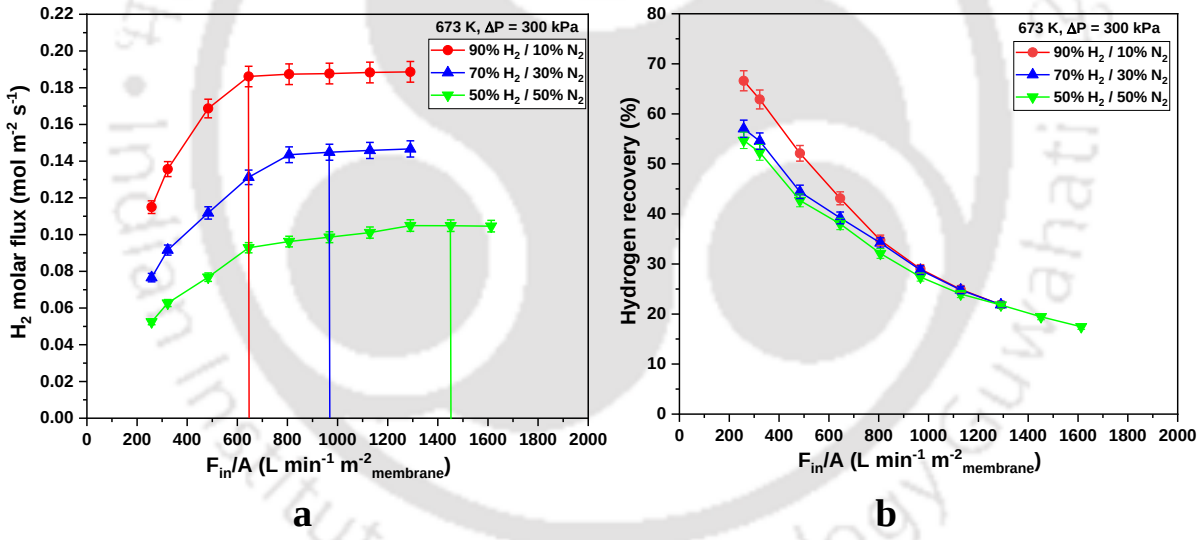

Figure 3. 22. (a) Permeate hydrogen flux and (b) H_2 recovery as a function of feed load for different H_2 concentrations in the feed mixture gas at 673 K and 300 kPaG for membrane M3.

3.4. Long-Term Thermal Heat Cycle Stability

The long-term thermal heat cycle stability of the membrane is determined at temperature different temperatures under pure H_2 and H_2/N_2 mixture gas. For the purpose of commercialization, the stability of the membrane needs to be examined as it has to undergo multiple heat cycles during continuous operation. The membrane may potentially develop pinholes, leading to a decrease in selectivity, which is essential for maintaining the purity of the permeate.

3.4.1. Durability of the Membrane Under H_2/N_2 Environment

After the deposition of Pd-Ag, the membrane is sealed using graphite ferrules that are produced internally. However, the use of these membranes is constrained as a result of the gradual and consistent development of leakage, which arises from the production of imperfections and small holes over a period of time. Consequently, this leads to a decline in the effectiveness of the membrane and ultimately reduces its lifespan. As a result, it is possible to see a decrease in hydrogen purity when exposed to conditions that are relevant in an industrial scenario. Therefore, the long-term thermal heat cycle stability of the membrane is another critical challenge. In order to examine the thermal stability of the membrane, another similar membrane M2 is conducted at a different temperature under pure H_2 and a mixture gas of 70% H_2 / 30% N_2. Multiple thermal heat cycles, each lasting 6 hours, are carried out at ΔP = 100 kPa, and the H_2 permeation is periodically measured as depicted in Figure 3.24 (a). During the first three cycles, pure H_2 is utilized at three distinct temperatures: 573 K, 623 K, and 623 K. The H_2 flux increased with an increase in temperature and maintained constant during the testing period. For the further cycle, a constant H_2 flux is observed, however, a continuous increase in the N_2 flux is seen which abruptly increased in the 10^{th} cycle by almost twice. Consequently, a constant decrease in the H_2/N_2 perm-selectivity is noticed which dropped to below 1000 after the 10^{th} heat cycle as shown in Figure 3.24 (b). This phenomenon is probably due to the damage to the membrane sealing near the fitting after multiple heat cycles. Due to the degradation of graphite near the fitting, the size of the leakage increases over time. A similar decrease in H_2/N_2 perm-selectivity as a function of time is also reported by Melendez et al. [39], Peters et al. [95], Maneerung et al. [96], and Guazzone and Ma [97] primarily caused due to the damage of membrane sealing or formation of new pinholes as a result of inhomogeneous sintering of Pd-Ag layer starting at about 673-723 K. Moreover, the expected lifetime of the membrane is rapidly reduced with increasing temperature, especially after 673 K. However, in

our case, two such pinholes are observed on the membrane surface as evident from the rising water bubble point testing, other than one leakage from the membrane sealing. After readjusting the fitting, the leakage near the fitting has been effectively sealed completely once again. An additional round of targeted plating near the pinhole area is performed by covering the rest of the membrane with Teflon tape. By implementing this approach, the utilization of the precious Pd is minimized, while simultaneously saving the additional permeation loss. Thereafter another cycle of testing of the same membrane is performed where it can be observed that in the 11th heat cycle, the initial H_2/N_2 perm-selectivity is again restored. However, a little decrease in the permeate H_2 flux is observed as a result of an extra round of plating near the pinholes formed earlier. To ascertain the morphological transformation that occurs throughout the long-term operation, a post-characterization of the same membrane is conducted.

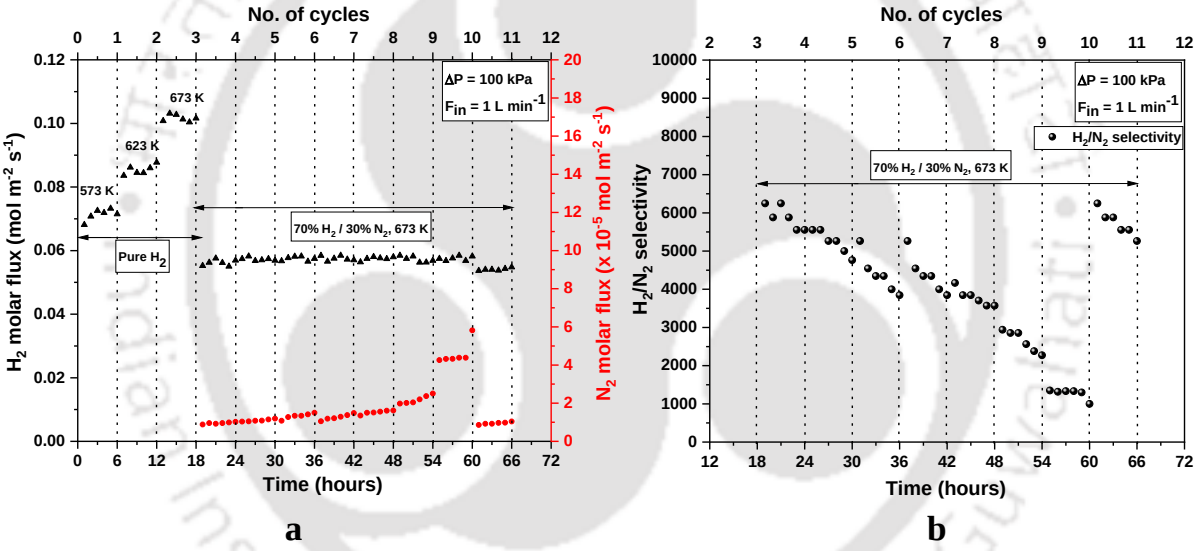

Figure 3. 23. (a) Long-term thermal heat cycle stability and (b) H_2/N_2 selectivity of Pd-Ag membrane (M2) under pure hydrogen and 70% H_2 / 30% N_2 gas mixture for 66 h at 673K and ΔP = 100 kPa for membrane M2.

3.4.2. Examination of SEM Analysis After Testing

In order to investigate the stability of the Pd-Ag layer and possible sources of leakage over time, the SEM analysis of the membrane is performed at different magnifications. The microstructure and the surface morphology are studied to visualize any defects on the membrane surface. Figure 3.25 (a) and (c) show the surface characteristics of the Pd-Ag membrane respectively before and after long-term thermal stability testing. In general, most of the organization of the grains and defects is assumed to take place during the early stage of

annealing. On the other hand, recrystallization and grain development during long-term operation may cause subsequent modifications. The microstructure revealed that the grains had recrystallized, which is why there are many dislocations in the grain boundaries and evidence of migration or rearrangement in the membrane surface. This is most likely the result of the hydrogen that has dissolved during the heat cycle across the miscibility gap creating strain in the membrane [65,98]. At higher magnification, some microcracks and voids are visible as shown in Figure 3.25 (c). No such defects were earlier observed on the membrane surface before testing. The formation of these pinholes and voids as illustrated in Figure 3.25 (d) is the main source of the increase in the permeate N_2 flux after long-term thermal heat treatment which was also earlier observed during the testing of M2 membrane. However, these cracks were not observed at the same magnification before testing as can be seen in Figure 3.25 (d). Usually, the extent and concentration of these defects decline with increasing membrane thickness.

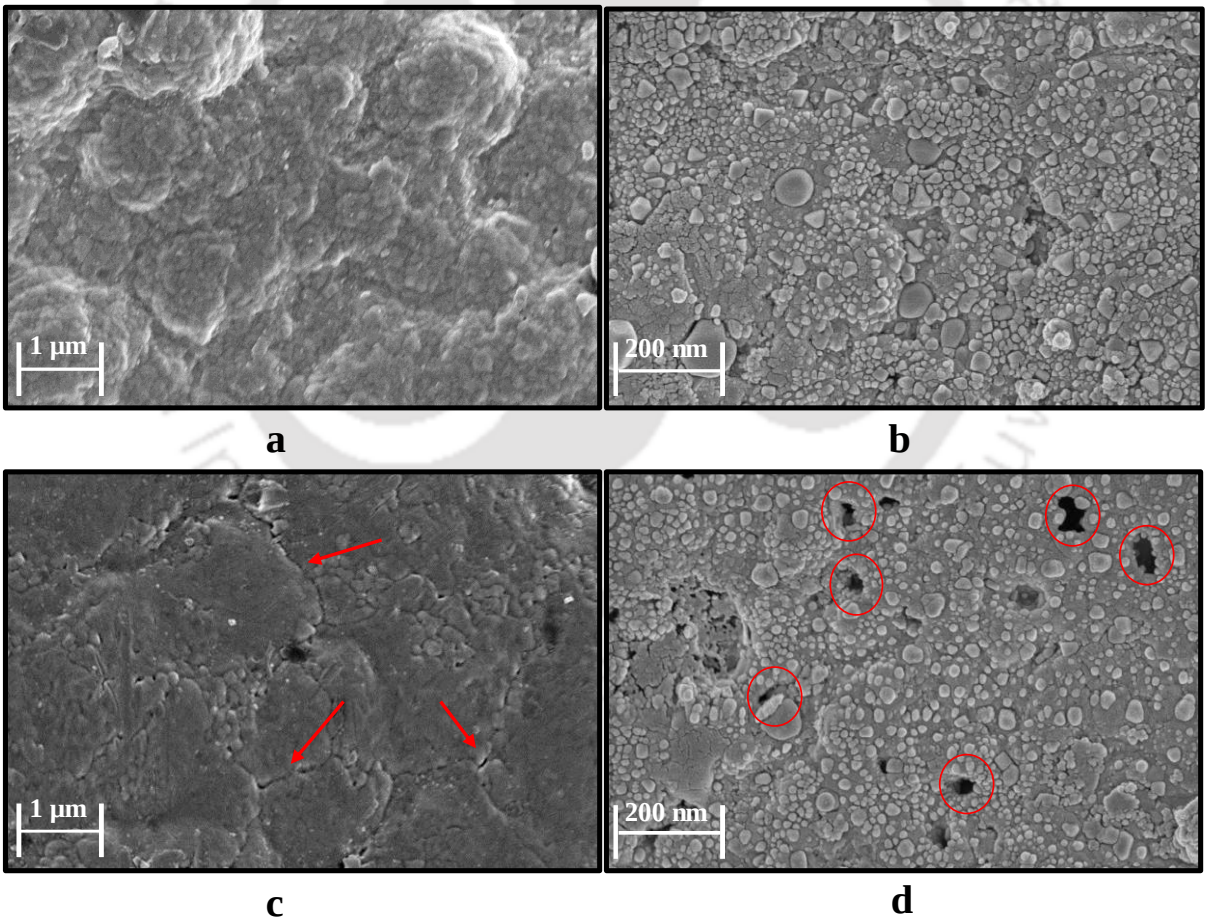

Figure 3. 24. (a, b) SEM characterization of the M2 membrane before and (c, d) after long-term thermal heat cycle stability testing at different magnifications.

3.5. Summary

A composite Pd-Ag membrane is prepared using the ELP technique over the porous alumina support. The surface pore-mouth of the support is modified using a 2B-graphite. Ten similar membranes are prepared following the same methodology. The surface morphology and elemental composition of the synthesized membrane are monitored by SEM and EDS. This study provides a systematic methodology for Pd-Ag membrane testing and determining its performance parameters such as permeate H_2 flux, selectivity, and permeation behavior in mixture gas environments such as H_2/N_2, H_2/CO_2, H_2/CO, and H_2/CH_4. In addition, the membrane performance is also determined at varying feed loads with pure H_2 as well as H_2/N_2 mixture gas. The membrane is tested leak free till 400kPaG. H_2 flux increases with partial pressure difference and temperature following liner trend as per Sievert's law and Arrhenius law respectively. The H_2/N_2 selectivity of the membrane is found to be above 5000 even after 10 thermal cycles and 60 hours of continuous operation. Increasing the CO content drastically reduces the H_2 flux due to the combined effect of surface inhibition and a decrease in H_2 partial pressure. Increasing the feed load increased the permeate H_2 flux and finally reached a stationary value at a high feed flow rate. At higher temperatures high feed load can be processed through the same membrane. In addition, it is observed that by changing the concentration of H_2 in the feed mixture gas, while keeping the feed pressure constant at 300 kPaG and the temperature at 673 K, the saturation value is obtained at a lower feed load for mixture gas with a higher H_2 concentration.

References

[1] S. Yun, S. Ted Oyama, Correlations in palladium membranes for hydrogen separation: A review, Journal of Membrane Science, 375 (2011), pp. 28–45.

[2] P.M. Thoen, F. Roa, J.D. Way, High flux palladium-copper composite membranes for hydrogen separations, Desalination, 193 (2006), pp. 224–229.

[3] S. Uemiya, T. Matsuda, E. Kikuchi, Hydrogen permeable palladium-silver alloy membrane supported on porous ceramics, Journal of Membrane Science, 56 (1991), pp. 315–325.

[4] F. Roa, J. Douglas Way, R.L. McCormick, S.N. Paglieri, Preparation and characterization of Pd-Cu composite membranes for hydrogen separation, Chemical Engineering Journal, 93 (2003), pp. 11–22.

[5] X. Hu, W. Chen, Y. Huang, Fabrication of Pd/ceramic membranes for hydrogen separation based on low-cost macroporous ceramics with pencil coating, International Journal of Hydrogen Energy, 35 (2010), pp. 7803–7808.

[6] B. Anzelmo, S. Liguori, I. Mardilovich, A. Iulianelli, Y.H. Ma, J. Wilcox, A. Basile, Fabrication & performance study of a palladium on alumina supported membrane reactor: Natural gas steam reforming, a case study, International Journal of Hydrogen Energy, 43 (2018), pp. 7713–7721.

[7] W. Chen, X. Hu, R. Wang, Y. Huang, On the assembling of Pd/ceramic composite membranes for hydrogen separation, Separation and Purification Technology, 72 (2010), pp. 92–97.

[8] E. Fernandez, A. Helmi, K. Coenen, J. Melendez, J.L. Viviente, D.A. Pacheco Tanaka, M. Van Sint Annaland, F. Gallucci, Development of thin Pd-Ag supported membranes for fluidized bed membrane reactors including WGS related gases, International Journal of Hydrogen Energy, 40 (2015), pp. 3506–3519.

[9] M.L. Bosko, J.B. Miller, E.A. Lombardo, A.J. Gellman, L.M. Cornaglia, Surface characterization of Pd-Ag composite membranes after annealing at various temperatures, Journal of Membrane Science, 369 (2011), pp. 267–276.

[10] H.B. Zhao, K. Pflanz, J.H. Gu, A.W. Li, N. Stroh, H. Brunner, G.X. Xiong, Preparation of palladium composite membranes by modified electroless plating procedure, Journal

of Membrane Science, 142 (1998), pp. 147–157.

[11] R. Sanz, J.A. Calles, D. Alique, L. Furones, S. Ordóñez, P. Marín, P. Corengia, E. Fernandez, Preparation, testing and modelling of a hydrogen selective Pd/YSZ/SS composite membrane, International Journal of Hydrogen Energy, 36 (2011), pp. 15783–15793.

[12] A. Tarditi, C. Gerboni, L. Cornaglia, PdAu membranes supported on top of vacuum-assisted ZrO2-modified porous stainless steel substrates, Journal of Membrane Science, 428 (2013), pp. 1–10.

[13] H. Gao, J.Y.S. Lin, Y. Li, B. Zhang, Electroless plating synthesis, characterization and permeation properties of Pd-Cu membranes supported on ZrO2 modified porous stainless steel, Journal of Membrane Science, 265 (2005), pp. 142–152.

[14] L. Wei, J. Yu, X. Hu, Y. Huang, Facile surface modification of porous stainless steel substrate with TiO2 intermediate layer for fabrication of H2-permeable composite palladium membranes, Separation Science and Technology (Philadelphia), 51 (2016), pp. 998–1006.

[15] A. Qiao, K. Zhang, Y. Tian, L. Xie, H. Luo, Y.S. Lin, Y. Li, Hydrogen separation through palladium-copper membranes on porous stainless steel with sol-gel derived ceria as diffusion barrier, Fuel, 89 (2010), pp. 1274–1279.

[16] M.L. Bosko, F.Ojeda, E.A. Lombardo, L.M. Cornaglia, NaA zeolite as an effective diffusion barrier in composite Pd/PSS membranes, Journal of Membrane Science, 331 (2009), pp. 57–65.

[17] L. Wei, J. Yu, X. Hu, Y. Huang, Fabrication of H2-permeable palladium membranes based on pencil-coated porous stainless steel substrate, International Journal of Hydrogen Energy, 37 (2012), pp. 13007–13012.

[18] M. Maroño, G. ĎAlessandro, A. Morales, D. Martinez-Diaz, D. Alique, J.M. Sánchez, Influence of Si and Fe/Cr oxides as intermediate layers in the fabrication of supported Pd membranes, Separation and Purification Technology, 234 (2020), pp. 116091.

[19] S. Samingprai, S. Tantayanon, Y.H. Ma, Chromium oxide intermetallic diffusion barrier for palladium membrane supported on porous stainless steel, Journal of Membrane Science, 347 (2010), pp. 8–16.

[20] E. Fernandez, Palladium-based supported membranes for membrane reactors for

hydrogen production, Eindhoven University of Technology, 2016.

[21] F.A. Lewis, The Palladium-Hydrogen System: A survey of hydride formation and the effects, Platinum Metals Review, 26 (1982), pp. 20–27.

[22] A.K.M. Fazle Kibria, Y. Sakamoto, Effect of alloying of palladium with silver and rhodium on the hydrogen solubility, miscibility gap and hysteresis, International Journal of Hydrogen Energy, 25 (2000), pp. 853–859.

[23] F.A.L. J. C. Barton, J. A. S. Green, Changes of Electrode Potential and Electrical Resistance as a Function of the Hydrogen Content of some Pd+Ni and Pd+Rh Alloys BY, Chemistry Dept., The Queen's University of Belfast, 1 (1965), pp. 960–970.

[24] V. Gryaznov, Metal containing membranes for the production of ultrapure hydrogen and the recovery of hydrogen isotopes, Separation and Purification Methods, 29 (2000), pp. 171–187.

[25] D.L. McKinley, Metal alloy for hydrogen separation and purification, 3350845, 1967.

[26] Y. Sakamoto, T. Ohishi, E. Kumashiro, K. Takao, Diffusivity and solubility of hydrogen in Pd-Fe and Pd-V alloys, Journal of The Less Common Metals, 88 (1982), pp. 379–385.

[27] M. Kajiwara, S. Uemiya, T. Kojima, E. Kikuchi, Rhodium- and iridium-dispersed porous alumina membranes and their hydrogen permeation properties, Catalysis Today, 56 (2000), pp. 83–87.

[28] K.J. Bryden, J.Y. Ying, Nanostructured palladium-iron membranes for hydrogen separation and membrane hydrogenation reactions, Journal of Membrane Science, 203 (2002), pp. 29–42.

[29] H. Yoshida, K. Okuno, Y. Naruse, T. Kashiwai, Metallurgical Considerations on Pd, Pd-Alloy and Their Metal-Hydrogen Systems, Fusion Technology, 8 (1985), pp. 2388–2394.

[30] Y. Sakamoto, F.L. Chen, M. Furukawa, K. Mine, The (α + β) hydrogen miscibility gaps in hydrogenated palladium-rich Pd-Y(Gd)-Ag ternary alloys, Journal of The Less-Common Metals, 166 (1990), pp. 45–56.

[31] A.C. Makrides, Absorption of hydrogen by silver-palladium alloys, Journal of Physical Chemistry, 68 (1964), pp. 2160–2169.

[32] M.E. Ayturk, Synthesis, Annealing Strategies and in-situ Characterization of Thermally Stable Composite Thin Pd-Ag Alloy Membranes for H2 Separation, Worcester Polutechnic Institute, 2007.

[33] N.J.W. and A.-M.M. Rhoda, R. N., Palladium plating by chemical reduction, 2,915,406, 1959.

[34] J. Shu, A. Adnot, B.P.A. Grandjean, S. Kaliaguine, Structurally stable composite Pd-Ag alloy membranes: Introduction of a diffusion barrier, Thin Solid Films, 286 (1996), pp. 72–79.

[35] R. Bhandari, The synthesis of Pd-Ag composite membranes for H2 separation using electroless plating method, Worcester Polytechnic Institute, 2010.

[36] J. Okazaki, T. Ikeda, D.A.P. Tanaka, K. Sato, T.M. Suzuki, F. Mizukami, An investigation of thermal stability of thin palladium-silver alloy membranes for high temperature hydrogen separation, Journal of Membrane Science, 366 (2011), pp. 212–219.

[37] J. Shu, B.P.A. Grandjean, E. Ghali, S. Kaliaguine, Simultaneous deposition of Pd and Ag on porous stainless steel by electroless plating, Journal of Membrane Science, 77 (1993), pp. 181–195.

[38] D.A. Pacheco Tanaka, M.A. Llosa Tanco, S.I. Niwa, Y. Wakui, F. Mizukami, T. Namba, T.M. Suzuki, Preparation of palladium and silver alloy membrane on a porous α-alumina tube via simultaneous electroless plating, Journal of Membrane Science, 247 (2005), pp. 21–27.

[39] J. Melendez, E. Fernandez, F. Gallucci, M. van Sint Annaland, P.L. Arias, D.A. Pacheco Tanaka, Preparation and characterization of ceramic supported ultra-thin (~1 μm) Pd-Ag membranes, Journal of Membrane Science, 528 (2017), pp. 12–23.

[40] A.L. Mejdell, M. Jøndahl, T.A. Peters, R. Bredesen, H.J. Venvik, Experimental investigation of a microchannel membrane configuration with a 1.4 μm Pd/Ag23 wt.% membrane-Effects of flow and pressure, Journal of Membrane Science, 327 (2009), pp. 6–10.

[41] T.A. Peters, M. Stange, R. Bredesen, On the high pressure performance of thin supported Pd-23%Ag membranes-Evidence of ultrahigh hydrogen flux after air treatment, Journal of Membrane Science, 378 (2011), pp. 28–34.

[42] S. Agnolin, F. Apostolo, L. Di Felice, J. Melendez Rey, A. Pacheko Tanaka, M. Llosa Tanco, F. Gallucci, Development of selective Pd–Ag membranes on porous metal filters, International Journal of Hydrogen Energy, 48 (2023), pp. 25398–25409.

[43] X. Hu, W. Yan, W. Ding, J. Yu, Y. Huang, Bifunctional palladium composite membrane for hydrogen separation and catalytic CO methanation, Cuihua Xuebao/Chinese Journal of Catalysis, 34 (2013), pp. 1720–1729.

[44] N.M. Terra, L.P. Bessa, V.L. Cardoso, M.H.M. Reis, Graphite coating on alumina substrate for the fabrication of hydrogen selective membranes, International Journal of Hydrogen Energy, 43 (2018), pp. 1534–1544.

[45] D. Martinez-Diaz, R. Sanz, A. Carrero, J.A. Calles, D. Alique, Effective H2 separation through electroless pore-plated pd membranes containing graphite lead barriers, Membranes, 10 (2020), pp. 1–17.

[46] J. Okazaki, T. Ikeda, D.A.P. Tanaka, M.A. Llosa Tanco, Y. Wakui, K. Sato, F. Mizukami, T.M. Suzuki, Strong interaction at the palladium/alumina interface of membrane during hydrogen permeation at elevated temperature, Chemistry Letters, 37 (2008), pp. 1004–1005.

[47] G. Straczewski, J. Völler-Blumenroth, H. Beyer, P. Pfeifer, M. Steffen, I. Felden, A. Heinzel, M. Wessling, R. Dittmeyer, Development of thin palladium membranes supported on large porous 310L tubes for a steam reformer operated with gas-to-liquid fuel, Chemical Engineering and Processing: Process Intensification, 81 (2014), pp. 13–23.

[48] A.M. Tarditi, M.L. Bosko, L.M. Cornaglia, Alloying and surface composition of model Pd-Ag films synthesized by electroless deposition, International Journal of Hydrogen Energy, 37 (2012), pp. 6020–6029.

[49] T.A. Peters, M. Stange, H. Klette, R. Bredesen, High pressure performance of thin Pd-23%Ag/stainless steel composite membranes in water gas shift gas mixtures; influence of dilution, mass transfer and surface effects on the hydrogen flux, Journal of Membrane Science, 316 (2008), pp. 119–127.

[50] G. Zeng, H. Jia, A. Goldbach, L. Zhao, S. Miao, L. Shi, C. Sun, H. Xu, Hydrogen-induced high-temperature segregation in palladium silver membranes, Physical Chemistry Chemical Physics, 16 (2014), pp. 25330–25336.

[51] H.W. Abu El Hawa, S.N. Paglieri, C.C. Morris, A. Harale, J. Douglas Way, Identification of thermally stable Pd-alloy composite membranes for high temperature applications, Journal of Membrane Science, 466 (2014), pp. 151–160.

[52] S.N. Paglieri, J.D. Way, Innovations in palladium membrane research, Separation and Purification Methods, 31 (2002), pp. 1–169.

[53] P.P. Mardilovich, Y. She, Y.H. Ma, M.H. Rei, Defect-Free Palladium Membranes on Porous Stainless-Steel Support, AIChE Journal, 44 (1998), pp. 310–322.

[54] Y.H. Ma, B.C. Akis, M.E. Ayturk, F. Guazzone, E.E. Engwall, I.P. Mardilovich, Characterization of Intermetallic Diffusion Barrier and Alloy Formation for Pd/Cu and Pd/Ag Porous Stainless Steel Composite Membranes, Industrial & Engineering Chemistry Research, 43 (2004), pp. 2936–2945.

[55] J. Okazaki, D.A.P. Tanaka, M.A.L. Tanco, Y. Wakui, F. Mizukami, T.M. Suzuki, Hydrogen permeability study of the thin Pd-Ag alloy membranes in the temperature range across the α-β phase transition, Journal of Membrane Science, 282 (2006), pp. 370–374.

[56] S.K. Ryi, J.S. Park, K.R. Hwang, C.B. Lee, S.W. Lee, Repair of Pd-based composite membrane by polishing treatment, International Journal of Hydrogen Energy, 36 (2011), pp. 13776–13780.

[57] M.M. Barreiro, M. Maroño, J.M. Sánchez, Hydrogen permeation through a Pd-based membrane and RWGS conversion in H2/CO2, H2/N2/CO2 and H2/H2O/CO2 mixtures, International Journal of Hydrogen Energy, 39 (2014), pp. 4710–4716.

[58] Y.W. Budhi, W. Suganda, H.K. Irawan, E. Restiawaty, M. Miyamoto, S. Uemiya, N. Nishiyama, M. van Sint Annaland, Hydrogen separation from mixed gas (H2, N2) using Pd/Al2O3 membrane under forced unsteady state operations, International Journal of Hydrogen Energy, 45 (2020), pp. 9821–9835.

[59] A.L. Mejdell, M. Jøndahl, T.A. Peters, R. Bredesen, H.J. Venvik, Effects of CO and CO2 on hydrogen permeation through a ~3 μm Pd/Ag 23 wt.% membrane employed in a microchannel membrane configuration, Separation and Purification Technology, 68 (2009), pp. 178–184.

[60] A. Alkali, K. Abdullahi, A Comparison of the Inhibiting Effect of CO and CO2 to Hydrogen Permeation and n-Value in Pd and Pd/Ag Membranes Prepared on Alumina

Support, Journal of Power and Energy Engineering, 07 (2019), pp. 1–14.

[61] G. Barbieri, F. Scura, F. Lentini, G. De Luca, E. Drioli, A novel model equation for the permeation of hydrogen in mixture with carbon monoxide through Pd-Ag membranes, Separation and Purification Technology, 61 (2008), pp. 217–224.

[62] K. Zhang, S.K. Gade, Ø. Hatlevik, J.D. Way, A sorption rate hypothesis for the increase in H 2 permeability of palladium-silver (Pd-Ag) membranes caused by air oxidation, International Journal of Hydrogen Energy, 37 (2012), pp. 583–593.

[63] N. de Nooijer, A.A. Plazaola, J.M. Rey, E. Fernandez, D.A.P. Tanaka, M. van S. Annaland, F. Gallucci, Long-term stability of thin-film Pd-based supported membranes, Processes, 7 (2019), pp. 1–23.

[64] W.M. Tucho, H.J. Venvik, M. Stange, J.C. Walmsley, R. Holmestad, R. Bredesen, Effects of thermal activation on hydrogen permeation properties of thin, self-supported Pd/Ag membranes, Separation and Purification Technology, 68 (2009), pp. 403–410.

[65] W.M. Tucho, H.J. Venvik, J.C. Walmsley, M. Stange, A. Ramachandran, R.H. Mathiesen, A. Borg, R. Bredesen, R. Holmestad, Microstructural studies of self-supported (1.5-10 μm) Pd/23 wt%Ag hydrogen separation membranes subjected to different heat treatments, Journal of Materials Science, 44 (2009), pp. 4429–4442.

[66] R.J.R. Uhlhorn, K. Keizer, A.J. Burggraaf, Gas and surface diffusion in modified γ-alumina systems, Journal of Membrane Science, 46 (1989), pp. 225–241.

[67] S. Liguori, A. Iulianelli, F. Dalena, P. Pinacci, F. Drago, M. Broglia, Y. Huang, A. Basile, Performance and long-term stability of Pd/PSS and Pd/Al2O3 membranes for hydrogen separation, Membranes, 4 (2014), pp. 143–162.

[68] F. Guazzone, E.E. Engwall, Y.H. Ma, Effects of surface activity, defects and mass transfer on hydrogen permeance and n-value in composite palladium-porous stainless steel membranes, Catalysis Today, 118 (2006), pp. 24–31.

[69] Y. Yang, X. Li, X. Liang, R. Chen, J. Guo, H. Fu, D. Liu, A two-step electroless plating method for Pd composite membranes with enhanced hydrogen selectivity and superior high-temperature stability, Journal of Environmental Chemical Engineering, 10 (2022), pp. 108477.

[70] S. Barison, S. Fasolin, S. Boldrini, A. Ferrario, M. Romano, F. Montagner, S.M. Deambrosis, M. Fabrizio, L. Armelao, PdAg/alumina membranes prepared by high

power impulse magnetron sputtering for hydrogen separation, International Journal of Hydrogen Energy, 43 (2018), pp. 7982–7989.

[71] G. Zeng, A. Goldbach, L. Shi, H. Xu, Compensation effect in H2 permeation kinetics of PdAg membranes, Journal of Physical Chemistry C, 116 (2012), pp. 18101–18107.

[72] M.L. Bosko, E.A. Lombardo, L.M. Cornaglia, The effect of electroless plating time on the morphology, alloy formation and H2 transport properties of Pd-Ag composite membranes, International Journal of Hydrogen Energy, 36 (2011), pp. 4068–4078.

[73] A. Caravella, F. Scura, G. Barbieri, E. Drioli, Sieverts law empirical exponent for Pd-based membranes: Critical analysis in pure H2 permeation, Journal of Physical Chemistry B, 114 (2010), pp. 6033–6047.

[74] R.A. Oriani, The Physical and Metallurgical Aspects of Hydrogen in Metals, in: In ICCF4, Fourth International Conference on Cold Fusion; Electric Power Research Institute, Lahaina, Maui, 1993: pp. 1–42.

[75] F. Gallucci, F. Chiaravalloti, S. Tosti, E. Drioli, A. Basile, The effect of mixture gas on hydrogen permeation through a palladium membrane: Experimental study and theoretical approach, International Journal of Hydrogen Energy, 32 (2007), pp. 1837–1845.

[76] S. Liguori, P. Pinacci, P.K. Seelam, R. Keiski, F. Drago, V. Calabrò, A. Basile, A. Iulianelli, Performance of a Pd/PSS membrane reactor to produce high purity hydrogen via WGS reaction, Catalysis Today, 193 (2012), pp. 87–94.

[77] J. Zhang, D. Liu, M. He, H. Xu, W. Li, Experimental and simulation studies on concentration polarization in H 2 enrichment by highly permeable and selective Pd membranes, Journal of Membrane Science, 274 (2006), pp. 83–91.

[78] W.H. Chen, C.N. Lin, Y.H. Chi, Y.L. Lin, Permeation characteristics of hydrogen through palladium membranes in binary and ternary gas mixtures, International Journal of Energy Research, 41 (2017), pp. 1579–1595.

[79] W. Wang, X. Pan, X. Zhang, W. Yang, G. Xiong, The effect of co-existing nitrogen on hydrogen permeation through thin Pd composite membranes, Separation and Purification Technology, 54 (2007), pp. 262–271.

[80] J. Catalano, M. Giacinti Baschetti, G.C. Sarti, Influence of the gas phase resistance on hydrogen flux through thin palladium-silver membranes, Journal of Membrane Science,

339 (2009), pp. 57–67.

[81] D. Pizzi, R. Worth, M. Giacinti Baschetti, G.C. Sarti, K. ichi Noda, Hydrogen permeability of 2.5 μm palladium–silver membranes deposited on ceramic supports, Journal of Membrane Science, 325 (2008), pp. 446–453.

[82] J.A. Calles, R. Sanz, D. Alique, L. Furones, Thermal stability and effect of typical water gas shift reactant composition on H2 permeability through a Pd-YSZ-PSS composite membrane, International Journal of Hydrogen Energy, 39 (2014), pp. 1398–1409.

[83] Y. Yang, X. Li, X. Liang, R. Chen, J. Guo, H. Fu, D. Liu, Preparation of thin (~2 μm) Pd membranes on ceramic supports with excellent selectivity and attrition resistance, International Journal of Hydrogen Energy, 48 (2023), pp. 662–675.

[84] H. Li, A. Goldbach, W. Li, H. Xu, CO2 decomposition over Pd membrane surfaces, Journal of Physical Chemistry B, 112 (2008), pp. 12182–12184.

[85] H. Kurokawa, H. Yakabe, I. Yasuda, T. Peters, R. Bredesen, Inhibition effect of CO on hydrogen permeability of Pd-Ag membrane applied in a microchannel module configuration, International Journal of Hydrogen Energy, 39 (2014), pp. 17201–17209.

[86] M. Eriksson, L.G. Ekedahl, Real time measurements of hydrogen desorption and absorption during CO exposures of Pd: Hydrogen sticking and dissolution, Applied Surface Science, 133 (1998), pp. 89–97.

[87] A.L. Mejdell, D. Chen, T.A. Peters, R. Bredesen, H.J. Venvik, The effect of heat treatment in air on CO inhibition of a ~3 μm Pd-Ag (23 wt.%) membrane, Journal of Membrane Science, 350 (2010), pp. 371–377.

[88] K. Hou, R. Hughes, The effect of external mass transfer, competitive adsorption and coking on hydrogen permeation through thin Pd/Ag membranes, Journal of Membrane Science, 206 (2002), pp. 119–130.

[89] L. Yue, C. Chen, J. Li, C. Xiao, X. Xia, G. Ran, X. Fu, J. Hou, Y. Gong, H. Wang, Inhibition Effect of CO on Hydrogen Permeation Through a Pd/Al2O3 Composite Membrane: A Comprehensive Study on Concentration Polarization and Competitive Adsorption Effect, Fusion Science and Technology, 00 (2020), pp. 1–10.

[90] A. Caravella, F. Scura, G. Barbieri, E. Drioli, Inhibition by CO and polarization in pd-based membranes: A novel permeation reduction coefficient, Journal of Physical Chemistry B, 114 (2010), pp. 12264–12276.

[91] N.H. Chen, D.F. Othmer, New Generalized Equation for Gas Diffusion Coefficient, Journal of Chemical and Engineering Data, 7 (1962), pp. 37–41.

[92] H. Takaba, S.I. Nakao, Computational fluid dynamics study on concentration polarization in H 2/CO separation membranes, Journal of Membrane Science, 249 (2005), pp. 83–88.

[93] M.M. Barreiro, M. Maroño, J.M. Sánchez, Hydrogen separation studies in a membrane reactor system: Influence of feed gas flow rate, temperature and concentration of the feed gases on hydrogen permeation, Applied Thermal Engineering, 74 (2015), pp. 186–193.

[94] H. Li, J.W. Dijkstra, J.A.Z. Pieterse, J. Boon, R.W. van den Brink, D. Jansen, Towards full-scale demonstration of hydrogen-selective membranes for CO2 capture: Inhibition effect of WGS-components on the H2 permeation through three Pd membranes of 44cm long, Journal of Membrane Science, 363 (2010), pp. 204–211.

[95] T.A. Peters, W.M. Tucho, A. Ramachandran, M. Stange, J.C. Walmsley, R. Holmestad, A. Borg, R. Bredesen, Thin Pd-23%Ag/stainless steel composite membranes: Long-term stability, life-time estimation and post-process characterisation, Journal of Membrane Science, 326 (2009), pp. 572–581.

[96] T. Maneerung, K. Hidajat, S. Kawi, Ultra-thin (<1μm) internally-coated Pd-Ag alloy hollow fiber membrane with superior thermal stability and durability for high temperature H2 separation, Journal of Membrane Science, 452 (2014), pp. 127–142.

[97] F. Guazzone, Y.H. Ma, Leak growth mechanism in composite Pd membranes prepared by the electroless deposition method, AIChE Journal, 54 (2008), pp. 487–494.

[98] T.A. Peters, P.A. Carvalho, J.F. van Wees, J.P. Overbeek, E. Sagvolden, F.P.F. van Berkel, O.M. Løvvik, R. Bredesen, Leakage evolution and atomic-scale changes in Pd-based membranes induced by long-term hydrogen permeation, Journal of Membrane Science, 563 (2018), pp. 398–404.

CHAPTER 4: Multi-Pass Membrane Separator: Design, Testing, Optimization, and Scale-up

Abstract

This chapter discusses the design, testing, and optimization of the multi-pass membrane separator (MPMS) to enhance hydrogen recovery from mixture gas. Hydrogen separation through the palladium-based membrane is evident due to its unique features of high hydrogen permeability and ideally infinite hydrogen perm-selectivity. However, the continuous permeation of hydrogen leads to the development of a mass transfer boundary layer. This layer consists of non-permeable gases that accumulate at the surface of the membrane, a phenomenon known as concentration polarization. To mitigate concentration polarization, the membrane separator incorporates three longitudinal baffles, resulting in the formation of four distinct passages (multi-pass). This configuration not only improved the regulation of the H_2 partial pressure across the separator but also optimized the interaction between the feed gas and the membrane. As a result, more time was available for hydrogen to move from the bulk of the retentate to the surface of the membrane, thereby improving the H_2 recovery. Starting with a single membrane, the multi-pass membrane separator performance is tuned for various locations inside the separator, baffle proximity, and feed load. Following the outcomes, a scale-up study with four and then ten membranes is performed. Finally, the effect of inlet feed distribution in each pass on separator performance is examined. The entire study is performed at 673 K temperature, 300 kPaG transmembrane pressure, 70% H_2 / 30% N_2 feed gas composition, and feed load of 320 L min^{-1} $m^{-2}_{membrane}$. Additionally, the feed load is increased from 194 to 1290 L min^{-1} $m^{-2}_{membrane}$ to examine the effect of convective feed flow as well. The study demonstrated that multi-pass membrane separators minimize concentration polarization. The effect of baffles is more pronounced for low feed loads and multiple membranes. Additionally, multiple membranes with baffles improved the separator performance to a higher degree compared to the same case without baffles. This study offers an in-depth investigation of the multi-pass membrane separator and approaches for scaling up using multiple membranes.

4.1. Introduction

Hydrogen is regarded as a promising energy carrier for the future due to its exceptional energy-to-weight ratio (141.9 kJ g^{-1}), which surpasses that of other comparable competitors such as petrol (47.5 kJ g^{-1}) and diesel (44.5 kJ g^{-1}). Traditionally, the predominant methods for producing hydrogen (H_2) have been steam reforming of natural gas, coal gasification, and oil and naphtha reforming, accounting for over 95% of the total production [1,2]. Nevertheless, these thermochemical processes result in the production of a mixture of gases that is rich in hydrogen yet additionally contains N_2, CO_2, CO, CH_4, and other gases with low concentrations. However, the majority of industrial applications and proton exchange membrane fuel cells (PEMFCs) require high-purity H_2 (>99.99%), which further necessitates downstream H_2 purification. Moreover, PEMFCs require ultra-pure hydrogen with a CO concentration of less than 10 ppm, as CO poisons the Pt-catalyst at the anode and subsequently degrades the performance over time [3]. Palladium membrane technology in hydrogen purification has demonstrated immense potential in achieving ultra-pure hydrogen. This is primarily attributed to its exceptional characteristics properties including high hydrogen permeability and ideally infinite hydrogen perm-selectivity [4–6]. In addition, the Pd membrane can be integrated with the reforming reaction and water gas shift (WGS) reaction in a single compact reactor unit for simultaneous H_2 production and separation called the membrane reactor (MR) for on-site or onboard applications. Moreover, these reactions are regulated by Le Chatelier's principle, which states that the constant removal of H_2 encourages the reaction to proceed in the forward direction, exceeding the constraints posed by thermodynamic equilibrium limitations. This phenomenon results in improved conversion of reactants and overall efficiency of the process. [7,8]. However, the performance of the MR is mostly determined by the process conditions, Pd membrane module, and reactor geometric configuration. In addition, the performance of the Pd membrane module is greatly influenced by two crucial parameters: the temperature gradient, and the H_2 partial pressure difference which can occur in either the axial as well as radial direction. The significance of these parameters becomes highly critical when addressing the scale-up of membrane separators, as multiple membranes restrict the heat and mass transfer throughout the separator. Moreover, the rapid permeation of H_2 through the membrane causes an H_2-depleted layer near the membrane surface on the retentate side called concentration polarization [9–11]. The presence of impermeable gases leads to the formation of a mass transfer boundary layer, which further restricts the movement of hydrogen from the bulk of the retentate to the surface of the membrane. Additionally, the extent of concentration polarization

becomes more prominent for (i) membrane with high permeability and selectivity [12,13], (ii) low feed flow rate [14–16], (iii) high operating temperature, and (iv) high H_2 partial pressure differences across the membrane [17–19]. Hence, it is imperative to mitigate the adverse effects of concentration polarization. The next part discusses the methods for mitigating the impact of concentration polarization as reported in the literature, as well as the challenges involved in scaling up for future commercial utilization.

4.1.1. Literature Review on Concentration Polarization

In order to minimize the effect of concentration polarization in the membrane separator module increasing the feed flow rate has been proposed. However, doing so significantly decreases the contact time between the feed gas and the membrane, leading to a substantial decrease in the H_2 recovery, which is defined as the ratio of the amount of hydrogen permeating through the membrane to the amount of H_2 supplied to the separator as shown in Equation 4.1 [18,20,21]. An alternative method for mitigating concentration polarisation involves the introduction of a sweep gas on the permeate side. This leads to an increase in the H_2 partial pressure across the membrane, hence enhancing the H_2 recovery. Nevertheless, Chen et al. [14] reported that the degree of recovery is very small, hence rendering this approach ineffective in enhancing H_2 separation. Furthermore, the utilization of sweep gas is not feasible when aiming to obtain hydrogen gas with high purity. In a separate investigation conducted by Chen et al. [22], it was observed that the application of a vacuum on the permeate side resulted in an increase in the H_2 permeation rate, which is found to be directly proportional to the degree of vacuum applied. Yet it is observed that the thickness of the boundary layer in close proximity to the membrane surface exhibited an increase. This suggests that the vacuum employed is inadequate in decreasing concentration polarisation in the retentate. Moreover, empirical evidence suggests that a high degree of vacuum is required to minimize the effects of concentration polarisation. However, a high degree of vacuum could result in a decline in the perm-selectivity and stability of the membrane due to heightened mechanical stress, thereby jeopardizing its structural integrity. Therefore, it is realized to devise a mechanism to reduce concentration polarization without compromising the H_2 recovery, perm-selectivity, and membrane stability. Recent studies have demonstrated that the incorporation of baffles on the retentate side has the potential to reduce concentration polarization. By doing so a more uniform distribution of H_2 partial pressure is achieved throughout the separator, both radially and axially, while maintaining a constant feed flow rate [14–16,23]. The presence of baffles induces a disturbance in the gas flow field and the boundary layer adjacent to the membrane, which causes extra

hydrogen to be forced toward the surface of the membrane [21,24–26]. In addition, baffles enhance the contact between the feed and the membrane by directing the flow pattern of the feed and promoting recirculation within the separator [27].

$$\text{Hydrogen recovery (\%)} = \frac{F_{H_2,permeate}}{F_{H_2,feed}} \times 100 \quad (4.1)$$

In which $F_{H_2,permeate}$ and $F_{H_2,feed}$ is the volumetric flow rate of H_2 in permeate and feed.

An interesting finding by Mori et al. [23] demonstrated the effect of horizontal and vertical baffles with a single membrane on the performance of the membrane reformer. They concluded that the utilization of baffles and a reduced inner diameter of the reactor is an effective strategy for enhancing the linear velocity of the gases involved in the reaction. As a result, a notable decrease in concentration polarisation is observed, leading to an improved H_2 recovery. Coroneo et al. [28] conducted a pilot-scale Computational fluid dynamics (CFD) investigation of the H_2, CH_4, CO_2, and H_2O mixture gas using three Pd-Ag membrane modules with the baffle. It's interesting to note that the compartmentalized baffled shape pushed gases toward the membrane module, eliminating the polarization effect. Additionally, they suggested that the next baffle should be placed adjacent to the region where the impact of the first baffle is minimal. In another study, Ma et al. [21] designed a seven-tube membrane module to model the effect of two semi-circular baffles placed for gas recirculation. Here, they contrasted the increase in feed flow rate with the inclusion of the baffle and found that using baffles significantly reduced the effect of concentration polarization. By increasing the number of tubes from seven to nineteen the concentration polarization effect is more severe and tube-to-tube performance variation is more unbalanced. Hence, it is absolutely essential to optimize the membrane number for a given feed load to minimize the adverse effects of concentration polarization. Choi et al. [29] computationally compared the catalytic MR and the baffled MR. For scale-up, the number of membrane tubes is increased from 4-tube to 7, 19, and 37 tubes with fourteen baffles (baffle cut = 25%) vertically arranged along the length of the reactor. Baffles produced complex flow patterns and reduced concentration polarization and temperature drop. The performance of baffled MR is observed to be higher than catalytic MR in terms of conversion and H_2 recovery. However, during the scale-up from 19-tube to 37-tube the extent of concentration polarization of baffled MR becomes larger than the catalytic MR. This is mainly due to the obstruction of feed flow in the radial direction which resulted in an increased local concentration gradient. Moreover, according to Chen et al. [14,16,24] adding more baffles should increase hydrogen recovery, but the increase is only slightly noted as more

baffles are introduced. Hence, it is critically important to optimally configure both the number and position of baffles relative to the location of the membrane to successfully minimize the boundary layer thickness as well as the overall cost. Recently Sharma et al. [25,26] designed a multi-pass membrane separator using longitudinal baffles. The use of an optimal number of membranes and strategic placement thereof resulted in a notable enhancement of 33% in the H_2 recovery while maintaining a consistent feed flow rate. The channelization of the feed gas down the length of the separator improved H_2 recovery. This arrangement provided better control over the H_2 partial pressure across the separator. The entire separator is optimized using only four membranes with a feed flow rate of 0.3 litres per minute (LPM) and a membrane-to-pass ratio of one which is the ratio of the number of membranes to the number of passes. The effect of increasing the feed flow rate and the number of membranes has not been investigated at high feed loads. The availability of H_2 for the membranes in the subsequent pass downstream is low which restricts the utilization of these membranes to its full capacity.

However, to obtain a high throughput multi-pass membrane separator that is at the forefront of technology, it is desirable to optimize the membrane-to-pass ratio, membrane area, and feed flow rate. Moreover, the proper distribution of feed in various passes of the membrane separator modules is of utmost importance to effectively maintain the H_2 partial pressure throughout the membrane separator. Furthermore, prior research on scale-up with baffle configurations revealed variations in hydrogen flux between individual tubes. The addition of several membrane tubes and baffles yielded favorable outcomes to a certain extent. However, beyond this point, a significant issue regarding the limits of radial heat and mass transport has been reported [21,29]. An additional experimental investigation is required to develop a more resilient membrane separator module that incorporates multiple membranes and baffles for the purpose of mitigating concentration polarization. Ensuring the optimal feed flow rate per unit membrane area is crucial for both scaling up and maximizing the separator performance.

This study presents the design of a compact membrane separator module consisting of ten membranes and three interchangeable longitudinal baffles. The baffles are strategically positioned within the separator to facilitate four distinct flow passes. Following the initial assessment of membrane permeability, subsequent experiments are conducted to upscale the 1-membrane module to a 4-membrane module and ultimately to 10-membrane modules. Initially, the separator is optimized using a single membrane with an increasing number of passes and proximity to the baffles. Following that, an investigation is conducted to evaluate the effect of membrane positioning and feed load without baffles and with baffles. To assess

the scalability, the separator is further optimized with four membrane modules. Thereafter, the membrane-to-pass ratio is increased from 0.25 to 2.5 to achieve maximum H_2 recovery at a constant feed load. In addition to this, multiple experiments are performed to evaluate the performance of each membrane tube at different locations. In the end, the optimization of separator performance is achieved by employing various combinations of feed inlets in each pass, with the aim of maintaining the H_2 partial pressure in each pass. The whole set of experiments is performed using ten $Pd_{85}Ag_{15}/Al_2O_3$ membranes prepared via the electroless plating (ELP) technique. The evaluation of the separator's performance is conducted by considering several key factors, including the H_2 recovery, membrane usage, enhancement factor, and the extent of concentration polarization. It is observed that the strategic location of the membrane and baffles significantly improved the H_2 recovery. The extent of the enhancement in the recovery of H_2 was amplified by the incorporation of multiple membranes and baffles. In addition to the baffles, feed load, and the number of membranes, the feed distribution is a crucial factor in regulating the H_2 partial pressure across the separator, hence improving the H_2 recovery. Depending on the specific application, the separator may involve tailoring the multi-pass membrane separator with longitudinal baffles to meet the unique requirements of a particular separation application. The design may incorporate features that make the multi-pass membrane separator scalable for different applications and production scales. This adaptability adds to the novelty, allowing the technology to be customized for various industrial settings.

4.2. Experimental Methodology

In order to effectively counter the occurrence of concentration polarization a compact membrane separator module consisting of ten membranes and three interchangeable longitudinal baffles. The baffles are strategically positioned within the separator to facilitate four distinct flow passes. Additionally, provisions have been made for feed distribution through multiple channels in different passes.

4.2.1. Membrane Separator Design: Silent Features and Benefits

Figure 4.1 (a) depicts the design and schematic of a multi-pass membrane separator with an inner diameter of 100 mm and a length of 300 mm. The membrane separator and baffles are made with Inconel-800 to permit operation at high temperatures. The separator is designed to accommodate two longitudinal baffles from the bottom flange and ten membrane tubes together with a central baffle from the top flange simultaneously creating four passes as shown in Figure 4.1 (b), (c), and (d). Figure 4.1 (e) shows the location and numbering of the membrane on the upper flange. To streamline the feed flow and prevent the formation of eddies within the separator, the baffles are designed with a vertical baffle cut of 31.5% which is the ratio of segment opened for the next pass to the separator length. The membranes are positioned such that the active membrane area does not lay in the feed flow path close to the baffle cut position to avoid a change in the permeation behavior due to sudden changes in the feed flow stream. The separator compartment is equipped with several feed inlet and outflow ports to ensure efficient distribution of the feed in a multi-pass configuration. These ports are versatile and can be used interchangeably as either an inlet or an outlet, depending on the requirements. The top section of the separator contains an outlet port that functions similarly to a conventional separator in the absence of baffles. The silent features and the benefits of the multi-pass arrangement are summarized in Table 4.1.

Table 4. 1. Salient features and benefits of the multi-pass membrane separator.

Salient Features	Benefits
Arrangements to accommodate 10 membranes	Baffles increase the residence time
Baffle locations are inter-changeable	Enhance hydrogen recovery
Interchangeable feed injection facility	Minimize concentration polarization
Arrangements for catalyst in each chamber	Control feed flow distribution pattern
Adjustable membrane and catalyst height	Better radial and axial gas mixing

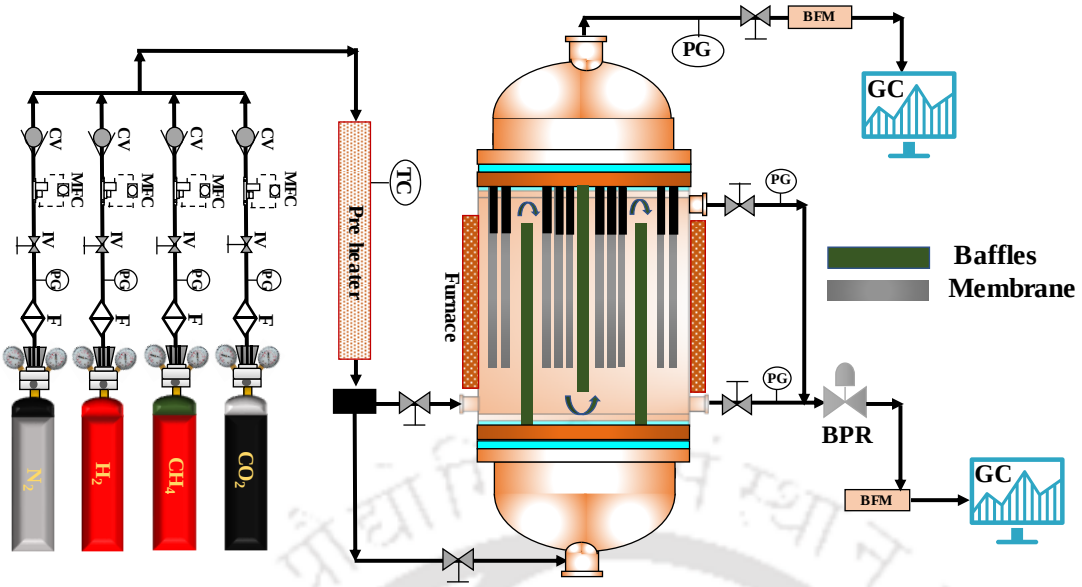

CV = Check Valve, **BFM** = Bubble Flow Meter, **BPR** = Back Pressure Regulator, **TC** = Thermocouple (K-type), **IV** = Isolation valve, **PG** = Pressure Gauge, **MFC** = Mass Flow Controller , **F** = Filter, **GC** = Gas Chromatography

a

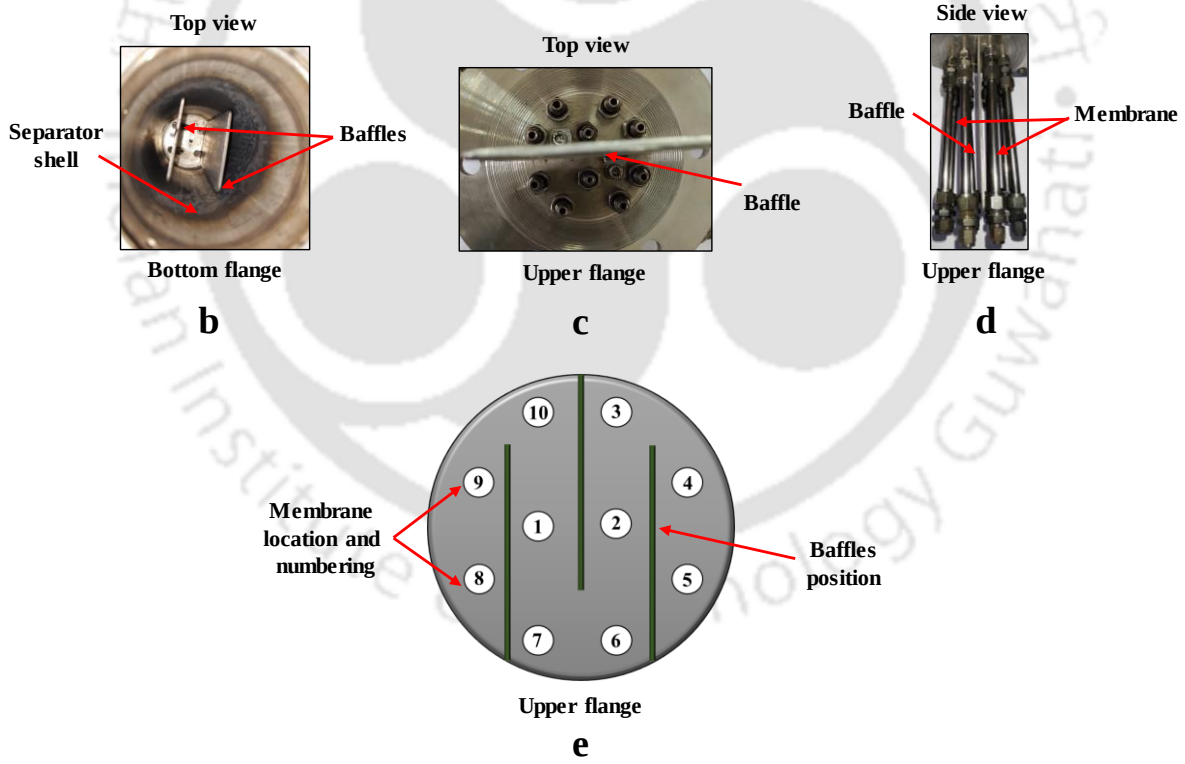

Figure 4. 1. (a) Multi-pass membrane separator design and schematic representation, (b) top view of bottom flange and baffles arrangements, (c) top view of the upper flange and membrane, and baffles arrangements, (d) side view of the upper flange with membrane integrated, (e) membrane location and numbering on the upper flange of the separator.

4.2.2. Methodology for Testing and Optimizing Process Conditions

The entire separator is optimized using a single membrane with and without baffles to examine the effect of baffles over the permeate H_2 flux and recovery. The effect of baffles and the separator geometry is studied for the shell side only where no sweep gas and/or vacuum is applied on the permeate side. Throughout the experiment, the permeate is maintained at atmospheric pressure. Permeate H_2 flux and recovery are evaluated at different temperatures (from 573 to 673 K) and pressures (from 50 to 100 kPaG) with varying (100-70 %) H_2 / (0-30 %) N_2 mixture gas while keeping the feed load per unit membrane area constant given in Equation 4.2. The study involving the single membrane is performed using the binary mixture of 70% H_2 / 30% N_2 at 673 K and 300 kPaG. The feed load per unit membrane area is kept constant at 320 L min^{-1} $m^{-2}_{membrane}$. In addition to this, to verify the homogeneous distribution of feed inside the pass the height of the membrane is adjusted at three different locations in one of the passes. The effect of baffles on the H_2 flux at various membrane locations is determined using different membranes prepared. To avoid variations in the H_2 permeate flux at various locations, the membrane corresponding to a specific location is utilized for subsequent studies involving multiple membranes. Thereafter the feed load is varied approximately from 200 to 1300 L min^{-1} $m^{-2}_{membrane}$ while maintaining the temperature and pressure constant at 673 K and 300 kPaG respectively, both with and without baffles. When the feed load is lower, the rate of hydrogen depletion inside the separator module is higher, which causes the membrane surface area along the axial direction to be wasted. At a high feed load, however, more H_2 is introduced into the separator module, thereby increasing membrane usage, which is the ratio of hydrogen permeated in reality to the maximum hydrogen permeation theoretically possible as given in Equation 4.3. The improvement in H_2 recovery with the inclusion of baffles is assessed in terms of the enhancement factor, which is the ratio of H_2 recovery with baffles to those without baffles as given in Equation 4.4. After optimizing the process conditions with a single membrane, the performance of the membrane separator is studied with multiple membranes for scale-up purposes. In the latter stage, the H_2 separation behavior at constant and variable feed flow rates for multiple membranes is investigated. For scale-up, the membrane-to-pass ratio defined as the ratio of the number of membranes to the number of passes as given in Equation 4.5 is increased from 0.25 to 2.5 by adding multiple membranes in different passes (up to 10 membranes are used). To further quantify the extent of concentration polarization Caravella et al. [30] introduced a more accurate expression to measure the overall permeation effectiveness in the entire separator module called effective average concentration

polarization coefficient (EACPC) as shown in Equation 4.6. EACPC becomes crucial during scale-up to optimize the design of membrane separators. If the value of EACPC is close to zero, the extent of polarization is negligible, whereas a value of one indicates that it is extremely severe. The overall H_2/N_2 ideal perm-selectivity is measured at more than 2500 before each set of experiments which implies that most of the hydrogen diffusion is through the bulk of the Pd-Ag metallic layer. The membrane corresponding to the particular position is used while investigating the separator performance with multiple membranes. The characteristics information of the membrane prepared for the optimization of the separator performance is given in Table 4.2.

$$F_{in}/A \text{ (L min}^{-1} \text{ m}^{-2}_{membrane}) = \frac{\text{Volumetric feed flow rate}}{\text{Active membrane area}} \quad (4.2)$$

$$\text{Membrane usage (\%)} = \frac{H_2 \text{ permeated in reality}}{\text{Maximum } H_2 \text{ permeation theoretically}} \times 100 \quad (4.3)$$

$$\text{Enhancement factor} = \frac{H_2 \text{ recovery with baffles}}{H_2 \text{ recovery without baffles}} \quad (4.4)$$

$$\text{Membrane-to-pass ratio (MPR)} = \frac{\text{Number of membranes inside the separator}}{\text{Total number of pass}} \quad (4.5)$$

$$\text{EACPC} = 1 - \frac{H_2 \text{ permeation rate with polarization}}{H_2 \text{ Permeation rate without polarization}} \quad (4.6)$$

Table 4. 2. Characteristics information of the membranes prepared for testing.

Name of membrane /Position inside the separator	Membrane layer	2B-graphite loading (mg cm^{-2})	Gravimetric membrane thickness (µm)	Permeate H_2 flux (mol m^{-2} s^{-1}) at 673 K, and 300 kPaG
M1/P1	Pd-Ag/2B graphite	1.064	10.08	0.2026
M2/P2	Pd-Ag/2B graphite	1.068	9.95	0.2031
M3/P3	Pd-Ag/2B graphite	1.140	9.38	0.2400
M4/P4	Pd-Ag/2B graphite	1.095	10.11	0.2020
M5/P5	Pd-Ag/2B graphite	1.142	9.52	0.2381
M6/P6	Pd-Ag/2B graphite	1.197	9.23	0.2785
M7/P7	Pd-Ag/2B graphite	1.114	9.55	0.2641
M8/P8	Pd-Ag/2B graphite	1.272	10.25	0.1948
M9/P9	Pd-Ag/2B graphite	1.005	9.39	0.2455
M10/P10	Pd-Ag/2B graphite	1.056	9.84	0.2286

4.3. Results and Discussion

The performance of the separator is optimized in three different stages including single membrane, multiple membrane, and scale-up study. The separator performance is investigated using ten membranes prepared earlier.

4.3.1. Effect of Passes on the Separator Performance: Single Membrane

This section investigates the effect of separator module geometry, membrane position, and baffles on the optimization of the multi-pass membrane separator. The separator is optimized with a single membrane at a particular condition of T = 673 K, ΔP = 300 kPa, F_{in}/A ~ 320 L min^{-1} $m^{-2}_{membrane}$, and 70% H_2 / 30% N_2 feed mixture composition. The study has investigated four different designs of separator modules based on the number of baffles. These designs include no passes, two passes, three passes, and four passes (also termed multi-pass), as shown in Figure 4.2 (a). Figure 4.2 (b) illustrates that incorporating baffles led to enhanced H_2 recovery and permeate H_2 flux by reducing the occurrence of concentration polarization, thereby increasing the membrane usage. A notable change in the H_2 recovery of 9% is found while transitioning from zero pass to four pass configurations. Additionally, there is a corresponding rise in effective membrane use by 7%. The addition of one baffle causes a 5% change in H_2 recovery, which is reduced to 3% with the addition of two baffles and to approximately 1% with the addition of a third baffle. The same trend holds for both membrane utilization and permeate H_2 flux. To further validate this observation, the EACPC is plotted against the number of passages, as illustrated in Figure 4.2 (c). The graph shows a significant reduction in EACPC from 0.55 to 0.48 with the introduction of two baffles. However, the inclusion of a third baffle resulted in a marginal decrease to 0.47. Meanwhile, Figure 4.2 (d) presents the enhancement in H_2 recovery achieved with the incorporation of baffles. The data demonstrates that the H_2 recovery is significantly improved in the two-pass, three-pass, and four-pass conditions compared to the zero-pass condition, with enhancements of 1.08, 1.14, and 1.16, respectively. The majority of improvement, with a notable degree of increment, is found when the first and second baffles are added. Conversely, a lesser degree of improvement is observed when a third baffle is added. Therefore, additional baffles result in a reduction in the degree of improvement, or the saturation of the effect becomes apparent. Similar behavior is also reported by Chen et al. [16] and Coroneo et al. [28] who numerically investigated the effect of baffles on the H_2 recovery. Once an appropriate number of baffles is introduced, the reduction in concentration polarization commences to approach a state of saturation. The use

of additional baffles resulted in a little enhancement of the H_2 recovery. Hence, it is essential to consider an optimal configuration of the separator incorporating baffles, mostly driven by economic considerations arising from the non-linear correlation between the H_2 recovery and the associated cost of adding baffles. The observed improvement in H_2 recovery can be attributed to a decrease in the thickness of the mass transfer boundary layer. This reduction has led to an increase in the effective driving force for H_2 permeation through the membrane. The addition of a longitudinal baffle resulted in the formation of a narrower channel for the feed flow. This modification led to an improvement in the intermixing of the feed and an increase in the linear flow velocity. Consequently, the presence of concentration polarization decreased to a certain extent. The elimination of impermeable gases in the vicinity of the membrane facilitates an increased induction of H_2 near the surface of the membrane. To put it simply, the implementation of a more defined feed flow pathway permitted the local H_2 mol fraction to increase radially along the length of the membrane [23,26].

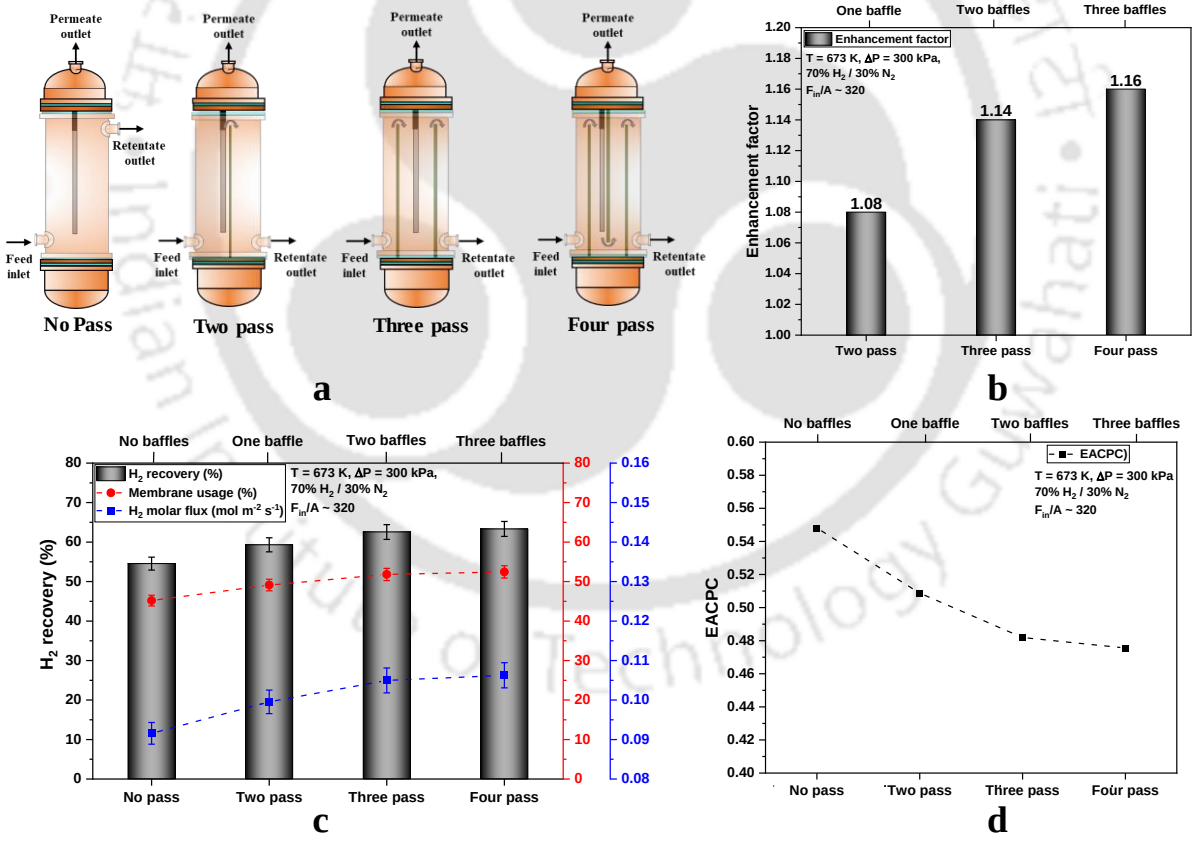

Figure 4. 2. (a) Membrane and baffles arrangements to create multi-pass inside the separator, (b) H_2 recovery, membrane usage, and permeate H_2 flux, (c) EACPC, and (d) enhancement factor as a function of the number of passes created by adding baffles.

4.3.2. Effect of Baffle Location Inside the Separator: Single Membrane

The effect of the baffle position relative to the membrane location as shown in Figure 4.3 (a) is further investigated to determine its sphere of influence of baffles to effectively counter the concentration polarization. Based on the results depicted in Figure 4.3 (b), it can be noticed that the inclusion of a baffle in proximity to the membrane from the upper flange (referred to as Case II) exhibits negligible impact on the recovery of H_2 in comparison to Case I, where no baffle is employed. This observation suggests that a significant portion of the H_2 present in the feed inlet does not come into contact with the membrane and instead passes the confined path present below the baffle. Despite the proximity of the baffle to the membrane, this configuration ultimately did not result in any substantial enhancement in the H_2 recovery. In contrast, when the baffle is suspended from the lower flange, as illustrated in Case V, a notable and sudden rise in H_2 recovery of 4% is noted in comparison to Case I, despite the rest of the parameters remaining the same. Hence, the sole probable explanation for the observed increase may be attributed to the improved feed gas contact pattern with the membrane, along with the enhanced linear gas velocity coming from the compartmentalization of the separator [29]. Nevertheless, experimental results indicate a slight 1.3% improvement in H_2 recovery when the baffle is positioned at a significant distance from the membrane, either on the left or right side, as seen in Case III and Case IV. This observation demonstrates that the extent of the baffle's influence is strongest when the membrane is positioned in close proximity, but diminishes as the distance between them increases. Furthermore, in the context of the identical feed load situation, the phenomenon of concentration polarization is further intensified when the membrane is situated within a bigger compartment as opposed to a smaller one [16]. This behavior becomes more clear in Figure 4.3 (c), where the extent of concentration polarization is virtually the same for Case I and Case II as well as for Case III and Case IV. However, a sharp decline in the EACPC of ~ 0.03 is noticed for Case V which is the result of the combined effect of feed gas contacting pattern and baffle proximity. Therefore, it is necessary to strategically position the baffles at regular intervals and utilize multiple membranes to ensure that the impact of the baffles is effectively sustained close to each membrane [28]. Based on the following discussion, it can be inferred that the implementation of a separator module equipped with longitudinal baffles effectively mitigated the occurrence of concentration polarization in proximity to the membrane surface. In our specific circumstance, the saturation of concentration polarization occurs with the incorporation of three baffles. Hence, our study

utilizes an ideal separator design that has three longitudinal baffles, resulting in the creation of four passes. This design is subsequently employed for further optimization in the course of our investigation.

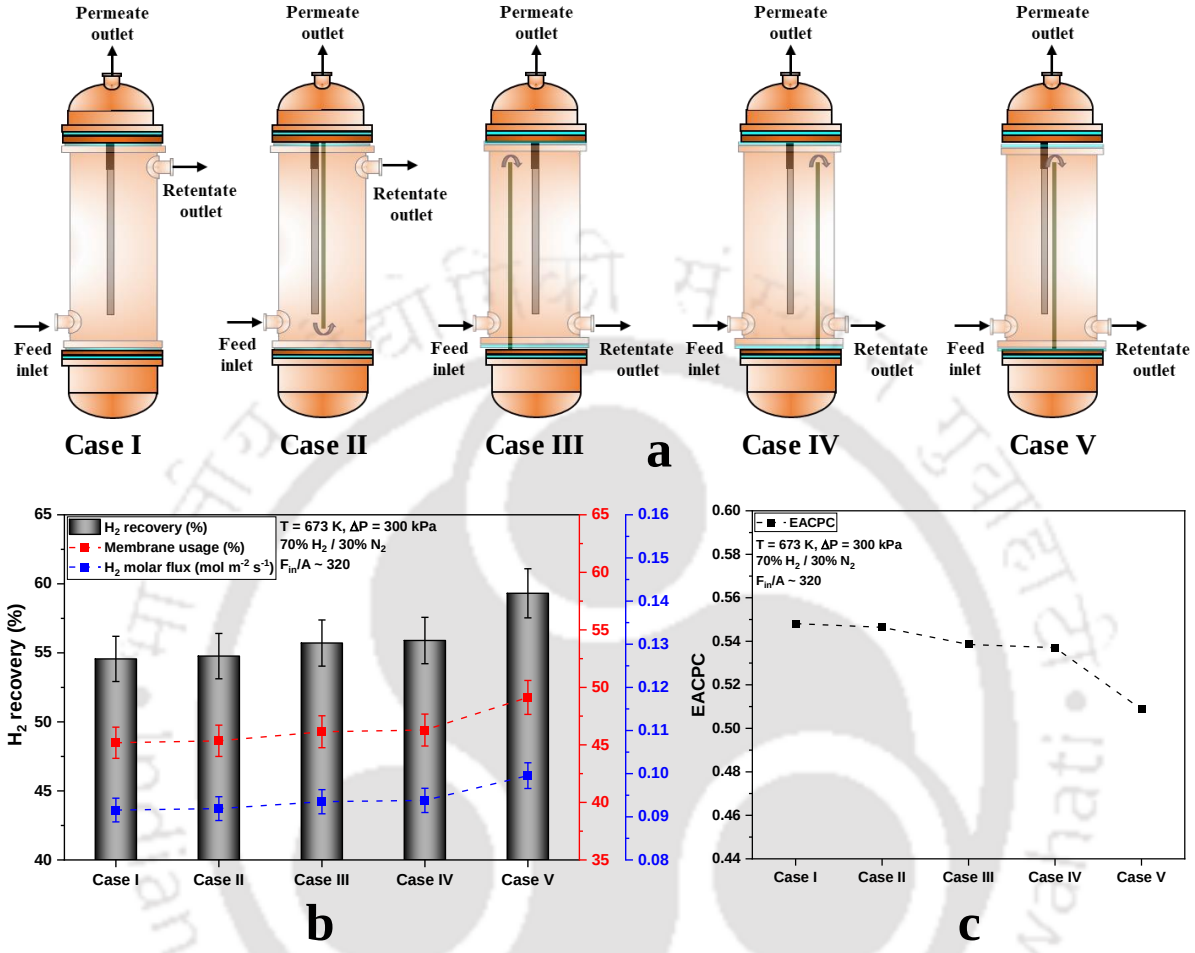

Figure 4. 3. (a) Membrane and baffles arrangements inside the separator, (b) H_2 recovery, membrane usage, and permeate H_2 flux, and (c) EACPC as a function of the baffle position relative to membrane location.

4.3.3. Effect of Membrane Height Inside the Pass: Single Membrane

A separate series of experiments is conducted to assess the variability in the performance of the separator by positioning the membrane at various locations. The examination of the heterogeneity in hydrogen recovery across different membrane locations is crucial to ascertain the equal contribution of each position. For this particular study, the entire separator is optimized at T = 673 K, ΔP = 300 kPa, $F_{in}/A \sim 320$ L min^{-1} $m^{-2}_{membrane}$, and 70% H_2 / 30% N_2 feed mixture composition. The membrane is positioned at three different elevations within the passage, as depicted in Figure 4.4 (a): the upper, the middle, and the bottom. The purpose of

this study is to examine the variation in H_2 recovery across various elevations within the pass. Figure 4.4 (b) illustrates that there are no discernible fluctuations in the H_2 recovery when the height of the membrane is varied from the upper to the bottom portion of the separator throughout a single pass. This observation demonstrates that the gas flow exhibits better symmetry, characterized by a homogeneous distribution of H_2 along the whole extent of the baffle.

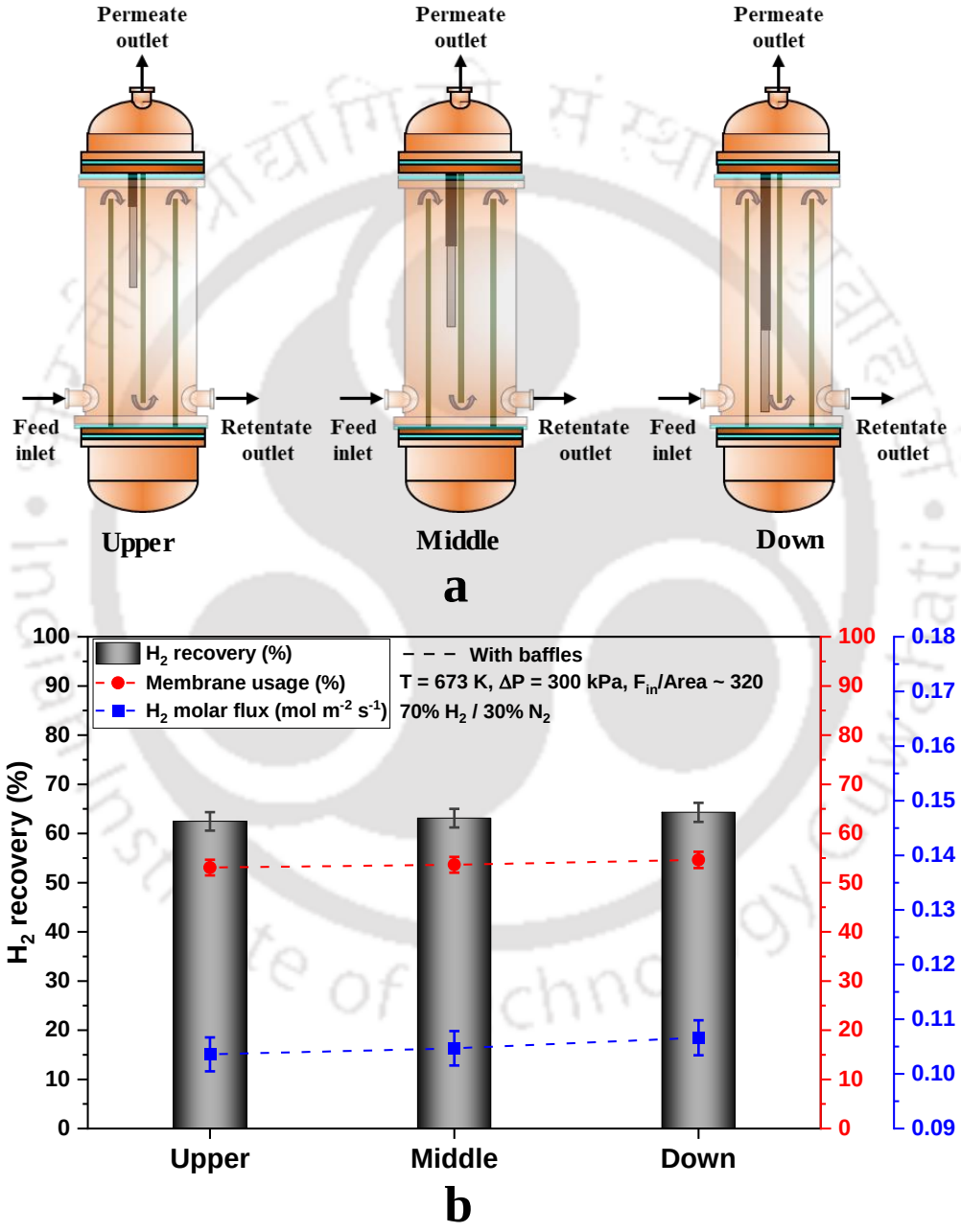

Figure 4. 4. (a) Membrane and baffles arrangements inside the separator and (b) H_2 recovery, membrane usage, and permeate H_2 flux as a function of the membrane height inside the separator.

4.3.4. Effect of Membrane Location Inside the Separator: Single Membrane

Other than the height, the performance of the membrane inside the separator is examined at three different locations as well: the inlet, the center, and the outlet, as illustrated in Figure 4.5 (a). H_2 recovery at each location with and without baffles is experimentally measured to quantify the effect of location and baffles inside the separator. As shown in Figure 4.5 (b), the H_2 recovery is observed to be maximum at the center while it decreases both at the inlet as well as the outlet of the separator. Without baffles, a marginal decrease of 3% in H_2 recovery is seen from the center to the inlet whereas it is 7% from the center to the outlet. The same trend is also observed with baffles, where the corresponding decrease is 7% and 12%. The H_2 recovery increases at each location with baffles compared to without baffles. Figure 4.5 (c) shows the enhancement in the H_2 recovery at each location with the addition of the baffles. An improvement of 9%, 16%, and 8% are seen respectively at the inlet, center, and outlet position of the separator with the baffles compared to without baffles. Moreover, the EACPC of the center position is calculated to be 0.54 and 0.47 without and with the baffle respectively, indicating that the feed distribution is more symmetrical with the baffle as shown in Figure 4.5 (d). The smaller EACPC also implies that the degree of concentration polarization is minimized at the central region when baffles are present [21,29]. The reduction in the EACPC is more pronounced in the central location when baffles are present, as opposed to the inlet and outlet positions. The impact of this phenomenon is reduced to a lesser extent in the absence of baffles. Earlier Richa et al. [26] also reported a similar behavior that arises due to the high feed gas velocity and inadequate contacting pattern with the membrane at the inlet and the outlet of the separator. The feed gas velocity is found to be higher at both the inlet and outlet of the separator, resulting from a higher pressure gradient. This discrepancy in velocity significantly decreases the residence time in comparison to the center of the separator. However, in our particular situation, the level of improvement in H_2 recovery is higher, possibly due to the elevated feed flow rate and the narrower path for the feed gas. Moreover, the feed mixture gas exhibited a substantial concentration of H_2, resulting in a significant proportion of H_2 within the separator. Consequently, the occurrence of concentration polarization was effectively minimized. Therefore, it is recommended to position the membrane in the center of the separator, incorporating baffles, to achieve optimal hydrogen recovery.

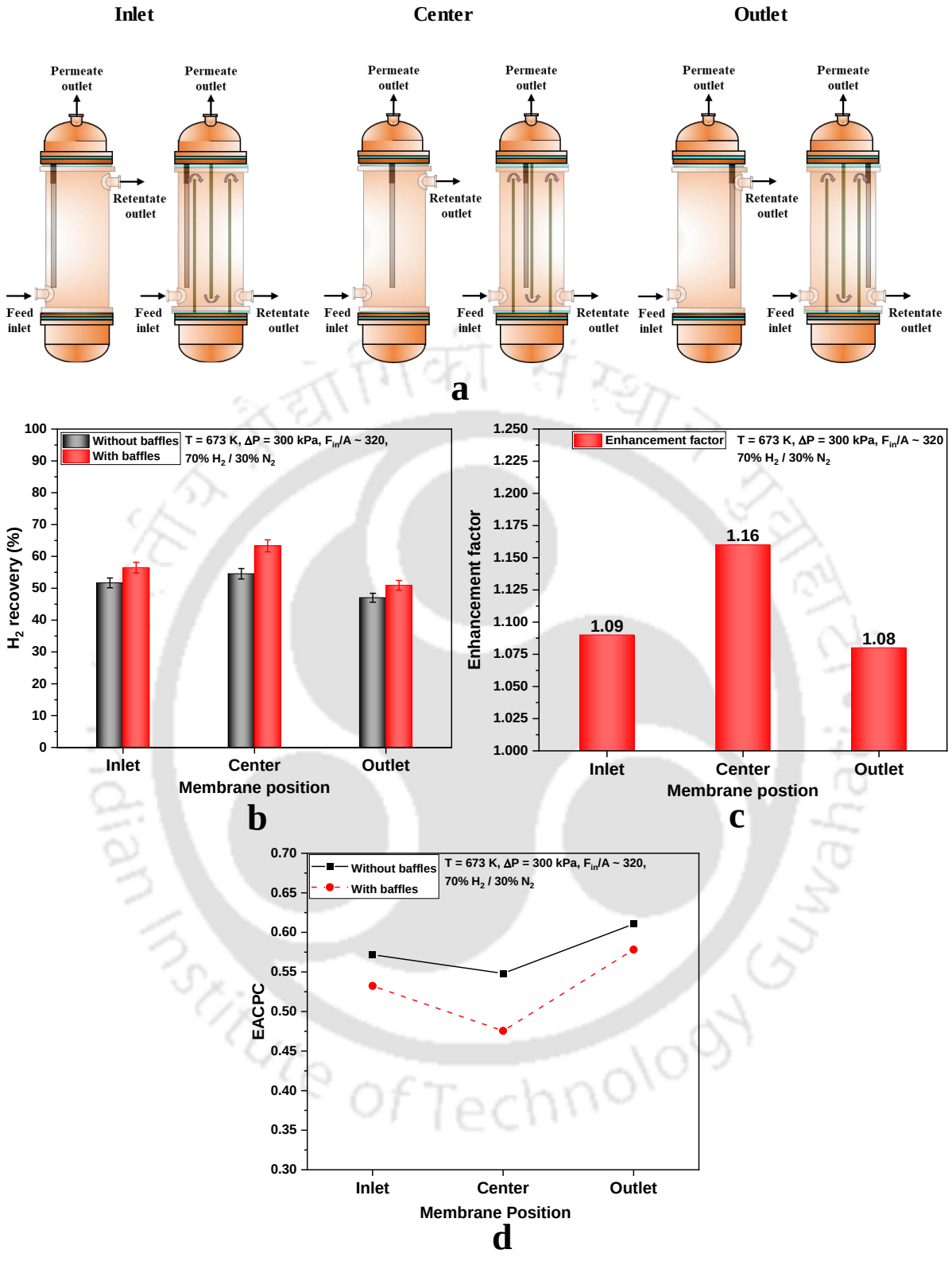

Figure 4. 5. (a) Membrane and baffles arrangements inside the separator at inlet, center, and outlet with and without baffles, (b) H_2 recovery, (c) enhancement factor, and (d) EACPC as a function of the membrane position inside the separator at $F_{in}/A \sim 320$.

Nevertheless, it is probable that the H_2 recovery will be limited by the feed load. This phenomenon can be explained by the inverse relationship between feed load and concentration polarization, wherein an increase in feed load leads to a decrease in concentration polarization. However, it is important to note that this decrease in concentration polarization is accompanied by a substantial reduction in H_2 recovery as shown in Figure 4.6 (a). When the feed load is increased from 320 L min^{-1} $m^{-2}_{membrane}$ to 1290 L min^{-1} $m^{-2}_{membrane}$ the hydrogen recovery virtually remains the same at each location even with the baffles. Figure 4.6 (b) shows that the enhancement in the H_2 recovery is below 1.016. The same holds for EACPC which is nearly the same with and without baffles as shown in Figure 4.6 (c). Consequently, it may be inferred that when the feed load is extremely high, the presence of baffles has minimal impact, and the membrane's ability to separate is solely determined by the feed load. The concentration polarization boundary layer is already at its minimal thickness, therefore the installation of baffles does not have a substantial impact. Hence, the resulting change in the performance characteristics of the separator becomes vital as the feed load increases, both with and without baffles.

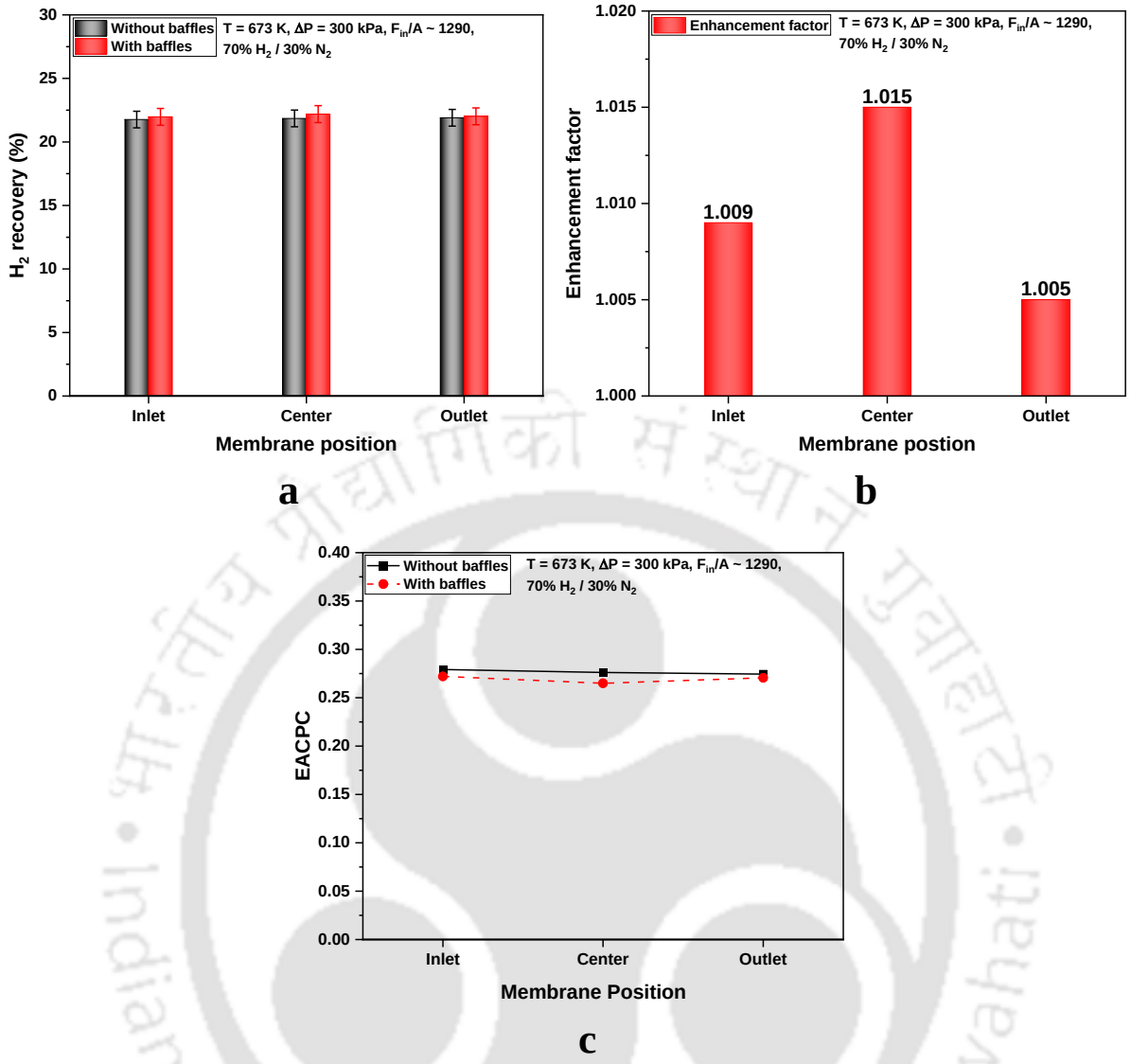

Figure 4. 6. (a) H_2 recovery, (b) enhancement factor, and (c) EACPC as a function of the membrane position inside the separator at $F_{in}/A \sim 1290$.

4.3.5. Effect of Feed Load with and without Baffles: Single Membrane

Rather than increasing the feed load, a more favorable approach would involve incorporating baffles into the separator module to minimize the effect of concentration polarization. However, despite the presence of baffles, the feed load remains a critical factor in determining the effective usage of the membrane and, consequently, the overall efficiency of the separator [18,20,21]. Therefore, H_2 recovery and membrane usage at the same operating condition of T = 673 K, ΔP = 300 kPa, and 70% H_2 / 30% N_2 feed mixture composition is investigated without and with baffles. A separate set of experiments is performed for two separator modules i.e. without and with baffles as shown in Figure 4.7 (a). The feed load is increased from 194 to

1290 L min^{-1} $m^{-2}_{membrane}$ to examine the effect of convective feed flow. H_2 recovery is plotted against the increasing feed load without and with baffles as shown in Figure 4.7 (b). At a lower feed load H_2 molecules have sufficient time to diffuse to the membrane surface, thereby increasing the H_2 recovery. At the same time, the rapid depletion of H_2 molecules in the separator thickness the mass transfer boundary layer down the length of the membrane as a result a significant part of the membrane area remains unutilized. Contrary to this, at a higher feed load, the effect of concentration polarization is less severe because the higher convective feed flow rate reduces the mass transfer boundary layer near the membrane surface. For instance, the change in H_2 recovery with the addition of baffles is 13% and 1% for the feed load of 194 L min^{-1} $m^{-2}_{membrane}$ and 1290 L min^{-1} $m^{-2}_{membrane}$ respectively. This is largely attributed to the covering of the membrane surface with a layer of dense non-permeable gases that further restricted the H_2 permeation through the membrane [18]. Meanwhile, an evident decrease in the H_2 recovery is observed when the feed load increases, mostly attributed to the limited residence time of H_2 molecules for diffusion and interaction with the membrane surface. Consequently, a significant portion of the hydrogen present in the feed stream is being dissipated in the retentate stream [21]. In our case, a reduction in the concentration polarization is observed in the case of baffles, and hence, an improvement in the H_2 recovery is noticed. Figure 4.7 (c) shows the enhancement in the H_2 recovery with baffles compared to the without baffles condition. At a lower feed load, the enhancement in the H_2 recovery is significantly high which started decreasing with increasing feed load. For instance, the enhancement is above 1.15 for the feed load below 500 L min^{-1} $m^{-2}_{membrane}$ which drastically reduced to 1.02-1.03 for the feed load above 800 L min^{-1} $m^{-2}_{membrane}$. In the case of higher feed loads, the presence of baffles leads to a little incremental improvement in H_2 recovery compared to the without baffles. Therefore, the influence of the baffle is more noticeable until the maximum attainable permeation capacity of the membrane. This observation has an obvious implication on the extent of concentration polarization, where a lower EACPC is observed at low feed load with baffles compared to without baffles as shown in Figure 4.7 (d). EACPC with baffles is noticeably low till the permeate saturation is achieved beyond which the value of EACPC gets almost constant at 0.28. This behavior holds for both without and with baffle conditions which indicate that the extent of concentration polarization has attenuated due to the covering of the membrane surface with a layer of dense non-permeable gases [20,21]. In other words, increasing the feed load after the attenuation of the EACPC does not have any meaningful influence on the degree of concentration polarization because the mass transfer boundary

thickness is already minimal. The significance of EACPC becomes more apparent as a result of the fact that the influence of radial diffusion is more pronounced at low feed loads. Therefore, a balanced trade-off between feed load and baffles is required to minimize concentration polarization for achieving maximum H_2 recovery. In addition, a multi-pass arrangement appears to have an advantage over a conventional separator at low feed loads, but the separation behavior is nearly identical at very high feed loads, where the influence of baffles is negligible.

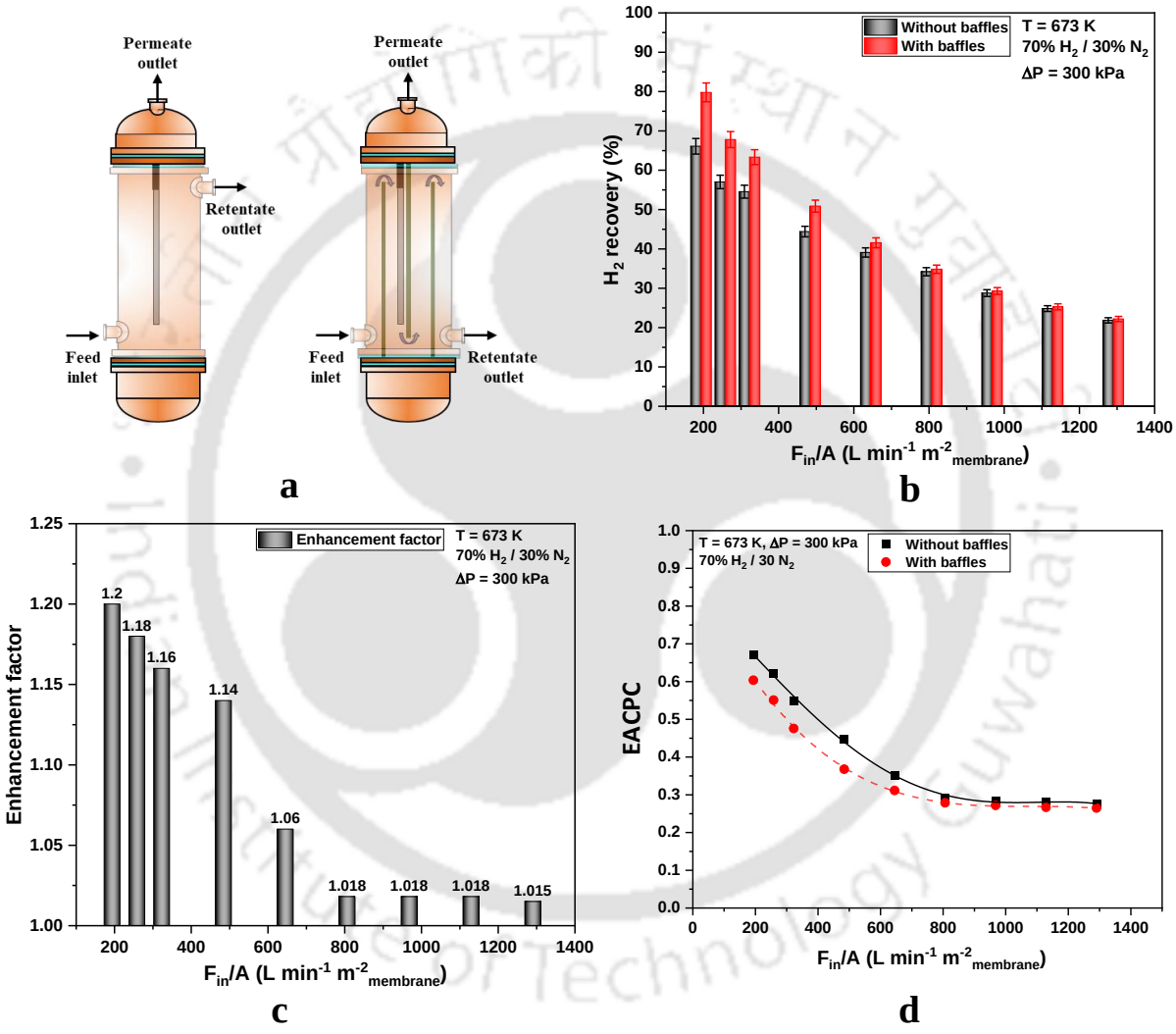

Figure 4. 7. (a) Membrane and baffles arrangements, (b) H_2 recovery with and without baffles, (c) enhancement factor, and (d) EACPC as a function of increasing the feed load.

4.3.6. Effect of Temperature, Pressure, and Concentration: Single Membrane

To examine the effect of baffles on flow dynamics taking into account variables such as temperature, pressure, and H_2 concentration. A separate study is performed employing a single membrane with and without baffles as shown in Figure 4.8 (a). A consistent feed load of 320 L min^{-1} $m^{-2}_{membrane}$ is maintained with the aim of understanding the intricate interplay between baffles and key parameters affecting the H_2 separation through the membrane. At lower levels of the driving force, such as temperature, pressure, and H_2 concentration as depicted in Figure 4.8 (b), Figure 4.8 (c), and Figure 4.8 (d) respectively, the impact of baffles in mitigating concentration polarization is less significant. However, at higher pressures, the advantages of enhanced flow dynamics become more evident, resulting in an increase in hydrogen permeation. The intensity of the increase is further amplified at a higher driving force while the rest of the parameters are kept constant. For instance, the enhancement in the H_2 recovery with the inclusion of the baffles is 1.06, 1.09, and 1.16 at 573 K, 623 K, and 673 K respectively. A similar trend is observed in the case of increasing pressure, and H_2 concentration. A significant increase of 1.24 in hydrogen recovery is observed when all parameters are set to their maximum values, including a temperature of 673 K, a pressure of 300 kPaG, and an H_2 concentration of 90%, as shown in Figure 4.8 (d).

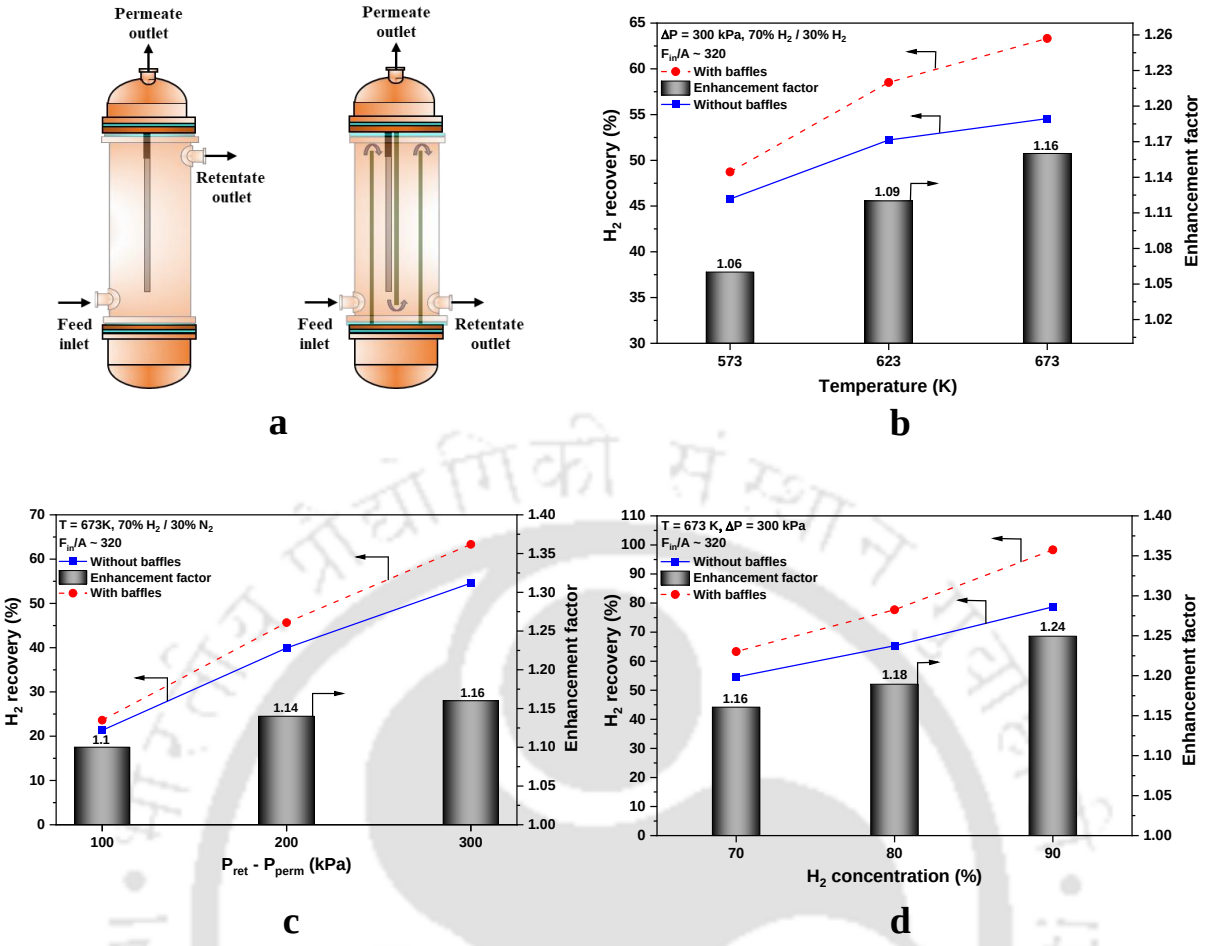

Figure 4. 8. (a) Membrane and baffles arrangements, H_2 recovery and enhancement factor with and without baffles as a function of (b) temperature, (c) pressure, and (c) H_2 concentration.

4.3.7. Effect of Membrane Length: Multiple Membranes

The thickness of the mass transfer boundary layer increases axially along the length of the membrane due to the fast depletion of H_2 as soon as the feed comes in contact with the membrane module [22]. The effect is more pronounced for the upper section of the membrane since the H_2 partial pressure difference is highest. The radial diffusion of H_2 becomes challenging due to a buildup of impermeable gases down the length of the membrane surface [32]. In addition, the apparent partial pressure of H_2 is decreased, resulting in a decrease in H_2 permeation. Consequently, the concentration polarization increases steadily and hence a significant portion of the membrane remains underutilized axially [33]. As the retentate and permeate sides reach equilibrium, the apparent driving force for H_2 permeation approaches zero adjacent to the bottom of the membrane module [31]. When this scenario plays out, the mass transfer boundary layer ends up becoming more dominant than the membrane resistance.

Previously, the incorporation of baffles enhanced the radial mixing of the feed gases, thereby minimizing the negative effects of concentration polarization. However, it is unclear from the literature whether a longer membrane or two small membranes with the same surface area is more effective. In this situation, a multi-pass membrane separator provides the flexibility to accommodate multiple membranes in the same or subsequent passes. To further examine the effect of membrane length, multiple membranes each with an identical surface area are cut from the same membrane tube. Four different case studies are performed at the feed load of 320 L min^{-1} $m^{-2}_{membrane}$, T = 673 K, ΔP = 300 kPa, and 70% H_2 / 30% N_2 feed mixture composition as shown in Figure 4.9 (a). When two small membranes are fitted in the same pass at the same height, as illustrated in Figure 4.9 (b), the H_2 recovery is enhanced by 5% when compared to the recovery achieved by using a single long membrane. In addition, the H_2 recovery increased by 4% when four small membranes were utilized instead of two long membranes. Therefore, the overall extent of concentration polarization is greater for longer membranes compared to multiple small membranes at the same convective feed load as observed in Figure 4.9 (c). This observation is surprising because the membrane's active surface area and all other operating parameters are the same. The difference in behavior is probably attributed to the contacting pattern of the feed gases. The entire surface area of the multiple small membranes is directly exposed to the fresh feed i.e. the localized H_2 partial pressure between the retentate and permeate sides is uniformly high across smaller membranes. By virtue of this, the steady development of the boundary layer thickness along the membrane module is restricted, and a more homogeneous distribution of H_2 is achieved [15,25]. Therefore, the membrane is utilized efficiently, increasing H_2 recovery. This study reiterates the fact that other than feed load and baffles, the contacting pattern of the feed gases with the membrane also plays a critical role in determining the efficiency of the membrane separator. At a low feed flow rate, it is advantageous to place multiple small membranes with the same surface area adjacently in the same pass as opposed to a longer membrane. At a higher feed flow rate, however, the boundary layer becomes narrower along the axial length of the membrane module, so it is more advantageous to place a longer membrane when scaling up with multiple membranes. Otherwise, arrangements should be made to distribute the feed along the membrane length through multiple injection ports to maintain the H_2 concentration in the bottom section.

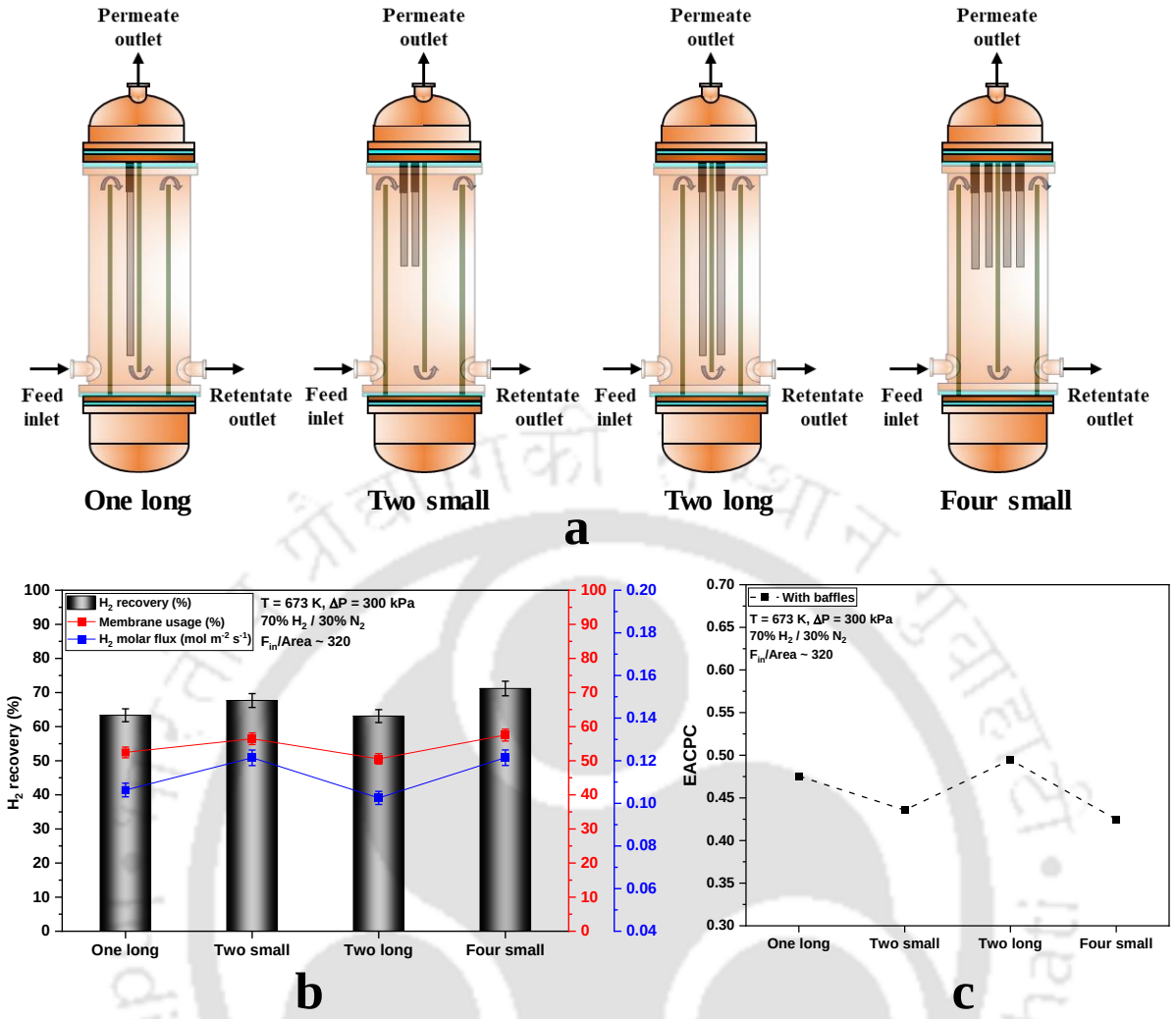

Figure 4. 9. (a) Membrane and baffles arrangements, (b) H_2 recovery, membrane usage, and permeate H_2 flux with baffles, and (c) EACPC as a function of membrane length at a constant feed load of 320 L min^{-1} $m^{-2}_{membrane}$.

4.3.8. Effect of Membrane Area and Feed Flow Rate: Multiple Membranes

The unique ability of the multi-pass membrane separator enhanced the contacting of feed gases with the membrane, thereby resulting in improved separator performance. Other than the prolonged residence time of feed gases, the multi-pass approach offers the versatility to arrange membranes in various passes according to specific needs. Previously Richa et al. [26] optimized the membrane arrangement to achieve maximum H_2 recovery using only four membranes. They achieved a maximum H_2 recovery of 79% with baffles, a 33% improvement over when all membranes were placed in the center of the separator without baffles. In contrast, a single membrane with baffles exhibits only a 2% enhancement in H_2 recovery compared to those without baffles. Further, they observed that the increase in H_2 recovery is not proportional

to the number of membranes. Although their study shows an analogy for scale-up, the effect of increasing the number of membranes on H_2 recovery and effective surface area utilization is not clear. The investigation of the feed flow rate is particularly lacking in their study, a significant aspect according to our findings. Furthermore, there is a need for an experimental study to determine the extent of concentration polarization in the scale-up separator module. During the course of our study, we conducted four distinct case studies, as seen in Figure 4.10 (a), to examine the effects of increasing membrane surface area with and without baffles. In order to examine the effect of increasing surface area or the number of membranes, a different set of experiments has been performed at F_{in} = 60 L h^{-1}, T = 673 K, ΔP = 300 kPa, and 70% H_2 / 30% N_2 feed mixture composition. The best possible arrangement for the membrane to enhance the H_2 recovery is to place it at the center of the separator with baffles. Therefore, the membranes are positioned in the center of the separator in this study as well. Figure 4.10 (b) illustrates the effect of increasing the number of membranes without and with baffles, respectively. Although the H_2 recovery showed improvement with an increase in the number of membranes, it is important to note that the increment seen is not directly equal to the corresponding increase in surface area. The incorporation of baffles successfully mitigated concentration polarization, while the enhancement in H_2 recovery does not exhibit a proportional relationship with the increase in surface area. As an example, the H_2 recovery showed an increase from 54% in the absence of baffles to 63% when baffles were introduced for a single membrane. In contrast, the H_2 recovery exhibited a notable increase from 77% in the absence of baffles to 95% with the incorporation of baffles across four membranes. The H_2 recovery showed a 9% improvement for a single membrane, whereas the improvement reached 18% when four membranes were utilized. This analogy illustrates that the reduction in hydrogen recovery when using baffles in a single membrane configuration is at least twice as significant compared to a configuration with four membranes. Thus, baffles are more effective with multiple membranes to enhance the overall H_2 recovery of the separator. To further substantiate this fact, hydrogen recovery is plotted against the number of membranes at different convective feed flow rates as shown in Figure 4.10 (c). At a reduced feed flow rate, however, the maximum individual performance of each membrane is not attained; consequently, a linear relationship is not observed. This implies, in turn, that the extent of concentration polarization is more severe when the membranes are added in the subsequent passes due to the fast depletion of hydrogen in the preceding pass. This profile begins to approach linearity as the convective feed flow rate increases. This is mostly owing to the availability of more H_2 in the next passes, which supports the separation of more H_2 while

approaching the maximum H_2 separation capacity. This observation indicates that baffles retain their significance even when subjected to a higher feed flow rate and the presence of multiple membranes. Hence, it can be inferred that by increasing the convective feed flow rate, the occurrence of concentration polarization can be minimized when employing baffles. A similar analogy is also concluded by Chen et al. [34] who reported that increasing the number of membranes at a higher feed flow rate is more economical to achieve high H_2 recovery. It is also observed that the enhancement in the H_2 recovery with baffles improved with the addition of multiple membranes to a larger extent compared to the corresponding configuration without baffles as shown in Figure 4.10 (d). While the enhancement factor for a single membrane is 1.16, it is 1.24 for four membranes. Therefore, it can be hypothesized that employing a membrane separator with multiple membranes at a higher feed flow rate is more suitable for commercialization and scaling up. To determine the viability of the multi-pass membrane separator, the next section investigates the effect of the membrane-to-pass ratio by adding more membranes in different passes.

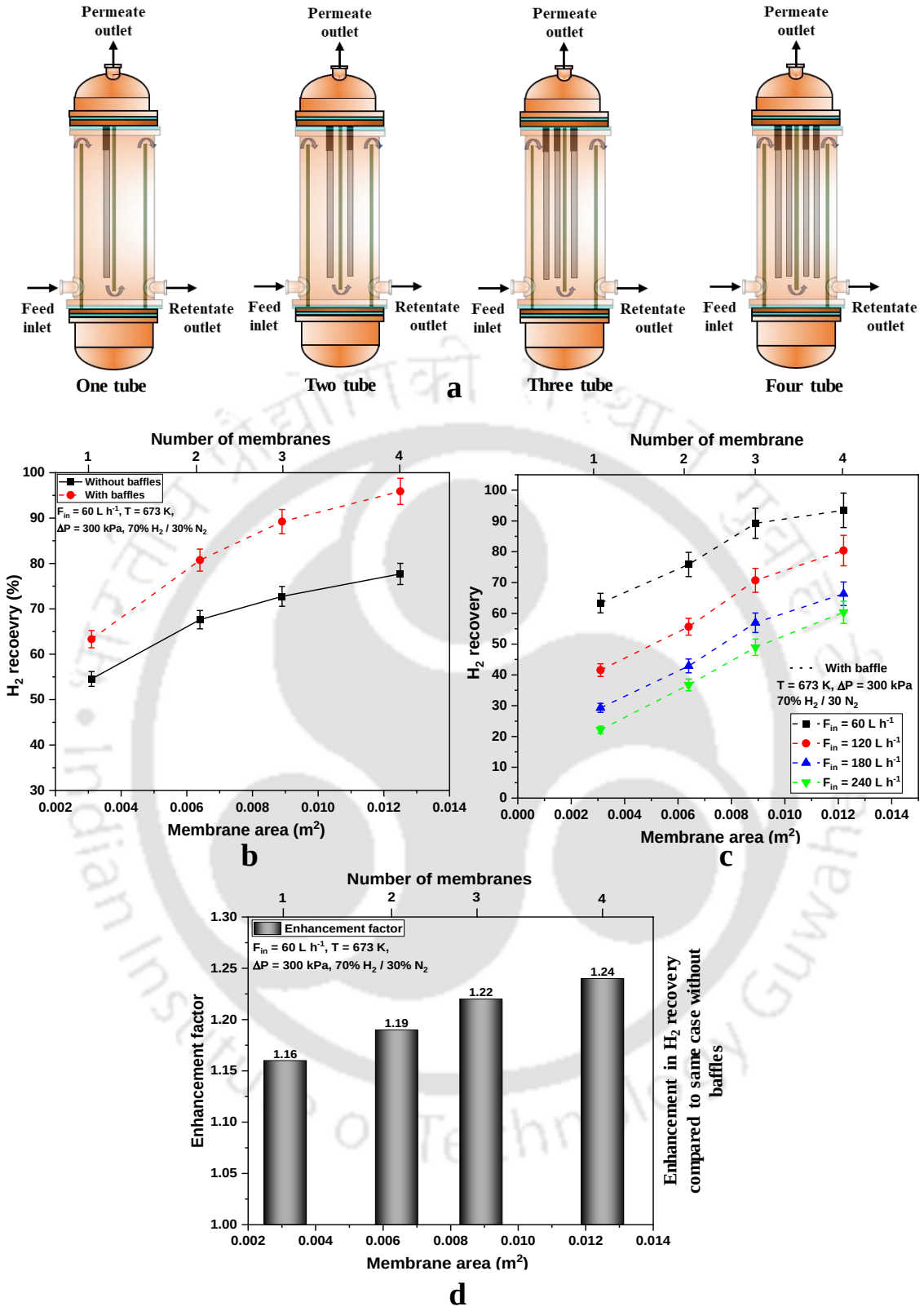

Figure 4. 10. (a) Membrane and baffles arrangements, (b) H_2 recovery as a function of the membrane area without and with baffles, (c) H_2 recovery as a function of the number of membranes at different feed flow rates, and (d) enhancement factor as a function of the membrane area.

4.3.9. Effect of Membrane-to-Pass Ratio (MPR): Multiple Membranes

In order to conduct a more comprehensive analysis of the efficiency of the multi-pass membrane separator including multiple membranes, the optimal membrane-to-pass ratio is determined. This study is performed at F_{in}/A ~ 320 L min^{-1} $m^{-2}_{membrane}$, T = 673 K, ΔP = 300 kPa, and 70% H_2 / 30% N_2 feed mixture composition using ten different membranes prepared earlier. Prior to optimizing the membrane-to-pass ratio (MPR), the permeate hydrogen flux of individual membranes (M1 to M10) is assessed at specific locations (P1 to P10) under identical operating conditions. Permeate H_2 flux is determined without and with baffles, as shown in Figure 4.11. The numbering of membrane positions on the top flange is already given in Figure 4.1 (e). It is important to note that the variations in permeate H_2 flux need to be taken care of at different locations inside the separator, especially in the large separator-diameter membrane separator [21,29]. Consequently, the membranes are placed at the corresponding locations within the separator to minimize the variation in results when multiple membranes are utilized. With the addition of baffles, it is observed that the permeate H_2 flux increases for each membrane. The permeate hydrogen flux remains comparatively lower at the outlet positions (namely, P4 and P5) of the separator, even when utilizing different membranes. The same applies to the feed inlet location (namely, P8 and P9). However, the variations in the values are observed due to the different permeation characteristics of each membrane as given in Table 4.2.

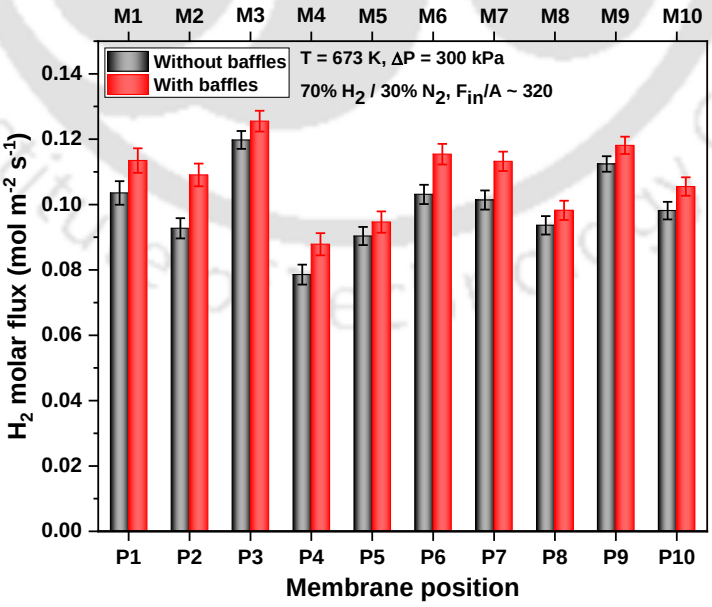

Figure 4. 11. Permeate H_2 flux variation of different membranes (M1 to M10) as a function of corresponding membrane location (P1 to P10) without and with baffles.

Table 4. 3. MPR and the corresponding membrane location in the separator.

MPR	Membrane position
0.25	P1
0.50	P1, P2
1.00	P1, P2, P6, P7
1.50	P1, P2, P6, P7, P3, P10
2.00	P1, P2, P6, P7, P3, P10, P8, P9
2.50	P1, P2, P6, P7, P3, P10, P8, P9, P4, P5

To assess the impact of MPR, the number of membranes is incrementally augmented at the central region of the separator till reaching an MPR of 1.5. The top flange design constraint prevents any additional accommodation of the membranes at the center of the separator. Subsequently, to achieve an MPR of 2 and 2.5, additional membranes are positioned at the inlet and outlet of the separator correspondingly. In the present study, the MPR is increased from 0.25 to 2.5 by adding multiple membranes in different passes whose corresponding locations with respect to MPR are given in Table 4.3. A small steady decrease in the H_2 recovery is observed when the membranes increased at the center of the separator i.e. until the MPR of 1.5 as shown in Figure 4.12 (a). However, a discernible disparity becomes apparent when the membranes are positioned at the inlet and outlet of the separator. The H_2 recovery exhibited a small decline of 2% when the MPR increased from 0.25 to 1.5. Since the feed load is always maintained constant, a significant amount of H_2 is available for separation in each pass therefore only a small percentage of decrease is observed. The decline in H_2 recovery is mostly owing to the decrease in the H_2 partial pressure for the downstream membrane specifically the membranes in the subsequent passes. In contrast, a significant reduction of 7% and 12% in H_2 recovery is noted when membranes are placed at the inlet (MPR = 2.0) and outlet (MPR = 2.5) of the separator, respectively, as compared to the MPR of 0.25. Moreover, there was a 15% decrease in membrane utilization for MPR = 2.5 as compared to MPR = 0.25. The observed behavior can be primarily attributed to the increased feed gas velocity at both the inlet and outlet of the separator, resulting from a higher pressure gradient. This, in turn, significantly reduced the residence time of the feed gases in comparison to the center of the separator. Furthermore, the considerable contribution might be attributed to the drop in the partial

pressure of H_2 in the downstream passes. As a consequence, the extent of concentration polarization also increased with the addition of multiple membranes as shown in Figure 4.12 (b). Therefore, the overall performance of the membrane separator module that includes multiple membranes is substantially influenced by the combined effect of membrane position and H_2 partial pressure. Based on the preceding discussion, it has been ascertained that a significant decrease in the partial pressure of H_2 for the downstream pass presents a major challenge. In order to address this issue, the multi-pass offers the flexibility of introducing the feed gas enriched with H_2 in a distributed manner within each pass. This approach has the potential to sustain a significant proportion of H_2 in each pass, thereby enhancing the H_2 partial pressure across the membrane. The next section of our study aims to examine the effect of feed distribution within the multi-pass membrane separator.

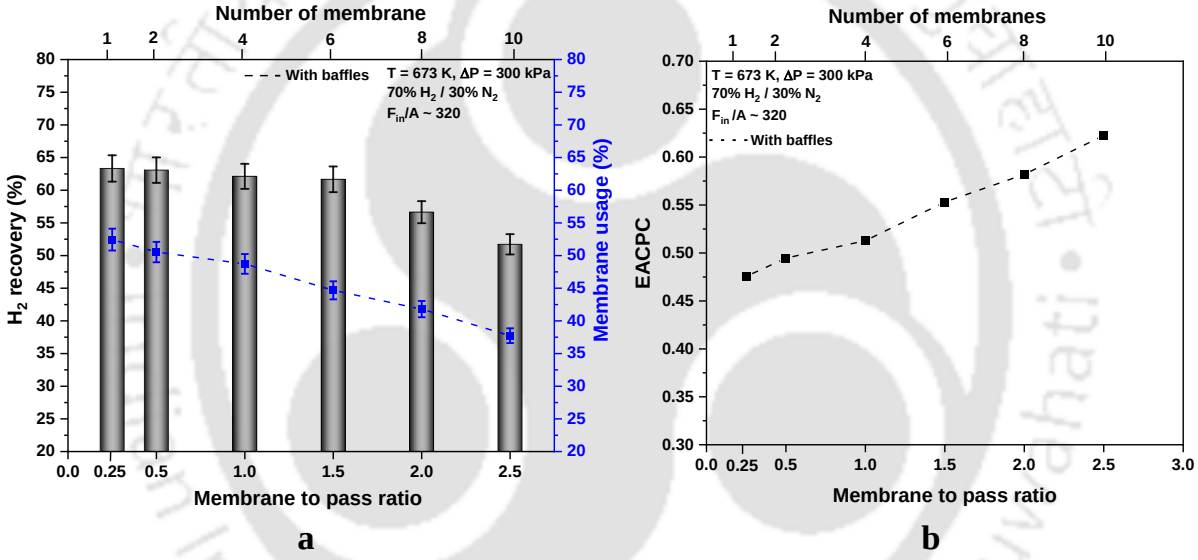

Figure 4. 12. (a) H_2 recovery and membrane usage, and (b) EACPC as a function of increasing membrane-to-pass ratio with baffles.

4.3.10. Effect of Feed Distribution in MPMS: Multiple Membranes

The rapid depletion of hydrogen by the membranes in close proximity to the feed inlet side results in a decrease in the H_2 partial pressure for subsequent passes. This leads to a further decrease in the effective driving force for H_2 permeation thereby reducing permeate H_2 flux [34]. Moreover, the membranes in subsequent passes are not properly exploited to their fullest capacity. To address this challenge, one potential solution is to increase the feed load. However, it is important to note that increasing the feed load may result in a significant decrease in the H_2 recovery. While the baffles effectively ensured a uniform distribution of H_2 throughout each

pass, it is not possible to compensate for the decrease in H_2 partial pressure for the next pass. Thus introducing the feed via multiple inlet facilities, the H_2 partial pressure in each pass may be significantly maintained without compromising on the feed load. As depicted in Figure 4.13 (a), four distinct flow patterns are investigated to assess the effect of feed distribution with multiple membranes. This study is performed at $F_{in}/A \sim 320$ L min^{-1} $m^{-2}_{membrane}$, T = 673 K, ΔP = 300 kPa, and 70% H_2 / 30% N_2 feed mixture composition using ten different membranes prepared earlier. The membrane-to-pass ratio is maintained at a value of 2.5 in all of the feed distribution strategies. In the context of FD I, the feed stream is injected into the separator from the left side, while the retentate stream is extracted from the right side. In the case of FD II, the feed is distributed into the separator from the left side, while the retentate is extracted from the bottom side on the right. In the third stage i.e. FD III, the feed is distributed in each pass via three distinct inlet locations, while the retentate is extracted from the upper side of the separator. At last in the fourth feed distribution scheme (FD IV), the feed is divided into two separate streams and injected into the separator from opposite sides while the retentate is taken out from the bottom of the separator. Other than the FD I scheme the baffle is used in all other schemes, namely FD II, FD III, and FD IV. To evaluate the effect of the feed distribution on the performance of the separator, H_2 recovery is plotted against the feed distribution scheme in Figure 4.13 (b). Due to the inadequate contact pattern between the feed gas and membranes, FD I yields the lowest H_2 recovery. In addition, the residence time of feed gases with membranes located at the separator's inlet and outlet is minimal. Therefore, the H_2 molecule has less time to diffuse to the surface of the membrane for further separation. In order to enhance the H_2 recovery, the baffles are added inside the separator. This modification resulted in a noteworthy increase in H_2 recovery, specifically an observed improvement of 11% in the case of FD II when compared to FD I. Earlier, a significant decrease in the partial pressure of H_2 has been seen in the downstream membranes as a result of the rapid depletion of H_2 in the preceding pass. Therefore, to maintain sufficient H_2 partial pressure in each pass, it is realized to distribute feed in different passes via multiple feed inlet points. When the feed is introduced in each pass through three different feed inlets as depicted in the case of FD III, a jump of 15% in H_2 recovery is observed compared to FD I. Furthermore, when the feed is introduced from two opposite sides, as suggested in FD IV, there has been a notable enhancement in H_2 recovery, reaching a 17% improvement compared to FD I. This finding indicates that the distribution of feed in each pass contributed to improving the H_2 partial pressure and thereby H_2 recovery. Additionally, the distribution of feed increased the residence time in each pass

which provided more opportunity for the H_2 molecules to diffuse and separate through the membrane surface. It is noteworthy to observe that the H_2 recovery is higher in the context of FD IV, which features only two feed inlets from opposite sides, as opposed to FD III, which incorporates three feed inlets in separate passes. This observation suggests that the introduction of the fresh H_2-rich feed from one side, where it mixes with H_2-depleted feed, ultimately results in a decrease in the partial pressure of H_2 for the majority of the membranes located in the center of the separator. Furthermore, it is possible for eddies and H_2-depleted bubbles to occur as a consequence of the back mixing of feed, leading to certain sections of the membrane not actively engaging in the separation of H_2. Thus, the membranes are efficiently employed in multi-pass configurations, where the same feed load is distributed evenly across each pass through multiple inlet facilities. Feed distribution effectively countered the extent of concentration polarization as shown in Figure 4.13 (c). To further substantiate this fact, Figure 4.13 (d) shows an appreciable improvement of 1.26, 1.35, and 1.39 in the enhancement factor for FD II, FD III, and FD IV respectively when compared to FD I. Other than the strategic placement of membranes and baffles, the appropriate distribution of feed gases within the separator is crucial for enhancing H_2 recovery in multi-pass configuration.

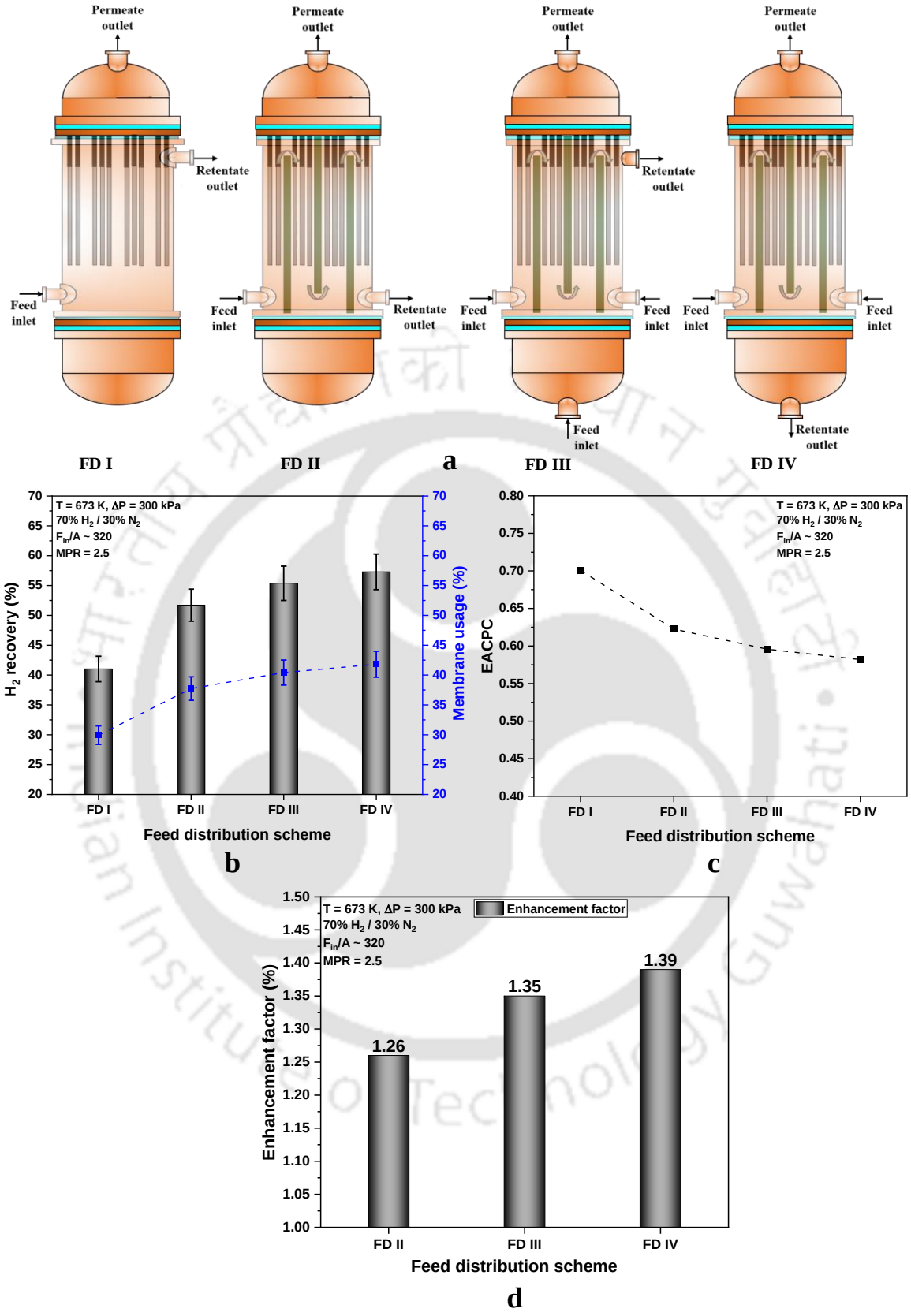

Figure 4. 13. (a) Membrane and baffles arrangements, (b) H_2 recovery and membrane usage, (c) EACPC, and (d) enhancement factor as a function of the feed distribution scheme.

4.4. Comparison of Separator Performance with and without Baffles for Scale-up

The process of scaling up a membrane separator entails the shift from laboratory or small-scale prototypes to larger industrial or commercial systems. Multiple variables must be meticulously evaluated during the scale-up procedure to guarantee the successful and effective functioning of the membrane separator. To thoroughly examine the performance of the multi-pass membrane separator during scale-up, it is necessary to analyze the effect of pressure, the incremental addition of membranes, and the presence of baffles. Modifications to the arrangement of membrane modules may be necessary for the implementation of large-scale applications. Increasing the size can have a detrimental effect on the mass transfer and the flow dynamics. Augmented magnitude can result in changes in pressure gradient, heat transfer, and overall system dynamics. Therefore, further investigation is essential for multi-pass membrane separators to handle these variations.

4.4.1. Effect of Pressure on Separator Performance during Scale-up

Three case studies are conducted to evaluate the scalability of the membrane separator. These case studies involve the use of one, four, and ten membranes, both with and without baffles as shown in Figure 4.14 (a). Increasing the pressure difference intensifies the difference in H_2 recovery when baffles are installed which is consistent in all three situations as observed in Figure 4.14 (b). It is observed that the degree of increase in H_2 recovery with baffles not only improved with increasing pressure but also increased with the addition of multiple membranes when compared with the same case without baffles. Figure 4.14 (c) shows the enhancement in the hydrogen recovery with the pressure and the number of membranes. The introduction of additional membranes resulted in an improvement in recovery, increasing it from 1.1 to 1.14 at 100 kPaG and from 1.16 to 1.26 at 300 kPaG. This trend implies that incorporating baffles with numerous membranes is more advantageous when operating under high pressure conditions. As a result, incorporating baffles into the separator allows for increased feed load capacity and enhanced H_2 recovery simultaneously. Thus, baffles play a vital role in reducing concentration polarization, improving mass transfer, and ensuring effective flow dynamics, all of which promote hydrogen penetration, especially at high pressure.

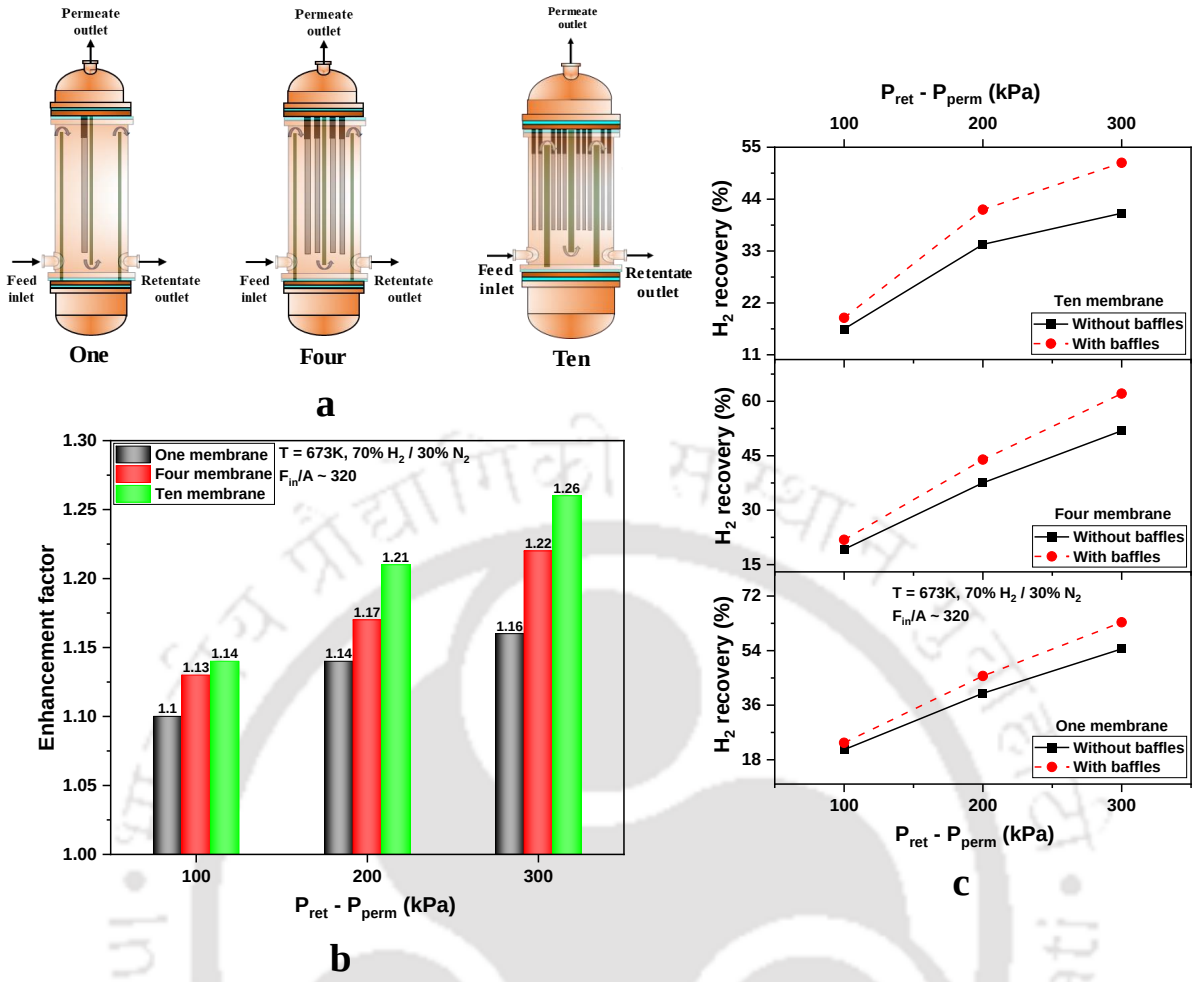

Figure 4. 14. (a) Membrane and baffles arrangements, (b) enhancement factor, and (c) H_2 recovery as a function of the difference in H_2 partial pressure during scale-up.

4.4.2. Effect of Baffles and Number of Membranes during Scale-up

In order to learn the effect of multiple membranes with and without baffles for scale-up different membrane separator modules are considered consisting of one (Case I), four (Case II), and ten (Case III) membranes as shown in Figure 4.15 (a). A separate case of the best feed distribution scheme with ten membranes is also considered as given in Case IV. Figure 4.15 (b) shows the enhancement in the H_2 recovery with baffles compared to the same case without baffles. This study is performed at $F_{in}/A \sim 320$ L min^{-1} $m^{-2}_{membrane}$, T = 673 K, ΔP = 300 kPa, and 70% H_2 / 30% N_2 feed mixture composition using ten different membranes prepared earlier. It is observed that increasing the number of membranes aggravated the separation efficiency. The effect of the baffles is more pronounced for multiple membranes. On one hand, the enhancement factor for a single membrane is 1.16, it significantly jumped to 1.26 for ten membranes. Additionally, the distribution of the feed (scheme FD IV) for ten membranes

improved the enhancement factor to 1.39 which is a significant increase. Even though the addition of multiple membranes results in increased concentration polarization due to restricted heat and mass transfer. The incorporation of baffles improved the performance by a significant proportion. Therefore, proper feed distribution during scale-up is the key to improving performance. Careful separator module design, optimization, and a thorough understanding of the separation requirements are crucial for realizing the potential benefits of incorporating multiple membranes with baffles. Uniform H_2 partial pressure distribution and better radial mass transfer are the major challenges during the scale-up of the separator module [21].

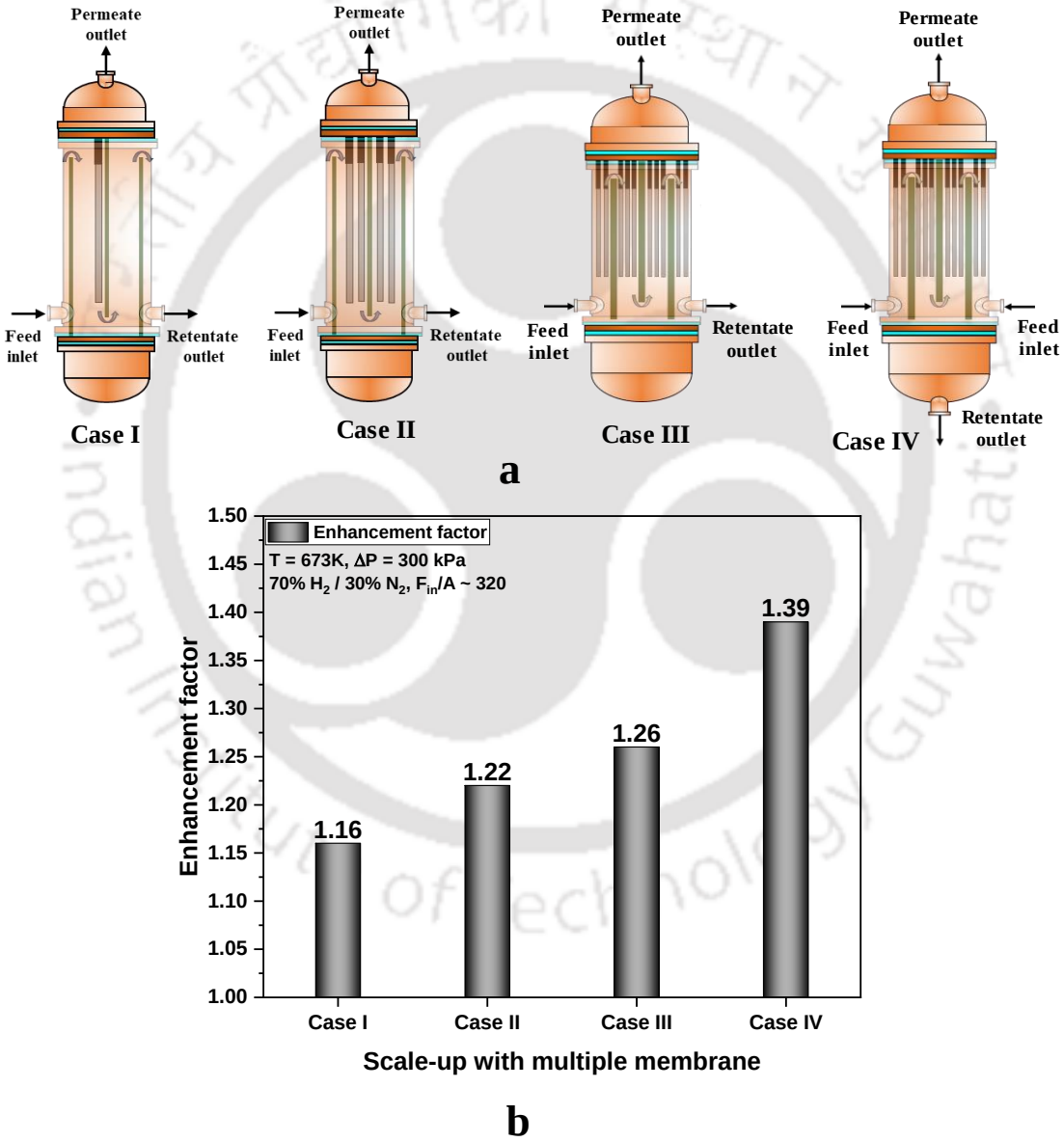

Figure 4. 15. (a) Membrane and baffles arrangements, (b) enhancement factor as a function of the different case studies during scale-up.

4.5. Summary

The present work introduces a novel design for a membrane separator module, using three longitudinal baffles that enable four passes. The entire separator design is optimized at 673 K temperature, 300 kPaG transmembrane pressure, 70% H_2 / 30% N_2 feed gas composition, and feed load of 320 L min^{-1} $m^{-2}_{membrane}$. Additionally, the feed load is increased from approximately 194 to 1290 L min^{-1} $m^{-2}_{membrane}$ to examine the effect of feed load on membrane separation efficiency. Initially, a series of experiments are conducted employing a single membrane, both with and without baffles, to assess the effect of the number of passes and the location of the membrane within the separator on membrane performance. A significant increase of 9% in H_2 recovery is observed with baffles compared to without baffles. Nevertheless, the incorporation of additional baffles resulted in a slight enhancement of the H_2 recovery. Regarding various locations, there is an observed enhancement of 9%, 16%, and 8% respectively at the inlet, center, and outlet position of the separator with the baffles compared to without baffles. When the feed load is increased, enhancement in H_2 recovery is above 1.15 for the feed load below 500 L min^{-1} $m^{-2}_{membrane}$ which drastically reduced to 1.02-1.03 for the feed load above 800 L min^{-1} $m^{-2}_{membrane}$. It is noteworthy to observe that once the saturation of permeate H_2 flux is achieved, the change in H_2 recovery appears similar for both without and with baffles. It is seen that the H_2 recovery improved by 9% for a single membrane whereas it improved by 18% for four membranes. When the feed flow rate is increased from 48 L h^{-1} to 240 L h^{-1}, a decrease of 46% in H_2 recovery is seen for a single membrane whereas it is 35% for four membranes with baffles. This observation implies that while the H_2 recovery decreases at a higher feed flow rate, the extent of this decrease is far less pronounced for multiple membranes in comparison to a single membrane. To facilitate scale-up, the MPR is increased from 0.25 to 2.5 by adding multiple membranes in different passes. The H_2 recovery exhibited a small decline of 2% when the MPR increased from 0.25 to 1.5. However, a significant reduction of 7% and 12% in H_2 recovery is noted when membranes are placed at the inlet (MPR = 2.0) and outlet (MPR = 2.5) of the separator, respectively, as compared to the MPR of 0.25. This is mostly attributed to the drop in the H_2 partial pressure in the downstream passes. To address this particular challenge, the distribution of feed in each pass is employed. It is observed that FD IV exhibited a notable enhancement in H_2 recovery, reaching a 17% improvement compared to FD I. Additionally, an appreciable improvement of 1.26, 1.35, and 1.39 in the enhancement factor for FD II, FD III, and FD IV respectively is seen when compared to FD I. The enhancement factor for a single membrane is 1.16, it significantly jumped to 1.26

for ten membranes. Additionally, the distribution of the feed (scheme FD IV) for ten membranes improved the enhancement factor to 1.39 which is a significant increase. Therefore, the overall performance of the multi-pass membrane separator module that includes multiple membranes is substantially influenced by the combined effect of membrane position and H_2 partial pressure in each pass. Furthermore, the appropriate distribution of feed gases in a multi-pass configuration significantly enhanced the overall efficiency by overcoming the radial mass transfer limitation. Therefore, this study offers an in-depth investigation of the multi-pass membrane separator and approaches for scaling up using multiple membranes. However, a significant decrease in H_2 recovery is observed at high feed load which remains a major bottleneck from a commercial standpoint. In our further investigation, the primary aim will be to enhance hydrogen recovery at higher feed loads by employing a double-stage membrane separator with a series-parallel configuration for further scale-up and recovery of more H_2.

References

[1] C. Koroneos, A. Dompros, G. Roumbas, N. Moussiopoulos, Life cycle assessment of hydrogen fuel production processes, International Journal of Hydrogen Energy, 29 (2004), pp. 1443–1450.

[2] I. Dincer, C. Acar, Review and evaluation of hydrogen production methods for better sustainability, International Journal of Hydrogen Energy, 40 (2014), pp. 11094–11111.

[3] X. Cheng, Z. Shi, N. Glass, L. Zhang, J. Zhang, D. Song, Z.S. Liu, H. Wang, J. Shen, A review of PEM hydrogen fuel cell contamination: Impacts, mechanisms, and mitigation, Journal of Power Sources, 165 (2007), pp. 739–756.

[4] P. Li, Z. Wang, Z. Qiao, Y. Liu, X. Cao, W. Li, J. Wang, S. Wang, Recent developments in membranes for efficient hydrogen purification, Journal of Membrane Science, 495 (2015), pp. 130–168.

[5] S. Yun, S. Ted Oyama, Correlations in palladium membranes for hydrogen separation: A review, Journal of Membrane Science, 375 (2011), pp. 28–45.

[6] G.J.J. Grashoff, C.E.E. Pilkington, C.W.W. Corti, Purification of Hydrogen, Platinum Metals Review, 27 (1983), pp. 157–169.

[7] S.M.M. Jokar, A. Farokhnia, M. Tavakolian, M. Pejman, P. Parvasi, J. Javanmardi, F. Zare, M.C. Gonçalves, A. Basile, The recent areas of applicability of palladium based membrane technologies for hydrogen production from methane and natural gas: A review, International Journal of Hydrogen Energy, 48 (2023), pp. 6451–6476.

[8] J. Il Yang, T.W. Kim, J. Chan Park, T.H. Lim, H. Jung, D.H. Chun, Development of a stand-alone steam methane reformer for on-site hydrogen production, International Journal of Hydrogen Energy, 41 (2016), pp. 8176–8183.

[9] F. Gallucci, A. Basile, Co-current and counter-current modes for methanol steam reforming membrane reactor, International Journal of Hydrogen Energy, 31 (2006), pp. 2243–2249.

[10] C. Zhao, A. Caravella, H. Xu, A. Brunetti, G. Barbieri, A. Goldbach, Support mass transfer resistance of Pd/ceramic composite membranes in the presence of sweep gas, Journal of Membrane Science, 550 (2018), pp. 365–376.

[11] M. Nordio, S. Soresi, G. Manzolini, J. Melendez, M. Van Sint Annaland, D.A. Pacheco

Tanaka, F. Gallucci, Effect of sweep gas on hydrogen permeation of supported Pd membranes: Experimental and modeling, International Journal of Hydrogen Energy, 44 (2019), pp. 4228–4239.

[12] S.K. Gade, P.M. Thoen, J.D. Way, Unsupported palladium alloy foil membranes fabricated by electroless plating, Journal of Membrane Science, 316 (2008), pp. 112–118.

[13] N. Vicinanza, I.H. Svenum, L.N. Næss, T.A. Peters, R. Bredesen, A. Borg, H.J. Venvik, Thickness dependent effects of solubility and surface phenomena on the hydrogen transport properties of sputtered Pd77%Ag23% thin film membranes, Journal of Membrane Science, 476 (2015), pp. 602–608.

[14] W.H. Chen, C.H. Lin, Y.L. Lin, Flow-field design for improving hydrogen recovery in a palladium membrane tube, Journal of Membrane Science, 472 (2014), pp. 45–54.

[15] M. Jafarkhani, M.K. Moraveji, R. Davarnejad, F. Moztarzadeh, M. Mozafari, Three-dimensional simulation of turbulent flow in a membrane tube filled with semi-circular baffles, Desalination, 294 (2012), pp. 8–16.

[16] W.H. Chen, W.Z. Syu, C.I. Hung, Y.L. Lin, C.C. Yang, Influences of geometry and flow pattern on hydrogen separation in a Pd-based membrane tube, International Journal of Hydrogen Energy, 38 (2013), pp. 1145–1156.

[17] C. V. Miguel, A. Mendes, S. Tosti, L.M. Madeira, Effect of CO and CO2 on H2 permeation through finger-like Pd-Ag membranes, International Journal of Hydrogen Energy, 37 (2012), pp. 12680–12687.

[18] M.M. Barreiro, M. Maroño, J.M. Sánchez, Hydrogen separation studies in a membrane reactor system: Influence of feed gas flow rate, temperature and concentration of the feed gases on hydrogen permeation, Applied Thermal Engineering, 74 (2015), pp. 186–193.

[19] W.H. Chen, M.H. Hsia, Y.L. Lin, Y.H. Chi, C.C. Yang, Hydrogen permeation and recovery from H2-N2 gas mixtures by Pd membranes with high permeance, International Journal of Hydrogen Energy, 38 (2013), pp. 14730–14742.

[20] M.M. Barreiro, M. Maroño, J.M. Sánchez, Hydrogen permeation through a Pd-based membrane and RWGS conversion in H2/CO2, H2/N2/CO2 and H2/H2O/CO2 mixtures, International Journal of Hydrogen Energy, 39 (2014), pp. 4710–4716.

[21] R. Ma, B. Castro-Dominguez, A.G. Dixon, Y.H. Ma, Scalability of multitube membrane modules for hydrogen separation: Technical considerations, issues and solutions, Journal of Membrane Science, 564 (2018), pp. 887–896.

[22] W.H. Chen, J. Escalante, Y.H. Chi, Y.L. Lin, Hydrogen permeation enhancement in a Pd membrane tube system under various vacuum degrees, International Journal of Hydrogen Energy, 45 (2020), pp. 7401–7411.

[23] N. Mori, T. Nakamura, K.I. Noda, O. Sakai, A. Takahashi, N. Ogawa, H. Sakai, Y. Iwamoto, T. Hattori, Reactor configuration and concentration polarization in methane steam reforming by a membrane reactor with a highly hydrogen-permeable membrane, Industrial and Engineering Chemistry Research, 46 (2007), pp. 1952–1958.

[24] W.H. Chen, C.W. Tsai, Y.L. Lin, Numerical studies of the influences of bypass on hydrogen separation in a multichannel Pd membrane system, Renewable Energy, 104 (2017), pp. 259–270.

[25] R. Sharma, A. Kumar, R.K. Upadhyay, Characteristics of a multi-pass membrane reactor to improve hydrogen recovery, International Journal of Hydrogen Energy, 46 (2021), pp. 14429–14440.

[26] R. Sharma, A. Kumar, R.K. Upadhyay, Characteristic of a multi-pass membrane separator for hydrogen separation through self-supported Pd–Ag membranes, International Journal of Hydrogen Energy, 43 (2018), pp. 5019–5032.

[27] J. Zhu, S.S. Araya, X. Cui, S.L. Sahlin, S.K. Kær, Zhu, Araya, Cui, S.L. Sahlin, Kær, Modeling and design of a multi-tubular packed-bed reactor for methanol steam reforming over a Cu/ZnO/Al2O3 catalyst, Energies, 13 (2020), pp. 610.

[28] M. Coroneo, G. Montante, A. Paglianti, Numerical and experimental fluid-dynamic analysis to improve the mass transfer performances of Pd-Ag membrane modules for hydrogen purification, Industrial and Engineering Chemistry Research, 49 (2010), pp. 9300–9309.

[29] H. Choi, S.H. Kim, J. Bae, S.P.R. Katikaneni, A. Jamal, A. Harale, S.N. Paglieri, J.H. Lee, CFD analysis and scale up of a baffled membrane reactor for hydrogen production by steam methane reforming, Computers and Chemical Engineering, 165 (2022), pp. 107912.

[30] A. Caravella, Y. Sun, Correct evaluation of the effective concentration polarization

influence in membrane-assisted devices. Case study: H2 production by Water Gas Shift in Pd-membrane reactors, International Journal of Hydrogen Energy, 41 (2016), pp. 11653–11659.

[31] M.K. Koukou, N. Papayannakos, N.C. Markatos, On the important of non-ideal flow effects in the operation of industrial-scale adiabatic membrane reactors, Chemical Engineering Journal, 83 (2001), pp. 95–105.

[32] J. Boon, H. Li, J.W. Dijkstra, J.A.Z. Pieterse, 2-Dimensional membrane separator modelling: Mass transfer by convection and diffusion, Energy Procedia, 4 (2011), pp. 699–706.

[33] W.H. Chen, C.H. Lin, Y.L. Lin, C.W. Tsai, R.Y. Chein, C.T. Yu, Interfacial permeation phenomena of hydrogen purification and carbon dioxide separation in a non-isothermal palladium membrane tube, Chemical Engineering Journal, 305 (2016), pp. 156–168.

[34] W.H. Chen, P.C. Kuo, Y.L. Lin, Evolutionary computation for maximizing CO2 and H2 separation in multiple-tube palladium-membrane systems, Applied Energy, 235 (2019), pp. 299–310.

CHAPTER 5: Experimental Investigation of Double-Stage Membrane Reformer (DSMR) for Enhanced Hydrogen Production via Methanol Steam Reforming

Abstract

Hydrogen is seen as an important substitute for fossil fuels due to its significant energy density, renewability, economic viability, and environmental friendliness. Methanol steam reformation (MSR) provides an effective option for on-site hydrogen generation through a membrane reformer (MR) equipped with the Pd-based membrane for H_2 separation from the mixture gas produced during MSR. However, a major obstacle toward scale-up and commercialization is the cost of the catalyst combined with mass and heat transfer. In addition to this, a substantial quantity of hydrogen is emitted in the retentate as a result of the membrane's limited ability to permeate the produced hydrogen. Therefore, in the present study, we have used the structured SiC scaffold coated with Cu-Fe/Al_2O_3-Zn-ZrO_2 (AZZ) catalyst to intensify the radial heat and mass transfer inside the reactor. Further, a multi-pass membrane separator (MPMS) is introduced on the retentate side of the MR to recover the leftover hydrogen, the integrated system is termed a double-stage membrane reformer (DSMR). The prepared catalyst is characterized using SEM, EDS, and BET techniques before and after testing. Different stages of Cu-Fe/AZZ catalyst coating over the SiC scaffold are also characterized using SEM and EDS. The performance of the DSMR was optimized at different temperatures (573 to 673 K), pressures (100 to 300 kPaG), weight hourly space velocity (WHSV, 12.23 to 48.92 $kg_{feed}\ h^{-1}\ kg^{-1}_{catalyst}$), and varying membrane areas (65 to 495 cm^2). The Cu-Fe/AZZ/SiC catalyst was tested in all three configurations for comparison including traditional reformer (TR), MR, and DSMR at 300 kPaG of pressure, 673 K of temperature, 3/1 of S/C ratio, 187 cm^2 of membrane area, and 12.23 $kg_{feed}\ h^{-1}\ kg^{-1}_{catalyst}$ of WHSV. Following the performance testing a higher methanol conversion is obtained in the case of DSMR. For instance, the methanol conversion of ~75 % is achieved in the case of DSMR compared to ~57% in MR and ~53% in TR. Moreover, H_2 recovery of more than 74.5% is achieved in DSMR which is 8.5% higher compared to MR.

5.1. Introduction

Currently, most of the energy demand in the world is fulfilled through greenhouse gases intensive fossil fuel-based energy resources including oil, coal, and natural gas. In order to overcome the foreseen challenges related to global warming 197 countries agreed to limit the average global temperature rise below 2K above the pre-industrial level during 'The Paris Agreement (2015, COP-21)' [1]. Therefore, hydrogen is seen as an important substitute for fossil fuels due to its high gravimetric energy density (~120 kJ g^{-1}, LHV), its combustion gives only water, abundancy on earth in the form of water and hydrocarbons, clean, non-toxic, green, and renewable source of energy [2,3]. However, hydrogen always exists in combined forms such as alcohols, water, coal, biomass, and other hydrocarbons. Extraction of H_2 from these sources is accomplished via several techniques such as steam reforming (SR), autothermal reforming (ATR), partial oxidation (PO_X), pyrolysis, gasification, fermentation, etc. Amongst them, steam reforming of hydrocarbon is economically viable owing to its high process efficiency (70-85%) [4]. Hydrogen produced through these thermochemical methods is accompanied by other gases (CO_2, CO, CH_4, N_2, and O_2) and impurities (H_2S, NO_x, SO_x, ash, tar, and other elements in the trace). Consequently, separating the hydrogen from the gas mixture before application is a crucial step. However, the purification of hydrogen with the presently available technologies like pressure swing adsorption (PSA), temperature swing adsorption (TSA), and cryogenic distillation (CR) are not economically viable due to their energy-intensive equipment and low hydrogen purification efficiency. The process of separating hydrogen using conventional PSA for mobile and on-site applications encounters the challenge of fast adsorption and phase equilibrium. Additionally, CR necessitates the use of energy-intensive equipment and substantial financial investment [5,6]. In this scenario, membrane technology especially Pd or Pd-alloy-based membranes are quite practical for small-scale (on-site) and portable (on-board) applications. This is attributed to its high hydrogen permeability, ideally infinite selectivity, compact size, low energy consumption, and the ability to operate continuously under reaction-separation conditions [7]. Thus, it can be integrated with the hydrogen generation system to produce high-purity hydrogen for further applications including low-temperature proton exchange membrane fuel cells (PEMFCs), which require hydrogen purity >99.99% and CO content <10 ppm [8–10]. The primary obstacle to commercialization revolves around the safe storage and transport of hydrogen owing to its low volumetric mass density (0.0813 kg m^{-3}, at 100 kPa, and 298 K) [3]. Therefore, producing and utilizing H_2 at

the application site is a preferable option which can be feasibly accomplished through methanol steam reforming (MSR). This is attributed to its low reforming temperature (573-623 K) due to the absence of a C-C bond which also lowers the possibility of coke production at high temperatures. The presence of the –OH functional group is also a good attribute, as it reduces the amount of water consumed in the steam reforming reaction to produce hydrogen, hence reducing the SR temperature [11]. Methanol substantially reduces emissions of SO_x, NO_x, and other particulates. Moreover, the gravimetric hydrogen storage density of methanol (99 kg m^{-3}, atm) is higher compared to liquid hydrogen (70 kg m^{-3}, 20 K), formic acid (53 kg m^{-3}, atm), H_2 compressed cylinder (39.9 kg m^{-3}, 70000 kPa), and even AlH_3 based metal-organic framework (85 kg m^{-3}, achieved in practice). Though it is toxic, it is neither carcinogenic nor mutagenic, unlike other common liquid petroleum fuels [2,12,13]. In addition to this, a high H/C ratio, low sulfur contents, low cost, ease of availability, and ability to be produced from a renewable source such as biomass and captured CO_2 make it an ideal source of hydrogen [14]. The integration of hydrogen generation through MSR and selective separation of H_2 through a Pd-based membrane in a compact reactor unit called Membrane Reformer (MR) shifts the thermodynamic equilibrium toward the desired product (i.e. H_2) according to the Le Chatelier's principle and hence the enhanced methanol conversion is anticipated [15]. One of the crucial components of MR is the catalyst for MSR. Traditionally, packed bed MR is investigated which suffers the critical issue of poor heat and mass transfer characteristics, particularly with endothermic MSR reaction. Moreover, channelization and uneven feed distribution during scale-up in packed beds leave a significant amount of catalyst underutilized resulting in reduced reactor efficiency and increased catalyst cost [16,17]. The cost of the catalyst therefore accounts for the major portion of the total investment, particularly while using noble metal-based catalysts to improve the catalytic activity and reduce coking [18]. Conversely, the use of fluidized bed MR can address this issue, however, the continuous striking of the fluidized bed catalyst particle on the membrane surface results in the erosion or damage of the membrane, thereby decreasing its performance and lifetime. Also, bubble-to-emulsion mass transfer limitations between the gas phase (bubbles) and the liquid or solid emulsion phase are a major challenge in fluidized beds [19]. Therefore, to overcome these challenges, structured porous catalyst support including monoliths, solid foam, 3D printed scaffolds, hollow fibers, etc are proposed for thermochemical reactions. For instance, SiC foam possesses high thermal conductivity (8.56 W m^{-1} K^{-1}, at 823 K) which is 1-2 orders of magnitude higher compared to alumina (0.26 W m^{-1} K^{-1}, at 823 K), thereby intensification in the radial heat transfer is anticipated. Further, better fluid phase mixing

helps to improve mass transfer properties due to their unique interconnected 3D structural characteristics. Moreover, catalyst coating over the porous structure of SiC foam supports significantly reduces the amount of catalyst loading while maintaining a high specific surface area. The observed phenomenon can be primarily linked to the existence of a rough porous SiO_2 layer at the micron scale, serving as the substrate for the application of the powder catalyst [20,21]. By ensuring that the catalyst is not in a fluidized bed state, it is possible to eliminate the persistent degradation of the membrane caused by the impact of catalyst particles. Furthermore, the foam-structured reactor can achieve device compactness, process flexibility, and small pressure drop, allowing for varied throughput requirements. SiC foam also helps increase the radial flow of the product gases and cellular turbulence, thereby minimizing the concentration polarization at the local level along the membrane surface [22–24]. Other than the catalyst, the membrane for hydrogen separation is another critical component in MR. Although a Pd-based membrane has high hydrogen permeability still it is not capable of separating all the produced hydrogen during MSR at moderate temperature (573-623 K) and pressure (100-400 kPa). Also, the unreacted methanol and steam get adsorbed over the membrane surface, negatively affecting the permeation capacity of the membrane. This effect is more prevalent at lower temperatures. Therefore, an additional separator is necessary on the retentate side to recover the leftover hydrogen [25–27]. In the following part, a succinct literature overview of the MSR, and SiC foam in MR is presented. Further, the possibility of integrated MR and membrane separator according to the literature is discussed for enhanced hydrogen recovery.

5.1.1. Literature Review on MSR in Membrane Reformer

In-situ onsite conversion of methanol to hydrogen through MR is an alternative route to utilize hydrogen energy while addressing the challenge of hydrogen storage and transportation. Accounting for the cost per kilogram of hydrogen storage, methanol (3.57 USD) once again has an advantage compared to compressed hydrogen (> 12 USD, 70000 kPa) and liquid H_2 (~ 8 USD, 20 K). However, to fully utilize the potential of hydrogen, it must be separated from methanol due to its lower heating value (~120 kJ g^{-1}) which is roughly 6.5 times higher compared to methanol (18.1 kJ g^{-1}) [2]. SR is the most efficient method and the only method that produces three molecules of hydrogen for every mole of methanol where one mole of H_2 is contributed by water [4]. Equation 1.1 represents the fundamental MSR reaction. In addition to the primary reaction, the literature describes two secondary reactions termed ‘Methanol Decomposition’ and ‘Water Gas Shift’ as shown in Equations 1.2 and Equation 1.3. These

reactions occur simultaneously, with CO and H_2 being produced by the methanolysis reaction and CO reacting with H_2O to produce CO_2 and H_2 via the WGS reaction.

$$CH_3OH + H_2O \rightleftarrows CO_2 + 3H_2 \qquad \Delta H = 49.7 \text{ kJ mol}^{-1} \qquad (5.1)$$

$$CH_3OH \rightleftarrows CO + 2H_2 \qquad \Delta H = 90.2 \text{ kJ mol}^{-1} \qquad (5.2)$$

$$CO + H_2O \rightleftarrows CO_2 + H_2 \qquad \Delta H = -41.2 \text{ kJ mol}^{-1} \qquad (5.3)$$

Nevertheless, the formation of CO may damage the Pt-based catalyst in the PEMFCs. Therefore the selection of the right catalyst is important to maximize H_2-selectivity and minimize CO-selectivity. This is also important while integrating the Pd-based membrane with MSR in MR having two different working temperature ranges i.e. >573 K for Pd-based membrane and 473-573 K for MSR. In this case, the operating temperature for MR will exceed 573 K, as a result of which an increase in the CO content is anticipated [28]. Moreover, the high CO concentration in product gas will negatively affect the permeation capacity of the membrane by getting adsorbed over the membrane surface. Hence, it is desired to prepare a catalyst with a working temperature above 573 K with minimum CO production. The performance characteristics of the catalyst are significantly affected by the metals being doped, support, and promoters. Traditionally, Cu-based catalysts have been extensively studied for MSR owing to their high H_2 selectivity and low carbon formation. Further, the incorporation of alkali promoters such as Fe, Mn, ZnO, ZrO_2, and CeO_2, as well as other alkali metal oxide supports, has been shown to inhibit catalyst sintering and deactivation [29,30]. The availability of acidic and basic sites is essential for catalyst activity and adherence to a specific reaction mechanism. Highly acidic sites facilitate the RWGS reaction, which reduces CO selectivity. On the other hand, the enhanced acidic sites facilitate in situ CO_2 sorption, thereby enhancing H_2 selectivity [31]. The addition of ZnO to Cu-based catalysts enhances the dispersion of Cu over the support and enhances CO oxidation. Incorporating alumina into the $CuO/ZnO/Al_2O_3$-based catalyst further improves the thermal stability and surface area of the catalyst. Here, alumina possesses the ability to absorb and activate methanol for subsequent reactions [30,32]. In addition to ZnO, zirconia also plays a vital role in enhancing the performance and stability of Cu-based catalysts by increasing the metal dispersion, increasing stability, and inhibiting sintering and carbon deposition. The incorporation of zirconia into Cu-based catalysts facilitates the alteration of their surface characteristics, including acidity, basicity, and redox properties. In addition, ZrO_2 has improved surface oxygen mobility and activation, which aids in the adsorption and activation of methanol and water molecules during MSR [33,34]. Other

than copper, the noble metal-based catalyst (Pd, Ru, and Pt) is also investigated due to its high reforming activity. However, high cost limits its large-scale commercial application [35]. Among other transition metals, iron is foreseen as an interesting non-precious abundant metal for MSR having multiple oxidation states and the ability to oxidize and reduce easily [36,37]. Since different metals have different promotional effects on the activity of the catalyst, bimetallic catalysts received attention due to their distinct electrical and chemical properties [38,39]. The next part discusses different literature reported earlier in context with the bimetallic catalyst for MSR.

5.1.2. Literature on Bimetallic Catalysts for MSR

Recently, Richa et al. [39] compared bimetallic catalysts including Cu-Fe, Ru-Fe, Ni-Fe, Ni-Cu, and Cu-Ru with a total of 3% metal loading supported on Al_2O_3-Zn-Zr (AZZ, 70:15:12). Their study demonstrated that the Cu-Fe (50:50 mole ratio) achieved ~48% methanol conversion with 3% total metal loading whereas the conversion increased up to 70% with 13% total metal loading. Cu-Fe/AZZ (13% metal loading) showed stable performance for 100 hours. Most importantly zero CO selectivity was observed for equimolar or with higher Cu percentage for temperatures up to 723 K. Khzouz et al. [40] studied the effect of the addition of Ni in Cu-based catalysts. Ni eventually led to an increase in the CO selectivity and decreased the coke formation. They compared the 5%Ni–5%Cu/Al_2O_3, Ni/Al_2O_3 and Cu/ZnO/Al_2O_3 catalysts for MSR. The addition of Ni increased the Cu dispersion over the support which resulted in the enhanced WGS reaction, thereby reducing the CO formation. Moreover, a reduction in the coke formation is observed in the Ni–Cu/Al_2O_3 catalyst. This behavior was attributed to the direct methanol decomposition in the presence of the Ni-Cu bimetallic phase. At 598 K a methanol conversion of 99% and H_2 selectivity of 89% were reported for Ni–Cu/Al_2O_3 compared to the 99% methanol conversion and 86% H_2 selectivity for Cu/ZnO/Al_2O_3. In addition to this, the WGS reaction equilibrium shifts toward the RWGS reaction resulting in the formation of more CO, particularly at the copper active phase. Mierczynski et al. [41] synthesized the bimetallic Au-Cu and Au-Ni-based MSR catalyst on the multi-walled carbon nanotube (MWCNTs) using the wet impregnation technique where Au was introduced on monometallic copper or nickel catalyst surface by deposition–precipitation method. They observed that the Au–Cu/MWCNTs have higher H_2 selectivity and lower CO selectivity. This behavior was probably due to the formation of the Au-Cu alloy compound. Another study by Lytkina et al. [38] reported bimetallic (Ru–Rh, Ni–Cu) catalysts synthesized on a surface of different carbon supports: detonation nano-diamonds (DND), infrared pyrolyzed polyacrylonitrile (PAN), carbon black

Vulcan-XC-72. For all the prepared catalysts a methanol conversion of more than 85% was achieved at 603 K. The catalytic activity decreased in the following trend DND> PAN> Vulcan. DND is highly rich in -OH, -C=O, -COOH, and -COOR groups which is a good attribute for enhancing the catalytic activity of the catalyst compared to other supports. With the advancement in recent technology, Qian et al. [21] optimized the structural design of porous SiC supports with gradient pore size distributions using numerical modeling. Thereafter, the optimized catalyst structure was fabricated using the 3D printing technique (dry ink writing) followed by catalyst loading and further testing. It was observed that the gradient pore size distributed in both directions has the highest methanol conversion owing to its uniform catalyst distribution and mass transfer behavior. For this catalyst, they achieved a maximum methanol conversion of 79.75% at a feed flow rate of 40 μl min^{-1} and 553 K. Hence, a catalyst possessing various oxidation states and the capacity to readily undergo reduction and oxidation is a desirable characteristic for an MSR as it effectively minimizes the formation of coke. In this case, a bimetallic catalyst offers the possibility of choosing two separate metal particles that have diverse effects on the catalyst's activity. Furthermore, it has been noted that these catalysts have the ability to function at high temperatures, making them appropriate for integration into the Pd-based membrane reformer for the simultaneous production and separation of hydrogen. Nevertheless, it has been previously reported that the transmission of heat and mass in the catalyst bed during scale-up is a significant challenge. In order to overcome this challenge, structured catalyst has been proposed. The next section presents the literature review of structured catalysts used for MSR.

5.1.3. Literature on the Structured Catalyst for MR

Among the structured catalysts mostly SiC foam-based catalysts are studied in MR for hydrogen production due to their ease of operation in a wide range of temperatures and pressure. Moreover, they can be tailored in different shapes with varying porosity according to the requirement. For example, Falco et al. [17] performed the experimental analysis of steam reforming of natural gas over an Rh-Pt/Al_2O_3 coated SiC foam-based catalyst. The study was conducted for almost 1000 operating hours with a heating/cooling cycle above 70 cycles. They achieved a conversion of 57.3% which is 26% more than the same traditional reformer at 873 K. SiC foam helped to improve the thermal transport property of the catalyst bed as well where at least an improvement of 20 K in the temperature on the membrane side is reported compared to packed bed. Patrascu and Sheintuch et al. [42] used Pt(3 wt. %)Ni(10 wt. %)/CeO_2 catalyst coated over SiC foam scaffold (30 PPI and 85% porosity) in a Pd-Ag membrane-based

membrane reactor. One dimensional mathematical model was used to predict the performance of the membrane reactor, temperature profile, gas composition, and permeate flow rate. Giaconia et al. [23,43] coated the Ni(10 wt. %)Pt (3 wt. %)/$CeZrLaO_x$ over SiC foam-based monolith using wash coating methods. The characteristics in terms of void fraction, size, and surface properties were optimized to achieve high conversion. The catalyst and membrane were then assembled inside the molten salt ($NaNO_3$/KNO_3 liquid mixture (60/40 w/w) heated pilot scale membrane reformer having ten distinct chambers. More than 60% of methane conversion was observed at 823 K with less than 10 ppm CO on the permeated side. Recently Yan and Cheng [22] investigated the performance of the 2.0 wt. % Ru/α-Al_2O_3 catalyst wash coated over the 3D SiC continuous skeleton in a membrane reactor. They observed that the membrane reactor with SiC-foam significantly improved the radial heat and mass transfer compared to the same traditional packed bed reactor. An increase of 20K in the temperature was seen along with a high H_2 concentration near the membrane surface. Moreover, they were able to save more than 78% of the catalyst while achieving almost 100% catalyst utilization efficiency. However, hydrogen recovery from the retentate side has always been a challenge. To overcome this issue, the addition of another separator unit is proposed in the literature. The next section outlines the literature reported earlier and recent advancements for the same.

5.1.4. Literature on the Integrated Membrane Reformer

In literature mostly two types of combination are reported i.e. reformer with membrane separator and membrane reformer with membrane separator. For instance, Falco et al. [44] conducted an economic analysis of the design variables and the cost of producing H_2 in a reformer-membrane module (RMM, reformer unit integrated with membrane separator module) plant that uses natural gas steam reforming. According to their analysis, incorporating RMM into the nuclear power plant or solar molten salt system resulted in a 10% reduction in the cost of H_2 generation compared to SR. Additionally, the overall CO_2 production decreased by 28%. In their subsequent study, Falco et al. [17] conducted an experimental study to evaluate the efficiency of RMM test plants in producing H_2. The plants had a production capacity of 20 N m^3 h^{-1}. At a temperature of 873 K, they achieved a methane conversion rate of 57.3%, which is 26% higher than that of the traditional SR reactor under identical operating conditions. The reforming unit has a Rh-Pt/Al_2O_3 catalyst that is applied to SiC foam, which has dimensions of 150 mm in length and 60 mm in diameter. A total of 1000 hours of continuous operation was conducted, involving over 70 cycles of heating and cooling. For the same RMM system, Barba et al. [45] utilized a physical-mathematical model for mass transfer to verify the accuracy

of the experimental findings. A strong correlation was established in the scale-up investigation, indicating a substantial decrease in the H_2 molar flux due to the presence of mass-transfer resistance i.e. concentration polarization. In addition, they also calculated the scaling-up correlations for the material exchange modules. Recently, Morico et al. [46] investigated the performance of the membrane reformer at the KT-Kinetics Technology pilot plant designed for pure H_2 production integrated with solar-assisted molten salt heating. The plant design consists of a pre-reformer where the methane conversion is accomplished, thereafter the unconverted methane and syngas are routed to the membrane reformer unit for further conversion and H_2 separation. The latter membrane reformer section is designed in a tube-in-tube configuration with bifunctional Ni-noble/SiC-foam-based catalysts in the annular section around the membrane tube. They achieved 60% feed conversion at a temperature of 813 K, pressure of 850 kPaG, and S: C ratio of 4. However, they were able to recover only 70% of the produced H_2 (permeate H_2 flow rate = 3.5 N m^3 h^{-1}) with 50 ppm (dry basis) of CO concentration on the permeate side. From the same research group, Franchi et al. [25] numerically compared three configurations for methane steam reforming for hydrogen production i.e. SR, MR, and RMM. They achieved an overall methane conversion of 92% with two reactors and membrane modules and hydrogen recovery of 88% for RMM configuration. This way they predicted 30% higher conversion could be achieved compared to SR. Iluianelli et al. [27] in a separate study designed a two-stage laboratory-scale hydrogen production system through biogas consisting of the MR and an additional membrane separator at the retentate of MR. They achieved 99% of CH_4 conversion (S/C = 2, feed pressure = 350 kPa, and 673 K) and 40% of CO_x-free H_2 recovery in Stage 1. Thereafter the retentate is sent to Stage 2 to recover more H_2 at the same temperature and pressure. For the integrated system, they were able to recover 67% of the 99.9% pure hydrogen contained in the retentate. This way they recovered overall 80% of the produced hydrogen. Following the same study, Ruales et al. [26] experimentally investigated the effectiveness of SR of biogas and/or biomethane integrated with a membrane separator for hydrogen generation. In the SR stage, they got 60% and 40 % of CH_4 conversion in the case of biomethane and biogas respectively, at 873 K, 100 kPa, and S/C = 4. Upon the integration of the membrane separator as the second stage, they achieved hydrogen recovery of 90% and 88% for biomethane and biogas respectively while obtaining 99.9999% of H_2 purity in each case at 773 K and ΔP = 250 kPa. Further, they compared the energy efficiency and exergy analysis of the integrated system. Their result demonstrated that the thermal efficiency of an integrated two-stage system was higher for biomethane (72% at 773K based on LHV) compared to biogas (60% at 773K based on LHV). Also, by increasing the temperature from 673 K to 773 K it was

possible to get 30% and 20% higher energy efficiency for biomethane and biogas respectively. Higher methane concentration in biomethane was attributed as the main reason for this behavior. An increase in the temperature has a substantial impact on the reaction kinetics of the chemical reaction. Most recently, Cerone et al. [47] developed a multi-stage WGS reactor consisting of two parallel Pd-Ag membrane reactors and two separator membrane separators in the initial stage. The entire system is set up to generate 0.25 N m^3 h^{-1} of hydrogen gas with high purity. At a temperature of 623 K, a pressure of 800 kPa, and S/C of 4, they successfully obtained a carbon monoxide conversion rate of 97.6%. In addition, the combination of a membrane reactor and a separator resulted in a 12% increase in H_2 recovery. The separator is utilized to recover hydrogen at its initial state before the reaction. Based on their findings, they determined that the single membrane reactor is a more economically viable option compared to the combined system. This is because the high concentration of CO negatively impacts the permeation of H_2, resulting in lower efficiency.

However, a systematic study on the effect of various parameters during scale- up including feed flow rate, membrane area, pressure, and temperature is missing. The scale-up study is crucial for hydrogen production and efficient separation before commercial application to enhance the overall efficiency of the entire system. Any change in the operating parameters leads to a coherent chain of events, consequently leading to significant changes in the performance of the membrane reformer. Most importantly, the reactor geometry, such as the membrane configuration, reactor dimensions, and reactor shape, significantly influences the mass transfer of reactants and products, heat transfer, and fluid dynamics within the reactor. Therefore, it is both valuable and imperative to investigate the capabilities of solid foam in membrane reformers and ultimately address the current issues. Additionally, the problem of hydrogen loss in the retentate stream must be resolved by incorporating a membrane separator with different membrane configurations capable of accommodating changes in the feed flow rate and other operational factors.

In this work, we have developed a membrane reformer including two separate units with a customized number of membranes and catalyst heights to meet specific needs. The first component, known as the membrane reformer (MR), is designed to house multiple membranes (at least 6 membranes) at the top flange and a catalyst at the bottom section of the reactor. The second component called the multi-pass membrane separator (MPMS, at least 10 membranes), is purposefully connected to the retentate side of the MR-I to recover extra hydrogen. MPMS has already demonstrated its suitability for enhanced hydrogen separation [48]. The complete

system is referred to as a double-stage membrane reformer (DSMR). Here SiC foam is wash-coated with the Cu-Fe/AZZ catalyst with 13% metal loading (Cu-Fe = 50:50 mole ratio, and AZZ = 70:15:12) for MSR due to its low CO selectivity, almost zero at 723 K as reported by Richa et al. [39]. This temperature is also suitable for Pd-based membranes integrated in MR-I for hydrogen separation. The whole set of experiments is performed using $Pd_{85}Ag_{15}/Al_2O_3$ membranes prepared via the electroless plating (ELP) technique. The use of a SiC-based foam significantly reduced the heat and mass transfer issue in endothermic MSR, owing to its exceptional thermal conductivity. Initially, the performance of the MR is evaluated with varying operational conditions such as weight hour space velocity (WHSV), temperature (573-673 K), pressure (100-400 kPaG), number of membranes (or membrane area), and steam-to-methanol (S/M) ratio. At last, the effect of adding MPMS is examined under the same operating conditions. The evaluation of the performance of the integrated DSMR is conducted by considering several key parameters including overall conversion, permeate hydrogen yield, H_2 production rate, hydrogen recovery, global permeate H_2 purity, and long term thermal stability. The detailed study and performance optimization of DSMR is first of its kind experimental investigation of MSR for enhanced hydrogen production and separation with multiple membrane integrated both in reformer and separator.

5.2. Experimental Methodology

To address the issue of heat and mass transfer in the packed bed catalytic reactor, we employed structured SiC foam that is coated with a catalyst. The approach for preparing the catalyst, applying it to the SiC foam, and the techniques used to characterize it are described in detail. Furthermore, the significant challenge in achieving high process efficiency is in the limited hydrogen recovery from the mixture gas, particularly when it is contaminated with CO in the MR. Therefore, a holistic DSMR is designed consisting of high a compact MR unit integrated with a membrane separator. The specific DSMR design is given in this section. Finally, the evaluation of catalytic activity and the optimization of the DSMR technique are presented in relation to the synthesis and separation of hydrogen.

5.2.1. Preparation and Coating of Cu-Fe/AZZ Catalyst over SiC-foam

The catalyst is prepared using the incipient wetness impregnation technique as outlined in Figure 5.1 [49,50]. 13% metal loading of Cu-Fe (50:50 mole ratio) supported on $73Al_2O_3$-15Zn-12Zr is prepared for MSR as optimized by Richa et al [39]. Reagent-grade chemicals were used as the metal precursor to prepare the catalyst including copper (II) nitrate trihydrate (Merck), ferric nitrate nonahydrate (Merck), zinc nitrate hexahydrate (Merck), zirconyl nitrate (Merck), and gamma aluminum pallets (Sigma). Initially, the alumina pallets were crushed in the ball mill for 10 hours and sieved in the size of 200 μm. Thereafter, the zinc nitrate and zirconyl nitrate were added in the appropriate amount in alumina using the incipient wetness impregnation method. Subsequently, copper nitrate and ferric nitrate were added for metal doping and left for aging for 6 hr under continuous stirring at room temperature. The pH of the solution (pH ~ 9) was adjusted above the iso-electric point of γ-alumina using aqueous ammonia. The prepared catalyst was then filtered using the Buchner Flask and washed several times with DI water till a neutral pH was achieved (pH paper was used as the indicator). The catalyst was further dried at 393 K for 12 hours in a hot air oven. After drying the catalyst is ground to a fine powder in a mortar pestle.

SiC foam with the following specifications was selected for the catalyst coating: pores per linear inch (PPI) = 20, diameter = 90 mm, bulk density = 0.45-0.50 g cm^3, height = 25 mm, and porosity = 80%. The SiC foam is initially cleaned with alkaline NaOH solution (20 wt.%) at 353 K for 1 hour to remove residual Si and other impurities from the surface of the SiC foam. Following that the SiC foam is further cleaned with ethanol and DI water several times before drying at 393 K overnight. The entire cleaning was performed under ultrasonic irradiation [51].

To apply the catalyst onto the SiC foam, a mixture of 10 wt. % Cu-Fe/AZZ catalyst in DI water is prepared and stirred continuously to form a homogeneous slurry. The wash coating method is adopted to coat the catalyst over the SiC foam. In order to do so, the SiC foam is completely submerged in the slurry for 30 seconds and taken out slowly. The excess of the slurry was removed using pressurized air. Then the coated SiC foam is dried in a hot air oven at 393 K for 1 hour with frequent rotation. During the first half-hour, the foam is rotated often to prevent the accumulation of catalyst mass in any one area of the SiC foam due to the gravitational pull effect. The aforementioned steps from wash coating to drying were repeated multiple times till 1 ± 0.2 gm of catalyst loading was achieved over the SiC foam. Finally, the catalyst was calcined in a tubular furnace at 773 K for 5 hours (ramping rate = 2 K min^{-1}) under an inert atmosphere maintained with N_2 (100 ml min^{-1}). The entire scheme of the catalyst coating over the SiC foam is presented in Figure 5.1. After the loading of 1 ± 0.2 gm of catalyst per piece of SiC foam, marginal or no change in the weight gain was observed gravimetrically. The overall weight of the catalyst loaded on each foam prepared for the present study (sixteen foams) is given in Table 5.1. Moreover, the optical image of the catalyst-coated SiC foam as given in Figure 5.2 (a) shows that the catalyst was evenly distributed without any relevant pore-clogging phenomena across the whole surface following the completion of the final round of coating, which required five to seven coating cycles. Multiple SiC foams were coated following the same methodology as shown in Figure 5.2 (b). Figure 5.2 (c) illustrates the results of the Cu-Fe/AZZ catalyst loading over the SiC foam per deposition cycle during the dipcoating procedure. A total of five SiC foams including Foam-SA, Foam-SB, Foam-SC, Foam-SD, and Foam-SE were studied for weight gain per cycle. It can be observed that there is very little or marginal change in the weight gain after five coating cycles. Therefore, for the rest of the catalyst it was decided to coat the SiC foam for seven cycles only. A total of sixteen catalyst-coated SiC foam was prepared for the present study following the same methodology.

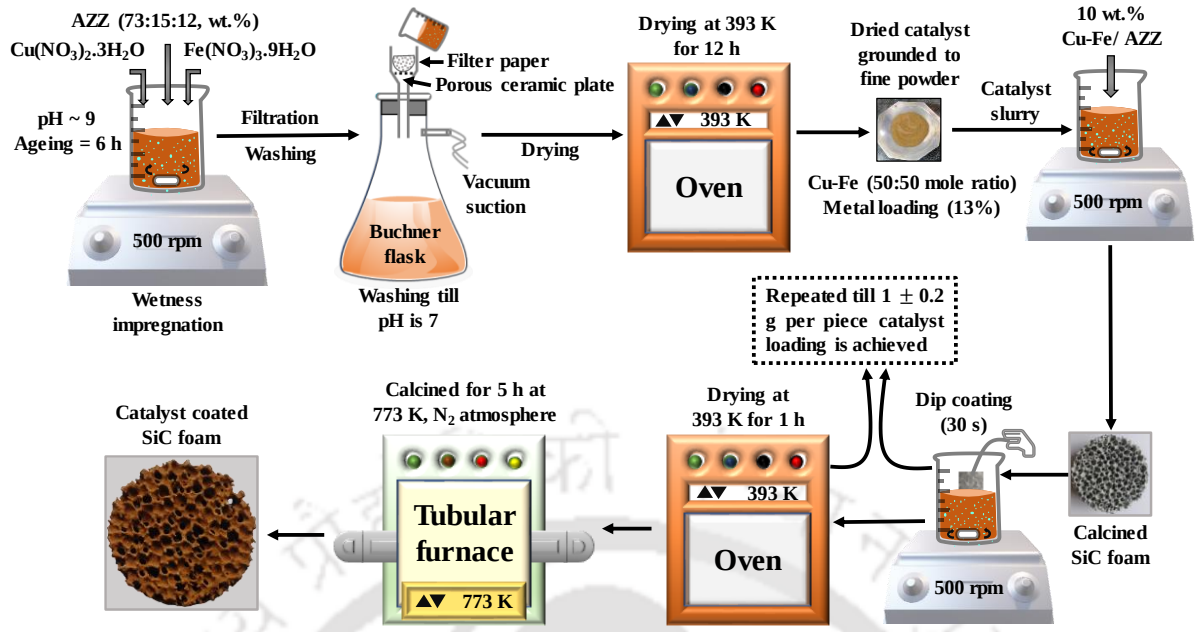

Figure 5. 1. Schematic of Cu-Fe/AZZ catalyst preparation methodology and its coating over the SiC foam.

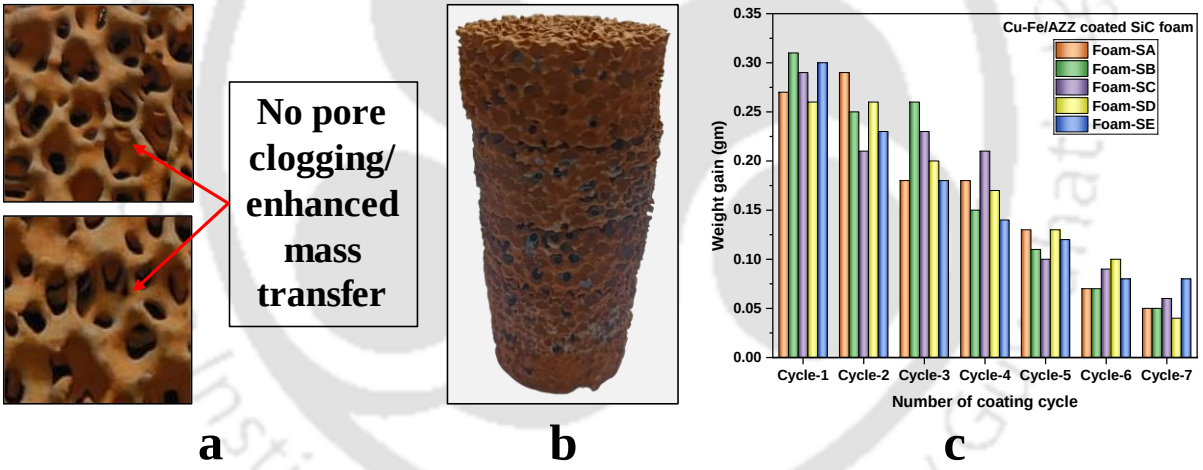

Figure 5. 2. Cu-Fe/AZZ coated SiC foam (a) without any relevant pore-clogging phenomena, (b) multiple catalysts used for the present study, and (c) weight gain as a function of the number of coating cycles for five different foams.

Table 5. 1. The total amount of catalyst loading on different SiC foam used in the present study after seven coating cycles.

Name	Catalyst weight (g)	Catalyst weight after testing (g)	Name	Catalyst weight (g)	Catalyst weight after testing (g)
Foam-SA	1.17	1.06	Foam-SI	0.94	0.80
Foam-SB	1.2	1.11	Foam-SJ	1.15	0.95
Foam-SC	1.19	0.96	Foam-SK	0.91	0.79
Foam-SD	1.16	1.03	Foam-SL	0.81	0.67
Foam-SE	1.13	0.94	Foam-SM	1.15	0.86
Foam-SF	1.01	0.88	Foam-SN	1.18	--
Foam-SG	1.18	0.97	Foam-SO	1.09	--
Foam-SH	1.03	0.86	Foam-SP	1.01	--

5.2.2. Characterization Technique for Catalyst and Coated SiC-Scaffold

The catalyst that was synthesized underwent characterization using several techniques, including scanning electron microscopy (SEM), energy-dispersive X-ray spectroscopy (EDS), and Brunauer-Emmett-Teller (BET) analysis. The catalyst underwent characterization at several phases of its preparation, including after-support preparation, metal loading, reduction, and testing. This study examines the development of catalysts and the changes that occur at different phases of preparation in a comparative manner. In addition, the SiC foam is analyzed using SEM and EDS at four distinct stages of its preparation: raw SiC (post-cleaning), after oxidation at 1173 K, after Cu-Fe/AZZ coating, and after testing (with catalyst).

In order to observe the surface morphology of the support and catalyst prepared, a scanning electron microscope (SEM, Nanoeye-SEM, Make: SEC-e-beam pioneer, Model: SNE-ALPHA, Serial No.: APH-089CD79) analysis was performed at various stages of preparation including fresh support, after metal loading, after reduction, and after testing. Additionally, the change in the surface characteristics of the SiC foam after cleaning, oxidation, catalyst coating (seven cycles), and testing was studied to observe any visible changes as a result of the different steps involved. This investigation ultimately facilitated the comprehension of the microscopic alteration in the catalyst preparation and its coating over the SiC foam. For instance,

agglomeration resulting from sintering at elevated temperatures and pore blocking due to coke deposition can be noticeable.

Energy-dispersive spectroscopy (EDS, FESEM with OXFORD EDS, Make: Zeiss, Model: Sigma) technique was used to determine the elemental composition of the support and catalyst. Additionally, the mapping of the elements over the support and catalyst is performed to ensure a uniform distribution. A similar study was also performed for SiC foam coated with Cu-Fe/AZZ catalyst at different stages of synthesis. This method allows for the observation of any changes in the elemental composition that may occur prior to and following the testing process, which is essential for the catalyst to maintain consistent performance. This way any trace of coke formation during the reaction process as a result of methanol decomposition can be noticed.

To assess the surface area of the catalyst at various stages of catalyst preparation and testing, we conducted a Brunauer–Emmett–Teller (BET) analysis using the Meso 112 instrument from Altamira Instruments Inc. In addition, the pore volume was calculated using the Barrett–Joyner–Halenda (BJH) model based on N_2 adsorption-desorption isotherms at a temperature of 77 K. The degassing process was carried out at a temperature of 523 K for a duration of 2 hours. This study helped to determine the surface area, pore volume, and pore diameter which are critical parameters to affect the performance of the catalyst. It is important to acknowledge that higher surface areas can improve the spreading of active metal phases, ensure the even distribution of metal particles, and result in better catalytic activity.

5.2.3. DSMR Design for Hydrogen Generation and Purification

The entire study was performed in a double-stage membrane reformer (Chemito Technologies Pvt. Ltd.) where a membrane reformer (ID = 90 mm, height = 400 mm, and number of membranes = 6) is integrated with a multi-pass membrane separator (MPMS, ID = 100 mm, height = 300 mm, number of membranes = 10, and longitudinal baffles = 3) having four passes to recover more hydrogen from the retentate of the membrane reformer as shown in Figure 5.3. Both MR and MPMS are made with Inconel-800 to allow the study at elevated temperatures. The MR is equipped with a 2-zone electrically operated split furnace (Durga Technology Corporation, Model: DTC-EF-7080, Maximum operating temperature = 1173 K) with independent temperature control to maintain the different temperatures required for MSR and H_2 permeation through the membrane. On the other hand, MPMS is facilitated with a single-zone heating furnace (Durga Technology Corporation, Model: DTC-EF-7100,

maximum operating temperature = 1173 K). Grundfos diaphragm pump (DDA, Model: A9772194210002028P11714) is used to supply feed (methanol-water mixture) to the reformer at a constant volume rate. The feed is first pumped to the vaporizer (operating temperature = 673 K) and then the pre-vaporized feed enters the pre-heater (operating temperature = 673 K) where the feed is mixed with the carrier gas before entering the reformer (N_2, Aalborg mass flow controller, Model: GFC-17, flow rate range 0 to 2 l min^{-1}). The K-type thermocouple was used to measure and control the required temperature. Following the reaction, the unreacted methanol and water were condensed using a condenser, while the reformated gas was separated using a gas-liquid separator (GLS). TESCOM (Model: 14-2363-24) backpressure regulator (BPR) was used to maintain the desired pressure inside the DSMR for the particular study. The composition of reformate and permeate gas was analyzed using gas chromatography (CENTURION SCIENTIFIC, Model: CS-5770) equipped with a thermal conductivity detector (TCD) and two columns including a Molecular-sieve and a Porapak-Q for gas separation. The gaseous product from the MR was further routed to MPMS for leftover hydrogen recovery. The entire operating parameters were digitally controlled with the help of SCADA software provided by Chemito Technologies Pvt. Ltd.

In each experiment, a catalyst bed with a height of 250 mm is placed in the lower section of the MR, while the membrane is suspended from the upper flange above the catalyst bed. The membranes were prepared using the electroless plating technique over the porous alumina tubular support (I.D. = 7 mm, O.D. = 10 mm,50 mm long) with 23% porosity provided by M/s Kumar Ceramics Pvt Ltd., India. Initially, the support was cleaned and modified with 2B graphite leading to reduce the surface roughness and pore size required to deposit a thin selective layer for hydrogen separation. Thereafter, the support was activated with Pd-nuclei using the traditional sensitization ($SnCl_2$)/activation ($PdCl_2$) process as mentioned by Mardilovich et al. [52]. Finally, $Pd_{85}Ag_{15}$ (85 wt.% Pd and 15 wt.% Ag) dense selective metallic layer was simultaneously deposited. The membrane was further annealed and polished before assembling to the SS-fitting using an in-house graphite ferrule as shown in Figure 5.4 (a). Several membranes, depicted in Figure 5.4 (b), were prepared employing the same methodology aforementioned for the present study. The DSMR was subsequently evaluated and optimized using these membranes after the preliminary leakage test. The side and top view of the membrane arrangement on the upper flange in MPMS is presented in Figure 5.4 (c). Two separate baffles were fitted in the bottom flange to create four passes to offer a better gas-contacting pattern with the membrane.

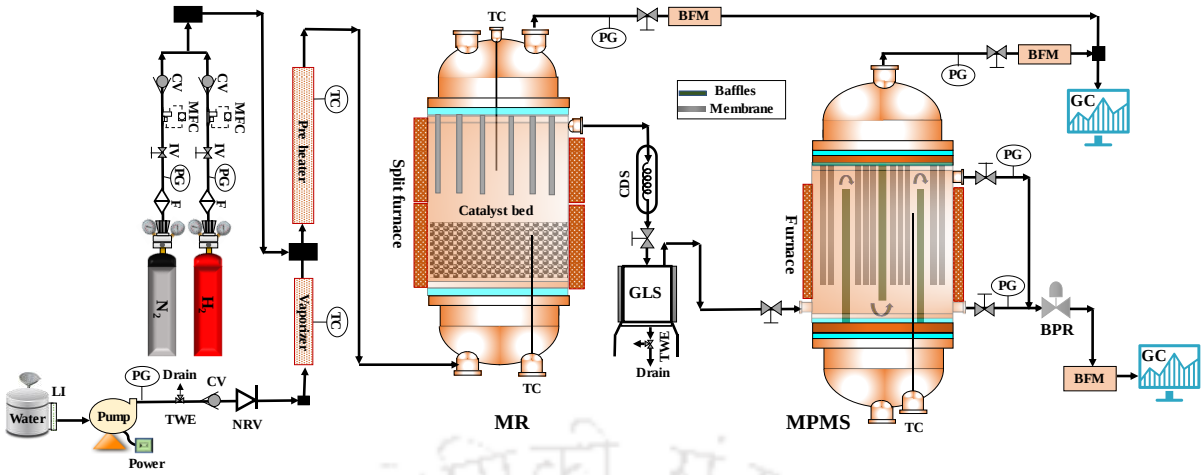

F = Filter, **CV** = Check valve, **LI** = Level indicator, **TC** = Thermocouple (K-type), **PH** = Pre-heater, **IV** = Isolation valve, **PG** = Pressure gauge, **NV** = Needle valve, **GC** = Gas chromatography, **BFM** = Bubble flow meter, **BPR** = Back pressure regulator, **MFC** = Mass flow controller, **TWV** = Two way valve, **NRV** = Non return valve, **GLS** = Gas liquid separator, **CDS** = Condenser

Figure 5. 3. Schematic of double-stage membrane reformer (DSMR).

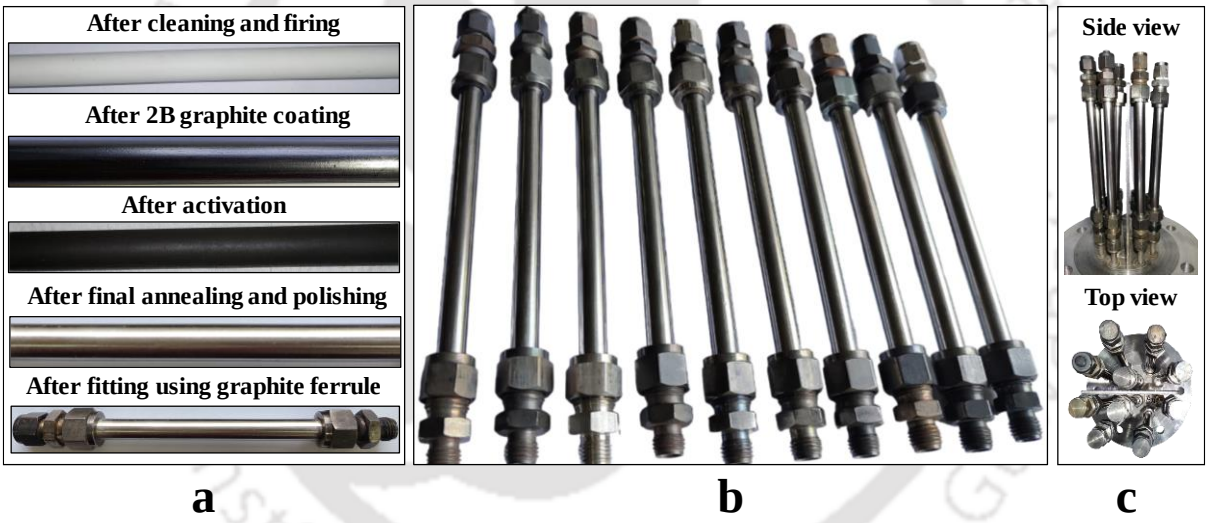

Figure 5. 4. (a) Different stages of membrane preparation, (b) visual representation of multiple membranes prepared using ELP, and (c) side and top view of membranes fitted in the flange for testing.

5.2.4. Catalytic Activity Testing and Performance Optimization of DSMR

The performance of the DSMR was experimentally investigated at different temperatures (573-673 K), pressures (100-400 kPaG), WHSV as defined in Equation 5.4, and varying membrane areas. Throughout the study steam-to-carbon ratio as defined in Equation 5.5 was maintained at 3 which was earlier optimized for membrane reformer by Richa et al. [16,39]. The performance was then evaluated based on the various parameters including methanol

conversion, permeate H_2 yield, H_2 production rate, permeate purity, and H_2 recovery which are defined from Equation 5.6 to Equation 5.10 respectively. Before performing the experiment the catalyst was reduced for 2 hours at 723 K using H_2/N_2 mixture gas (1:1 vol.%, 500 ml min^{-1}). The desired temperature was achieved under pure N_2 used as internal standard gas at ambient pressure (500 ml min^{-1}, heating rate of 3 K min^{-1}) both for reformer and MPMS. Once the temperature was reached the N_2 flow rate was lowered to 50 ml min^{-1} to use as carrier gas during testing. Every experiment under the particular operating condition was performed at least 5 times at intervals of 20 minutes each to ensure consistency in the result. The retentate stream of the reformer was cooled down using a condenser while the gas and condensed methanol-water mixture was successively separated using the gas-liquid separator. The product gas composition of the retentate and permeate (under dry state) was analyzed in GC. The catalyst was regenerated after each series of the experiment. The unseparated retentate stream under dry conditions is then routed to the MPMS to recover more hydrogen. The MPMS temperature was consistently kept at 673 K for all the sets of experimental studies including different pressures and feed flow rates as studied for the reformer part. The permeate side was always maintained at 100 kPa for both MR and MPMS. In the current study, no sweep gas was utilized on the permeate side for the purpose of facilitating testing at the laboratory scale. However, in industrial-scale systems, steam can be employed to decrease the partial pressure of H_2 and retrieve pure hydrogen through condensation. Prior to the studies, the performance of individual membranes was assessed in terms of hydrogen permeation flux and selectivity using pure H_2 and N_2 as given in Table 5.2. The membrane surface area was increased by adding more membranes according to the feed load. Once the testing was concluded the entire system was cooled down to room temperature under pure N_2 (500 ml min^{-1}) at ambient pressure. At last, the thermal stability testing for 50 hours was performed, during which the methanol conversion and overall permeate purity were monitored. The testing was conducted under the operating conditions of 673 K, 300 kPaG, S/C = 3, and WHSV = 12.23 $kg_{feed}\ h^{-1}\ kg^{-1}_{catalyst}$.

$$\text{Weight hourly space velocity } (kg_{feed}\ h^{-1}\ kg^{-1}_{catalyst}) = \frac{\text{Mass flow rate of the feed}}{\text{Mass of the catalyst}} \tag{5.4}$$

$$\text{Steam: Carbon (S/C)} = \frac{\text{Moles of steam in the feed}}{\text{Moles of carbon in feed}} \tag{5.5}$$

$$\text{Methanol conversion (\%)} = \frac{F(H_2)_{retentate} + F(H_2)_{permeate}}{3 \times F(CH_3OH)_{feed}} \times 100 \tag{5.6}$$

$$\text{Permeate hydrogen yield } (Y_{H_2}) = \frac{F(H_2)_{permeate}}{3 \times F(CH_3OH)_{feed}} \times 100 \tag{5.7}$$

$$\text{Hydrogen production rate (mol h}^{-1}\text{ kg}^{-1}_{\text{catalyst}}) = \frac{F(H_2)_{\text{retentate}} + F(H_2)_{\text{permeate}}}{\text{Mass of catalyst}} \quad (5.8)$$

$$\text{Permeate purity (\%)} = \frac{F(H_2)_{\text{permeate}}}{\text{Total molar flow rate of all the gases in the permeate}} \times 100 \quad (5.9)$$

$$\text{Hydrogen recovery (\%)} = \frac{F(H_2)_{\text{permeate}}}{F(H_2)_{\text{retentate}} + F(H_2)_{\text{permeate}}} \times 100 \quad (5.10)$$

where $F(H_2)_{\text{retentate}}$ is the molar flow rate of hydrogen in the retentate, $F(H_2)_{\text{permeate}}$ is the molar flow rate of hydrogen in the permeate, and $F(CH_3OH)_{\text{feed}}$ is the molar flow rate of methanol in the feed.

Table 5. 2. Molar H_2 flux and H_2/N_2 perm-selectivity of the prepared Pd-Ag membranes using pure hydrogen and nitrogen at 300 kPaG and 673 K.

Serial No.	H_2 flux (mol m^{-2} s^{-1})	H_2/N_2 perm-selectivity	Serial No.	H_2 flux (mol m^{-2} s^{-1})	H_2/N_2 perm-selectivity
M1	0.197	2797	M9	0.263	3195
M2	0.185	3248	M10	0.221	3596
M3	0.251	4013	M11	0.221	3062
M4	0.196	3869	M12	0.200	3041
M5	0.212	4020	M13	0.235	3182
M6	0.249	4498	M14	0.212	2808
M7	0.235	4439	M15	0.248	3613
M8	0.200	3349	M16	0.249	4211

5.3. Results and Discussion

Initially, the performance of the MR is evaluated with varying operational conditions such as WHSV, temperature, pressure, and membrane area. At last, the effect of adding MPMS is examined under the same operating conditions. The evaluation of the performance of the integrated DSMR is conducted by considering several key parameters including overall conversion, permeate hydrogen yield, H_2 production rate, hydrogen recovery, overall permeate H_2 purity, and long-term thermal stability.

5.3.1. SEM, EDS, and BET Analysis of Cu-Fe/AZZ Catalyst

In order to observe the surface morphology of the prepared catalyst at different stages of its preparation and testing, SEM analysis was performed. The corresponding digital image of the catalyst is also given for visual representation. Figure 5.5 (a) shows the SEM analysis of the fresh γ-Al_2O_3 used as the base support for catalyst preparation. The mesoporous commercial γ-Al_2O_3 was used to pertaining to its high surface area. The morphology was characterized by lumpy textures consisting of clusters of anhedral maro-crystallites that were formed during the initial crushing and were present on the surface. Zinc and zirconia were further doped to prepare the alumina-zinc-zirconia as given in Figure 5.5 (b). SEM analysis of AZZ reveals that the high doping concentrations of Zn and Zr resulted in the nucleation and growth of particles thereby forming dopant clusters. Zn helps to enhance the copper dispersion and Zr suppresses the formation of CO during MSR. Moreover, Zr enhances thermal stability and inhibits the transformation to alpha alumina at elevated temperatures [33,53]. After Cu and Fe deposition the support turned reddish-brown as presented in Figure 5.5 (c). This is primarily attributed to the electronic transition of metal oxides involving CuO (Cu^{2+}) and Fe_2O_3 (Fe^{3+}). The SEM image displays the existence of agglomerates and colloidal particles of Cu and Fe oxides with asymmetric structure after the process of calcination. Several small particles get self-agglomerated to form a bigger particle. Before performing the experiments, the catalyst was reduced which visually appears as dark gray as given in Figure 5.5 (d). This is probably due to the formation of the metallic Cu^0 (gray) and Fe^0 (silvery gray) after reduction. Moreover, the potential formation of Cu-Fe alloy also exhibits a dark gray to black appearance. According to the SEM image large amount of Cu-particle was observed on the surface of γ-Al_2O_3 after reduction. After testing the catalyst appeared dark brown as shown in Figure 5.5 (e) which may be due to the presence of a mixture of metallic Cu and Fe as well as its oxides. Additionally, the powder catalysts turned into lumped form with various sizes after testing. This fact is

attributed to the agglomeration of the catalyst at elevated temperatures. Since the testing was performed at an elevated temperature (573 K), therefore it is anticipated that the Cu and Fe particles can migrate and coalesce leading to the phenomena of sintering. Multiple reduction-oxidation cycles during the reaction lead to a repeated change in the size and mobility. Consequently, the metal particle grows and agglomerates. Coke formation also contributed to the encapsulation of the metal particle by carbon, thereby forming a cluster of metal particles.

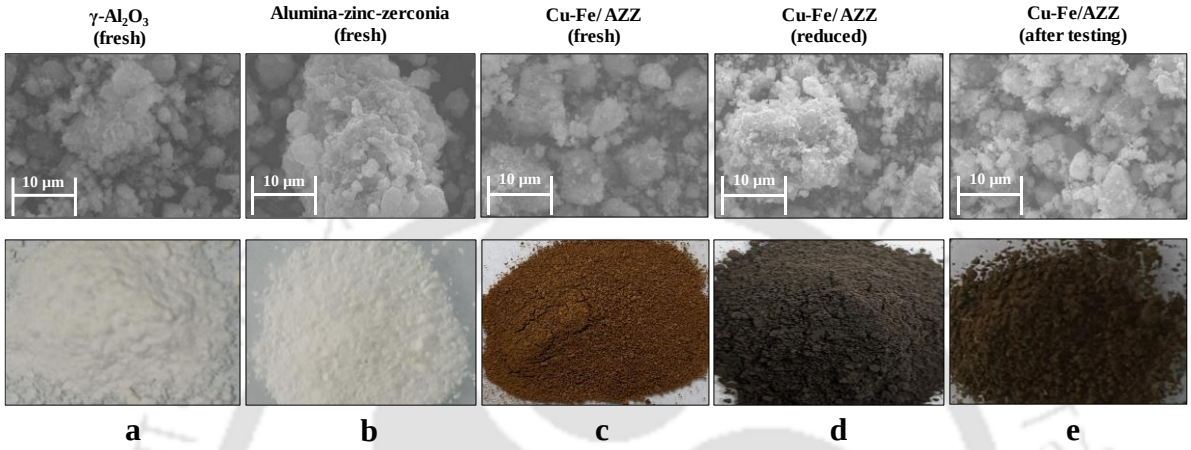

Figure 5. 5. SEM and the digital image of different stages of the catalyst cu-Fe/AZZ catalyst preparation (a) fresh γ-Al_2O_3, (b) fresh AZZ, (c) Cu-Fe/AZZ catalyst, (d) catalyst after reduction, and (e) recovered catalyst after testing.

Figure 5.6 presents the N_2 adsorption-desorption isotherm of the catalyst at different stages of preparation and testing. These include fresh γ-Al_2O_3 support, γ-Al_2O_3 support after Zn and Zr doping, fresh Cu-Fe/AZZ catalyst, Cu-Fe/AZZ catalyst after reduction, and Cu-Fe/AZZ catalyst after testing. It was observed that the γ-Al_2O_3 support and AZZ have similar adsorption isotherms which correspond to Type IV with type H1 hysteresis loop [39,54]. The isotherm and hysteresis revealed the mesoporous characteristics of the support and the presence of cylindrical channels with non-uniform shapes or sizes. The catalyst developed exhibited a shift from Type-IV to Type-V in its N_2 adsorption-desorption isotherm, following a type H3 hysteresis loop. This behavior is identified in solids composed of agglomerated particles containing slit-shaped pores. The comparison of the catalyst's isotherm before and after testing reveals the existence of enlarged pore size and reduced specific surface area. Table 5.3 shows that the doping of metals including Zn, Zr, Cu, and Fe over the support consistently reduced specific surface area as a result of pores clogging. For instance, the BET surface area of γ-Al_2O_3 reduced from 247.56 m^2 g^{-1} to 192.68 m^2 g^{-1} after Zn and Zr doping which further reduced to 107.68 m^2 g^{-1} after Cu and Fe doping. Furthermore, a similar pattern was noted for

the pore volume and average pore diameter calculated using the Barrett–Joyner–Halenda (BJH) method. The decrease in the pore volume confirms the deposition of metal particles inside the pores as these metal particles settle into the pores, they reduce the available space for gas adsorption. This behavior is associated with the reduction in the concentration of alumina as the primary constituent in the formation of the surface and the partial blockage of pores by metal oxides at the entrance of the narrow pore channels [53]. In fact, after reduction at 773 K, a slight decrease in the pore volume and specific surface area (91.53 m^2 g^{-1}) was observed. As metal particles are reduced, they may grow or relocate within the pore structure, partially blocking some of the pores. This is attributed to the collapse of some small pores at higher temperatures. A further reduction in the pore volume (85.36 m^2 g^{-1}) is observed after testing which is the result of more pore blocking or deposition of fine carbon particles. In addition to that, pore collapse and sintering at high temperatures for prolonged testing also contributed to the decrease in the specific surface area and pore volume [55,56].

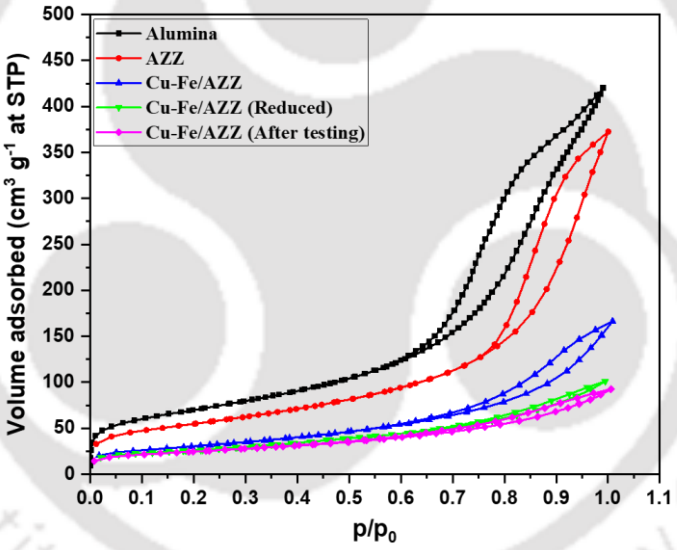

Figure 5. 6. BET N_2 adsorption-desorption isotherm of support and Cu-Fe/AZZ catalyst at different stages of preparation and testing.

Table 5. 3. BET surface area, pore volume, and average pore diameter of support and Cu-Fe/AZZ catalysts at different stages of preparation.

Sample	S_{BET} ($m^2\ g^{-1}$)	Pore volume ($cm^3\ g^{-1}$)	Average pore diameter (nm)
γ-alumina	247.56	0.648	10.47
AZZ	192.68	0.552	11.46
Cu-Fe/AZZ	107.91	0.237	8.76
Cu-Fe/AZZ (Reduced)	91.53	0.154	6.72
Cu-Fe/AZZ (After testing)	85.36	0.135	6.34

Before performing the experiment the Cu-Fe/AZZ catalyst was coated over the SiC foam using the wash coating method. After cleaning the SiC foam the surface appears to be quite rough with a lot of craters as seen in Figure 5.7 (a). These sites actually serve as the locations for uniform powder catalyst coating and adherence. Figure 5.7 (b) shows that the entire surface was covered with the catalyst powder after seven coating cycles. The surface texture was similar to the original SEM image of the catalyst after preparation. However, some parts of the SiC foam were partially coated as appeared in the SEM image. This is apparently due to the difference in the surface texture at various locations in terms of catalyst deposition sites. After testing some loss of catalyst, particle agglomeration, and sintering at high temperatures is observed in Figure 5.7 (c). Catalysts turned into lumped form with various sizes after testing. Moreover, some parts of the SiC foam skeleton visually appeared empty having a significant loss of catalyst. This behavior is mostly attributed to the weak adherence of the catalyst particle over the surface after multiple cycles of testing. In addition to that, performance testing at higher WHSV possibly eroded loosely adhered catalysts. The overall gravimetrical loss in the catalyst weight after testing is reported in Table 5.1. The loss in the catalyst weight ranged from 0.13 g to 0.29 g per piece of SiC foam. Once the testing was concluded, the catalyst was recovered under ultrasonic irradiation for 2 hours in DI water for further characterization after drying at 393 K. The SEM image of the recovered SiC foam is presented in Figure 5.7 (d). Under the given reaction condition at high temperatures, the SiC foam surface may undergo etching resulting in surface deformation. Moreover, the formation of a SiO_2 layer was also observed due to the reaction of steam with SiC foam. However, the formation of the SiO_2 layer decreases the thermal conductivity of the SiC foam which increases with the increase in the SiO_2 layer thickness [57]. The porous SiO_2 structure was clearly visible over the surface with micro-scale size irregularly shaped pores.

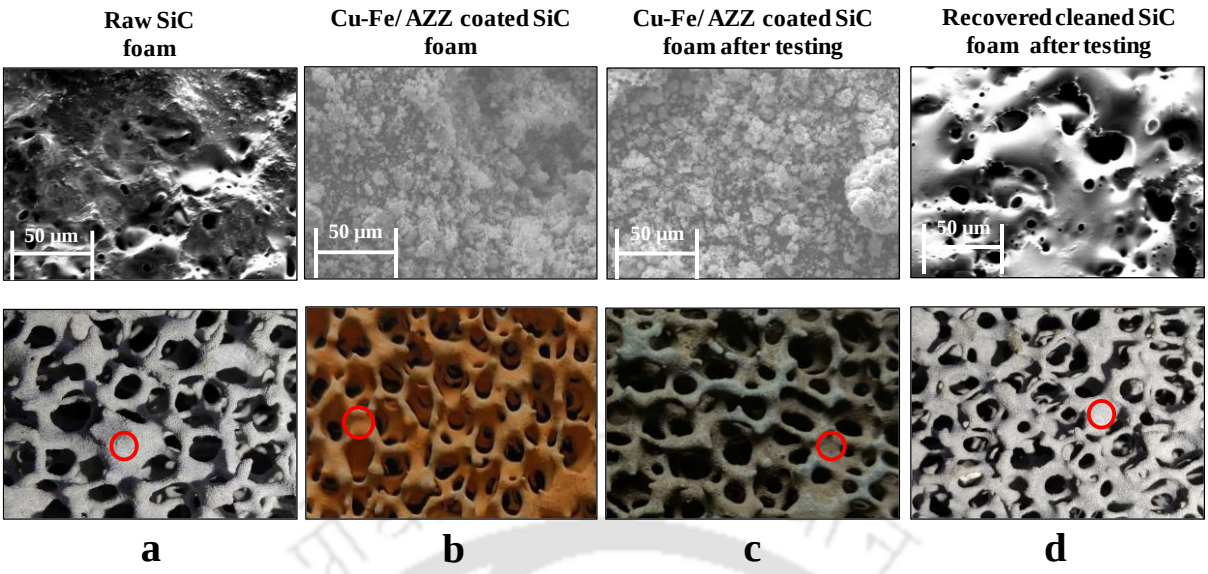

Figure 5. 7. SEM and the digital image of different stages of the catalyst coating over SiC foam (a) raw SiC foam after cleaning, (b) SiC foam after Cu-Fe/AZZ coating, (c) SiC foam after testing, and (d) recovered SiC foam after cleaning.

Table 5.4 presents the elemental composition of SiC foam and catalyst at various stages of its preparation. Quantitative analysis of EDS data verifies the presence of all active metals on the corresponding catalysts. EDS analysis of the SiC foam after cleaning shows a significant amount of the constituent elements including Al, Si, C, Na, and Ca. After catalyst coating the EDS analysis of the coated SiC foam was performed which shows an elemental composition similar to the catalyst. No other peaks were observed which shows that the entire surface was fully covered with the catalyst. Figure 5.8 (a) shows the respective elemental mapping of different metals doped. A uniform dispersion of dopant elements including Zn, Zr, Cu, and Fe is observed. After testing an increase in the Si and C peaks was seen. This is mostly attributed to the erosion of some amount of catalyst from the surface. In addition to that, coke deposition during the testing also contributed to the increase in the carbon content. Analysis of the catalyst's elemental composition following testing verifies the existence of a minor quantity of coke deposition, as depicted in Figure 5.8 (b). A heterogeneous carbon distribution was detected on the surface of the catalyst. Although the coke deposition is observed in mapping, its composition in the bulk of the catalyst might not be sufficient to be registered by EDS (due to the low X-ray signal for the EDS detector which is below the detection limit). While elemental mapping can visually capture carbon deposits, EDS might not detect them due to limitations in sensitivity [56]. Therefore, it is expected that there are a lot of active metal particles are still present inside the catalyst. Once the SiC foam was cleaned after testing, no

trace of the catalyst was observed on the surface. However, a significant change in the surface composition is seen due to its exposure to the reaction environment during testing. The presence of steam may result in the formation of SiO_2 due to hydrothermal degradation where SiC can react with water vapor at high temperatures. Consequently, an increase in the silicon and oxygen content is observed. Nevertheless, somewhat higher carbon content is observed, maybe due to the carburization reaction at high temperatures between SiC and CO (formed due to RWGS reaction in MSR) causing carbon deposition on the surface. Coke production during MSR also played a role in the rise of carbon content that might have remained adsorbed within the pores on the surface [57].

Table 5. 4. Elemental compositions of Cu-Fe/AZZ catalyst and SiC foam at different stages of preparation and testing using EDS.

Sample	Elemental composition (wt. %)									
	Cu	**Fe**	**Al**	**Zn**	**Zr**	**O**	**C**	**Si**	**Na**	**Ca**
Raw SiC foam	--	--	20.58	--	--	54.10	1.83	18.67	3.14	1.66
Cleaned SiC foam (after testing)	--	--	8.79	--	--	60.6	3.37	21.47	4.98	1.05
Cu-Fe/AZZ catalyst	7.4	8.8	25.2	11.5	9.5	37.6	--	--	--	--
Cu-Fe/AZZ coated SiC foam	7.0	8.2	27.8	13.9	5.2	38	--	--	--	--
Cu-Fe/AZZ catalyst (after testing)	6.9	6.4	28.0	12.1	4.4	42.2	00.0	--	--	--

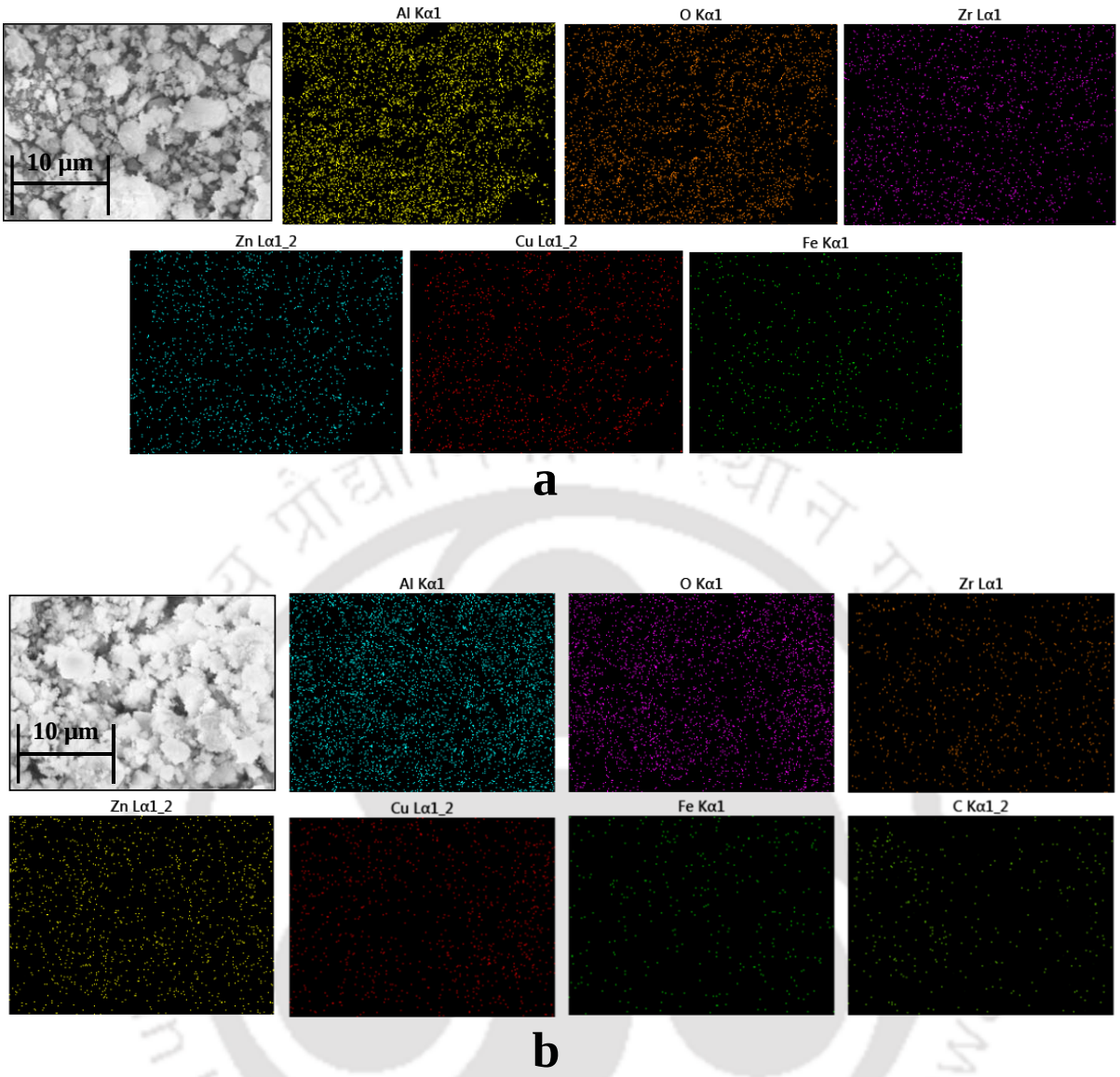

Figure 5. 8. Respective SEM image of Cu-Fe/AZZ catalyst (a) before testing and (b) after testing along with the EDS elemental mapping image of Al, O, Zr, Zn, Cu, Fe, and C.

5.3.2. Effect of Temperature on the MSR in DSMR

Temperature is the primary factor that substantially affects the rate of reaction of MSR, conversion efficiency of the reactor, and overall hydrogen production rate. The negative effect on the H_2 permeation caused by the adsorption of CO and steam over the Pd-Ag membrane surface is more prominent at temperatures below 673 K and a pressure range of 100-300 kPaG. The endothermic nature of MSR means that elevated temperatures enhance hydrogen production, which is further facilitated by the continual permeation of H_2 via membranes. However, at elevated temperatures, more CO formation is anticipated as a result of methanol decomposition and RWGS reaction. Therefore, a balanced trade-off between the shift effect

due to hydrogen permeation and the RWGS reaction is required to optimize the temperature. Figure 5.9 (a) shows the DSMR performance in terms of CH_3OH conversion, H_2 recovery, and H_2 production rate at different temperatures while maintaining other parameters such as S/C = 3, ΔP = 300 kPaG, membrane area = 495 cm^2, and WHSV = 12.23 kg_{feed} h^{-1} $kg^{-1}_{catalyst}$ constant. As the temperature is increased from 523 K to 673 K the overall CH_3OH conversion increases from 70.39% to 94.93% whereas the H_2 recovery improved by 8% in the same temperature range. Additionally, the H_2 production rate increased from 300 to 404.58 mol h^{-1} $kg^{-1}_{catalyst}$. Increased temperature correlates with elevated hydrogen permeability, facilitating a greater volume of hydrogen to permeate through the membrane, hence improving hydrogen recovery. As a result, there is a shift in the thermodynamic equilibrium in accordance with Le Chatelier's principle, leading to an increase in CH_3OH conversion [26]. Obviously, the same trend was observed in the case of the permeate H_2 yield which increased from 54.67% to 80.44% in the same temperature range as shown in Figure 5.9 (b). More importantly, it is noteworthy to mention that the H_2 purity increased with temperature. This behavior is ascribed to the increased H_2 permeation across the membrane. Nonetheless, regarding permeate purity, all experimental tests recorded an average H_2 level exceeding 99.2% (vol. %, dry basis).

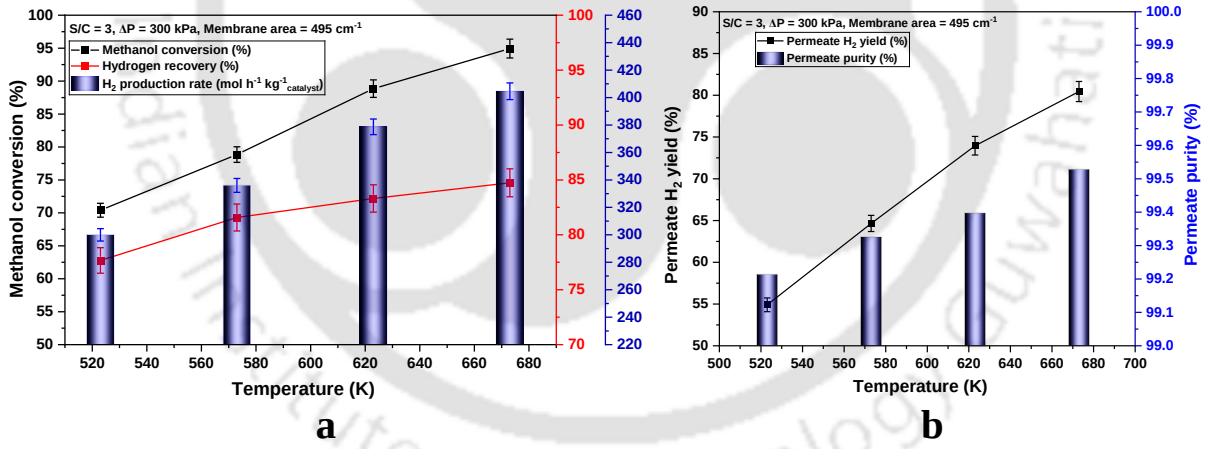

Figure 5. 9. (a) Methanol conversion, H_2 recovery, and H_2 production rate and (b) permeate H_2 yield, and permeate purity as a function of temperature using Cu-Fe/ AZZ catalyst and $Pd_{85}Ag_{15}$ at WHSV of 12.23 kg_{feed} h^{-1} $kg^{-1}_{catalyst}$.

5.3.3. Effect of Pressure on the MSR in DSMR

An increase in pressure influences traditional and membrane reformers differently. Increasing the pressure on the traditional reformer leads to a reduction in CH_3OH conversion because of the thermodynamic constraints associated with the stoichiometry of the MSR process. The rise

in moles within the retentate leads to a reduction in conversion, whereas in the membrane reformer, this adverse effect is mitigated by the favorable effect of H_2 permeation via the Pd-Ag membrane, which improves CH_3OH conversion. The combination of these two opposing effects ultimately enhances the overall methanol conversion by removing a large amount of H_2 from the retentate, promoting the MSR towards the product side, and offsetting the thermodynamic limitations of the traditional reformer. Figure 5.10 (a) shows the DSMR performance in terms of CH_3OH conversion, H_2 recovery, and H_2 production rate at different pressures while maintaining other parameters such as S/C = 3, temperature = 673 K, membrane area = 495 cm^2, and WHSV = 12.23 $kg_{feed}\ h^{-1}\ kg^{-1}_{catalyst}$ constant. As the pressure is increased from 50 kPaG to 300 kPaG the overall CH_3OH conversion increases from 66.30% to 94.93% whereas the H_2 recovery improved by almost 10% in the same pressure range. Additionally, the H_2 production rate increased from 282.55 to 404.58 mol $h^{-1}\ kg^{-1}_{catalyst}$ as the overall reaction is driven toward the desired production formation. As a result of the availability of more hydrogen in the feed side the H_2 partial pressure increased which is reflected in the form of an increase in the permeate H_2 yield as depicted in Figure 5.10 (b). The permeate H_2 flux is governed by Sieverts' law, where the driving force is directly proportional to the square root of the H_2 partial pressure present on the feed side of the membrane. The H_2 recovery shows a rapid increase at first, followed by a gradual rise as the partial pressure of hydrogen on the feed side increases. This behavior is attributed to the negative effect of CO and CO_2 on the H_2 permeation via the membrane [58]. According to the Sieverts-Langmuir equation proposed by Barbieri et al. [59], The H_2 permeation is inversely related to the partial pressure of carbon monoxide, signifying that carbon monoxide is detrimental to hydrogen permeation. A minimal quantity of CO production can significantly impact hydrogen permeation. The diffusion of CO, governed by microporous diffusion, is directly proportional to the partial pressure difference of CO raised to the first power. The deviation from Sieverts' law is also the result of concentration polarization caused by the presence of other gases. The formation of the boundary layer near the membrane surface further restricted the transport of H_2 from the bulk of the retentate to the membrane surface [60]. This can be clearly observed in the permeate purity graph which decreases with an increase in the pressure as shown in Figure 5.10 (b). The permeate purity decreased from 99.95% at 50 kPaG to 99.52% at 300 kPaG. At the same time, the CO concentration also increased in the permeate from 0.02% to 0.09% when the pressure was increased from 200 kPaG to 300 kPaG. Nevertheless, at reduced pressure, no CO concentration was detected on the permeate side. It can be posited that at elevated pressures,

the augmentation of CO diffusion due to pressure rise surpasses that of hydrogen diffusion. While the CO flux is also rising, it is negligible compared to the increase in hydrogen flux.

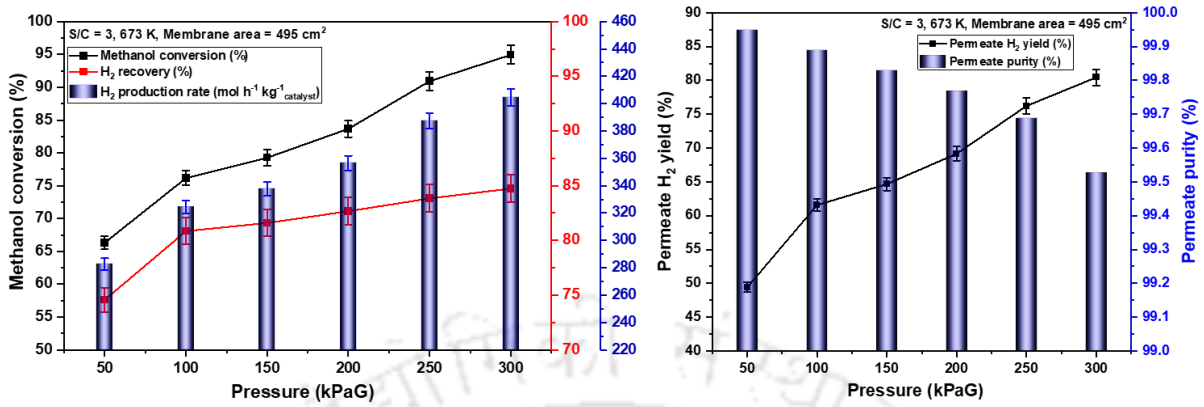

Figure 5. 10. (a) Methanol conversion, H_2 recovery, and H_2 production rate and (b) permeate H_2 yield, and permeate purity as a function of pressure using Cu-Fe/ AZZ catalyst and $Pd_{85}Ag_{15}$ at WHSV of 12.23 kg_{feed} h^{-1} $kg^{-1}_{catalyst}$.

5.3.4. Effect of WHSV on the MSR in DSMR

At lower WHSV, the gas has an extended contact duration with the catalyst, enhancing methanol conversion; conversely, at greater WHSV, the reduced contact time between reactants and catalyst diminishes methanol conversion. An extended residence period facilitates the reaction's progression toward equilibrium. Figure 5.11 (a) shows the DSMR performance in terms of CH_3OH conversion, H_2 recovery, and H_2 production rate at different WHSV while maintaining other parameters such as S/C = 3, temperature = 673 K, membrane area = 495 cm^2, and ΔP = 300 kPaG constant. As the WHSV increased from 2.45 to 48.92 kg_{feed} h^{-1} $kg^{-1}_{catalyst}$ the overall CH_3OH conversion decreased from 99.03% to 63.36% whereas the H_2 recovery reduced by almost 11% in the same WHSV range. Additionally, the H_2 production rate significantly increased from 84.41 to 1080 mol h^{-1} $kg^{-1}_{catalyst}$ as the overall reaction is driven toward the desired production formation. Even though the methanol conversion decreased with the increasing WHSV, it was maintained above 90% for the WHSV below 12.23 kg_{feed} h^{-1} $kg^{-1}_{catalyst}$. Thereafter a sharp decline in the conversion was observed with increasing WHSV. The initial decrease in the conversion is low because of the gradual increase in the H_2 recovery till 12.23 kg_{feed} h^{-1} $kg^{-1}_{catalyst}$. The increase in H_2 recovery partially compensated for the decrease in the methanol conversion with increasing WHSV. However, beyond the given limit both H_2 recovery and methanol conversion decreased with WHSV, which means that the effect of the feed flow rate dominated over the shift effect of the membrane reformer. Increasing the WHSV helped to minimize the effect of concentration

polarization caused by the competitive adsorption of CO over the Pd-Ag membrane and thinning the mass transfer boundary layer near the membrane surface. Consequently, the H_2 recovery increased with the WHSV up to a certain limit. When the WHSV exceeds 12.23 kg_{feed} h^{-1} $kg^{-1}_{catalyst}$, the permeate H_2 flux attains its saturation point, indicating that any further increase in WHSV will not enhance hydrogen recovery; instead, a significant portion of H_2 will be lost in the retentate stream, resulting in a substantial reduction in hydrogen recovery [58,61]. The ideal purification of the Pd-Ag membrane was attained at a WHSV of 12.23 kg_{feed} h^{-1} $kg^{-1}_{catalyst}$ catalyst for the gas mixture, yielding the maximum hydrogen recovery of 84.73% and a CO concentration in the permeate of 0.09%. Similar behavior was also observed in the case of permeate H_2 yield as depicted in Figure 5.11 (b), which shows that the permeate H_2 yield decreased from 74.91% to 40.84% in the same WHSV range aforementioned. As a result of the availability of more hydrogen on the feed side the H_2 partial pressure increased, therefore more H_2 permeated through the membrane resulting in improved H_2 yield. This phenomenon was visible till the WHSV of 12.23 kg_{feed} h^{-1} $kg^{-1}_{catalyst}$. However, the increase in the WHSV reduced the contact time of the product gases with the membrane surface, hence the H_2 recovery and permeate H_2 yield declined sharply. In order to maximize hydrogen recovery and permeate hydrogen yield, a WHSV of 12.23 kg_{feed} h^{-1} $kg^{-1}_{catalyst}$ is the best choice for further study. In addition to this, the permeate purity increased from 99.37% at 2.45 kg_{feed} h^{-1} $kg^{-1}_{catalyst}$ to 99.78% at 48.92 kg_{feed} h^{-1} $kg^{-1}_{catalyst}$ as shown in Figure 5.11 (b). At the same time, the CO concentration also decreased in the permeate from 0.16% to 0.06%. Augmenting the WHSV creates turbulence near the membrane's surface, so diminishing the adsorption of CO and consequently lowering the quantity of CO permeating through the membrane. Furthermore, CO diffusion through the membrane via defects and/or pinholes at the same pressure differential exhibits minimal reduction at elevated WHSV [62].

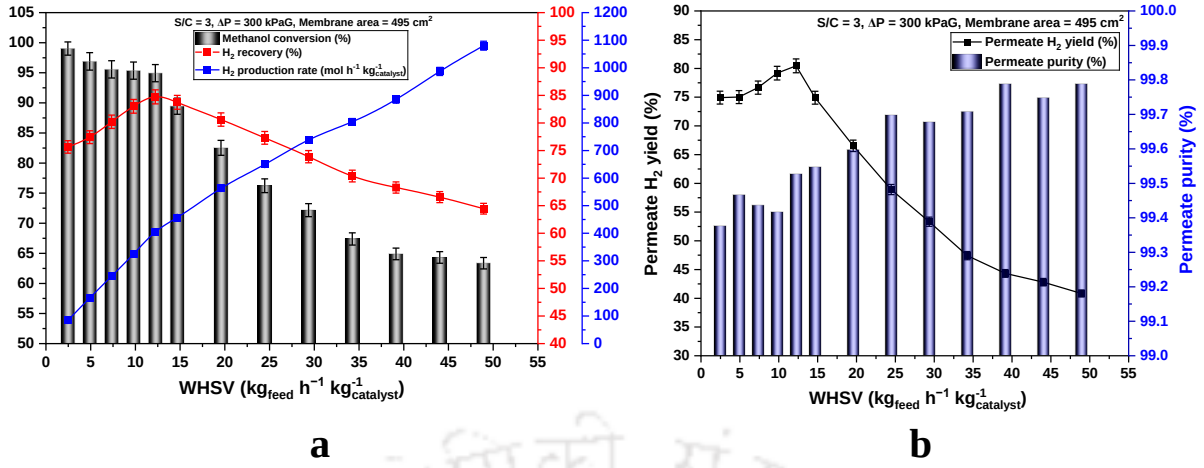

Figure 5. 11. (a) Methanol conversion, H_2 recovery, and H_2 production rate and (b) permeate H_2 yield, and permeate purity as a function of WHSV using Cu-Fe/ AZZ catalyst and $Pd_{85}Ag_{15}$.

5.3.5. Effect of Pd-Ag Membrane Area on the MSR in DSMR

The augmentation of the Pd-Ag membrane surface area in MSR markedly improves methanol conversion and hydrogen recovery. This enhancement is attributed to the increased surface available for hydrogen permeation, which in turn elevates separation efficiency. With a constant WSHV, increasing the membrane areas enhances the separation of hydrogen, resulting in improved hydrogen recovery. Nevertheless, as WSHV is increased, the duration of contact between methanol and the catalyst diminishes, leading to a decrease in overall reaction efficiency and a reduction in both methanol conversion and hydrogen recovery, despite the presence of larger membrane areas. This is related to the decrease in the hydrogen production rate, thereby the reduced H_2 partial pressure. Consequently, although expanding the membrane area alleviates the adverse effects of elevated WSHV to a degree, the overall efficiency is still constrained by the reduced residence time associated with increased feed flow rates. This study is conducted to optimize the membrane area concerning the increasing WHSV [58]. Figures 5.12 (a) and Figure 5.12 (b) depict the performance metrics of DSMR, in terms of methanol conversion and hydrogen recovery as functions of membrane area under different WSHV. The enhancement of methanol conversion and hydrogen recovery is observed with an increase in membrane area; however, both metrics exhibit a decrease as WSHV rises. At the maximum membrane area (0.05 cm²), methanol conversion reaches ~95% and hydrogen recovery ~85% for the lowest WSHV (12.23 kg_{feed} h^{-1} $kg^{-1}_{catalyst}$), while at the highest WSHV (48.92 kg_{feed} h^{-1} $kg^{-1}_{catalyst}$), conversion drops to ~75% and recovery to ~65%. This emphasizes the importance

of the balance between WSHV and membrane area for improved performance, where increased membrane areas and reduced WSHVs result in greater efficiency. While it is expected that the influence of concentration polarization will decrease with higher WHSV, thereby enhancing hydrogen permeation, the negative impact of reduced contact time of the product gas with the membrane prevails, ultimately resulting in a reduction of the permeate H_2 flux [58,61].

It is noteworthy that the methanol conversion and H_2 recovery exhibit saturation at elevated surface areas when subjected to lower WHSV conditions. This phenomenon primarily results from the interplay between kinetic and thermodynamic constraints within the process. Under conditions of low WHSV, the contact time of reactants with the catalyst is high, allowing the reaction to approach its equilibrium limit. The methanol conversion attains its thermodynamic equilibrium, indicating that additional increases in membrane area don't improve conversion, as the reaction rate is no longer the limiting factor. As the reaction nears equilibrium, the driving force for hydrogen permeation diminishes, resulting in a saturation effect in hydrogen recovery [63,64]. Figure 5.13 (a) illustrates that the hydrogen production rate diminishes at reduced WHSV, indicating a lower availability of hydrogen for permeation across the same membrane area. At this stage, the level of concentration polarization is at its peak, hindering the movement of H_2 molecules from the bulk product to the membrane surface. This step is crucial in the solution-diffusion mechanism for H_2 permeation through Pd-Ag-based membranes. However, at higher WHSV, the conversion of methanol is constrained by the kinetics of the reaction instead of equilibrium limitations. However, at higher WHSV, the methanol conversion is limited by reaction kinetics rather than equilibrium constraints, meaning increasing membrane area provides a continuous improvement in hydrogen recovery by removing hydrogen and shifting the reaction forward (Le Chatelier's principle). The short contact time prevents the system from reaching equilibrium, so there is no saturation. Instead, the membrane's ability to selectively remove hydrogen becomes the dominant factor [65]. Furthermore, the linear trend for increased WHSV noted for the permeate H_2 yield, as illustrated in Figure 5.13 (b), indicates that the membrane retains the ability to permeate additional hydrogen, with the influence of concentration polarization being negligible. The diminished concentration polarization, however, was significantly influenced by the limited contact time of the product gas with the membrane, which contributed to the decreased H_2 recovery.

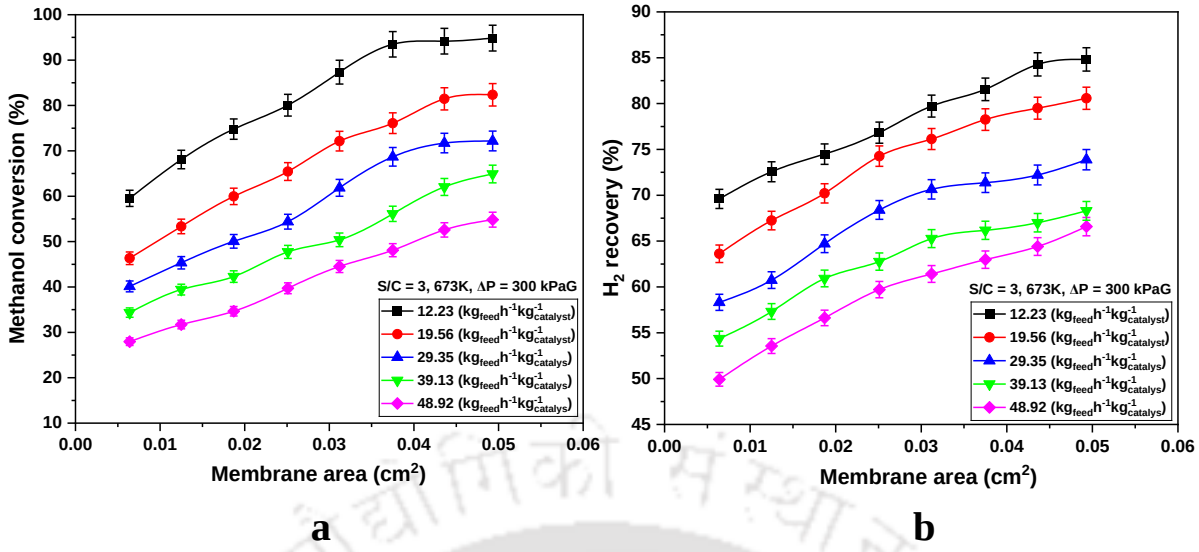

Figure 5. 12. (a) Methanol conversion and (b) H_2 recovery as a function of the membrane area using Cu-Fe/ AZZ catalyst and $Pd_{85}Ag_{15}$ at various WHSV.

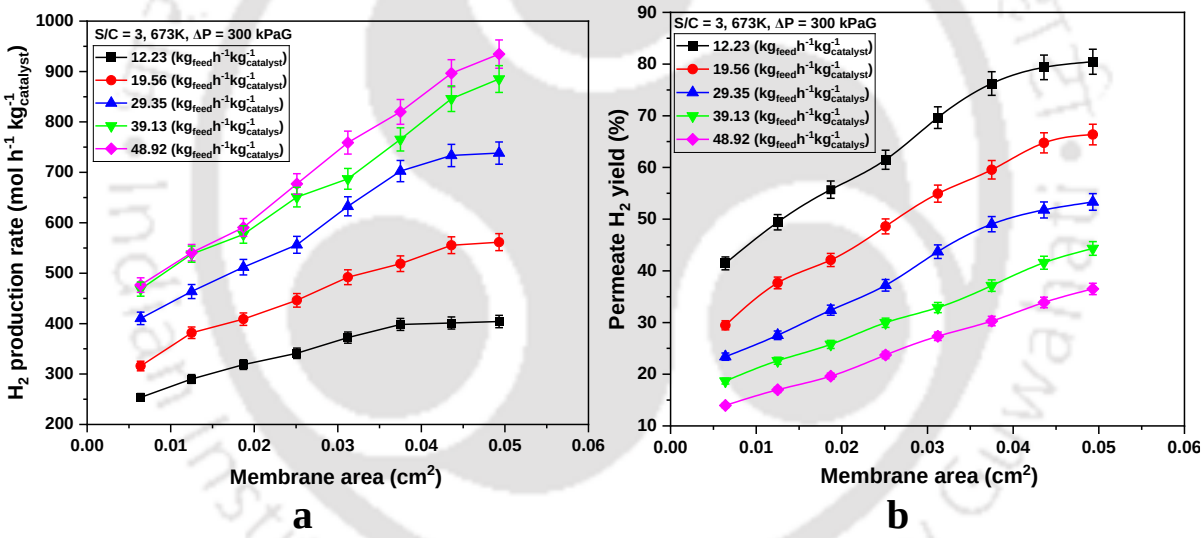

Figure 5. 13. (a) H_2 production rate and (b) permeate H_2 yield as a function of pressure using Cu-Fe/ AZZ catalyst and $Pd_{85}Ag_{15}$ at various WHSV.

5.3.6. Thermal Stability and Overall Permeate Purity Testing of DSMR

The thermal stability of both the catalyst and the membrane in a membrane reformer designed for hydrogen production via methanol steam reforming is essential for maintaining long-term operational efficiency and performance. Extended exposure to elevated temperatures can result in catalyst sintering, which subsequently diminishes the active surface area and decreases methanol conversion efficiency. Pd-Ag membranes exhibit susceptibility to thermal stress, embrittlement, and fouling, factors that can lead to a decline in hydrogen selectivity and purity

as time progresses. Consequently, ongoing assessment of thermal stability is crucial to avert performance degradation and maintain consistent hydrogen recovery and purity. Figure 5.14 shows the catalytic stability test of the DSMR based on H_2 recovery (%), permeate purity (%), and CH_3OH conversion (%) for 50 hours at 673 K, 300 kPaG, and WHSV of 12.23 $kg_{feed}\ h^{-1}\ kg^{-1}_{catalyst}$. The methanol conversion initiates at around 95% during the initial phase (0–2 hours) and swiftly escalates to 98%. The methanol conversion further exhibited stability over an extended duration of 2 to 30 hours, with minor fluctuations observed between 97% and 98%. This consistency suggests reliable catalyst performance and optimal reaction conditions. After a duration of 30 hours, a gradual decrease in methanol conversion is noted, falling from 98% to approximately 90% by the conclusion of the 50-hour operational period. The observed decline is likely due to catalyst deactivation mechanisms, including fouling, coking, or poisoning, which progressively diminish the efficiency of methanol steam reforming over time [30]. The recovery of H_2 demonstrated a steady increase from 84.9% to 88% over the initial 12-hour period, indicating that a substantial fraction of the hydrogen generated is successfully permeated through the membrane. The H_2 recovery subsequently stabilized and exhibited minimal variation throughout the remaining period. The preliminary rise in H_2 recovery can be attributed to the gradual activation of the membrane, which is necessary to achieve a consistent permeation capacity. The phenomenon represents a unique feature of the Pd-Ag-based membrane system, frequently referred to as "permeation stabilization". The behavior observed can primarily be linked to the swift infiltration of hydrogen atoms into the Pd-Ag lattice, which then occupy the lattice sites, thereby facilitating further permeation. Nonetheless, the ongoing permeation of H_2 leads to the saturation of lattice sites with hydrogen atoms, ultimately achieving a state of equilibrium. The hydrogen concentration at this stage is consistently uniform throughout both the upstream and downstream areas of the membrane, leading to a stabilization of the permeate H_2 flux [66,67]. Additionally, it was observed that the purity of the H_2 permeate remained above 99.9% and exhibited stable performance throughout the initial 25 hours of operation. The observed purity level suggests that the membrane operates effectively, permitting the passage of hydrogen while excluding contaminants such as CO and CO_2. Subsequently, the purity of the permeate H_2 exhibited a gradual decline throughout the remaining, continuing until the 50-hour mark, and reflecting a pattern akin to that of methanol conversion. After 50 hours, the purity of H_2 diminishes to around 98%. This decline can be linked to a decrease in hydrogen partial pressure resulting from reduced methanol conversion and possible membrane fouling, which decreases selectivity and permits a greater influx of impurities through pin-holes [68].

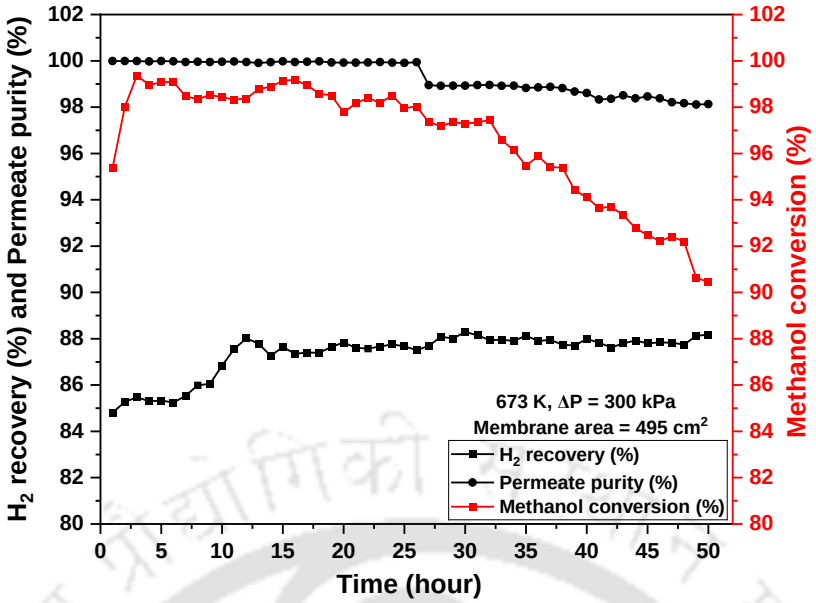

Figure 5. 14. Catalytic stability test of the DSMR based on H_2 recovery (%), permeate purity (%), and CH_3OH conversion (%) for 50 hours at WHSV of 12.23 kg_{feed} h^{-1} $kg^{-1}_{catalyst}$.

5.4. Comparison between the MR and DSMR Configuration

The evaluation of TR, MR, and DSMR is essential for assessing performance, refining reactor design, and progressing hydrogen production methods. TR acts as the reference point but is constrained by its inability to separate hydrogen, which affects its overall efficiency. MR improves performance through the incorporation of membranes that facilitate selective hydrogen extraction, whereas DSMR reaches optimal efficiency with its dual-stage setup, allowing for enhanced conversion rates due to the removal of H_2 in two separate stages. Figure 15 (a) illustrates the comparison of TR, MR, and DSMR based on the methanol conversion with increasing WHSV at an S/C ratio of 3, 673 K, ΔP = 300 kPaG, and a total membrane area of 187 cm^2. A total of six membranes were selected for this study, as the design constraints of the MR component allow for the accommodation of only six membranes. During the evaluation of the DSMR performance, these membranes were equally distributed between the MR and MPMS. The DSMR consistently achieves the highest conversion, followed by MR and then TR. At the lowest WHSV (12.23 $kg_{feed}\ h^{-1}\ kg^{-1}_{catalyst}$), DSMR achieves ~75% conversion, whereas MR and TR respectively were able to achieve a conversion of ~57% and ~53%. However, at elevated WHSV (48.92 $kg_{feed}\ h^{-1}\ kg^{-1}_{catalyst}$) the conversion was observed to be very low such as 31%, 32%, and 34% for TR, MR, and DSMR respectively. Furthermore, the alteration in the conversion rate was also diminished in comparison to the observations made at a comparatively lower WHSV. In this scenario, a significant portion of the reactant traverses the catalyst bed without undergoing any reaction. The saturation observed in the permeation capacity of the membrane for both MR and DSMR also played a significant role in this phenomenon [69]. Notwithstanding this, the DSMR persists in exhibiting its exceptional performance attributed to the improved hydrogen separation across both stages. The rate of hydrogen production exhibits an increase with the WHSV, as illustrated in Figure 15 (b). This is attributed to the elevated methanol feed rates, even though there is a corresponding decrease in conversion. Increased WHSV is expected to minimize the impact of concentration polarization; however, the short interaction time of the product gases with the membrane results in decreased hydrogen recovery and permeate H_2 yield, as illustrated in Figure 15 (c) and Figure 15 (d) respectively. At lower WHSV it is observed that the difference in the H_2 recovery and permeate H_2 yield for MR and DSMR were more compared to higher WHSV. For instance, H_2 recovery increased by 8.5% in DSMR compared to MR at 12.23 $kg_{feed}\ h^{-1}\ kg^{-1}_{catalyst}$ whereas an increase of merely 2% was observed at 48.92 $kg_{feed}\ h^{-1}\ kg^{-1}_{catalyst}$. Similarly, the respective changes in the permeate H_2 yield were 18% and 1.9%. Consequently, DSMR demonstrates

superior performance compared to MR and TR in terms of methanol conversion and hydrogen production rates. The dual-stage configuration facilitates enhanced hydrogen separation and promotes equilibrium shifting [17].

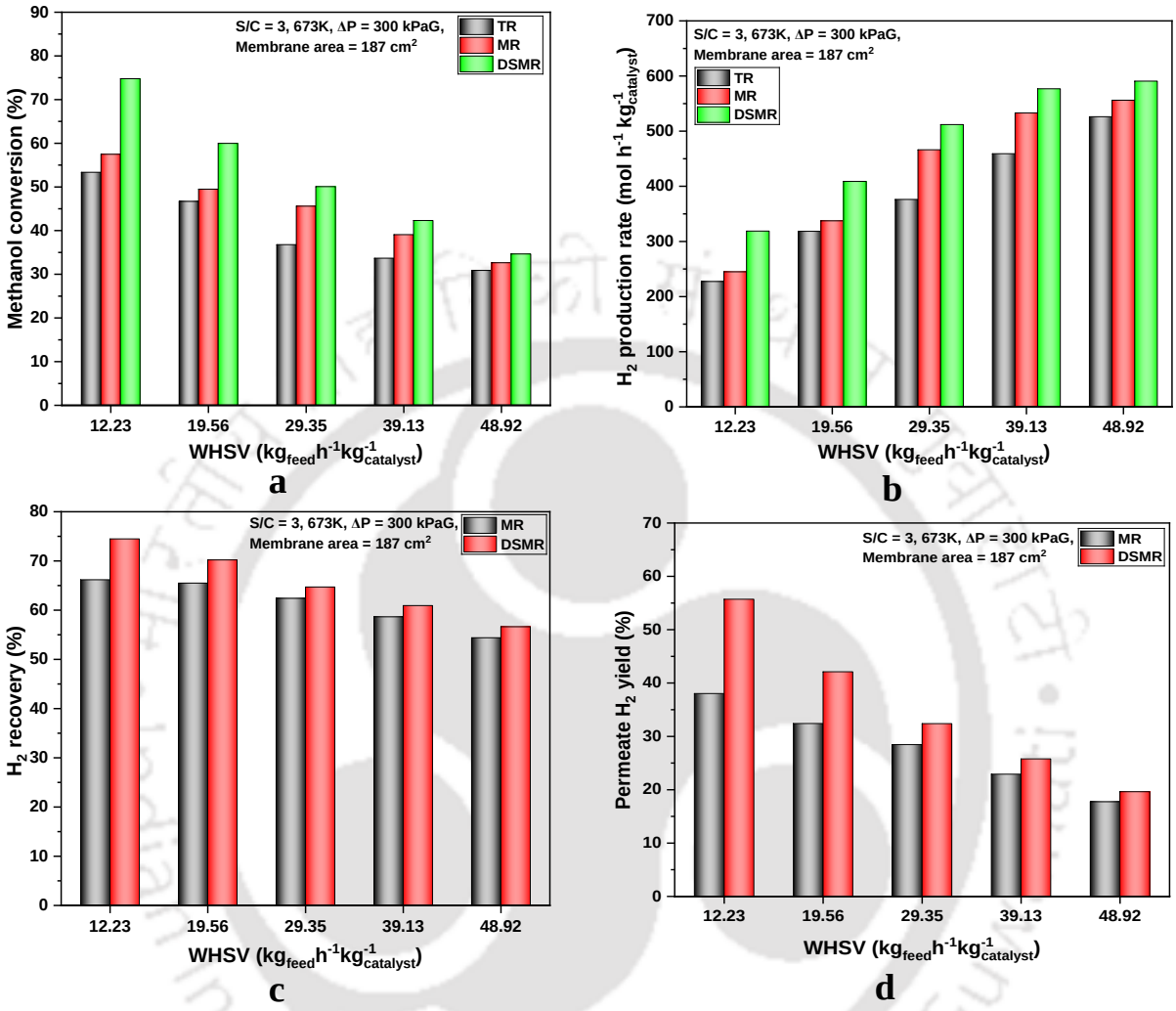

Figure 5. 15. Comparison of TR, MR, and DSMR based on (a) methanol conversion, (b) H_2 production rate, (c) H_2 recovery, and (d) permeate H_2 yield as a function of increasing WHSV.

The activity of the prepared Cu-Fe/AZZ coated over SiC foam in the present study shows superior performance compared to the similar reported data in the literature. However, there are only few similar studies are available in the literature on two stage membrane reformer. For instance, in this study the methanol conversion of ~75 % and H_2 recovery of more than 74.5% is achieved in the case of DSMR at 300 kPaG of pressure, 673 K of temperature, 3/1 of S/C ratio, 187 cm^2 of membrane area, and 12.23 kg_{feed} h^{-1} $kg^{-1}_{catalyst}$ of WHSV. In a similar study, Falco et al. [17] performed the experimental analysis of steam reforming of natural gas over an

Rh-Pt/Al_2O_3 coated SiC foam-based catalyst. They achieved a conversion of 57.3% which is 26% more than the same traditional reformer at 873 K. SiC foam helped to improve the thermal transport property of the catalyst bed as well where at least an improvement of 20 K in the temperature on the membrane side is reported compared to packed bed. In another study, Morico et al. [46] investigated the performance of the membrane reformer at the KT-Kinetics Technology pilot plant designed for pure H_2 production. The plant design consists of a pre-reformer where the methane conversion is accomplished, thereafter the unconverted methane and syngas are routed to the membrane reformer unit for further conversion and H_2 separation. The latter membrane reformer section is designed in a tube-in-tube configuration with bifunctional Ni-noble/SiC-foam-based catalysts in the annular section around the membrane tube. They achieved 60% feed conversion at a temperature of 813 K, pressure of 850 kPaG, and S: C ratio of 4. However, they were able to recover only 70% of the produced H_2 (permeate H_2 flow rate = 3.5 N m^3 h^{-1}). From the same research group, Franchi et al. [25] numerically compared three configurations for methane steam reforming for hydrogen production i.e. SR, MR, and RMM. They achieved an overall methane conversion of 92% with two reactors and membrane modules and hydrogen recovery of 88% for RMM configuration. This way they predicted 30% higher conversion could be achieved compared to SR. Iluianelli et al. [27] in a separate study designed a two-stage laboratory-scale hydrogen production system through biogas consisting of the MR and an additional membrane separator at the retentate of MR. They achieved 99% of CH_4 conversion (S/C = 2, feed pressure = 350 kPa, and 673 K) and 40% of CO_x-free H_2 recovery in Stage 1. Thereafter the retentate is sent to Stage 2 to recover more H_2 at the same temperature and pressure. For the integrated system, they were able to recover 67% of the 99.9% pure hydrogen contained in the retentate. Following the same study, Ruales et al. [26] experimentally investigated the effectiveness of SR of biogas and/or biomethane integrated with a membrane separator for hydrogen generation. In the SR stage, they got 60% and 40 % of CH_4 conversion in the case of biomethane and biogas respectively, at 873 K, 100 kPa, and S/C = 4. Upon the integration of the membrane separator as the second stage, they achieved hydrogen recovery of 90% and 88% for biomethane and biogas respectively while obtaining 99.9999% of H_2 purity in each case at 773 K and ΔP = 250 kPa. Most recently, Cerone et al. [47] developed a multi-stage WGS reactor consisting of two parallel Pd-Ag membrane reactors and two separator membrane separators in the initial stage. The entire system is set up to generate 0.25 N m^3 h^{-1} of hydrogen gas with high purity. At a temperature of 623 K, a pressure of 800 kPa, and S/C of 4, they successfully obtained a carbon monoxide conversion rate of 97.6%. In addition, the combination of a membrane reactor and a separator

resulted in a 12% increase in H_2 recovery. From the above discussion, it can be said that achieving conversion and H_2 recovery of more than 75% for MSR in DSMR is a significant achievement at moderate temperature and pressure having high feed load of 12.23 kg_{feed} h^{-1} $kg^{-1}_{catalyst}$ of WHSV. At the maximum membrane area (0.05 cm^2), methanol conversion reaches ~95% and hydrogen recovery ~85% for the lowest WSHV (12.23 kg_{feed} h^{-1} $kg^{-1}_{catalyst}$), while at the highest WSHV (48.92 kg_{feed} h^{-1} $kg^{-1}_{catalyst}$), conversion drops to ~75% and recovery to ~65% in the current investigation. Moreover, the present study, gives the flexibility to adjust the number of membranes in MPMS as per the requirement to further enhance the DSMR performance.

5.5. Summary

The main scope of this study is to design an integrated double-stage membrane reformer that incorporates both MR and MPMS, functioning as a standalone separation module, to effectively separate the unrecovered H_2 from the retentate stream of the MR. Furthermore, our objective is to improve the radial heat and mass transfer characteristics of the packed bed catalyst by employing an interconnected 3D SiC scaffold, attributed to its superior thermal conductivity. To achieve this, the SiC scaffold was coated with the Cu-Fe/AZZ catalyst used for MSR. After the loading of 1 ± 0.2 gm of catalyst per piece of SiC foam, marginal or no change in the weight gain was observed gravimetrically. This indicates that the entire surface of the SiC foam was effectively coated with the Cu-Fe/AZZ catalyst powder, a process that typically required five to seven cycles of coating. To separate hydrogen multiple $Pd_{85}Ag_{15}$ membranes were employed in both MR and MPMS. The performance of the DSMR was optimized at different temperatures (573 to 673 K), pressures (100 to 300 kPaG), WHSV (12.23 to 48.92 $kg_{feed}\ h^{-1}\ kg^{-1}_{catalyst}$), and varying membrane areas (65 to 495 cm^2). The Cu-Fe/AZZ/SiC catalyst was tested in all three configurations for comparison including TR, MR, and DSMR at 300 kPaG of pressure, 673 K of temperature, 3/1 of S/C ratio, 187 cm^2 of membrane area, and 12.23 $kg_{feed}\ h^{-1}\ kg^{-1}_{catalyst}$ of WHSV. Following the performance testing a higher methanol conversion is obtained in the case of DSMR. For instance, the methanol conversion of ~75 % is achieved in the case of DSMR compared to ~57% in MR and ~53% in TR. Moreover, H_2 recovery of more than 74.5% is achieved in DSMR which is 8.5% higher compared to MR. The structured SiC scaffold coated with Cu-Fe/AZZ catalyst intensified the radial heat and mass transfer inside the reformer. Further, the integration of MPMS on the retentate side of the MR significantly helped to recover the leftover hydrogen from the retentate of the MR. Therefore, the DSMR configuration demonstrated superior performance compared to MR and TR in terms of methanol conversion and hydrogen production rates. The dual-stage configuration facilitated enhanced hydrogen separation and promoted equilibrium shifting. The forthcoming research will concentrate on creating a power generation system that integrates DSMR with low-temperature proton exchange membrane fuel cells. Various DSMR configurations will be developed, each rated according to power output for diverse applications. Furthermore, the potential for incorporating a CO_2 capture unit will be investigated to mitigate the carbon footprint.

References

[1] United Nations Framework Convention on Climate Change, Paris Agreement (COP-21), Paris, 2015. https://unfccc.int/files/meetings/paris_nov_2015/application/pdf/paris_agreement_english_.pdf?gad_source=1&gclid=CjwKCAjwnK60BhA9EiwAmpHZw2mOvr1a-G1ML0sHwPGw4e3Z1zwMCv_xeeAW5WyL28c_9gtXG3eIWRoCh1cQAvD_BwE.

[2] I. Dincer, C. Acar, Review and evaluation of hydrogen production methods for better sustainability, International Journal of Hydrogen Energy, 40 (2014), pp. 11094–11111.

[3] K.T. Møller, T.R. Jensen, E. Akiba, H. wen Li, Hydrogen - A sustainable energy carrier, Progress in Natural Science: Materials International, 27 (2017), pp. 34–40.

[4] P. Nikolaidis, A. Poullikkas, A comparative overview of hydrogen production processes, Renewable and Sustainable Energy Reviews, 67 (2017), pp. 597–611.

[5] S. Liguori, K. Kian, N. Buggy, B.H. Anzelmo, J. Wilcox, Opportunities and Challenges of Low-Carbon Hydrogen via Metallic Membranes, Progress in Energy and Combustion Science, 80 (2020), pp. 100851.

[6] Z. Du, C. Liu, J. Zhai, X. Guo, Y. Xiong, W. Su, G. He, A review of hydrogen purification technologies for fuel cell vehicles, Catalysts, 11 (2021), pp. 1–19.

[7] S. Yun, S. Ted Oyama, Correlations in palladium membranes for hydrogen separation: A review, Journal of Membrane Science, 375 (2011), pp. 28–45.

[8] H.Y. Do, C.H. Kim, J.Y. Han, H.S. Kim, S.K. Ryi, Low-temperature proton-exchange membrane fuel cell-grade hydrogen production by membrane reformer equipped with Pd-composite membrane and methanation catalyst on permeation stream, Journal of Membrane Science, 634 (2021), pp. 119373.

[9] S. Sharma, S.K. Ghoshal, Hydrogen the future transportation fuel: From production to applications, Renewable and Sustainable Energy Reviews, 43 (2015), pp. 1151–1158.

[10] A. Sánchez, E.C. Blanco, M. Martín, Comparative assessment of methanol and ammonia: Green fuels vs. hydrogen carriers in fuel cell power generation, Applied Energy, 374 (2024), pp. 124009.

[11] D. Teichmann, W. Arlt, P. Wasserscheid, Liquid Organic Hydrogen Carriers as an efficient vector for the transport and storage of renewable energy, International Journal

of Hydrogen Energy, 37 (2012), pp. 18118–18132.

[12] G.D. Berry, J. Martinez-Frias, F. Espinosa-Loza, S.M. Aceves, Hydrogen Storage and Transportation, Encyclopedia of Energy, 3 (2004), pp. 267–281.

[13] J. Andersson, S. Grönkvist, Large-scale storage of hydrogen, International Journal of Hydrogen Energy, 44 (2019), pp. 11901–11919.

[14] M. Rivarolo, D. Bellotti, L. Magistri, A.F. Massardo, Feasibility study of methanol production from different renewable sources and thermo-economic analysis, International Journal of Hydrogen Energy, 41 (2016), pp. 2105–2116.

[15] P. Parvasi, S.M. Jokar, A. Basile, A. Iulianelli, An on-board pure H2 supply system based on a membrane reactor for a fuel cell vehicle: A theoretical study, Membranes, 10 (2020), pp. 1–17.

[16] R. Sharma, A. Kumar, R.K. Upadhyay, Performance comparison of methanol steam reforming integrated to Pd-Ag membrane: Membrane reformer vs. membrane separator, Separation and Purification Technology, 183 (2017), pp. 194–203.

[17] M. De Falco, G. Iaquaniello, A. Salladini, Experimental tests on steam reforming of natural gas in a reformer and membrane modules (RMM) plant, Journal of Membrane Science, 368 (2011), pp. 264–274.

[18] M.A. Achomo, A. Kumar, N.R. Peela, P. Muthukumar, Hydrogen production from steam reforming of methanol: A comprehensive review on thermodynamics, catalysts, reactors, and kinetic studies, International Journal of Hydrogen Energy, 58 (2024), pp. 1640–1672.

[19] A. Arratibel, J.A. Medrano, J. Melendez, D.A. Pacheco Tanaka, M. van Sint Annaland, F. Gallucci, Attrition-resistant membranes for fluidized-bed membrane reactors: Double-skin membranes, Journal of Membrane Science, 563 (2018), pp. 419–426.

[20] V. Palma, M. Martino, A. Ricca, P. Ciambelli, Structured Catalysts and Support for Membrane Reactors, in: G.C. and G.I. Angelo Basile, Marcello De Falco (Ed.), Membrane Reactor Engineering: Applications for a Greener Process Industry, John Wiley & Sons, Ltd, 2016: pp. 37–58.

[21] S. Qian, H. Liu, Y. Wang, D. Mei, Structural optimization of 3D printed SiC scaffold with gradient pore size distribution as catalyst support for methanol steam reforming,

Fuel, 341 (2023), pp. 127612.

[22] P. Yan, Y. Cheng, Foam structured membrane reactor for distributed hydrogen production, Journal of Membrane Science, 661 (2022), pp. 120927.

[23] A. Giaconia, G. Iaquaniello, G. Caputo, B. Morico, A. Salladini, L. Turchetti, G. Monteleone, A. Giannini, E. Palo, Experimental validation of a pilot membrane reactor for hydrogen production by solar steam reforming of methane at maximum 550 °C using molten salts as heat transfer fluid, International Journal of Hydrogen Energy, 45 (2020), pp. 33088–33101.

[24] K.Y. Koo, H.B. Im, D. Song, U. Jung, Ammonia decomposition over Ru-coated metal-structured catalysts for COx-free hydrogen production, International Journal of Hydrogen Energy, 52 (2024), pp. 534–545.

[25] G. Franchi, M. Capocelli, M. De Falco, V. Piemonte, D. Barba, Hydrogen production via steam reforming: A critical analysis of MR and RMM technologies, Membranes, 10 (2020), pp. 1–20.

[26] H. Bryan Trujillo Ruales, A. Spadafora, P. Fiore, J. Veres, A. Caravella, A. Iulianelli, Reformer + Membrane separator plant for decarbonized hydrogen production from Biogas/Biomethane: An experimental study combined to energy efficiency and exergy analyses, Energy Conversion and Management, 315 (2024), pp. 1–12.

[27] A. Iulianelli, A. Brunetti, L. Pino, C. Italiano, G.D. Ferrante, M. Gensini, A. Vita, An integrated two stages inorganic membrane-based system to generate and recover decarbonized H2: An experimental study and performance indexes analysis, Renewable Energy, 210 (2023), pp. 472–485.

[28] C. Wang, J. Weng, M. Liao, Q. Luo, X. Luo, Z. Tian, R. Shu, Y. Chen, Y. Du, Configuration of coupling methanol steam reforming over Cu-based catalyst in a synthetic palladium membrane for one-step high purity hydrogen production, Journal of the Energy Institute, 108 (2023), pp. 101245.

[29] M. Rostami, A.H. Farajollahi, R. Amirkhani, M.E. Farshchi, A review study on methanol steam reforming catalysts: Evaluation of the catalytic performance, characterizations, and operational parameters, AIP Advances, 13 (2023), pp. 030701.

[30] S.T. Yong, C.W. Ooi, S.P. Chai, X.S. Wu, Review of methanol reforming-Cu-based catalysts, surface reaction mechanisms, and reaction schemes, International Journal of

Hydrogen Energy, 38 (2013), pp. 9541–9552.

[31] H. Li, H. Tian, S. Chen, Z. Sun, T. Liu, R. Liu, S. Assabumrungrat, J. Saupsor, R. Mu, C. Pei, J. Gong, Sorption enhanced steam reforming of methanol for high-purity hydrogen production over Cu-MgO/Al2O3 bifunctional catalysts, Applied Catalysis B: Environmental, 276 (2020), pp. 119052.

[32] M. Mrad, C. Gennequin, A. Aboukaïs, E. Abi-Aad, Cu/Zn-based catalysts for H2 production via steam reforming of methanol, Catalysis Today, 176 (2011), pp. 88–92.

[33] F. Ahmadi, M. Haghighi, H. Ajamein, Sonochemically coprecipitation synthesis of CuO/ZnO/ZrO2/Al2O3 nanocatalyst for fuel cell grade hydrogen production via steam methanol reforming, Journal of Molecular Catalysis A: Chemical, 421 (2016), pp. 196–208.

[34] M. Chen, G. Sun, Y. Wang, D. Liang, C. Li, J. Wang, Q. Liu, Steam reforming of methanol for hydrogen production over attapulgite-based zeolite-supported Cu-Zr catalyst, Fuel, 314 (2022), pp. 122733.

[35] N. Iwasa, S. Masuda, N. Ogawa, N. Takezawa, Steam reforming of methanol over Pd/ZnO: Effect of the formation of PdZn alloys upon the reaction, Applied Catalysis A, General, 125 (1995), pp. 145–157.

[36] L.Y. Dolgikh, L.O. Staraya, I.L. Stolyarchuk, Y.I. Pyatnitsky, Low-Temperature Steam Reforming of Ethanol Over Iron Catalysts on Oxide and Carbon Supports, Theoretical and Experimental Chemistry, 56 (2020), pp. 192–198.

[37] L. Chen, C.K.S. Choong, Z. Zhong, L. Huang, T.P. Ang, L. Hong, J. Lin, Carbon monoxide-free hydrogen production via low-temperature steam reforming of ethanol over iron-promoted Rh catalyst, Journal of Catalysis, 276 (2010), pp. 197–200.

[38] A.A. Lytkina, N. V. Orekhova, M.M. Ermilova, S. V. Belenov, V.E. Guterman, M.N. Efimov, A.B. Yaroslavtsev, Bimetallic carbon nanocatalysts for methanol steam reforming in conventional and membrane reactors, Catalysis Today, 268 (2016), pp. 60–67.

[39] R. Sharma, A. Kumar, R.K. Upadhyay, Bimetallic Fe-Promoted Catalyst for CO-Free Hydrogen Production in High-Temperature-Methanol Steam Reforming, ChemCatChem, 11 (2019), pp. 4568–4580.

[40] M. Khzouz, J. Wood, B. Pollet, W. Bujalski, Characterization and activity test of commercial Ni/Al2O3, Cu/ZnO/Al2O3 and prepared Ni-Cu/Al2O3 catalysts for hydrogen production from methane and methanol fuels, International Journal of Hydrogen Energy, 38 (2013), pp. 1664–1675.

[41] P. Mierczynski, K. Vasilev, A. Mierczynska, W. Maniukiewicz, M.I. Szynkowska, T.P. Maniecki, Bimetallic Au-Cu, Au-Ni catalysts supported on MWCNTs for oxy-steam reforming of methanol, Applied Catalysis B: Environmental, 185 (2016), pp. 281–294.

[42] M. Patrascu, M. Sheintuch, On-site pure hydrogen production by methane steam reforming in high flux membrane reactor: Experimental validation, model predictions and membrane inhibition, Chemical Engineering Journal, 262 (2015), pp. 862–874.

[43] A. Giaconia, G. Monteleone, B. Morico, A. Salladini, K. Shabtai, M. Sheintuch, D. Boettge, J. Adler, V. Palma, S. Voutetakis, A. Lemonidou, M.C. Annesini, M. Den Exter, H. Balzer, L. Turchetti, Multi-fuelled Solar Steam Reforming for Pure Hydrogen Production Using Solar Salts as Heat Transfer Fluid, Energy Procedia, 69 (2015), pp. 1750–1758.

[44] M. De Falco, D. Barba, S. Cosenza, G. Iaquaniello, L. Marrelli, Reformer and membrane modules plant powered by a nuclear reactor or by a solar heated molten salts: Assessment of the design variables and production cost evaluation, International Journal of Hydrogen Energy, 33 (2008), pp. 5326–5334.

[45] D. Barba, M. Capocelli, M. De Falco, G. Franchi, V. Piemonte, Mass transfer coefficient in multi-stage reformer/membrane modules for hydrogen production, Membranes, 8 (2018), pp. 1–17.

[46] B. Morico, A. Salladini, E. Palo, G. Iaquaniello, Solar energy assisted membrane reactor for hydrogen production, ChemEngineering, 3 (2019), pp. 1–12.

[47] N. Cerone, F. Zimbardi, L. Contuzzi, S. Tosti, L. Fabbiano, G.D. Zito, M.O. Carnevale, V. Valerio, Pre-pilot scale study of hydrogen production from biomass syngas via water-gas shift in Pd–Ag catalytic membrane reactor and dedicated hydrogen permeation unit, International Journal of Hydrogen Energy, 95 (2024), pp. 1204–1214.

[48] R. Sharma, A. Kumar, R.K. Upadhyay, Characteristics of a multi-pass membrane reactor to improve hydrogen recovery, International Journal of Hydrogen Energy, 46 (2021), pp. 14429–14440.

[49] B. Lindström, L.J. Pettersson, G. Menon, Activity and characterization of Cu/Zn, Cu/Cr and Cu/Zr on γ-alumina for methanol reforming for fuel cell vehicles, Applied Catalysis A: General, 234 (2002), pp. 111–125.

[50] S. Patel, K.K. Pant, Influence of preparation method on performance of Cu(Zn)(Zr)-alumina catalysts for the hydrogen production via steam reforming of methanol, Journal of Porous Materials, 13 (2006), pp. 373–378.

[51] S. Yu, Y. Wang, H. Liu, Q. Wu, D. Mei, Development of centrifugal coating device to load CuZnZr/γ-Al2O3 catalyst on porous substrates for methanol steam reforming, Surface and Coatings Technology, 457 (2023), pp. 129314.

[52] P.P. Mardilovich, Y. She, Y.H. Ma, M.H. Rei, Defect-Free Palladium Membranes on Porous Stainless-Steel Support, AIChE Journal, 44 (1998), pp. 310–322.

[53] C.C. Chang, J.W. Wang, C.T. Chang, B.J. Liaw, Y.Z. Chen, Effect of ZrO2 on steam reforming of methanol over CuO/ZnO/ZrO2/Al2O3 catalysts, Chemical Engineering Journal, 192 (2012), pp. 350–356.

[54] G. Leofanti, M. Padovan, G. Tozzola, B. Venturelli, Surface area and pore texture of catalysts, Catalysis Today, 41 (1998), pp. 207–219.

[55] O.Z. Tajrishi, M. Taghizadeh, A.D. Kiadehi, Methanol steam reforming in a microchannel reactor by Zn-, Ce- and Zr- modified mesoporous Cu/SBA-15 nanocatalyst, International Journal of Hydrogen Energy, 43 (2018), pp. 14103–14120.

[56] H. Shahsavar, M. Taghizadeh, A.D. Kiadehi, Effects of catalyst preparation route and promoters (Ce and Zr) on catalytic activity of CuZn/CNTs catalysts for hydrogen production from methanol steam reforming, International Journal of Hydrogen Energy, 46 (2021), pp. 8906–8921.

[57] E.M. Cepollaro, S. Cimino, L. Lisi, M. Biesuz, B. Santhosh, G.D. Sorarù, Ru/Al2O3 on Polymer-Derived SiC Foams as Structured Catalysts for CO2 Methanation, Catalysts, 12 (2022), pp. 1–12.

[58] J. Shi, Q. Wu, D. Mei, H. Liu, Y. Wang, Development of pure hydrogen generation system based on methanol steam reforming and Pd membrane, International Journal of Hydrogen Energy, 69 (2024), pp. 147–157.

[59] G. Barbieri, F. Scura, F. Lentini, G. De Luca, E. Drioli, A novel model equation for the

permeation of hydrogen in mixture with carbon monoxide through Pd-Ag membranes, Separation and Purification Technology, 61 (2008), pp. 217–224.

[60] A. Caravella, L. Melone, Y. Sun, A. Brunetti, E. Drioli, G. Barbieri, Concentration polarization distribution along Pd-based membrane reactors: A modelling approach applied to Water-Gas Shift, International Journal of Hydrogen Energy, 41 (2016), pp. 2660–2670.

[61] W.H. Chen, M.H. Hsia, Y.H. Chi, Y.L. Lin, C.C. Yang, Polarization phenomena of hydrogen-rich gas in high-permeance Pd and Pd-Cu membrane tubes, Applied Energy, 113 (2014), pp. 41–50.

[62] A.L. Mejdell, M. Jøndahl, T.A. Peters, R. Bredesen, H.J. Venvik, Effects of CO and CO2 on hydrogen permeation through a ~3 μm Pd/Ag 23 wt.% membrane employed in a microchannel membrane configuration, Separation and Purification Technology, 68 (2009), pp. 178–184.

[63] Y. Choi, H.G. Stenger, Kinetics, simulation and optimization of methanol steam reformer for fuel cell applications, Journal of Power Sources, 142 (2005), pp. 81–91.

[64] K. Ghasemzadeh, N. Jafar Harasi, A. Iulianelli, A. Basile, Theoretical evaluation of various configurations of silica membrane reactor in methanol steam reforming using CFD method, International Journal of Hydrogen Energy, 45 (2020), pp. 7354–7363.

[65] T. Chompupun, S. Limtrakul, T. Vatanatham, C. Kanhari, P.A. Ramachandran, Experiments, modeling and scaling-up of membrane reactors for hydrogen production via steam methane reforming, Chemical Engineering and Processing - Process Intensification, 134 (2018), pp. 124–140.

[66] W.M. Tucho, H.J. Venvik, J.C. Walmsley, M. Stange, A. Ramachandran, R.H. Mathiesen, A. Borg, R. Bredesen, R. Holmestad, Microstructural studies of self-supported (1.5-10 μm) Pd/23 wt%Ag hydrogen separation membranes subjected to different heat treatments, Journal of Materials Science, 44 (2009), pp. 4429–4442.

[67] K. Zhang, S.K. Gade, Ø. Hatlevik, J.D. Way, A sorption rate hypothesis for the increase in H 2 permeability of palladium-silver (Pd-Ag) membranes caused by air oxidation, International Journal of Hydrogen Energy, 37 (2012), pp. 583–593.

[68] T.A. Peters, W.M. Tucho, A. Ramachandran, M. Stange, J.C. Walmsley, R. Holmestad, A. Borg, R. Bredesen, Thin Pd-23%Ag/stainless steel composite membranes: Long-term

stability, life-time estimation and post-process characterisation, Journal of Membrane Science, 326 (2009), pp. 572–581.

[69] T. Nakajima, T. Kume, Y. Ikeda, M. Shiraki, H. Kurokawa, T. Iseki, M. Kajitani, H. Tanaka, H. Hikosaka, Y. Takagi, M. Ito, Effect of concentration polarization on hydrogen production performance of ceramic-supported Pd membrane module, International Journal of Hydrogen Energy, 40 (2015), pp. 11451–11456.

CHAPTER 6: Conclusions and Recommendations

At the end of each chapter, there is a summary that is derived from the research findings of the topic presented in that particular chapter. This section provides a concise overview of the main findings made during the research, evaluates the initial goals established at the start, and presents a comprehensive perspective on the importance of the study. In addition to this, the present section also outlines potential avenues for future research and practical implementations based on the results of our study.

6.1. Conclusions

The main aim of the present study is to perform a comprehensive investigation of the design of membrane reformers and the production of fuel cell grade high-purity hydrogen through methanol steam reforming using Pd-Ag membrane. In order to achieve the objectives outlined earlier in Chapeter-1, a composite Pd-Ag membrane is prepared using the ELP technique over the alumina support. Multiple cycles of deposition are performed to obtain a dense Pd-Ag membrane till 400 kPaG. After the preliminary leak test, the membrane performance is examined by subjecting it to pure H_2 and N_2 under varying temperatures (573-773 K) and pressure (100-300 kPaG) conditions. The investigation also encompasses the examination of the effect of mixture gases, such as H_2/N_2, H_2/CO_2, H_2/CH_4, H_2/CO, and feed load on the performance of the membrane. In addition to this, the long-term thermal heat cycle stability of the membrane is performed to assess its potential for commercial exploitation. However, the effect of concentration polarization significantly reduces the H_2 permeation capacity of the membrane. Therefore, a multi-pass membrane separator is designed to have four passes and multiple feed injection facilities to enhance the H_2 recovery from the mixture gas. This configuration not only improved the regulation of the H_2 partial pressure across the separator but also optimized the interaction between the feed gas and the membrane. MPMS performance is tuned for various locations inside the separator, baffle proximity, feed load, and membrane-to-pass ratio. The study demonstrated that multi-pass membrane separators minimize concentration polarization. Additionally, multiple membranes with baffles improved the separator performance to a higher degree compared to the same case without baffles. After optimizing the MPMS, the same system is integrated with an additional membrane reformer unit to recover more hydrogen from the retentate side. The MR was packed with the SiC-foam-supported Cu-Fe/AZZ catalyst prepared via a wash-coating technique. The use of a SiC-based significantly reduced the heat and mass transfer issue in endothermic MSR, owing to its

exceptional thermal conductivity. Initially, the performance of the MR is evaluated with varying operational parameters such as WHSV, temperature (523-673 K), pressure (100-400 kPaG), and number of membranes. Last, the effect of adding MPMS is examined at the same operating parameters, and the entire system is termed a Double Stage Membrane Reformer. A comparative study of the MR and DSMR is done based on the various parameters including conversion, hydrogen recovery, hydrogen yield, H_2 production rate, and overall permeate H_2 purity. Following the present study, the overall conclusions of the thesis are as follows:

- The membrane was tested leak free till 400kPaG, and no pin-hole was observed in the bubble point test. H_2 flux increases with partial pressure difference and temperature following liner trend as per Sievert's Law and Arrhenius Law respectively. The H_2/N_2 selectivity was maintained even after 10 thermal cycles and 60 hours of continuous operation.
- Concentration polarization was more severe at higher pressure due to the build-up of a hydrogen-depleted layer adjacent to the membrane surface. Increasing the CO content significantly reduces the H_2 flux due to the combined effect of surface inhibition and a decrease in H_2 partial pressure. Increasing the feed flow rate increased the H_2 flux and finally reached a pseudo-plateau value due to surface saturation. Also, it has been noticed that by changing the concentration of H_2 in the feed mixture gas, while keeping the feed pressure constant at 300 kPaG and the temperature at 673 K, the saturation value is obtained at a lower feed load for mixture gas with a higher H_2 concentration.
- In the present study, it was observed that the baffles successfully enhanced the H_2 recovery and membrane utilization. Additionally, MPMS gives better control over the H_2 partial pressure radially due to localized turbulence and enhanced inter-mixing of the gases. Integrating the baffles further reduced the formation of dead zones and stagnant regions which helped to significantly enhance the hydrogen recovery. The effect of baffles was more pronounced for low feed loads and multiple membranes. Additionally, multiple membranes with baffles improved the separator performance to a higher degree compared to the same case without baffles.
- During the optimization of the MPMS performance, it was observed that the concentration polarization was more severe for downstream membranes in other passes compared to those membranes exposed to the fresh feed. The overall performance of the MPMS module that includes multiple membranes was

substantially influenced by the combined effect of membrane position and H_2 partial pressure in each pass. Furthermore, the appropriate distribution of feed gases in an MPMS was required to significantly enhance the overall efficiency by overcoming the radial mass transfer limitation. Therefore, it was realized that the proper feed distribution inside each pass was necessary to overcome the challenges associated with the reduced H_2 partial pressure.

- Feed distribution in each pass significantly improved the hydrogen recovery by 39% in MPMS compared to the same configuration without baffles. However, a significant decrease in H_2 recovery was observed at high feed load which remains a major bottleneck from a commercial point of view. The overall performance of the multi-pass membrane separator module that includes multiple membranes was substantially influenced by the combined effect of membrane position and H_2 partial pressure in each pass.
- Increasing the membrane-to-pass ratio didn't have a major change in the H_2 recovery when hung at the center compared to the inlet and outlet position. A trade-off between feed load, and H_2 recovery was important for the efficient utilization of the membrane. To facilitate scale-up, the MPR was increased from 0.25 to 2.5 by adding multiple membranes in different passes. The H_2 recovery exhibited a small decline of 2% when the MPR increased from 0.25 to 1.5. However, a significant reduction of 7% and 12% in H_2 recovery was noted when membranes were placed at the inlet (MPR = 2.0) and outlet (MPR = 2.5) of the separator, respectively, as compared to the MPR of 0.25. This was mainly due to the drop in the H_2 partial pressure in the downstream passes.
- The main scope of this study was to design an integrated double-stage membrane reformer that incorporates both MR and MPMS, functioning as a standalone separation module, to effectively separate the unrecovered H_2 from the retentate stream of the MR. Furthermore, the objective was to improve the radial heat and mass transfer characteristics of the packed bed catalyst by employing an interconnected 3D SiC scaffold, attributed to its superior thermal conductivity. 3D interconnected void space and framework of SiC-scaffold reduced heat and mass transfer limitations. The same conversion and H_2 yield were achieved with reduced catalyst loading and hence the cost was reduced.
- The Cu-Fe/AZZ/SiC catalyst was tested in all three configurations for comparison including TR, MR, and DSMR at 300 kPaG of pressure, 673 K of temperature, 3/1 of

S/C ratio, 187 cm^2 of membrane area, and 12.23 kg_{feed} h^{-1} $kg^{-1}_{catalyst}$ of WHSV. Following the performance testing, a higher methanol conversion was obtained in the case of DSMR. For instance, the methanol conversion of ~75 % was achieved in the case of DSMR compared to ~57% in MR and ~53% in TR. Moreover, H_2 recovery of more than 74.5% was achieved in DSMR which was 8.5% higher compared to MR. The integration of MPMS on the retentate side of the MR significantly helped to recover the leftover hydrogen from the retentate of the MR. Therefore, the DSMR configuration demonstrated superior performance compared to MR and TR in terms of methanol conversion and hydrogen production rates. The dual-stage configuration facilitated enhanced hydrogen separation and promoted equilibrium shifting.

6.2. Recommendations

Future perspectives are considered crucial in the realm of research initiatives. As science advances, it is frequently noted that we become aware of a greater number of unknowns than knowns. Therefore, forthcoming investigations should take into account the subsequent avenues to expand upon the findings of the present study.

- **For membrane preparation:** Ceramic supports are economical and offer narrow pore-size distribution compared to other supports such as PSS, and Hastelloy, which is an essential parameter for the deposition of a thin Pd-Ag layer. However, the presence of some big through-through pores makes it difficult to prepare a dense membrane at reduced thickness. Therefore, future work should focus on minimizing the surface pore size distribution of the support to prepare thin dense membranes (< 5 μm). Consequently, the cost of the membrane will also be reduced. Moreover, a methodology needs to be developed to reduce the steps required to prepare the membrane especially multiple annealing required after each deposition cycle. It increases the overall auxiliary cost and time required for the preparation of the membrane.

- **For membrane integration and stability:** The integration of ceramic-supported Pd-Ag membrane with the metallic reactor is a challenge and requires a special type of fittings comprising graphite ferrule. Gradual development of the pin-hole and degradation of the graphite ferrule during long-term operation is a major challenge, that needs to be taken care of to maintain the required purity of the permeate, particularly while using multiple membranes in the same separator. It is very difficult

to identify and replace the membrane responsible for the decrease in the selectivity. Therefore, future work should focus on the enhancement of the stability of the membrane and graphite ferrule, particularly for high-temperature operation (more than 773 K). The stability of the membrane may be compromised at elevated temperatures as a result of the increased bulk diffusion of H-atom. Additionally, silver atoms start migrating in the crystal structure of the Pd-Ag alloy with high energy above its Tamman temperature i.e. 617 K. Fitting the membrane with graphite ferrule is purely based on the hands-on practice to make it leak-proof. Additionally, multiple connections increase the overall stress over the membrane, as a result, there is a potential for membrane failure during the thermal heat cycle. Hence, it is advised to reduce the number of metallic fittings by using figure-like support and a mechanism needs to be developed to reduce the mechanical stress over the membrane.

- **For separator design:** A significant increase in hydrogen recovery was observed in multi-pass membrane separators while using multiple membranes. Additionally, feed distribution in each pass plays a critical role in maintaining the H_2 partial pressure across the membrane. However, the present study is limited to small-size membranes (~10 cm each) with a maximum of three membranes in each pass. It is anticipated that during scale-up more number of membrane will be required in each pass with increased length. As a result, a gradual development of the H_2-depleted boundary layer will be observed along the length of the membrane and less hydrogen will be available for separation for the latter part of the membrane. Therefore, a more robust separator design will be required in terms of feed distribution along the length of the membrane to maintain sufficient hydrogen concentration. It is suggested to carefully optimize the feed load and feed inlet position along the length of the membrane during scale-up based on the operating parameters and permeation characteristics of the membranes. For a stand-alone membrane separator multi-pass membrane separator is the best choice.

- **For structured catalyst:** The SiC foam-based interconnected 3D scaffold has shown promise as a support structure for coating catalysts, allowing for efficient utilization of the catalyst. Continuous interconnected cellular architectures facilitate radial mass transfer and promote local turbulence. The high thermal conductivity of SiC foam further intensifies the heat transfer. However, the better adherence of the catalyst particle to the support is critical at high WHSV, particularly for methanol steam

reforming where it takes just a fraction of a second to complete the reaction. Therefore, proper methodology for catalyst coating is necessary. Future research should focus on the exploration of effective methods for loading and dispersing catalytic materials on SiC foam. Techniques like atomic layer deposition (ALD) and chemical vapor deposition could ensure a uniform distribution of catalyst particles, enhancing the overall catalytic performance. In addition to this, the pore structure of SiC foam should be optimized to maximize surface area and improve mass transport properties. Future studies may explore the possibility of using computational modeling and advanced manufacturing techniques, such as 3D printing in designing optimal pore architectures. SiC foam should be designed to accommodate the membrane coaxially. Multiple SiC foams can be staked around the membrane based on the membrane permeability, feed flow rate, and operating parameters.

- **For membrane reformer and scale-up:** The integration of hydrogen generation and separation process in a single reactor unit enhances the conversion rate and overall efficiency. However, operating parameters, amount of catalyst, and membrane area need to be carefully optimized based on the feed load and the desired permeate hydrogen output. During scale-up, special attention should be given to the design of the reactor system to accommodate the adverse effects of heat and mass transfer. Therefore, it is suggested to use multiple tubular membrane reformers with small diameters and single membranes, packed around each other as per the requirement of hydrogen production rate. Optimizing the performance of the single reformer unit will be relatively easy. Moreover, in the case of membrane failure, it will be easy to identify and replace the concerned unit quickly or its usability can be temporarily stopped to maintain the permeate purity. In order to separate more hydrogen from the retentate an additional auxiliary multi-pass membrane separator unit may also be considered depending upon the budget and feasibility study. Furthermore, burning the waste retentate stream may be explored to meet the energy requirements of the reactor as well as the separator instead of using the electrically operated heater. The possibility of integrating the carbon capture unit should be considered to achieve a more green process. It is also advised to integrate the system with a solar panel with a battery management system to power the entire system during the initial startup process and even during standby.

- **For catalyst support and membrane reusability:** Long-term operation has shown that the catalyst and membrane experience a decline in their initial performance over time. Therefore, it is recommended to establish a more resilient system for swiftly and effortlessly replacing the catalyst and membrane. In order to restore the original performance, it is necessary to completely recover the catalyst support and apply a new coating of fresh catalysts. To ensure the desired conversion rate and H_2 yield, it is crucial to minimize the fluctuations in catalyst performance. Replacing a membrane with a new one, while the old membrane is being repaired or recycled, necessitates a methodical investigation. In this scenario, it is crucial that the performance of both the repaired and replacement membranes closely resemble the original qualities.
- **For more advanced reactor and process simulation models:** Developing advanced reactor and process simulation models for baffled-membrane reactors utilizing Pd-Ag membranes for hydrogen separation through MSR over Cu-Fe/AZZ catalysts coated on SiC foam necessitates a comprehensive multiphysics and multiscale modeling approach. Models must incorporate comprehensive MSR kinetics, accounting for side reactions, alongside non-isothermal behavior resulting from the endothermic characteristics of reforming. Mass transport phenomena require precise modeling to accurately represent hydrogen permeation through the Pd-Ag membrane according to Sieverts' law, while accounting for changes in permeance influenced by temperature, pressure, and membrane life. Parameters including membrane position, proximity from the baffles, MPR, and feed distribution need to be accounted for modeling. CFD simulations must address flow distribution, velocity fields, and temperature gradients across different baffle configurations to enhance reactor hydrodynamics. Catalyst performance modeling must incorporate experimentally obtained kinetic parameters, effectiveness factors, and mechanisms of deactivation. Dynamic and steady-state simulations utilizing platforms such as COMSOL, or Aspen Custom Modeler are advisable for assessing reactor performance. Important conditions encompass temperature, pressure, steam-to-methanol ratio, membrane area, and baffle geometry, aiming to balance conversion efficiency, hydrogen recovery, and purity. Experimental validation with lab-scale baffled-membrane reactors is essential for model calibration and enhancing reliability. Modular scale-up strategies must be analyzed, integrating heat management and optimizing system-level processes to facilitate efficient hydrogen production for downstream applications such as PEM fuel cells.

BIO – DATA:

Name: Keshav Kumar

Date of Birth: 16th August 1996

Place of Birth: Samastipur, Bihar, India

Email: kumar176107017@iitg.ac.in / thekeshavchoudhary@gmail.com

Mobile: 7979039554 / 9472823457

Educational Qualifications:

Degree/Course	University/Board	Year
Ph.D. (Chemical Engineering)	Indian Institute of Technology Guwahati, Assam, India	2025
B. Tech. (Chemical Engineering)	National Institute of Technology Hazratbal, J&K, India	2017
Intermediate (12th) (Science)	Central Board of Secondary Education, New Delhi, India	2013
High School (10th)	Central Board of Secondary Education, New Delhi, India	2011

Conferences Presented (National / International):

1. "Pd-alloy/Al_2O_3 membrane using hybrid electroless pore plating and magnetron sputtering for ultra-pure hydrogen production through membrane reactor", ***Keshav Kumar***, Amit Kumar, and Rajesh Kumar Upadhyay, **ISCRE-26 and APCRE-9**, New Delhi, India, 5-8 December 2021. (**Oral**)
2. "Preparation and testing of $Pd_{60}Cu_{40}/Al_2O_3$ membrane for production of ultra-pure hydrogen in membrane separator for low-temperature application", ***Keshav Kumar***, Amit Kumar, and Rajesh Kumar Upadhyay, **RIC-2022**, Guwahati, India, 20-23 January 2022. (**Oral**)
3. "Enhanced hydrogen recovery using Pd-Ag-based membrane by channelizing the gas flow pattern in multi-pass membrane separator", ***Keshav Kumar***, Amit Kumar, and Rajesh Kumar Upadhyay, **HEET-5**, Osaka, Japan, 18-19 November 2022. (**Oral**)

4. "On the preparation, testing, and stability of $Pd_{60}Cu_{40}/Al_2O_3$ membrane using electroless pore plating for hydrogen separation at low temperature", Sachin Kumar Vishwakarma, ***Keshav Kumar***, and Rajesh Kumar Upadhyay, **ISPT-2022**, Online, China, 10-14 December 2022. (**Poster**)

5. "Comparative study of hydrogen recovery through membrane reactor and multi-pass membrane reactor via methanol steam reforming", ***Keshav Kumar***, Punampriya Borgohain, Amit Kumar, and Rajesh Kumar Upadhyay, **CHEMCON-2022**, Kanpur, India, 27-30 December 2022. (**Oral**)

6. "Methanol steam reforming over nanostructured ceria supported copper catalyst for PEM fuel cell applications", Punampriya Borgohain, ***Keshav Kumar***, Pankaj Tiwari, and Rajesh Kumar Upadhyay, **CHEMCON-2022**, Kanpur, India, 27-30 December 2022. (**Oral**)

7. "Separation of hydrogen from Pd-Cu/α-Al_2O_3 based membrane prepared by the hybrid method of magnetron sputtering and targeted electroless plating", Abhishek Anand, ***Keshav Kumar***, Om Prakash Pratape, Satya Vir Singh, and Rajesh Kumar Upadhyay, **CHEMCON-2022**, Kanpur, India, 27-30 December 2022. (**Oral**)

8. "Preparation, testing, and stability of $Pd_{60}Cu_{40}/ Al_2O_3$ membrane using electroless pore plating for hydrogen separation at low temperature", Sachin Kumar Vishwakarma, ***Keshav Kumar***, Rahul Sharma, and Rajesh Kumar Upadhyay, **CHEMCON-2022**, Kanpur, India, 27-30 December 2022. (**Oral**)

9. "Catalyst and membrane optimization for hydrogen production via methanol steam reforming in multi-pass membrane reactor", ***Keshav Kumar***, Amit Kumar, and Rajesh Kumar Upadhyay, **RCON-2023**, Indore, India, 20-22 January 2023. (**Poster**)

10. "A comparative scale-up analogy of traditional Vs multi-pass membrane separator module for enhanced H_2 recovery", ***Keshav Kumar***, Sachin Kumar Vishwakarma, Amit Kumar, and Rajesh Kumar Upadhyay, **ICPHD-2023**, Guwahati, India, 03-05 November 2023. (**Poster**)

11. "Investigation of circular baffles on the performance of Pd-Ag membrane module for hydrogen separation: Effect of baffle pitch and aperture ratio", Sachin Kumar Vishwakarma, ***Keshav Kumar***, and Rajesh Kumar Upadhyay, **ICPHD-2023**, Guwahati, India, 03-05 November 2023. (**Oral**)

12. "Series-parallel configuration of the double-stage membrane separator for improved hydrogen recovery through Pd-Based membrane", ***Keshav Kumar***, Sachin Kumar Vishwakarma, Amit Kumar, and Rajesh Kumar Upadhyay, **HEET-6**, Osaka, Japan, 10-11 November 2023. (**Oral**)

13. "Preparation, testing, and thermal-cycle stability of thin Pd-Cu/SBA-15/Al_2O_3 (< 5 µm) membrane for hydrogen separation", Abhishek Anand, ***Keshav Kumar***, Rahul Sharma, Satya Vir Singh, and Rajesh Kumar Upadhyay, **HEET-6**, Osaka, Japan, 10-11 November 2023. (**Oral**)

14. "Effect of circular baffle pitch and annular spacing over concentration polarization in Pd-Ag membrane to enhance H_2 recovery", Sachin Kumar Vishwakarma, ***Keshav Kumar***, and Rajesh Kumar Upadhyay, **HEET-6**, Osaka, Japan, 10-11 November 2023. (**Oral**)

15. "Performance study and scalability of multi-pass membrane separator for improved hydrogen recovery using palladium-based membrane", ***Keshav Kumar***, Sachin Kumar Vishwakarma, Amit Kumar, and Rajesh Kumar Upadhyay, **CHEMCON-2023**, Kolkata, India, 27-30 December 2023. (**Best Paper Award, Oral**)

16. "Effect of concentration polarization in Pd-Ag membrane and enhance H_2 recovery", Sachin Kumar Vishwakarma, ***Keshav Kumar***, and Rajesh Kumar Upadhyay, **CHEMCON-2023**, Kolkata, India, 27-30 December 2023. (**Oral**)

17. "Experimental investigation of double-stage membrane reformer (DSMR) for hydrogen production via methanol steam reforming", ***Keshav Kumar***, Sachin Kumar Vishwakarma, Amit Kumar, and Rajesh Kumar Upadhyay, **RIC-2024**, Guwahati, India, 09-11 August 2024. (**Oral**)

18. "Performance optimization and scale-up of Pd-Ag-based catalytic membrane reformer for on-site hydrogen production via methanol steam reforming", ***Keshav Kumar***, Amit Kumar, and Rajesh Kumar Upadhyay, **RIC-2024**, Guwahati, India, 09-11 August 2024. (**3-minute Thesis Presentation**)

Publications (Journals):

1. "Design Study of Multi-pass Membrane Separator for Improved Hydrogen Recovery Using Pd-Ag Membranes for On-site Hydrogen Generation", ***Keshav Kumar***, Sachin

Kumar Vishwakarma, Amit Kumar, and Rajesh Kumar Upadhyay **(Submitted in 'Chemical Engineering Research and Design' Under Review)**

2. "Experimental Investigation of Double-Stage Membrane Reformer (DSMR) for Enhanced Hydrogen Production via Methanol Steam Reforming", ***Keshav Kumar***, Sachin Kumar Vishwakarma, Amit Kumar, and Rajesh Kumar Upadhyay **(Submitted in 'Journal of the Energy Institute', Under Review)**

3. "Experimental Investigation of Circular Baffles Pitch and Aperture Ratio on the Concentration Polarization of Pd-Ag Membrane Module for Enhanced Hydrogen Separation" ***Sachin Kumar Vishwakarma***, Keshav Kumar, and Rajesh Kumar Upadhyay **(Submitted in 'International Journal of Hydrogen Energy', Under Review)**

4. "Influence of the gas phase resistance on the performance of 2B-graphite modified Pd-Ag/α-Al_2O_3 membrane for hydrogen purification", ***Keshav Kumar***, Amit Kumar, and Rajesh Kumar Upadhyay **(Manuscript to be communicated)**

5. "On the effect of concentration polarization in the palladium-based membrane for hydrogen separation: A review", ***Keshav Kumar***, Amit Kumar, and Rajesh Kumar Upadhyay **(Manuscript to be communicated)**

Date: 13th June, 2025 **Keshav Kumar**